Professional Development Course

AMR/GMR Read Heads, Materials and Devices

Material For Magnetic Recording Heads

by Bruce A. Gurney

&

AMR, GMR/Spin Valve Read Heads and Write Heads

by Edgar M. Williams

Sponsored by:

The Institute for Information Storage Technology

Materials For Magnetic Recording Heads

Bruce A. Gurney
IBM Almaden Research Center
gurney@almaden.ibm.com

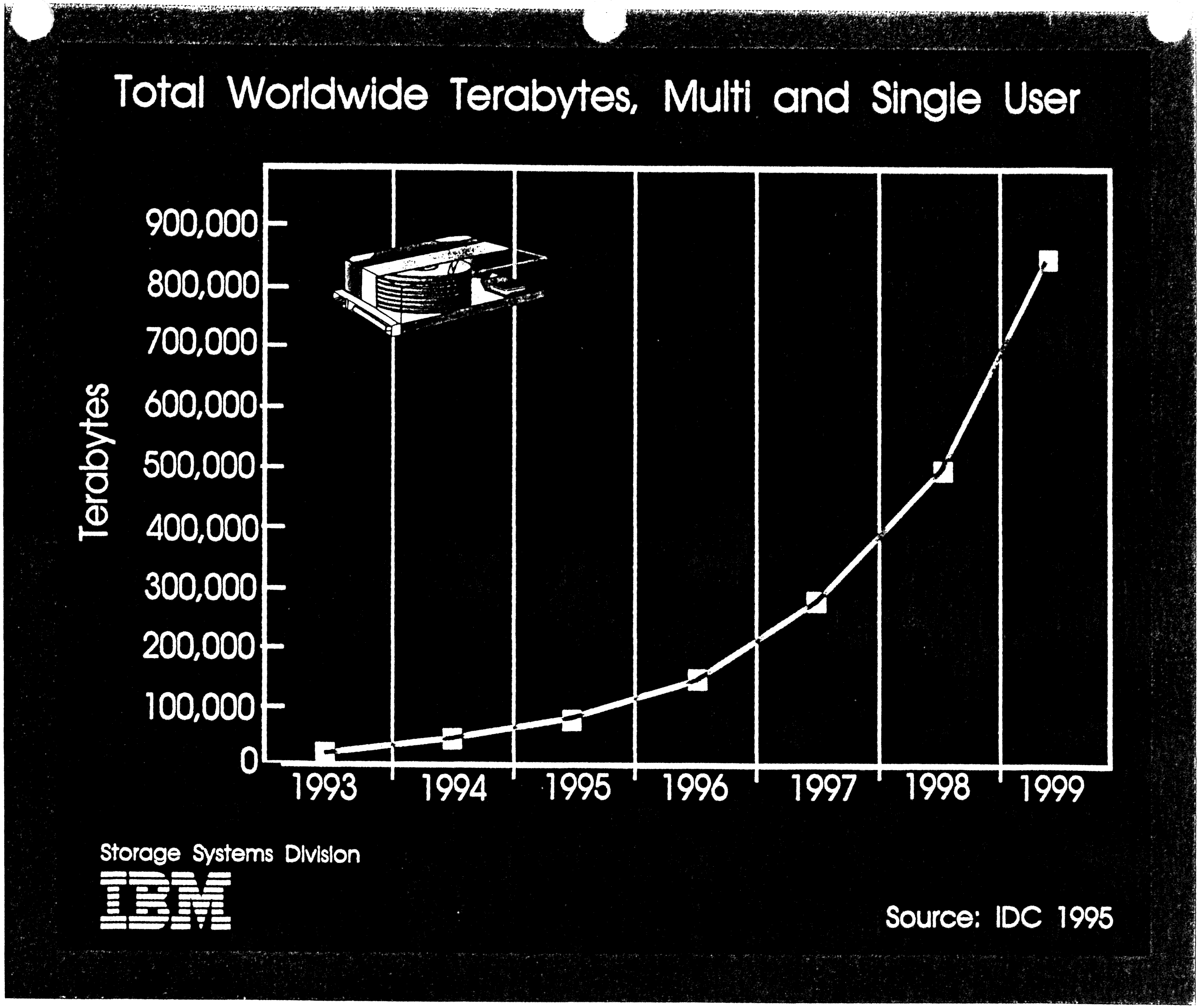

GRCHWSKI at ALMADEN

ANALST5B.CDR

price of storage

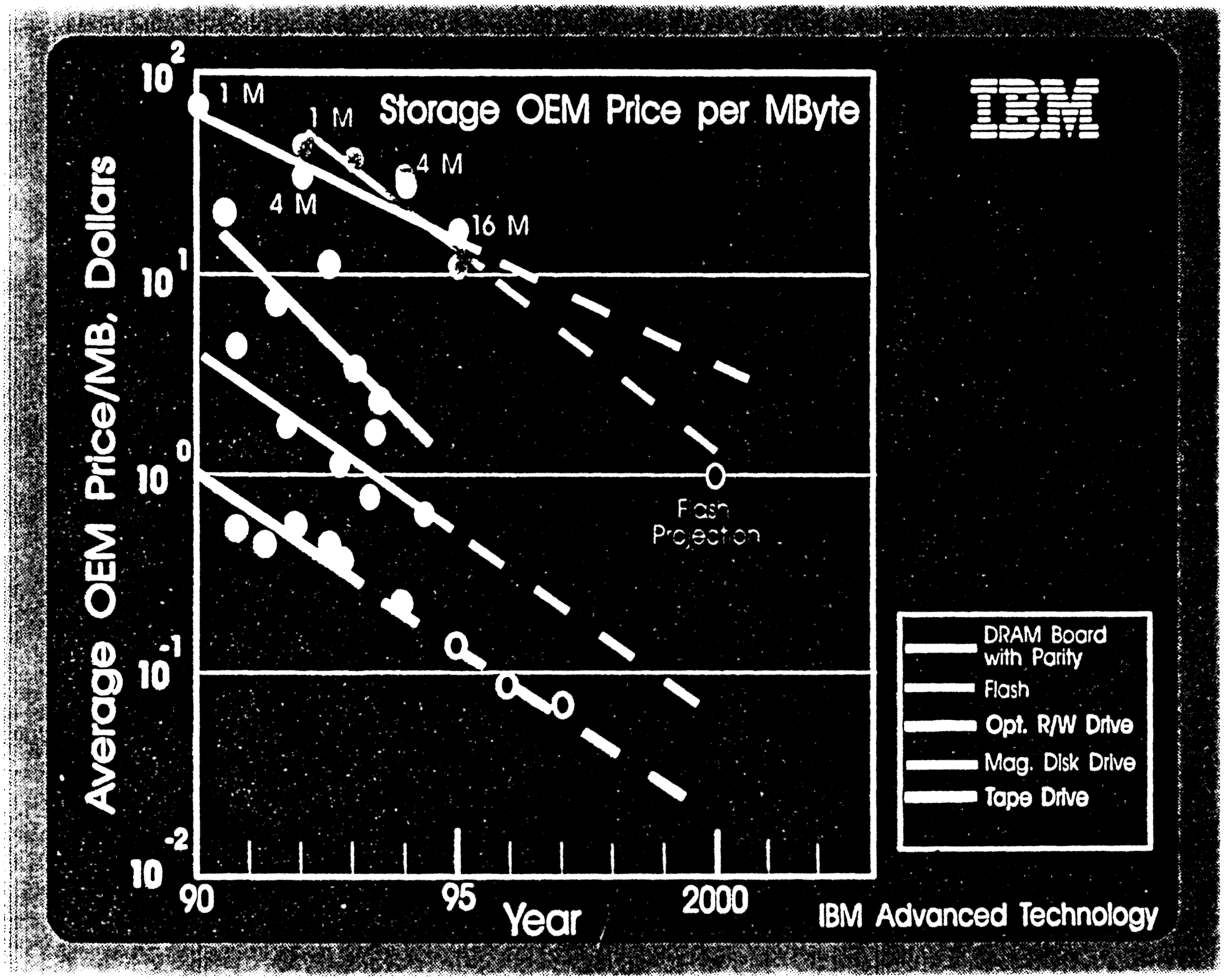

GRCHWSKI at ALMADEN

Hard Disk Drive Components Business

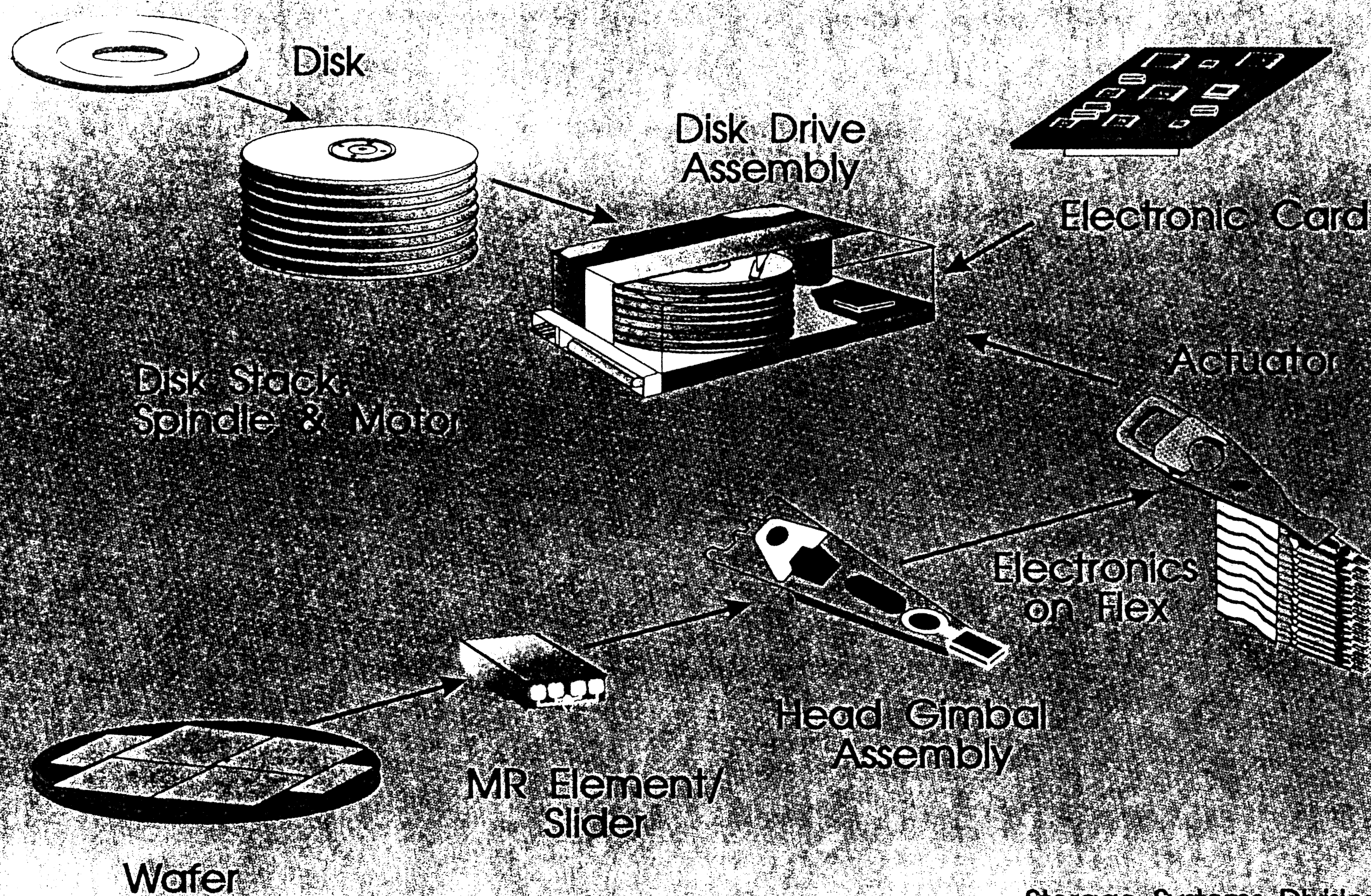

Storage Systems Division

IBM Advanced Technology

ANALYSTZ.CDR

yearly delivered units

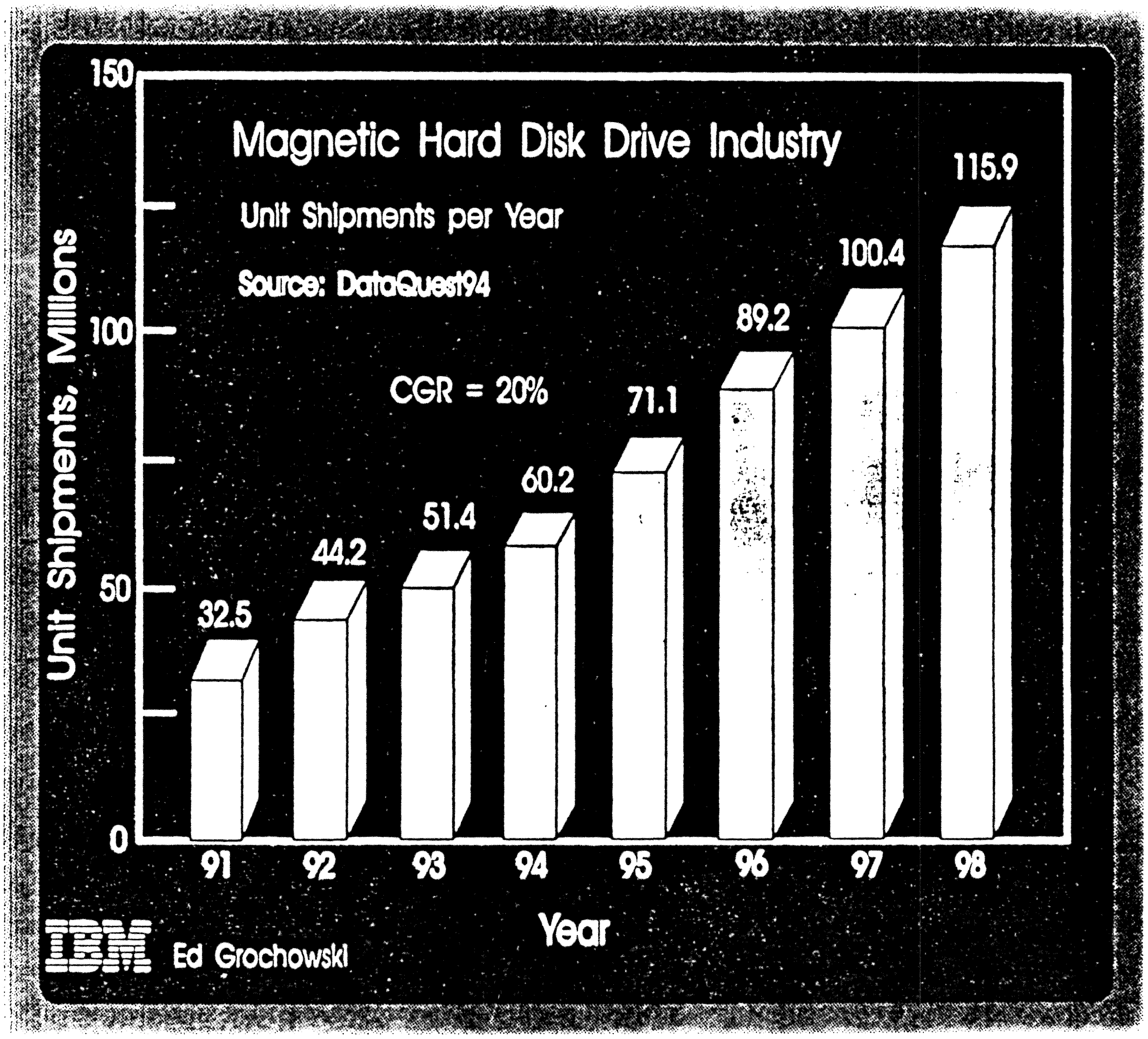

yearly delivered capacity

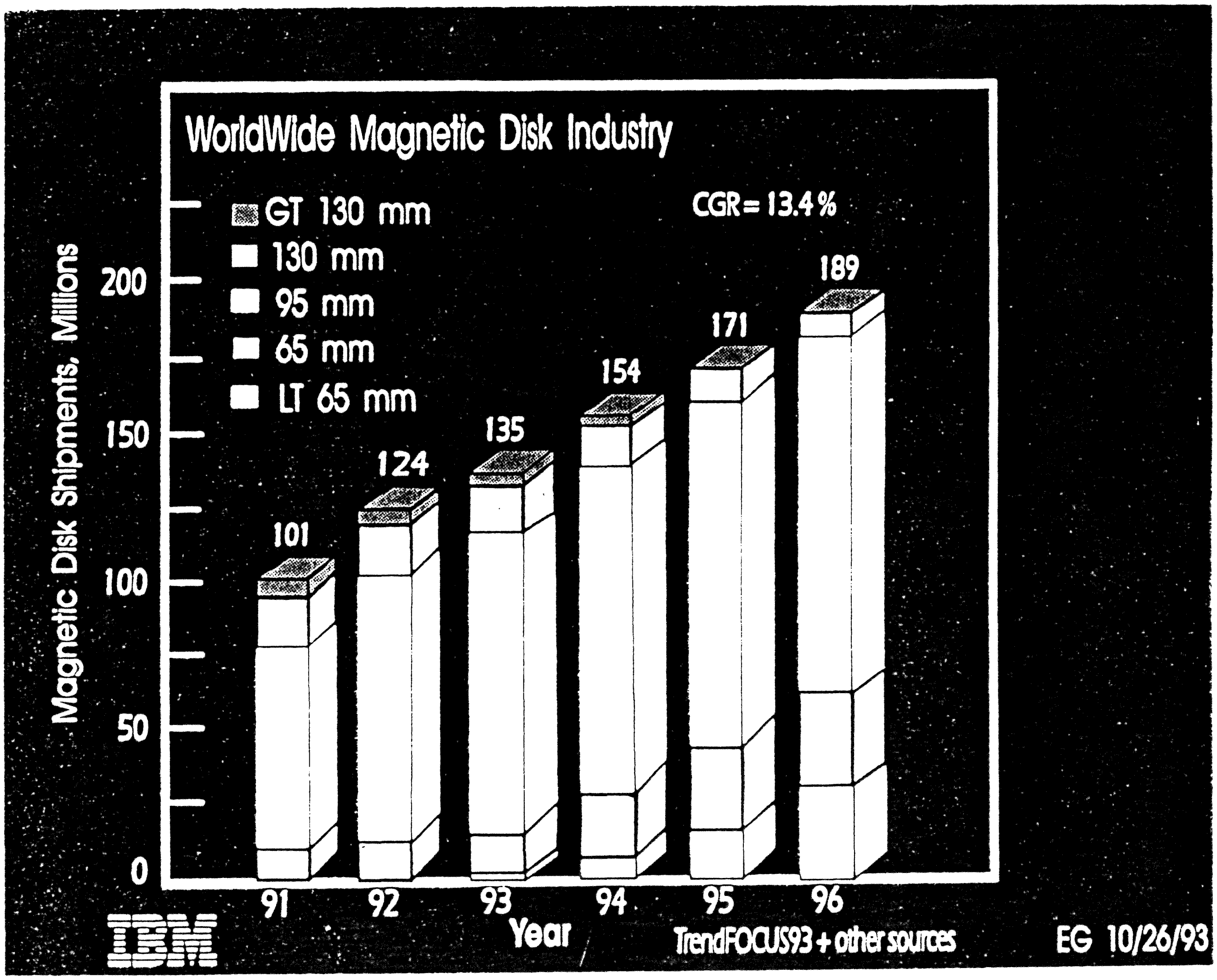

magnetic head industry

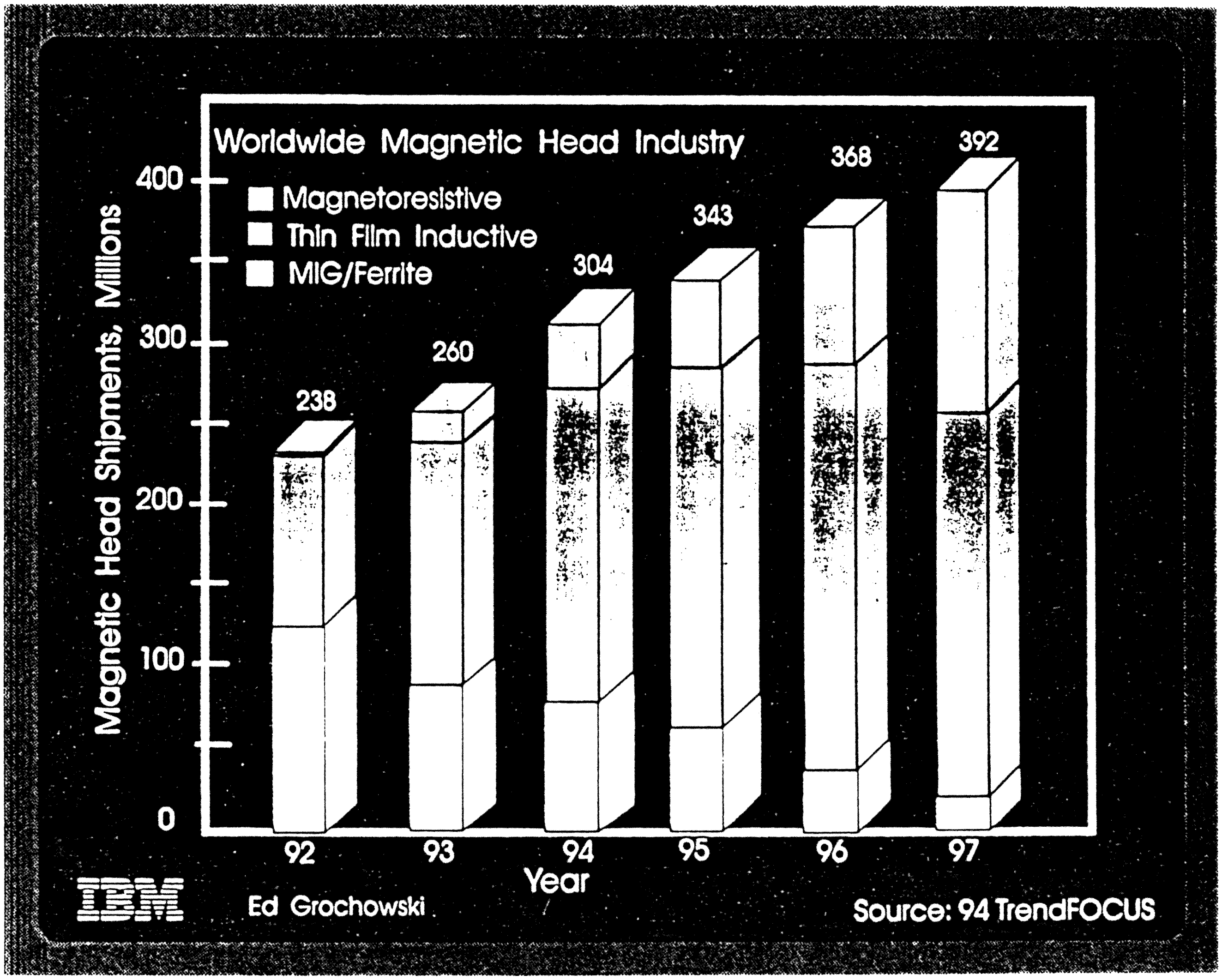

magnetic recording hard disk drive

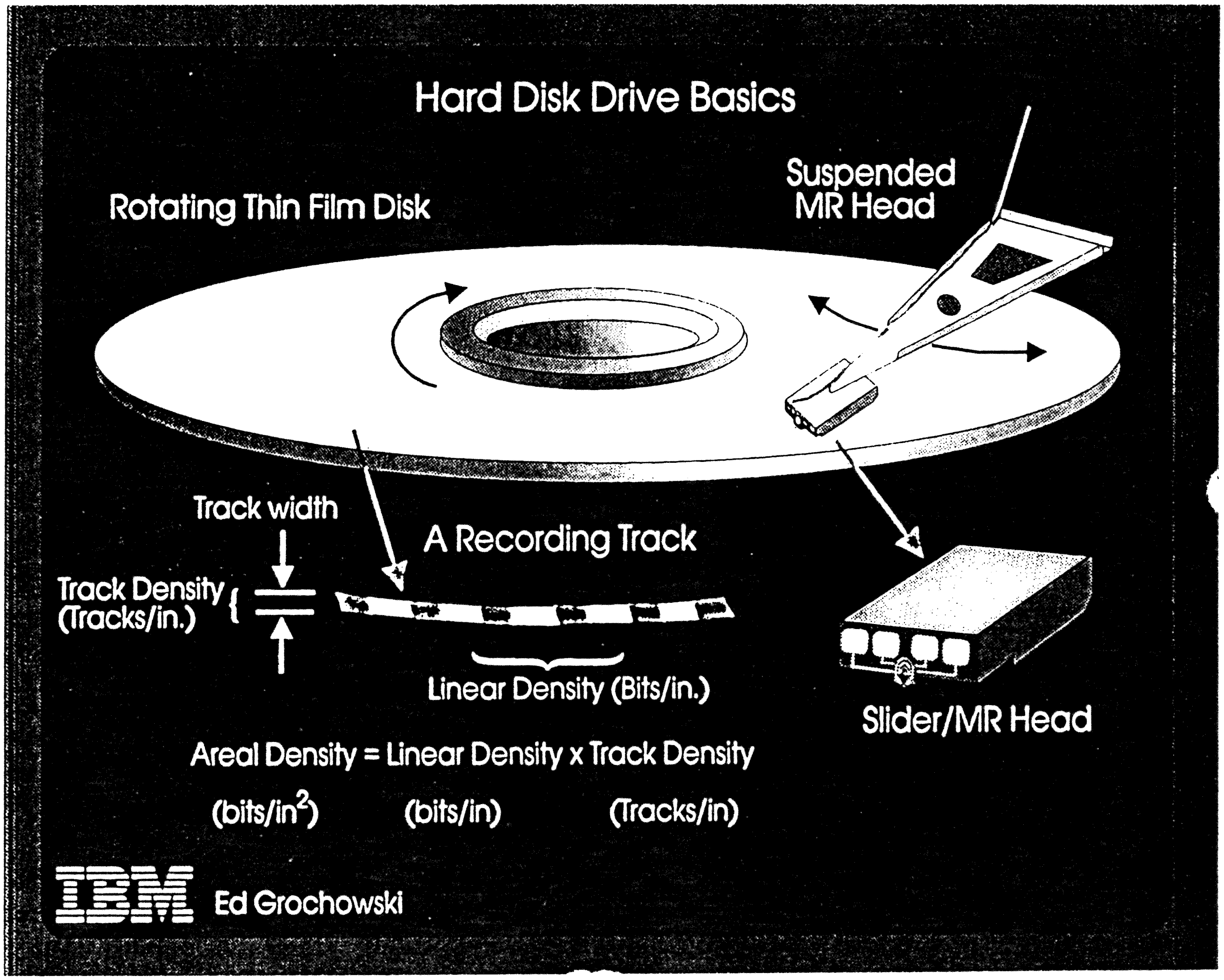

magnetic recording

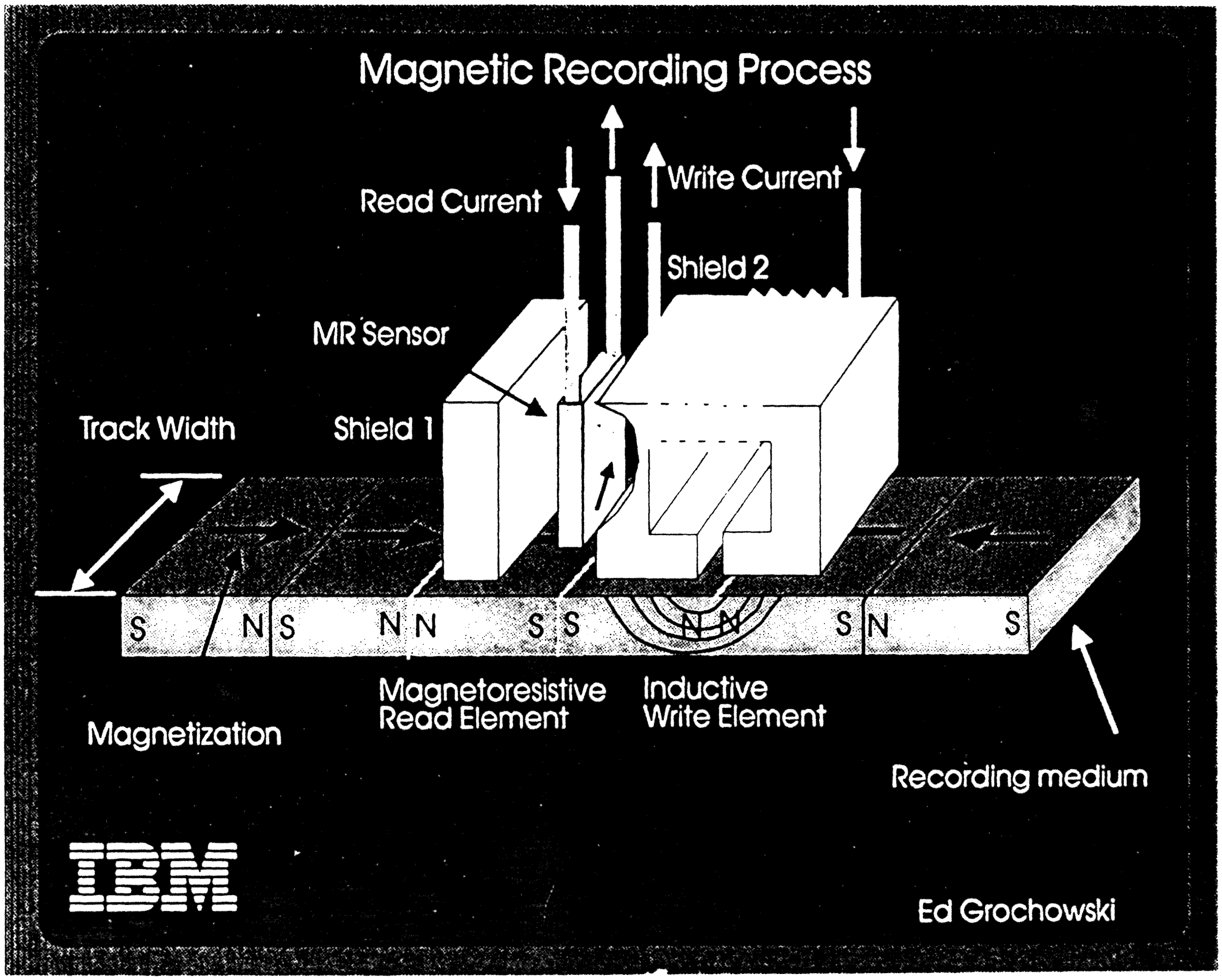

magnetic recording

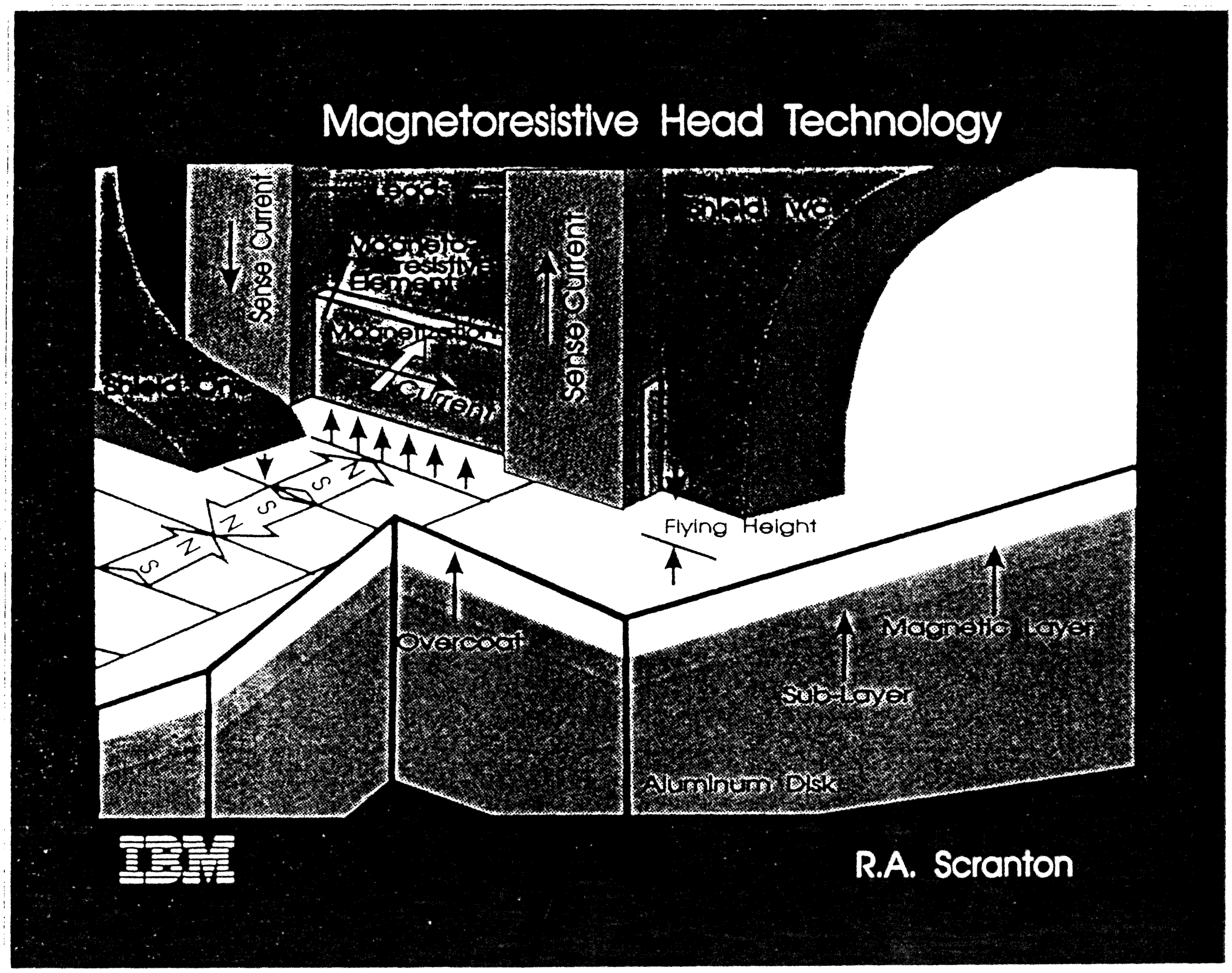

head/media spacing

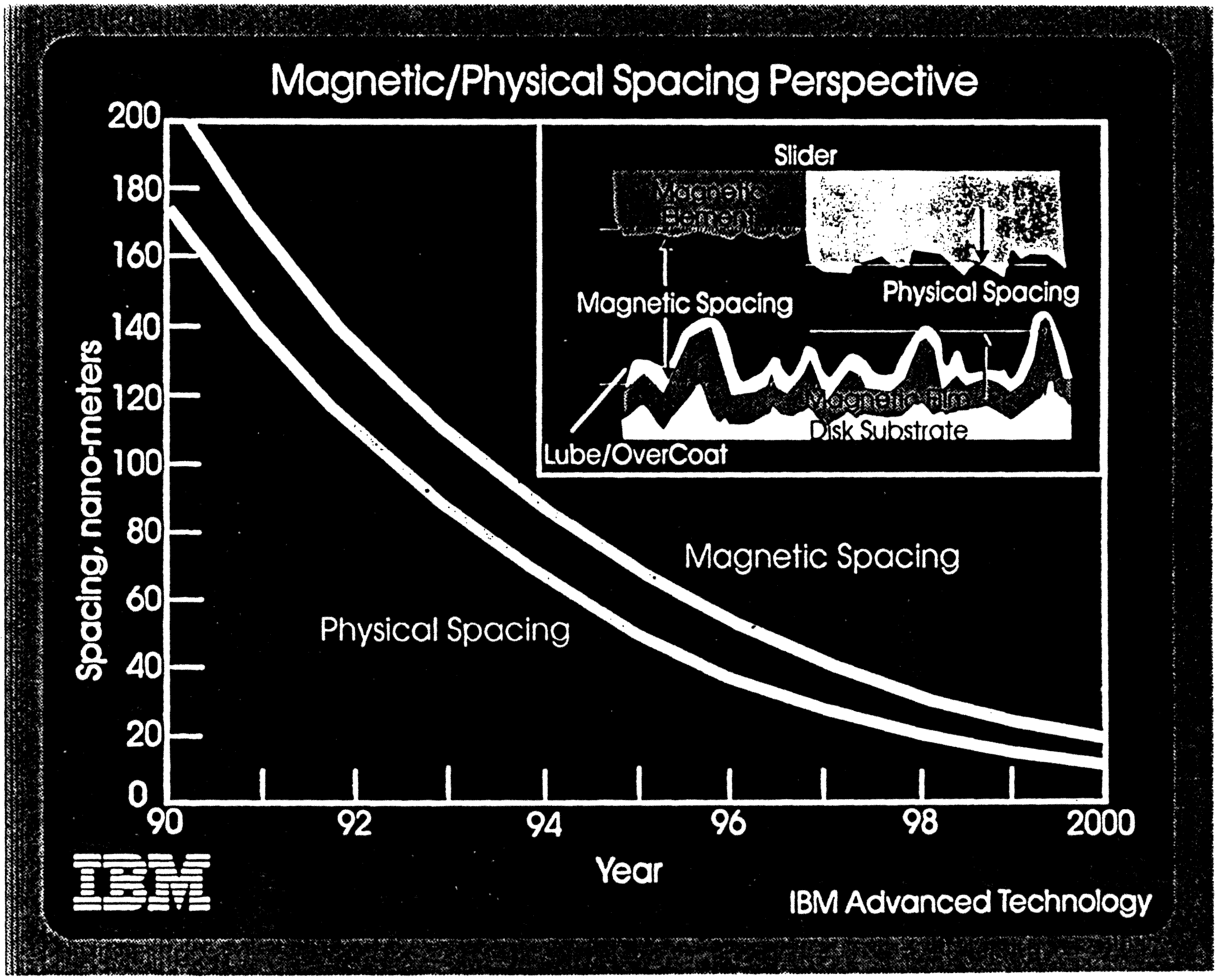

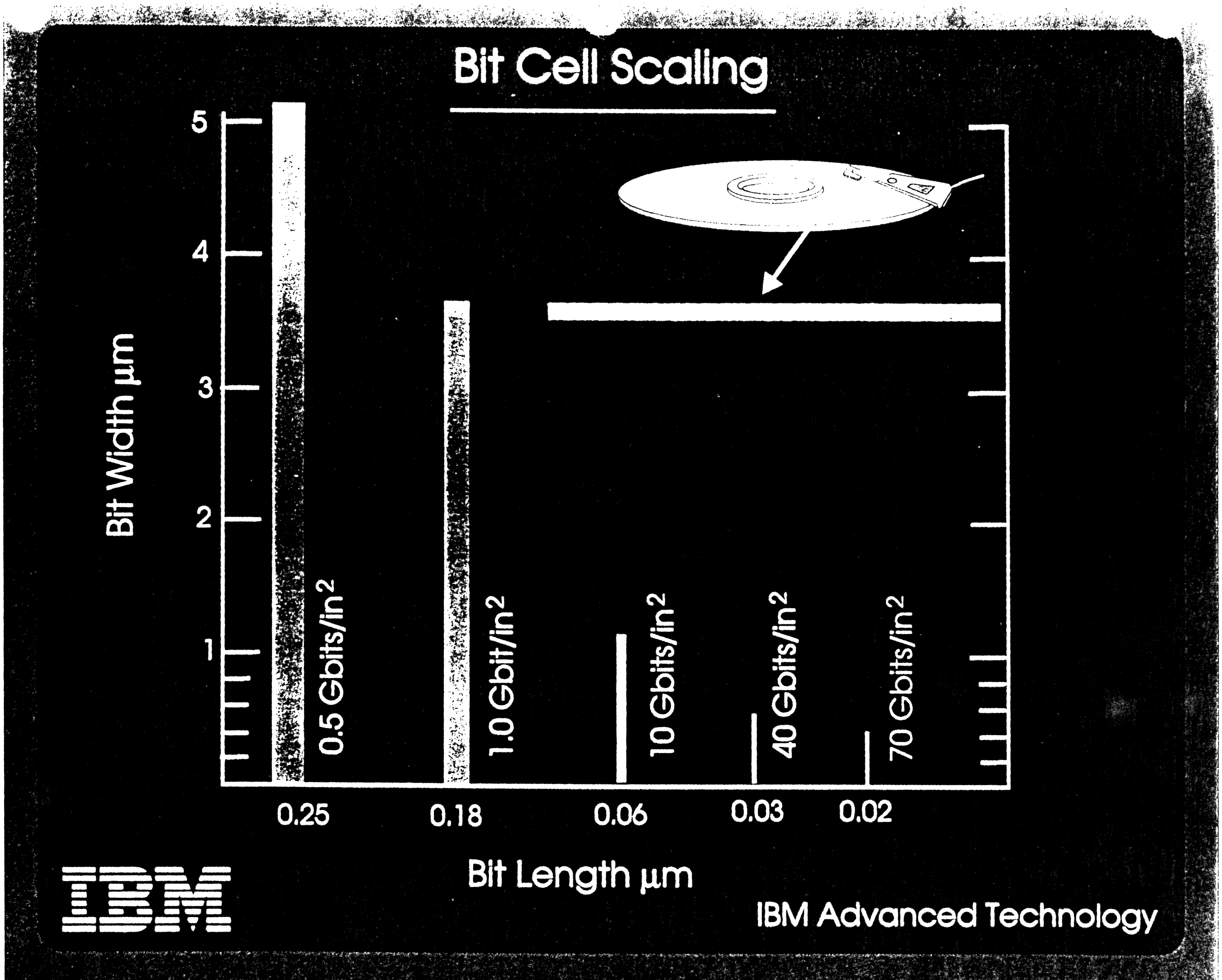

RABCM96N.CDR

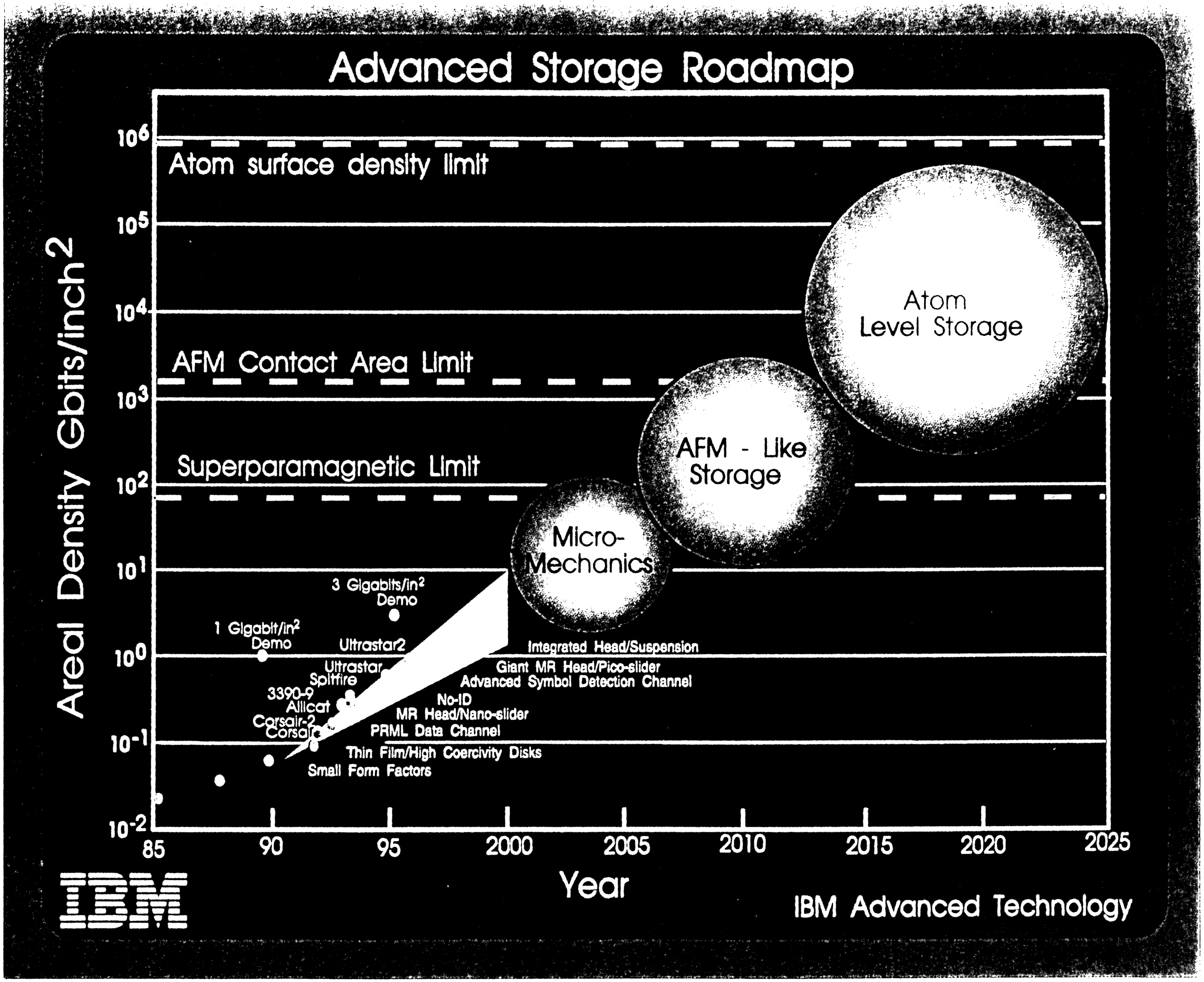

ADVRDMPM.PS8IN

areal density

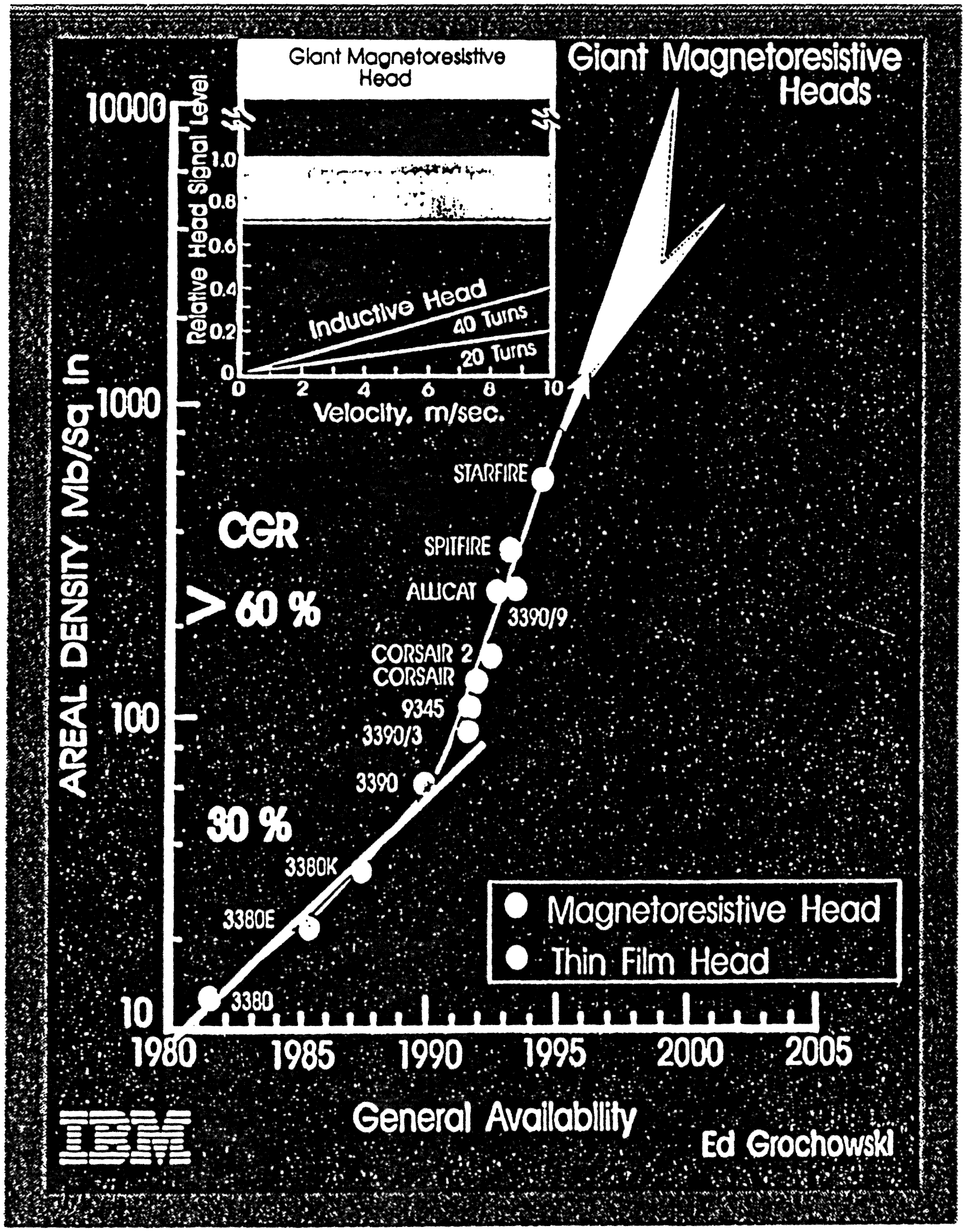

Ansiotropic Magnetoresistance[1]

- $\frac{\Delta R}{R} = A_{AMR} \times \cos^2[\theta_{magnetization} - \theta_{current}]$

- origin: spin - orbit interaction

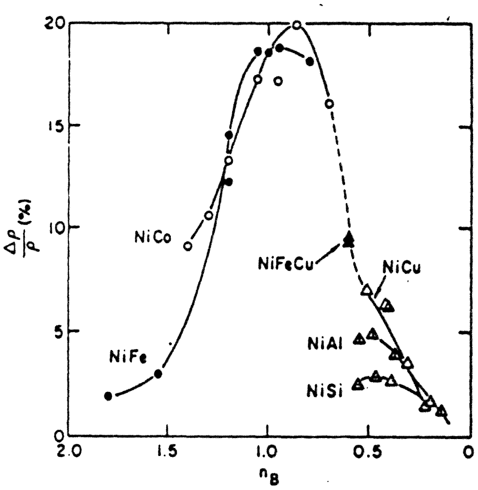

Fig. 14b. Anisotropic magnetoresistivity ratio at 20°K plotted against number of Bohr magnetons, n_B, for Ni-Co (○), Ni-Fe (●), Ni-Cu (△), Ni-Fe-Cu (▲), Ni-Al (△), Ni-Si (△), and Ni-Zn (x) (Van Elst [10]).

TABLE III
Ternary Alloys

Alloy	Temp °K	$\Delta\rho/\rho_0$ %	ρ_0 μΩcm	$\Delta\rho$ μΩcm	$4\pi M^*$ G	n_B^*	T_c^* °K	Ref	Comment
$Ni_{.69}Fe_{.16}Cu_{.14}$	20	3.30	12.2	.36	8640			71	g
$Ni_{.922}Fe_{.025}Cu_{.045}$	RT	3.6	14.4	.52				10	
	77	8.3	5.34	.45					
	14	9.5	4.51	.43		.6			
$Ni_{.845}Fe_{.047}Cu_{.108}$	RT	3.3	19.1	.59				10	
	77	8.2	9.95	.82					
	14	9.2	8.86	.83		.6			
$Ni_{.355}Co_{.496}Cu_{.153}$	RT	3.3	17.3	.57	11000			70	
$Ni_{.80}Fe_{.163}Mn_{.037}$	RT	2.2	28.6	.62	10200			70	h
$Ni_{.13}Fe_{.15}Mn_{.11}$	RT	0.4	64	.25	8400			70	h
$Ni_{.24}Co_{.60}Zn_{.17}$	RT	.7	27.8	.20				70	

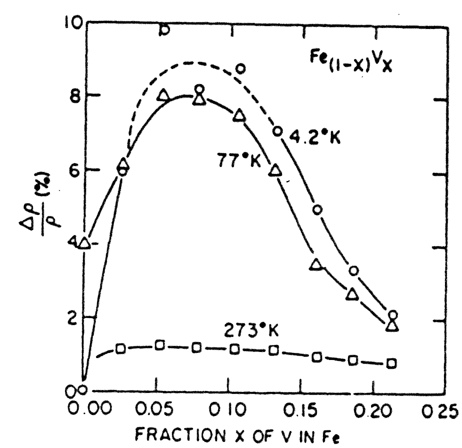

Fig. 21. A plot of the anisotropic magnetoresistivity ratio as a function of alloy composition for $Fe_{1-x}V_x$ (Sueda and Fujiwara [67]).

[1]T.R. McGuire, et al., IEEE Trans. Mag. 11, 1018 (1975).

AMR Recording Sensor[2]

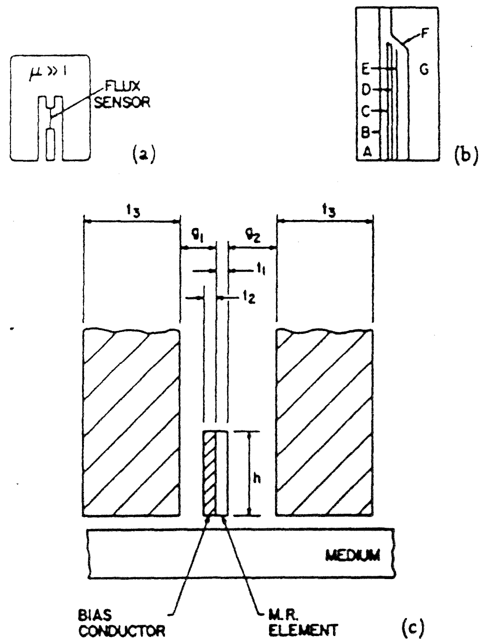

Fig. 10. (a) Conceptual sketch of a shielded magnetoresistive head. (b) Close-up of the magnetoresistive sensor: A is the ferrite substrate. B is the initial SiO_2 gap (2,000 A). C is the permanent magnet bias layer containing 75 A Ti, 150 A Fe (then oxidized, 250 A Ni-Fe and 75 A Ti. D is a spacer layer of SiO_2 (1,000 A). E is the magnetoresistive film (200 A). F is a SiO_2 gap (3,500 A). G is the permalloy shield, part of the write head [23]. (c) Shunt biased magnetoresistance sensor. Biasing is obtained by passing a portion of the excitation current through a conductive nonmagnetic layer in intimate contact with the magnetoresistance element. The element is offset in the gap so that the coupling with one shield is enhanced [27].

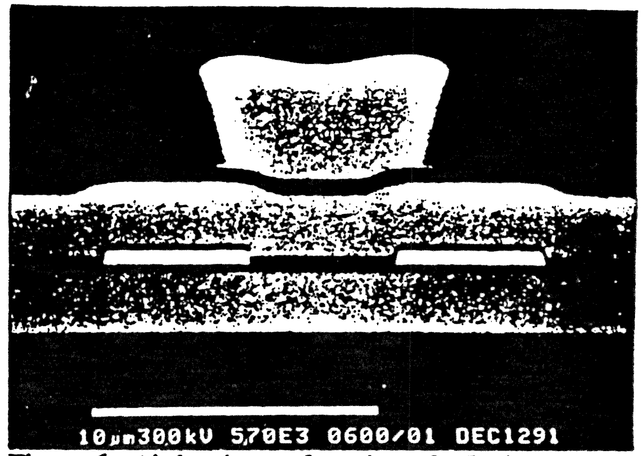

Figure 6. Air bearing surface view of a 5 micrometer track width MR head with combined pole/shield layer. Read gap-to-trailing pole dimension is 3 micrometers.

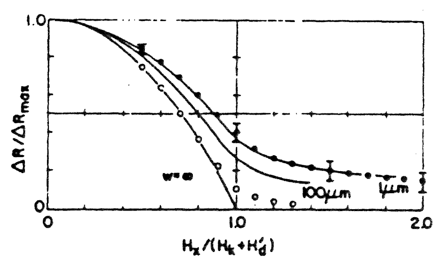

(b)

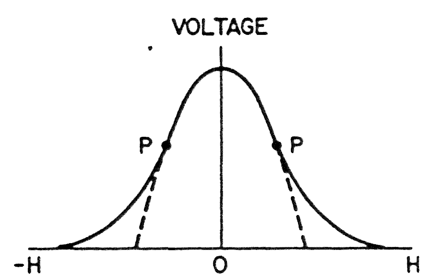

Fig. 8. (a) The effect of demagnetization due to strip width on t anisotropic magnetoresistance ratio. The solid curves are calculate The data for all stripe widths (3 to 100 μm) and film thickness (' or 200 A) fall within the error bars of the single set of data poin This is because the horizontal scale has been normalized using t demagnetizing field $H_d' = (tM)/(\mu_0 w)$. This scaling differs by factor of twenty among different samples. (b) Magnetoresisti curve showing biased operating point P. The dashed curve sho the ideal quadratic shape that would apply in the absence of dem: netizing effects.

---

[2] D.A. Thompson, et al., IEEE Trans. Mag 11, 1039 (1975), F.B. Shelledy, et al., IEE Trans. Mag. 28, 2283 (1992).

Magnetic Head Design

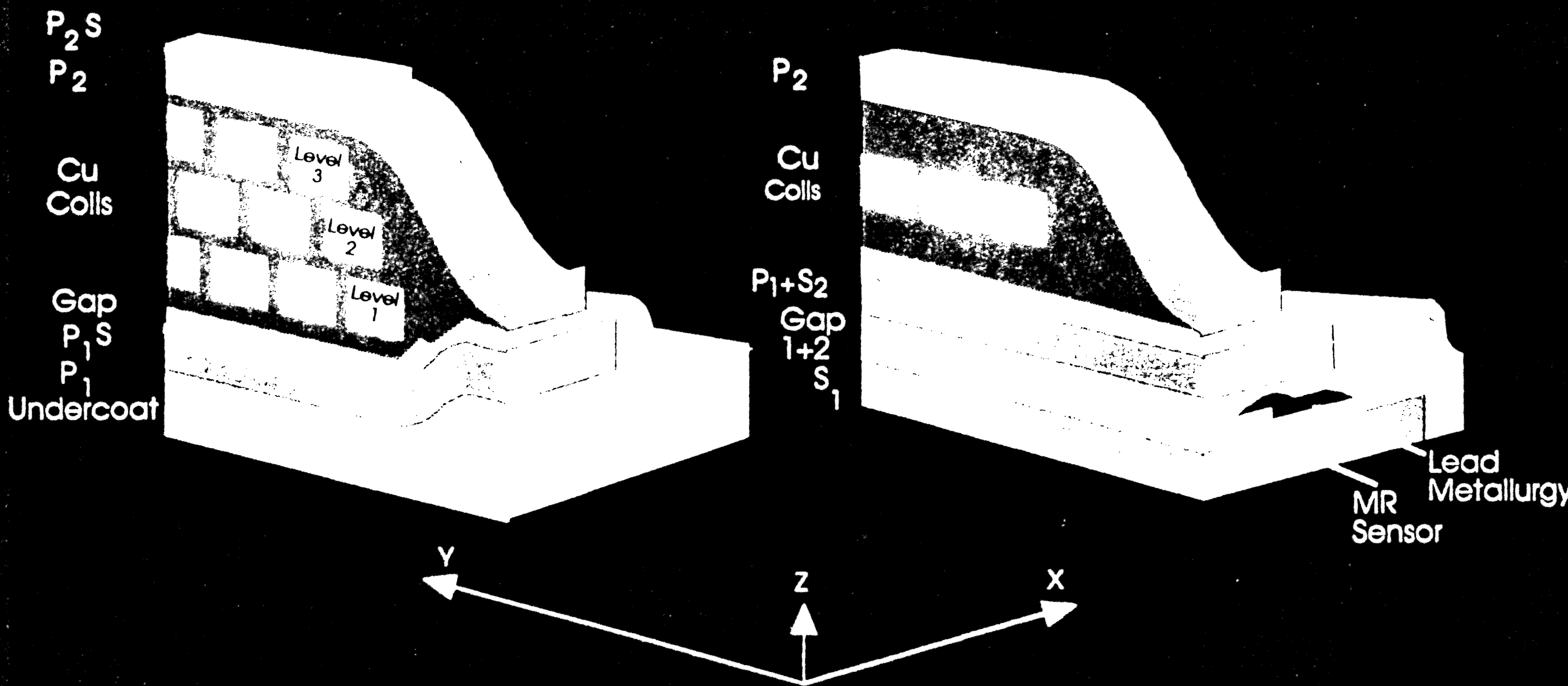

Thin Film Inductive Head Design

Merged MR Head Design

IBM

Ed Grochowski

GRCHWSKI at ALMADEN

Advanced MR Head Designs

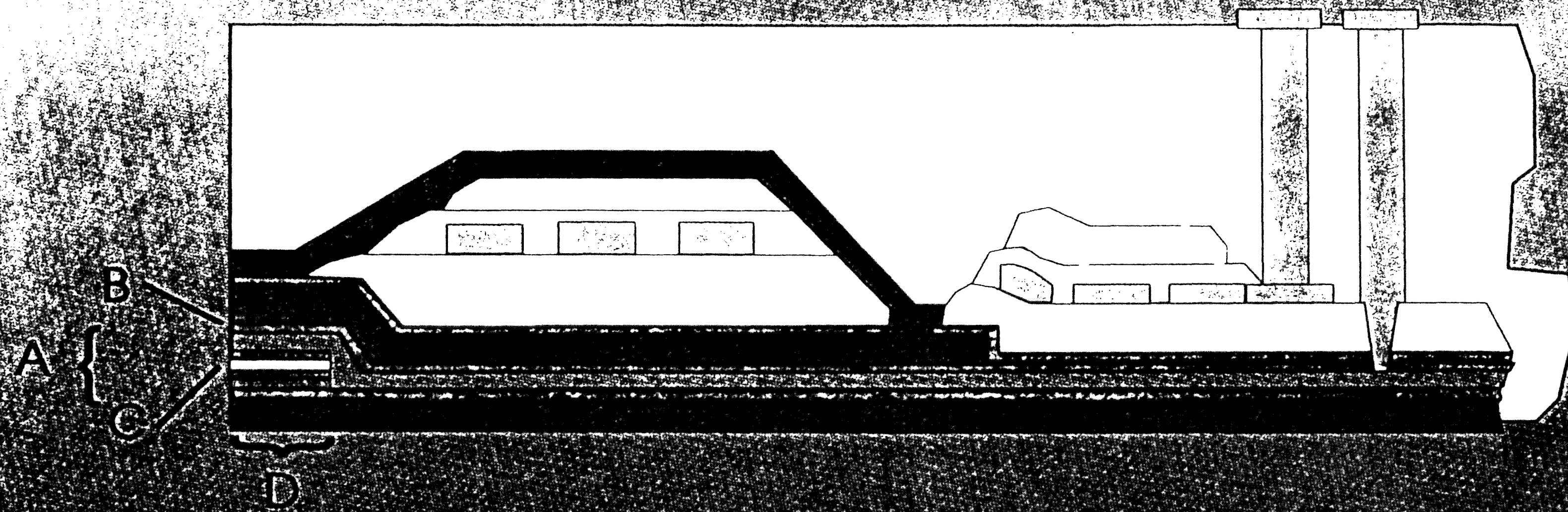

		1 Gbit/in^2 Head	3 Gbits/in^2 Head	5 Gbits/in^2 Head
A	Total Read Gap	0.25 μm	0.20 μm	0.20 μm
B	Sensor/Shield Spacing	<1200 Å	<1000 Å	<1000 Å
	Read Trackwidth	2 μm	1.1 μm	0.7 μm
C	MR Film	150 Å	120 Å	90 Å
D	Sensor Height	1.0 μm	0.5 μm	0.5 μm
	Flying Height	1.5 μ-in	1.5 μ-in	1.0 μ-in
	TAA (Signal Amp.)	300 μV/μm	600 μV/μm	900 μV/μm

3GBIT95W.PSBIN

AMR Head Basics

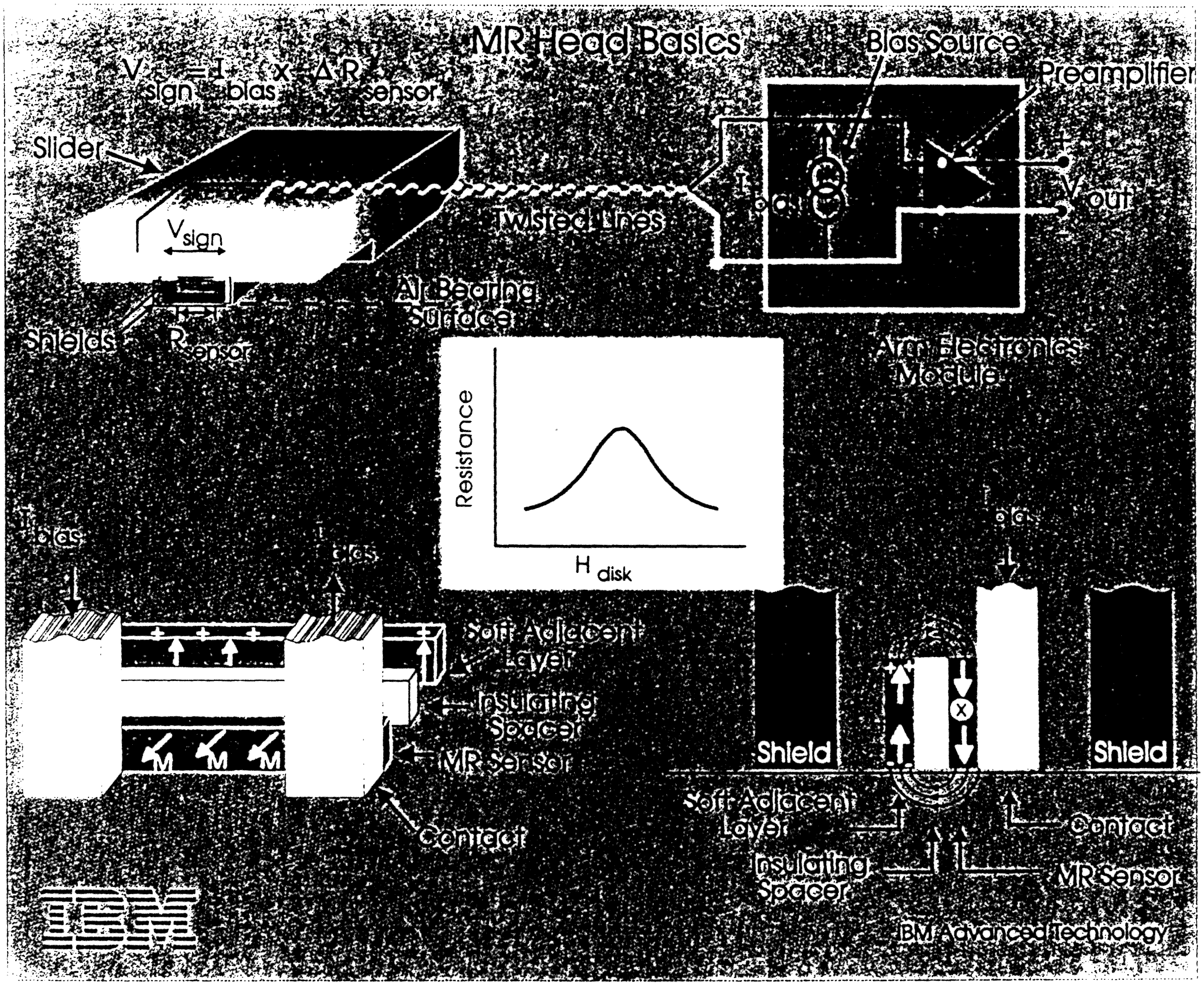

IBM Almaden Research Center

Bruce A. Gurney

Some MR Head Biasing Techniques

Magnetoresistive Head Biasing Alternatives

Technology	Advocate	Advantages
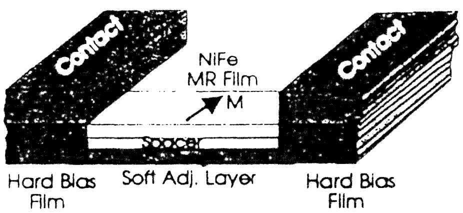 Soft Adj. Layer, Hard or Exchange Bias	IBM Quantum Seagate Hitachi Read Rite Fujitsu TDK AMC	Over 100M heads in operation 3 Gbit/sq.in. demo Simple, high yield process
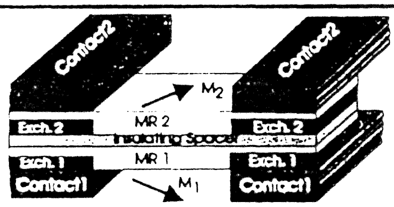 Differential-Dual Stripe/Exchange Bias	Headway	Large output Thermal spike protection
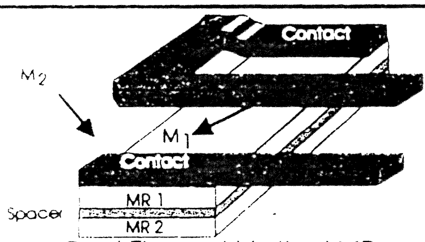 Dual Element Vertical MR	Sony	Thermal spike protection Constant output with trackwidth

IBM Advanced Technology

MR heads

Magnetoresistive Head Biasing Alternatives

Technology	Advocate	Advantages	Disadvantages
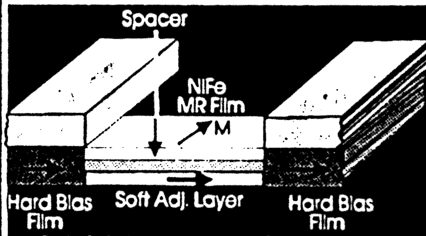 Soft Adj. Layer, Hard or Exchange Bias	IBM QUANTUM /RMM HITACHI FUJITSU	Over 40M heads in operation 1 Gbit/sq.in. demo Simple process	
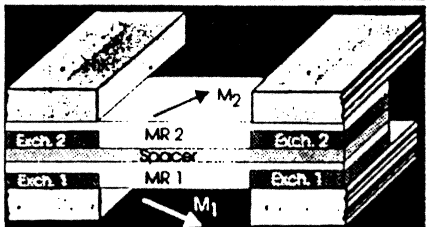 Dual Stripe/Exchange Bias	HP/ Headway	Large output Thermal spike protection	Complex structure 2 MR films 1-2 additional contacts 2 exchange structures Interstripe shorts Matched, aligned MR's Unproven
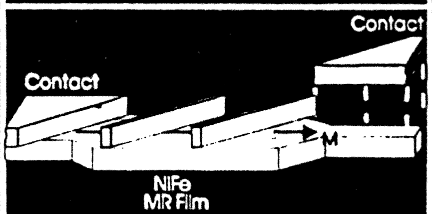 Barberpole/Bottleneck shape film	Seagate	Simple structure Single level MR film	Barkhausen noise sensitivity Rotates I not M WRT easy axis Unproven

IBM Advanced Technology

Write Wide / Read Narrow

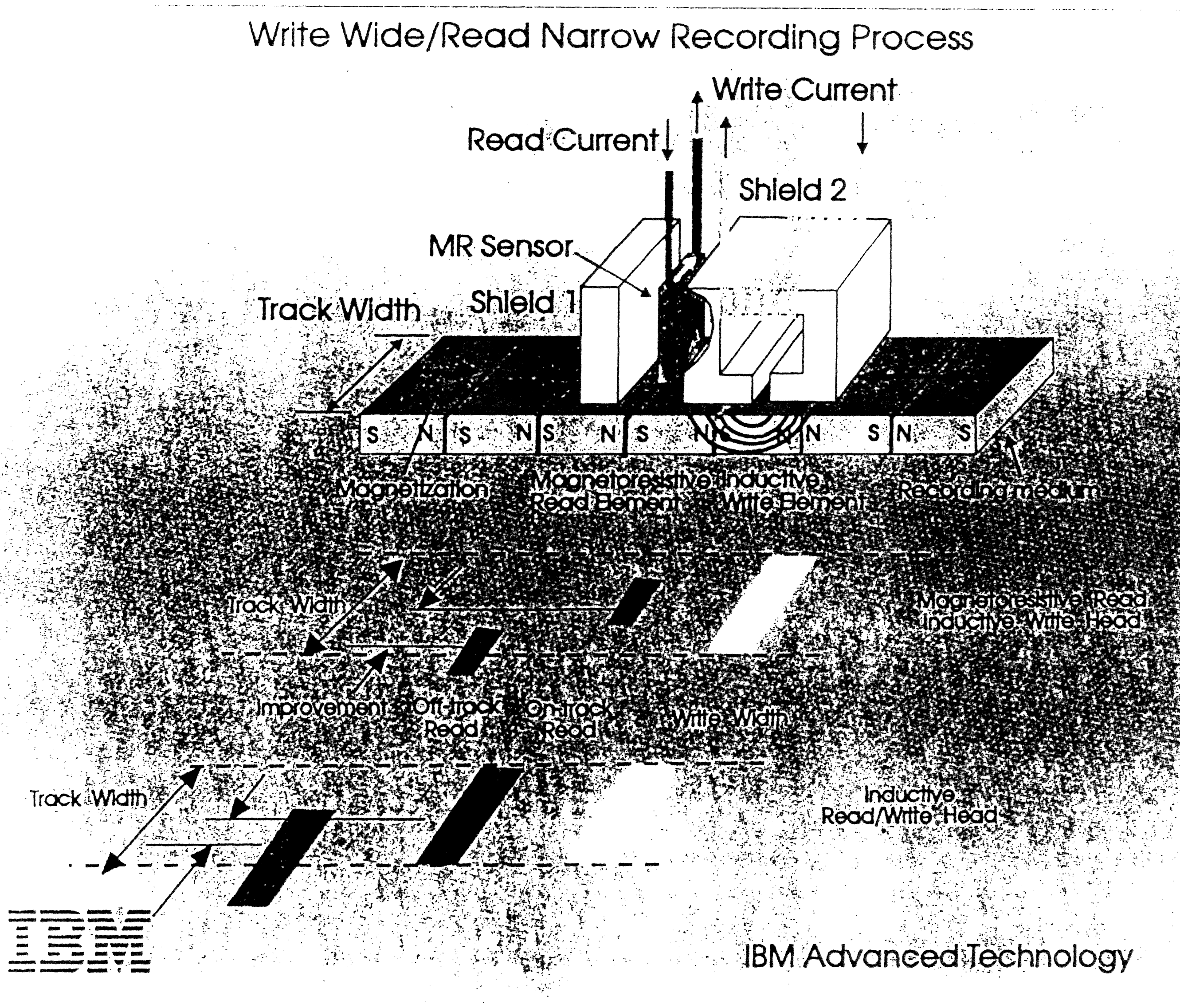

High Density Fabrication[2]

TABLE I
Lithography Comparisons - DRAM[4] vs Film Head[3]
(volume production)

YEAR	Minimum Feature-DRAM		Minimum Feature-Film Head	
1980	$3.00\mu m$	64 Kbit	$23.0\mu m$	12 Mbit/in^2
1984	$1.50\mu m$	256 Kbit	$16.0\mu m$	24 Mbit/in^2
1988	$0.90\mu m$	1 Mbit	$11.0\mu m$	50 Mbit/in^2
1990	$0.60\mu m$	4 Mbit	$6.0\mu m$	150 Mbit/in^2
1993	$0.50\mu m$	16 Mbit	$4.0\mu m$	350 Mbit/in^2
1996	$0.35\mu m$	64 Mbit	$3.0\mu m$	800 Mbit/in^2
199X	$0.25\mu m$	256 Mbit	$1.0\mu m$	5 Gbit/in^2
200X	$0.18\mu m$	1 Gbit	$0.7\mu m$	10 Gbit/in^2

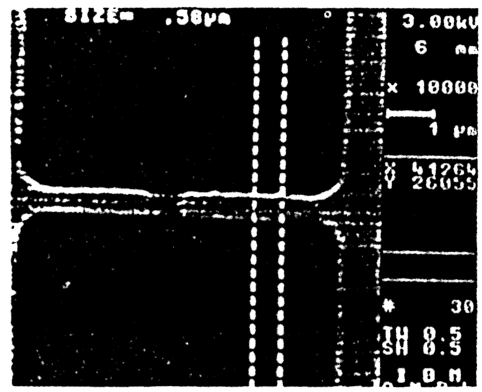

TW = 0.5 µ
SH = 0.5 µ

Fig. 3. SEM Photomicrograph of Submicron Contiguous Junction Sensors

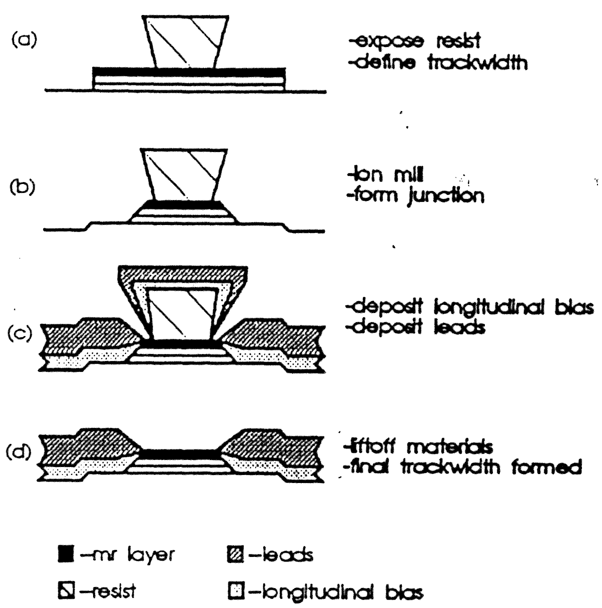

Fig. 2. Process Sequence for Contiguous Junction Structures

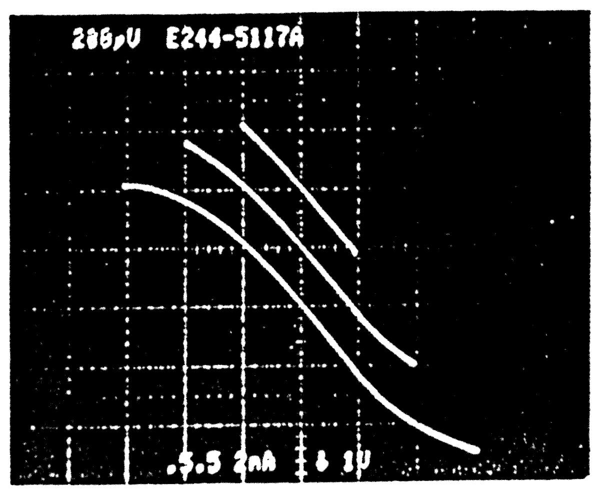

Fig. 4. Transfer Curve of Submicron, 0.5 μm x 0.5 μm, Contiguous Junction Sensors (horizontal scale 50 Oe/divison)

---

[2] R.E. Fontana, Jr., et al., IEEE Trans. Mag. 32, 3440 (1996)

GRCHWSKI at ALMADEN

MR/SAL Longitudinal Biasing and Trackwidth Definition

Patterned Exchange (Exchange and Contact Films Aligned) IBM Corsair	
Contiguous Junction (Contact and Stabilization Films Self Aligned) IBM Allicat Ultrastar2	
Patterned Hard Bias (Contact Film Defines Trackwidth)	
Contiguous Junction (Contact Film Defines Trackwidth)	
Patterned Spacer Defines Trackwidth	

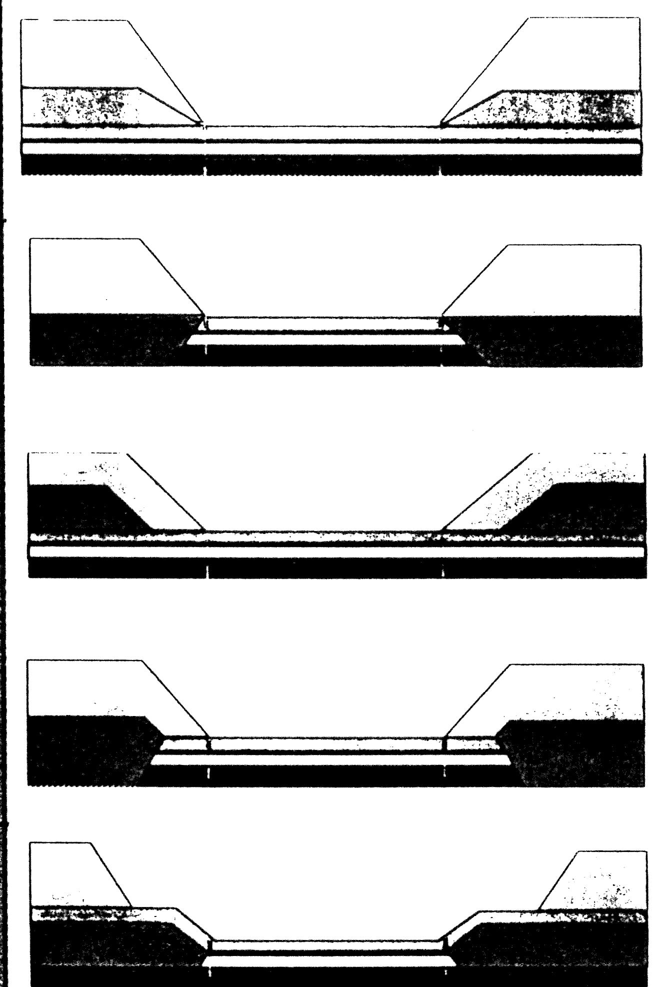

Contacts
Exchange
Hard Bias
NiFe - MR
Spacer
Soft Film

IBM

IBM Advanced Technology

MRBIASW.PSBIN

High Density Longitudinal Stabilization[3]

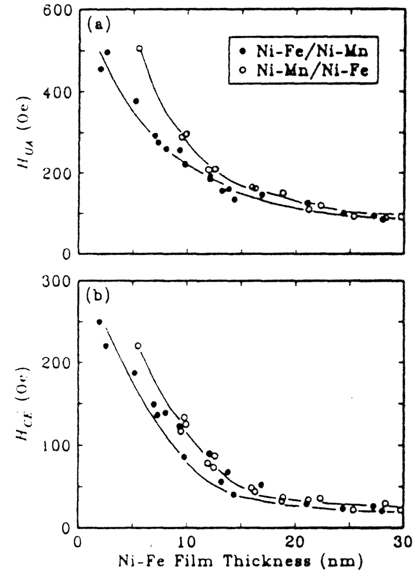

Fig. 1 (a) H_{UA} and (b) H_{CE} of annealed Ni-Fe/Ni-Mn(30 nm) and Ni-Mn(30 nm)/Ni-Fe films vs Ni-Fe film thickness.

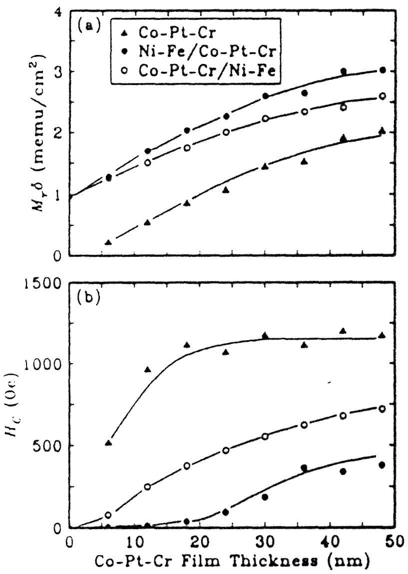

Fig. 2 (a) $M_r\delta$ and (b) H_C of annealed Co-Pt-Cr, Ni-Fe(12 nm)/Co-Pt-Cr and Co-Pt-Cr/Ni-Fe(12 nm) films vs Co-Pt-Cr film thickness.

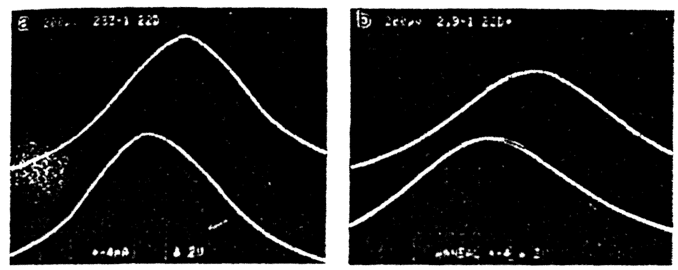

Fig. 3 MR responses of unshielded MR sensors (a) overlaid with a Ni-Mn film in tail regions and (b) abutted with a Co-Pt-Cr film. Two examples are shown for each MR sensor.

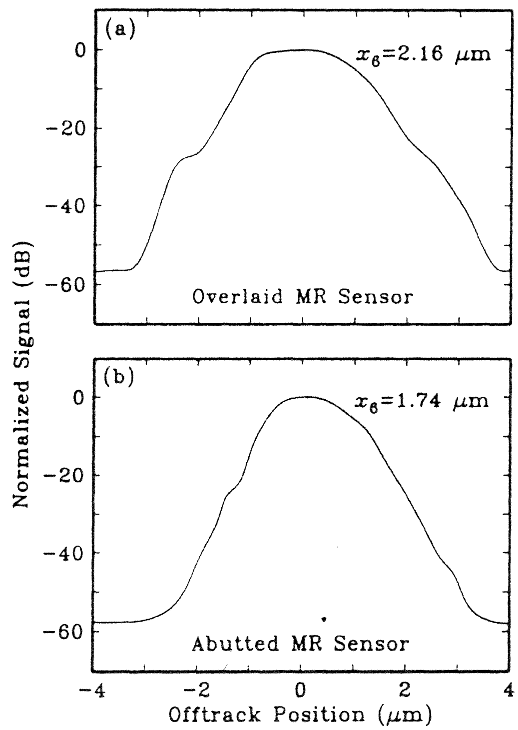

Fig. 4 Microtrack profiles of shielded MR sensors (a) overlaid with a Ni-Mn film in tail regions and (b) abutted with a Co-Pt-Cr film.

[3]T. Lin, et al., IEEE Trans. Mag. 32, 3443 (1996)

CoPt and CoPtCr for longitudinal bias

High coercivity CoPtCr, CoPt films deposited at high power and high bias conditions for hard bias applications in magnetoresistive heads

G. Choe, S. Funada, A. Tsoukatos, and S. Gupta
Materials Research Corporation, Route 303, Orangeburg, New York 10962

We report, for the first time, coercivity values greater than 2000 Oe with Mrt values of 3.0 memu/cm^2 for Cr/CoPt$_{12}$Cr$_{13}$ and Cr/CoPt$_{20}$ bilayer films deposited by dc magnetron sputtering at room temperature. CoPtCr films sputtered at a deposition rate of 98 Å/s and high bias voltage showed H_c of 1965 Oe with Mrt of 3 memu/cm^2, while CoPt films sputtered at 99 Å/s and moderate substrate bias showed H_c of 2350 Oe with Mrt of 3 memu/cm^2. X-ray diffraction studies indicated that Co(10.0) and (11.0) texture leading to in-plane orientation of c axis are promoted in the films sputtered at high deposition rate and bias conditions. Furthermore, the grain-to-grain epitaxy between the Cr underlayer and the Co alloy layer as well as the dense Co grains growing in a columnar shape without voids resulted in higher H_c and Mrt without degradation of coercive squareness. Plots of H_c vs Mrt for films deposited under the optimum bias conditions offer a wide range of useful H_c and Mrt combinations for hard bias applications in magnetoresistive heads.
 [S0021-8979(97)16008-X]

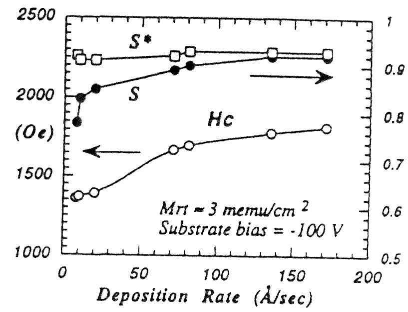

FIG. 1. Variation of H_c, S, and S^* for CoPt$_{12}$Cr$_{13}$ films sputtered at varying deposition rate (substrate bias = −100 V).

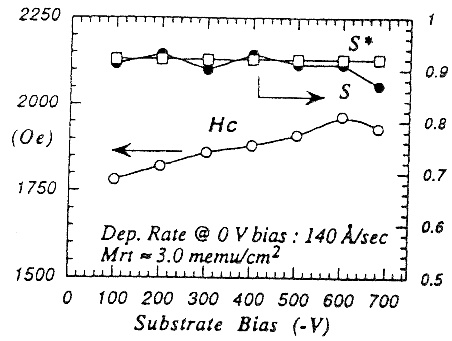

FIG. 2. Variation of H_c, S, and S^* for CoPt$_{12}$Cr$_{13}$ films sputtered at varying substrate bias (deposition rate at 0 V bias = 140 Å/s).

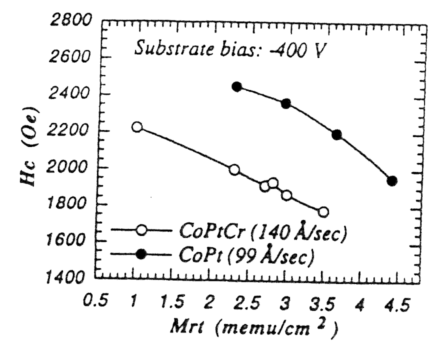

FIG. 4. H_c vs Mrt for CoPt$_{12}$Cr$_{13}$ and CoPt$_{20}$ films sputtered at −400 V bias.

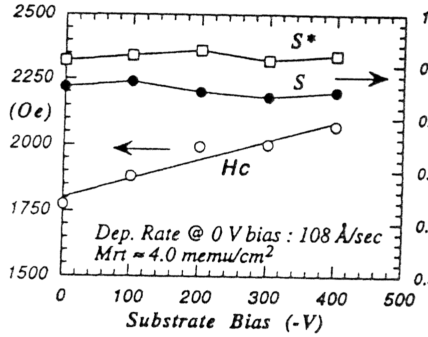

FIG. 3. Variation of H_c, S, and S^* for CoPt$_{20}$ films sputtered at varying substrate bias (deposition rate at 0 V bias = 108 Å/s).

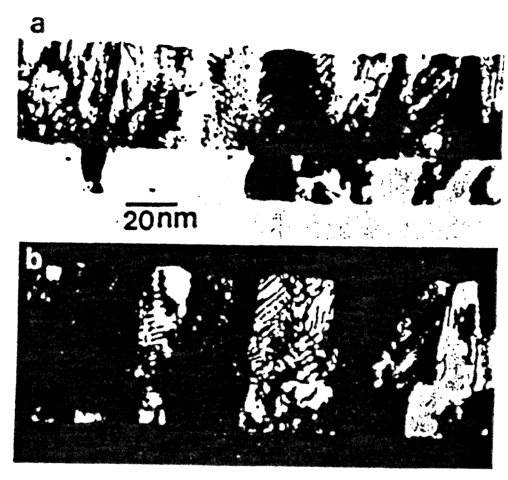

FIG. 5. Cross-sectional TEM view of CoPt$_{12}$Cr$_{13}$ films sputtered at 127 Å/s, −400 V bias onto a Cr underlayer: (a) bright field image and (b) dark field image.

Role of atomic mass of underlayer material in the transition noise of longitudinal media (abstract)

Tadashi Yogi,[a] Thao Nguyen,[a] Steven E. Lambert,[a]
Grace L. Gorman, Michael A. Kakalec,[b] and Gil Castillo
IBM Research Division, Almaden Research Center, 650 Harry Road, San Jose, California 95120-6099

grain isolation and underlayer

4749 J. Appl. Phys. 69 (8), 15 April 1991

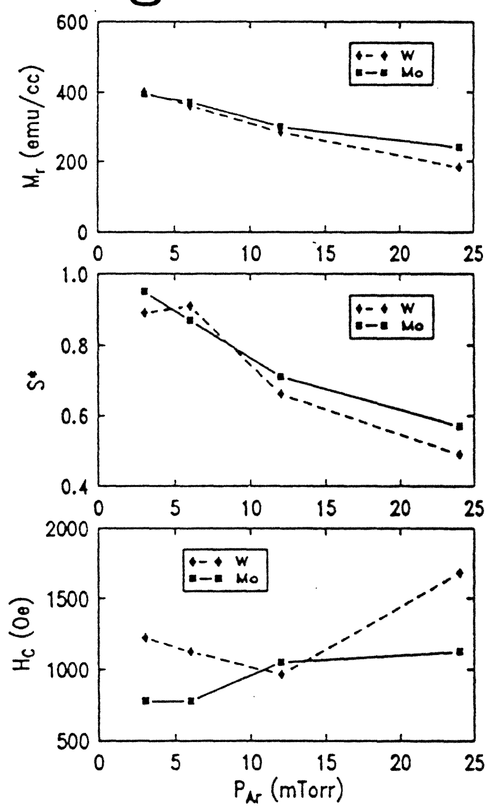

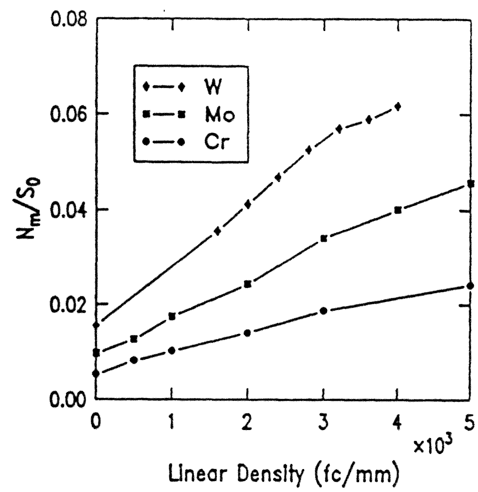

Figure 2. Normalized media transition noise as a function of linear density for Cr, Mo and W underlayers for 6 mTorr sputtering pressure. Cr data from Ref. 5 and W data from Ref. 6.

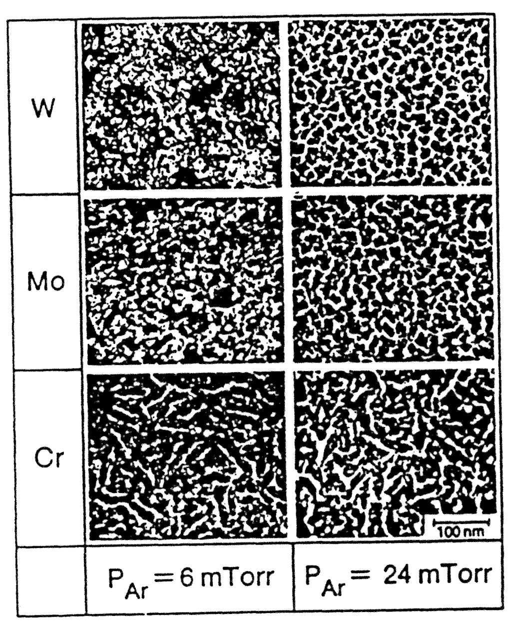

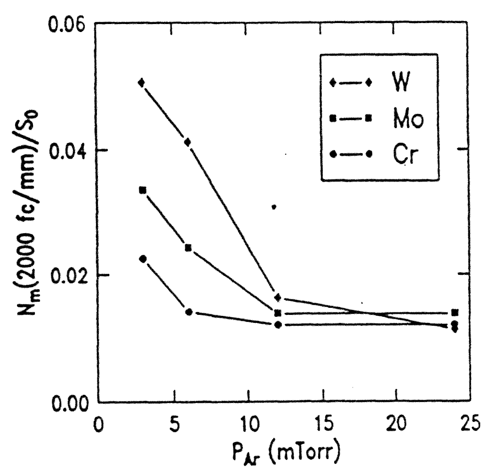

Figure 3. Media transition noise at 2000 fc/mm normalized to the base-to-peak isolated pulse amplitude as a function of sputtering pressure for Cr, Mo and W underlayers of 100 nm in thickness. Cr data from Ref. 5.

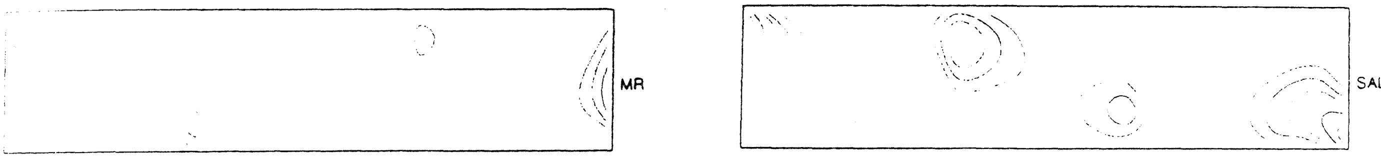

FIG. 8. Change of local resistivity for overlay MR head.

Perturbation From The Write Head[5]

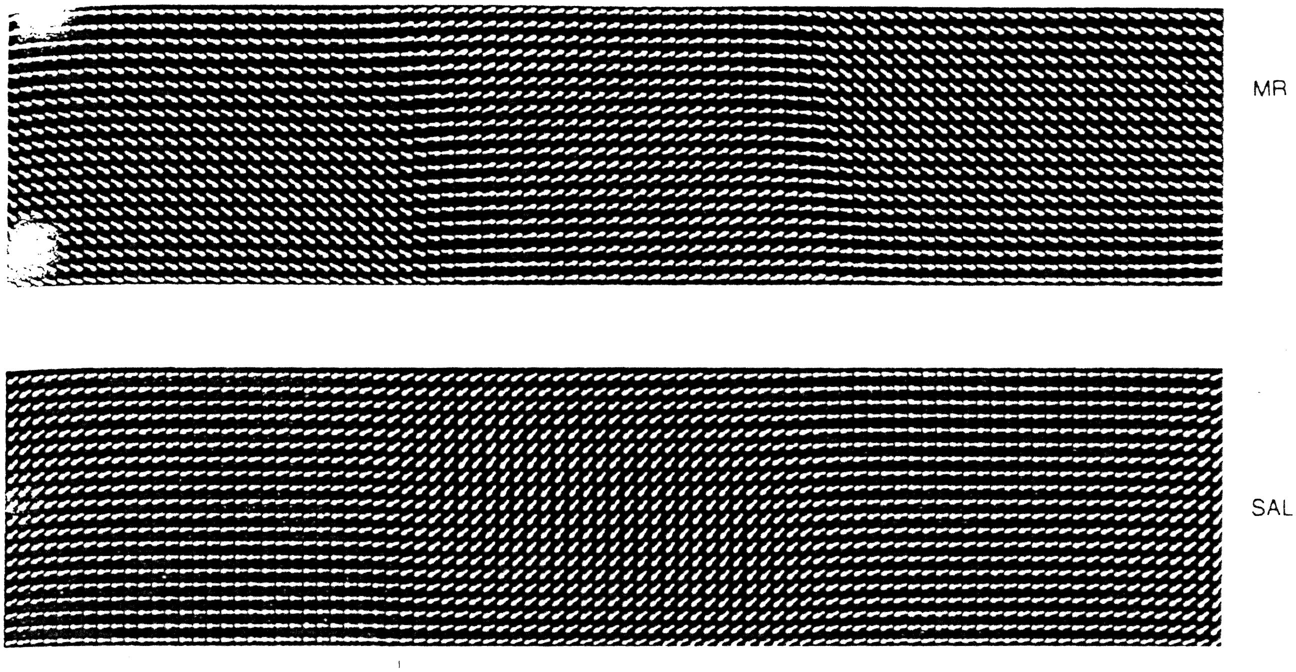

FIG. 7. Biasing state of overlay MR sensor. The vertical lines represent the lead/hard-bias contact locations.

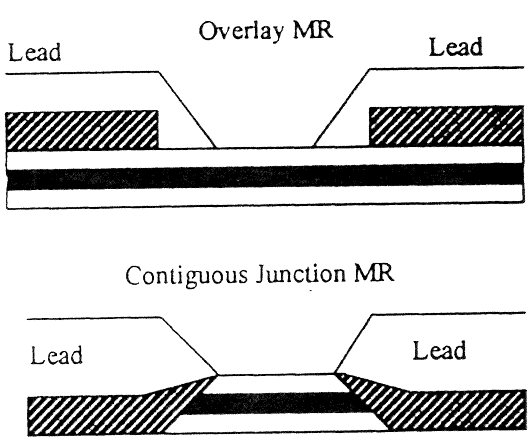

FIG. 2. Cross-sectional schematic view of MR sensors.

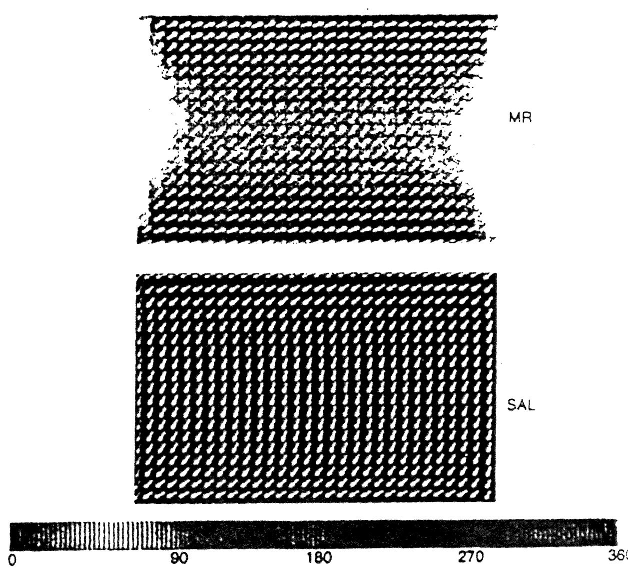

FIG. 6. Biasing state of contiguous junction MR sensor.

[5] S. Yuan, et. al, IEEE Trans. Mag. 32, 3461 (1996)

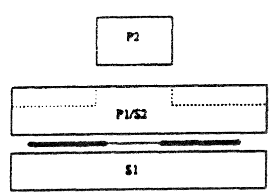

FIG. 1. ABS schematic view of a dual-element read-write head.

materials requirements for magnetic recording heads

Table I: Materials Requirements for Magnetic Recording Heads.

Property	Reason
Large saturation magnetization	Large gap field Easier fabrication process
High permeability at all frequencies	High efficiency over wide frequency range
Small coercivity with low hysteresis losses	Low thermal noise
Small but nonzero uniaxial anisotropy	Control of domain structure and permeability at high frequency
Low magnetostriction (negative λ_s)	Low media contact noise and anisotropy control
High resistivity	Minimize eddy current losses and improve high frequency permeability
Wear resistant	Long life
Corrosion resistant	Long life
Good thermal and time stability	Reliability
Low forming effect	Easy and reliable manufacturing process

[8] T. Jagielinski, Materials Research Society Bulletin 15, 36 (1990).

M-H loop definitions

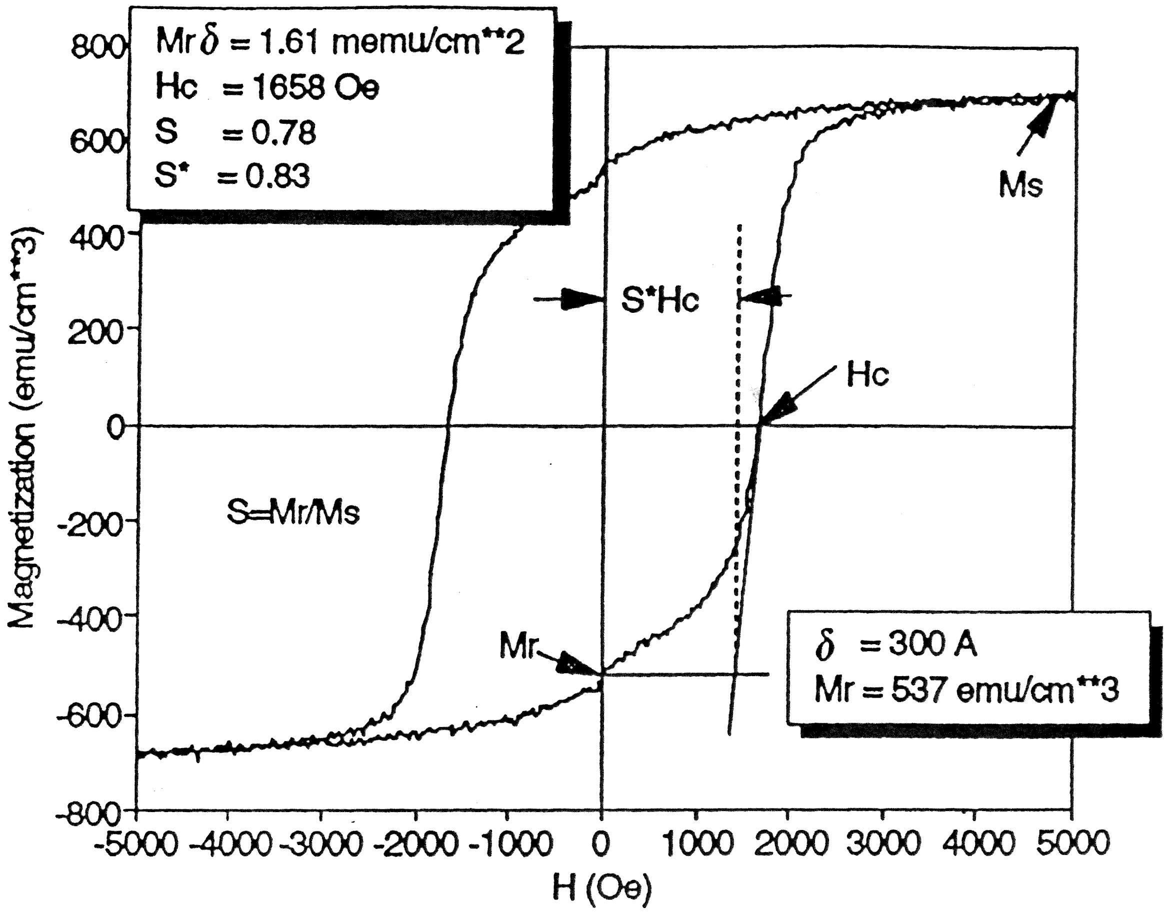

magnetization

- magnetic moment quantized: $\mu_B = e\hbar/2mc = 0.92 \times 10^{-10}\ erg/G$
- orbital contribution quenched by crystal field: electron spin dominates.
- example: generalized Slater Pauling curve:[2]

FIG. 1 Generalized Slater-Pauling curve. Magnetization per alloy atom versus average magnetic valence. Magnetic valence ($Z_m \equiv 2N_d^{\uparrow} - Z$) is an integer for each column of the periodic table; it is the negative of the valence charge Z, except for the Fe, Co and Ni columns, for which $2N_d^{\uparrow} = 10$ gives $Z_m = 2$, 1 and 0 respectively. The 45° line corresponds to a fixed number (0.3) of *sp* up-spin electrons. The experimental data were taken from Refs. 2 and 8.

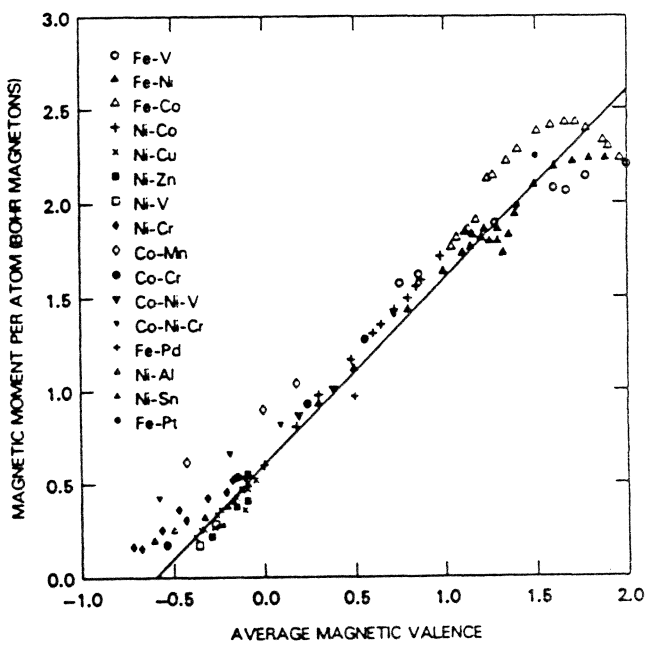

total moment $\mu = (n_\uparrow + n_\downarrow)\mu_B$

valence $N = n_\downarrow + n_\uparrow$

band structure $n_\downarrow = n_{d\downarrow} + n_{sp\downarrow}$

for Ni, Fe, Co: $n_{d\uparrow} \approx 5$, $n_{sp\uparrow} \approx 0.3$

so

$$\mu = (2(2n_{d\uparrow} + n_{sp\uparrow}) - N)\mu_B = (10.6 - N)\mu_B$$

(Fe:Z=8, μ=2.6μ_B(2.22 meas) (Co:Z=9, μ=1.6μ_B(1.72) (Ni:Z=10,μ=0.6μ_B(0.60)

[2] A.R. Williams, et al., IEEE Trans. Magn. MAG-19 (1993)

vibrating sample magnetometer

VSM[3]

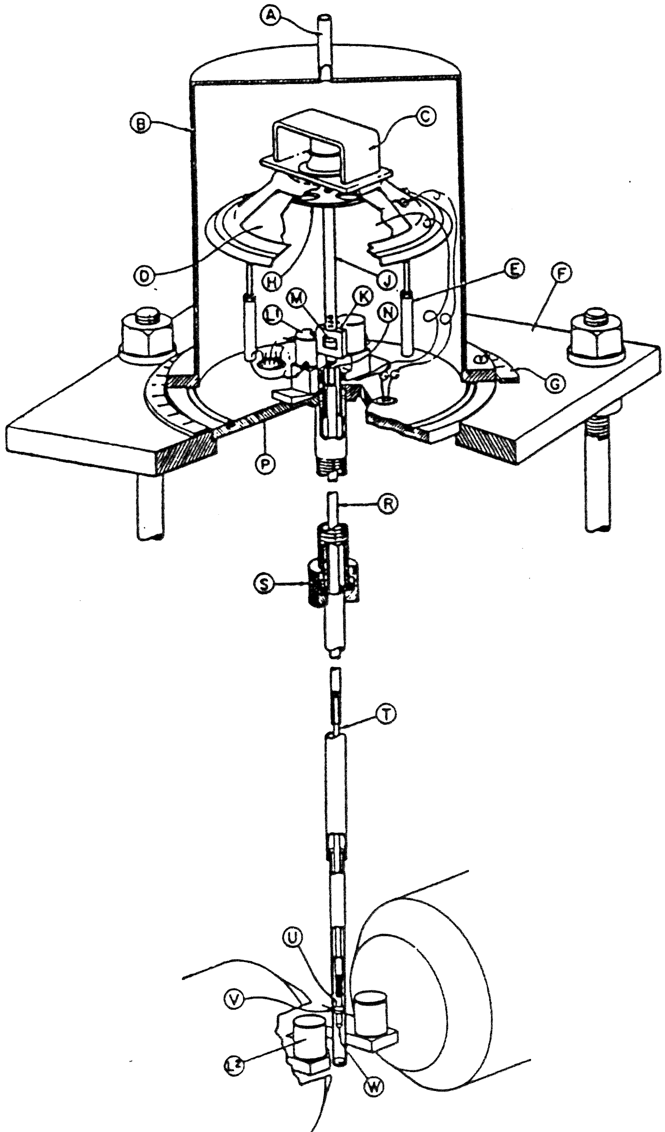

sensitivity $\sim$ 2×10^{-5} emu for $\tau \approx 1\ sec$
or about $1\ ML \times 1\ cm^2$ of Fe

---

[3] S. Foner, Rev. Sci. Instrum. 30, 548 (1959).

alternating gradient magnetometer

AGM[4]

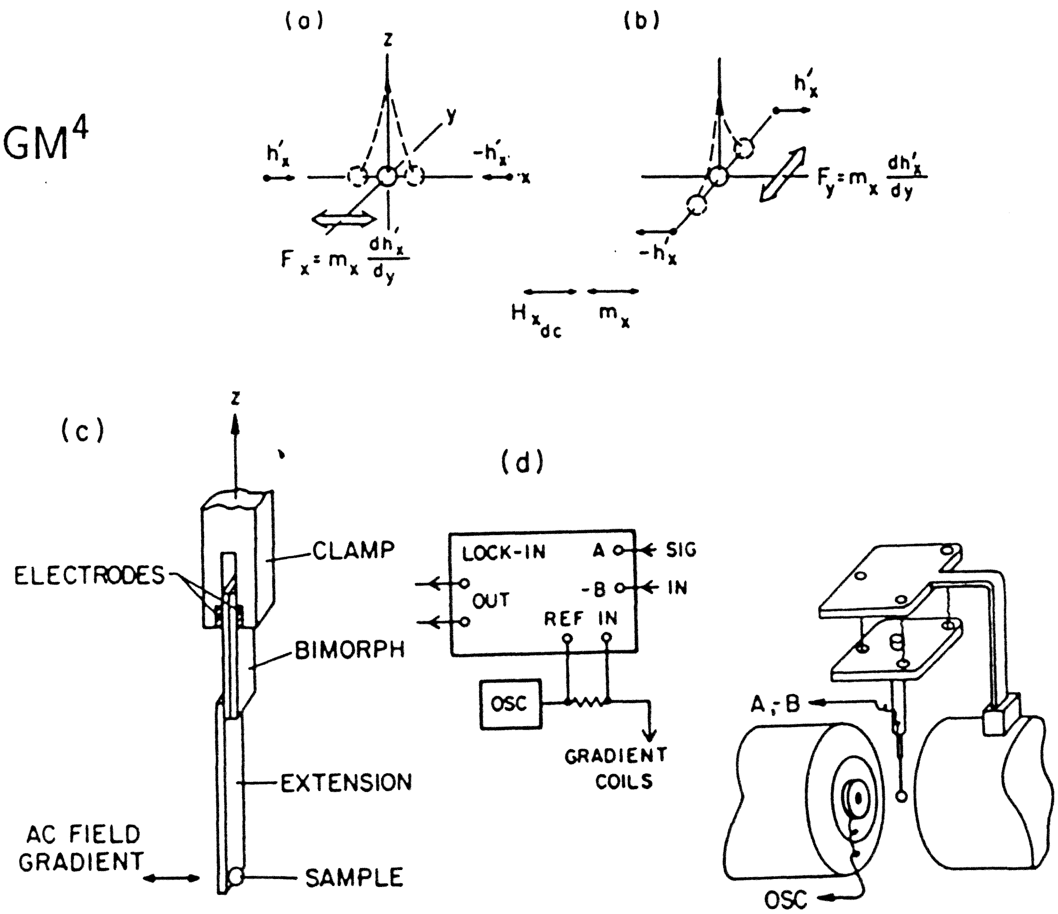

FIG. 1. Configuration of the magnetizing and gradient fields (a) and (b); the bimorph, extension, and sample (c); and the overall system (d).

sensitivity $\sim 1 \times 10^{-8}$ emu for $\tau \approx 1$ sec

or about 0.1 ML $\times$ 0.1 cm^2 of Fe

[4] P.J. FLanders, J. Appl. Phys. 63, 3940 (1988).

FeN

Giant magnetic moment and other magnetic properties of epitaxially grown $Fe_{16}N_2$ single-crystal films (invited)

Y. Sugita,[a] K. Mitsuoka, M. Komuro, H. Hoshiya, Y. Kozono, and M. Hanazono
Hitachi Research Laboratory, Hitachi, Limited, 4026 Kuji-cho, Hitachi, Ibaraki 319-12, Japan

5981 J. Appl. Phys., Vol. 70, No. 10, 15 November 1991

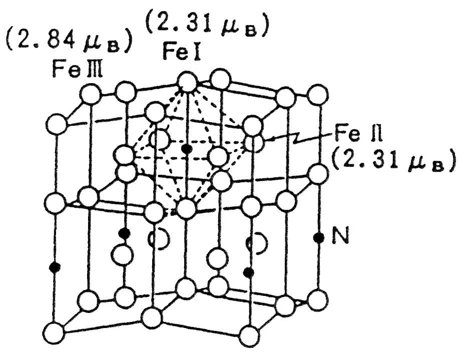

FIG. 12. Three sites of Fe atoms and their magnetic moments of $Fe_{16}N_2$ after Sakuma.[13]

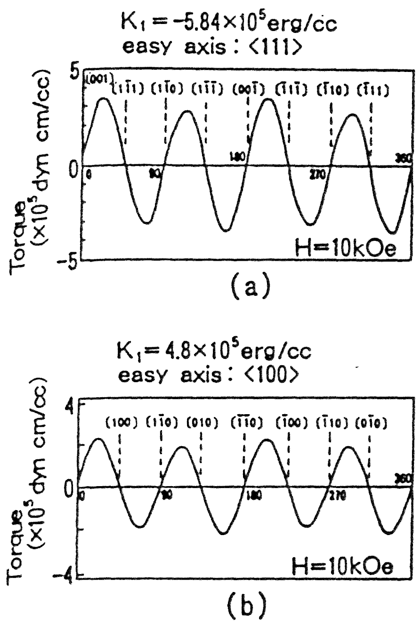

FIG. 10. Torque curves for (a) $Fe_{16}N_2(110)$ (1000 Å) film grown on Fe(001) (100 Å)/InGaAs(001) (Ref. 10) and (b) $Fe_{16}N_2(001)$ (500 Å) film grown on InGaAs(001).

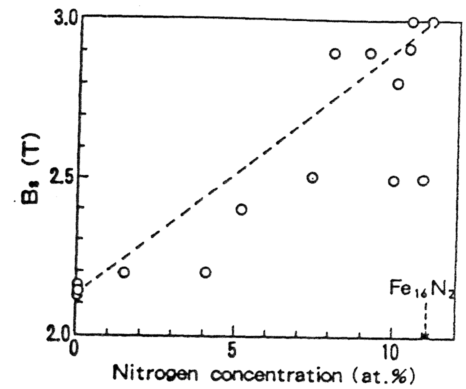

FIG. 6. B_s as a function of N concentration in the epitaxially grown $Fe_{16}N_2(001)$ film on InGaAs(001).

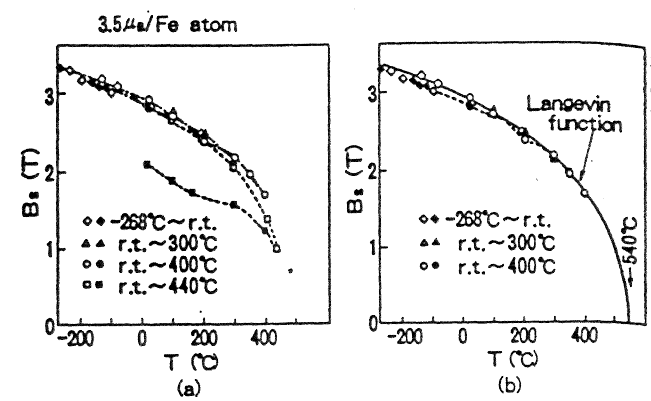

FIG. 8. (a) Temperature dependence of B_s for $Fe_{16}N_2(001)$ film grown on InGaAs(001). (b) Fitted curve by Langevin function. Open and close marks show B_s with increasing and decreasing temperature, respectively.

FeN

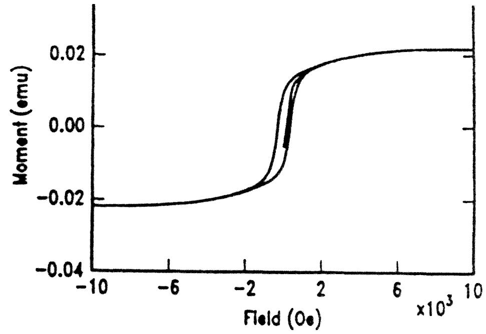

FIG. 3. Magnetization curve from sample with the epitaxial martensite phases [Fig. 1(a)].

Epitaxial $Fe_{16}N_2$ films grown by sputtering

C. Ortiz
IBM Research Division, Almaden Research Center, San Jose, California 95120

G. Dumpich
Exp. Tieftemperaturphysik, Duisburg University, D-47048 Duisburg, Germany

A. H. Morrish
Department of Physics, University of Manitoba, Winnipeg, Manitoba, Canada R3T2N2

(Received 13 July 1994; accepted for publication 21 September 1994)

We have been able to obtain α''-$Fe_{16}N_2$ films using an underlayer template to induce the epitaxial growth of this metastable phase. They are epitaxial in the (001) direction and show single crystallinity in plane. Furthermore, they are deposited by simple reactive nitrogen sputtering. They have an average magnetic moment of 250 emu/g, considerably larger than the moment (217 emu/g) for pure bcc iron. Conversion electron Mössbauer spectroscopy gives three hyperfine fields corresponding to three different iron sites, as expected for this structure. © *1994 American Institute of Physics.*

K. H. JACK
PROC. R. SOC. LONDON A 208, 216 (1951)

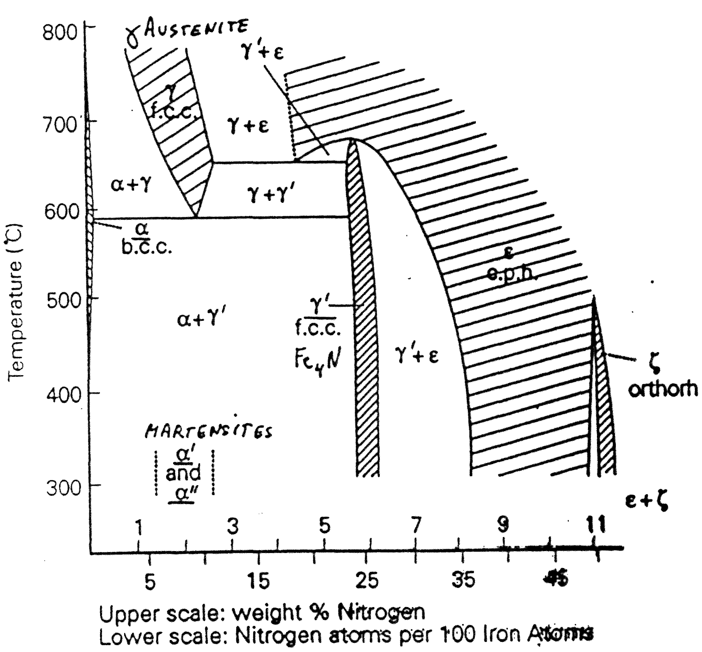

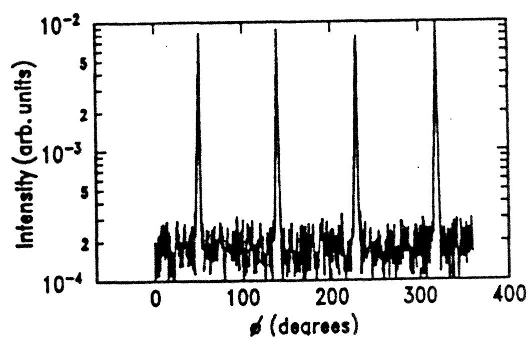

FIG. 2. X-ray ϕ scan of the same sample as shown in Fig. 1(a).

2738 Appl. Phys. Lett., Vol. 65, No. 21, 21 November 1994

TABLE I. Mössbauer parameters for the α'' $Fe_{12}N_2$. Here, δ is the isomer shift with respect to α-Fe, ϵ is the quadrupole splitting, H_{hf} is the hyperfine field, and S is the relative area for the three patterns.

	δ (mm/s)	ϵ (mm/s)	H_{hf} (kOe)	S (%)
Fe I	0.02	−0.28	289	16.7
Fe II	0.12	0.11	313	38.4
Fe III	0.11	−0.13	.397	17.1

crystalline anisotropy

origin: spin-orbit coupling $(\vec{L} \cdot \vec{S})$
depends on crystal symmetry: cubic, uniaxial, hexagonal, . . .[8]

Fe

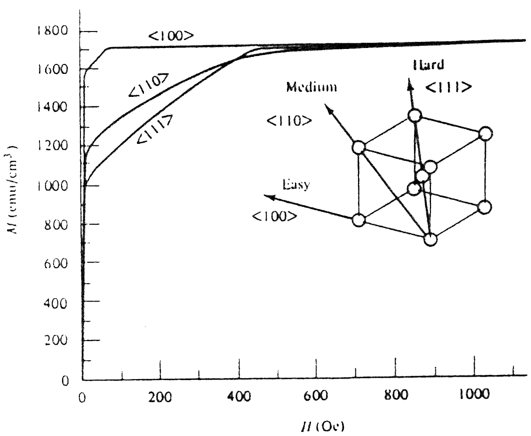

Ni

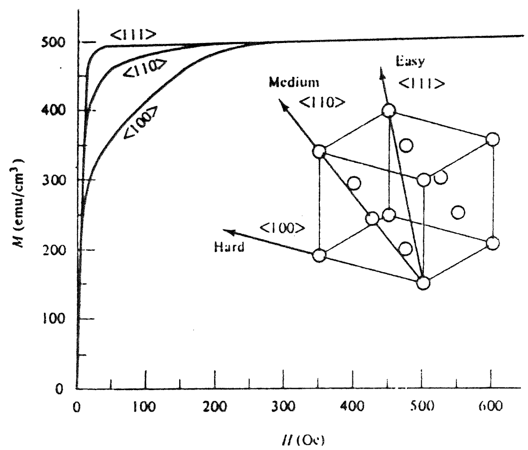

Co

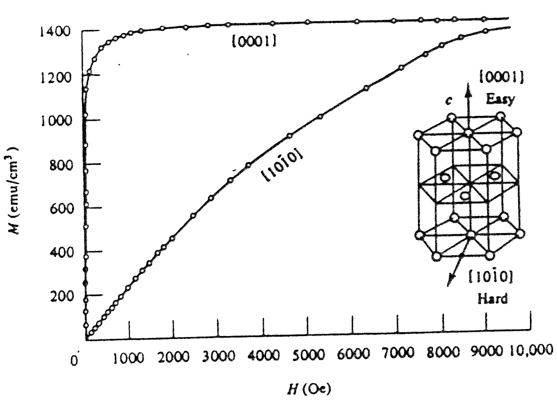

[8] taken from B.D. Cullity, *Introduction to Magnetic Materials*, Addison-Wesley, Reading MA, (1972).

torque magnetometry: apparatus

TM[9]

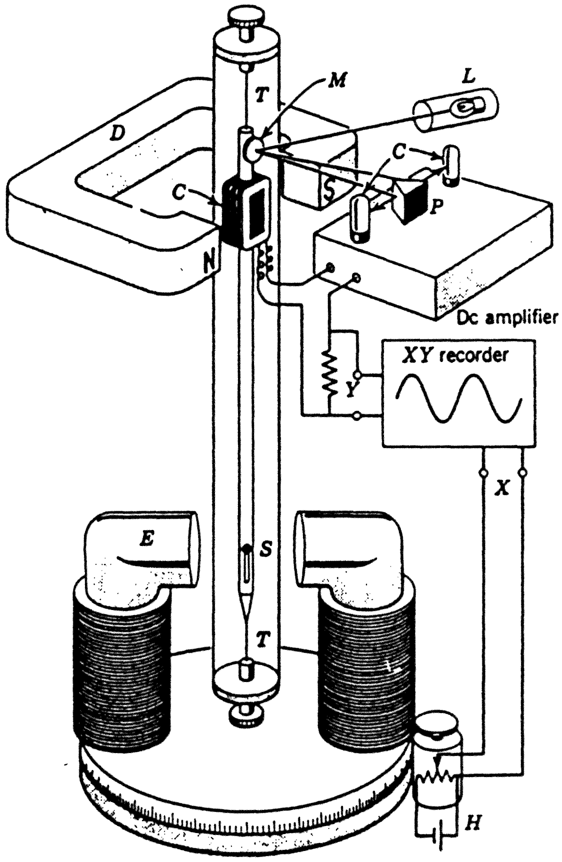

9 from Chikazumi, op. cit.

torque magnetometry: curves

$$
\begin{aligned}
E &= -MH cos(\alpha - \theta) + K_1 \sin^2\theta + \cdots \\
\Rightarrow L &= -\partial E/\partial\theta \\
&= MH\sin(\alpha - \theta) - K_1 \sin 2\theta + \cdots
\end{aligned}
$$

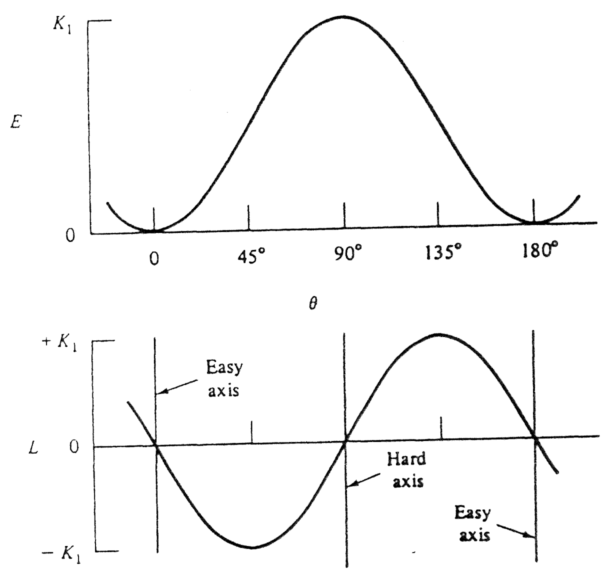

- anisotropy from 5 Oe (NiFe) to 2×10^4 Oe
- magnetic moment
- rotational hysteresis

effect of topography on FeN and FeN/AlN magnetic properties

Effects of lamination on soft magnetic properties of FeN films on sloping surfaces

Kyusik Sin, Chuei-Tang Wang, Shan X. Wang, and Bruce M. Clemens
Department of Materials Science and Engineering, Stanford University, Stanford, California 94305

We have found that the soft magnetic properties of FeN/AlN laminated films do not degrade on sloping surfaces. The easy axis coercivities of FeN/AlN multilayer films are approximately 1.5 Oe and have little variation with slope angle, α. The anisotropy fields slightly vary from 13 to 17 Oe when the slope angles (α) change from 0° to 60°. In contrast, single layer FeN films show a significant degradation of soft magnetic properties with the slope angle. Residual stress does not have a significant correlation with magnetic properties. The large coercivities and saturation fields in the single layer FeN films can be ascribed to a change in the (110) texture of the films. [S0021-8979(97)91208-1]

4508 J. Appl. Phys., Vol. 81, No. 8, 15 April 1997

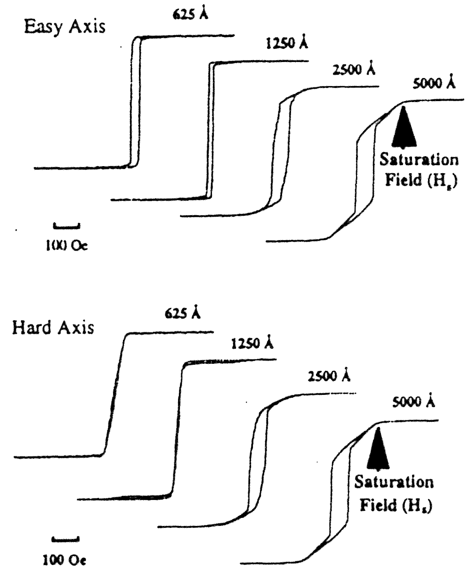

FIG. 1. Dependence of hysteresis loop on the thickness of single layer FeN films on sloping surfaces. Slope angle (α) is 45°.

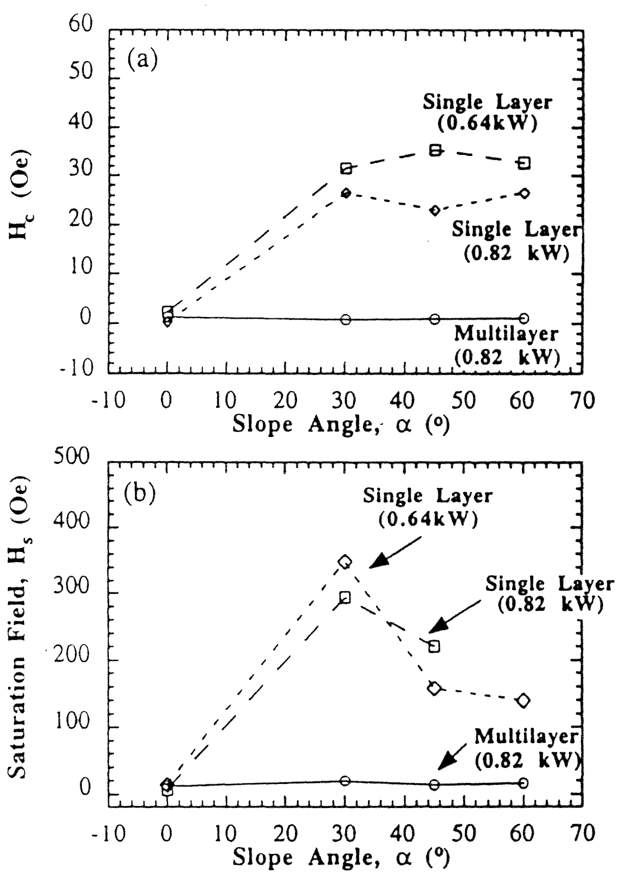

FIG. 2. Dependence of (a) coercivity and (b) saturation field on slope angle (α) for single layer and multilayer films. Multilayer (625 Å FeN/30 Å AlN) ×8.

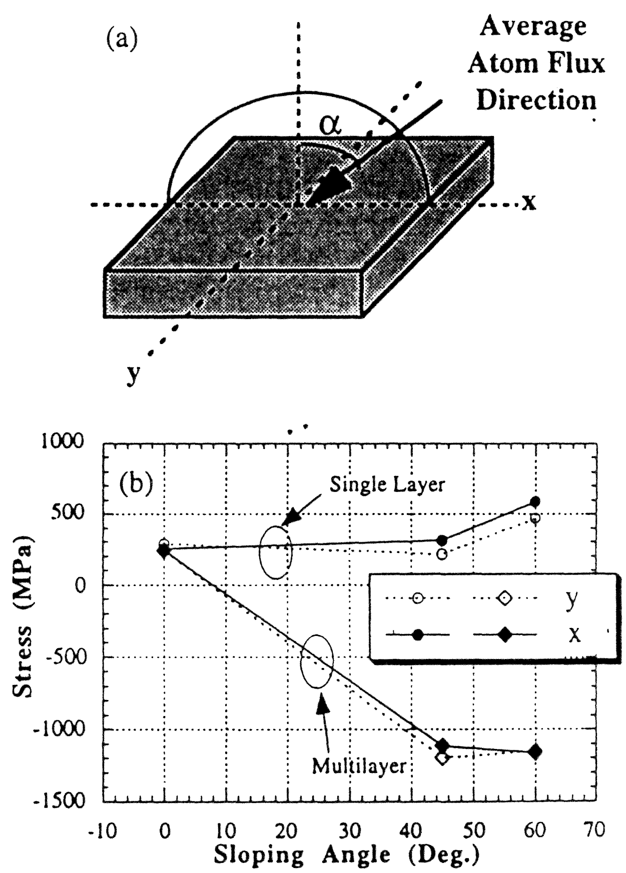

FIG. 3. (a) Average atom flux direction and (b) stress of single layer and multilayer films. The total thickness of the films is approximately 5000 Å. Multilayer: (625 Å FeN/30 Å AlN)×8.

FeXN

3912 IEEE TRANSACTIONS ON MAGNETICS, VOL. 30, NO. 6, NOVEMBER 1994

Effects of Nitrogen Content on the Microstructure and Magnetic Properties of FeTaN Films

Jiang-Ching Lin, Lih-Juann Chen
Department of Materials Science and Engineering, National Tsing Hua University, Taiwan, ROC

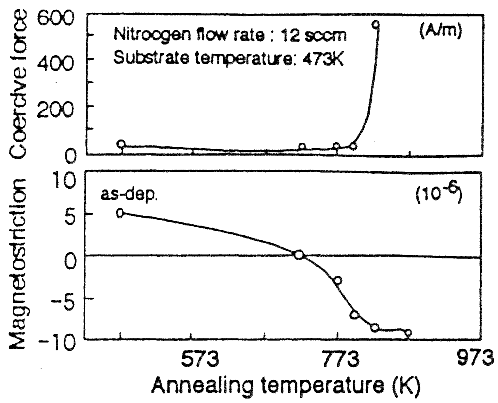

Fig. 4 Magnetostriction and coercive force versus annealing temperature at N_2 12 sccm and at 473K.

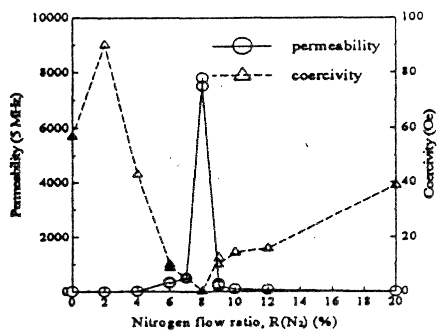

Fig. 1 Soft magnetic properties as a function of nitrogen flow ratio of the FeTaN films post annealed at 475 °C

IEEE TRANSACTIONS ON MAGNETICS, VOL. 30, NO. 6, NOVEMBER 199

FeSiN Films for a Narrow Track Head

M. Kadono, T. Yamamoto, M. Michijima, M. Kyoho, T. Matsuda, T. Muramatsu
Precision Technology Development Center, Production Technology Development Group, Sharp Corporation
2613-1, Ichinomoto, Tenri, Nara 632, Japan

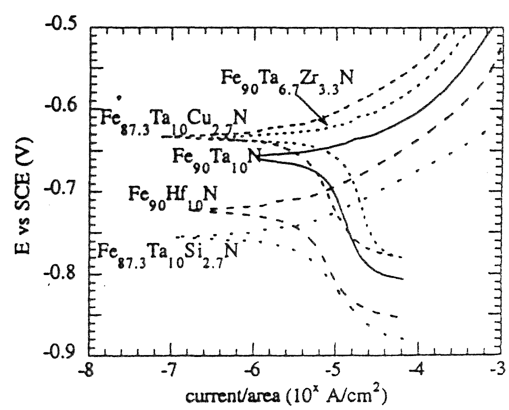

Fig. 4. Effect of the third element dopant (X) on the anodic polariozation of FeXN (N2=10 sccm) thin films in 0.5M NaCl at pH 6.

3918 IEEE TRANSACTIONS ON MAGNETICS, VOL. 30, NO. 6, NOVEMBER 1994

ELECTROCHEMICAL CORROSION STUDY OF HIGH MOMENT THIN FILM HEAD MATERIALS.

S. Gangopadhyay, V. R. Inturi†, J. A. Barnard†, M. R. Parker‡, H. M. Saffarian† and G. W. Warren†

IBM Almaden Research Center

Bruce A. Gurney

FeN/Al_2O_3 head

Magnetic and structural characterization of sputtered FeN multilayer films

Michael A. Russak, Christopher V. Jahnes, Erik Klokholm, Jo-Won Lee, Mark E. Re and Bucknell C. Webb

IBM Research Division, T.J. Watson Research Center, Yorktown Heights, NY 10598, USA

Journal of Magnetism and Magnetic Materials 104–107 (1992) 1851–1854
North-Holland

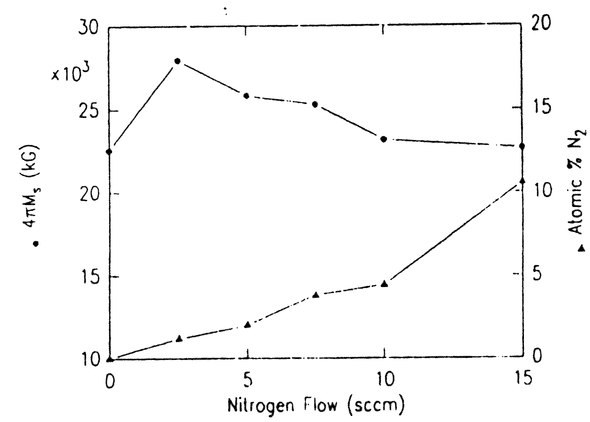

Fig. 1. $4\pi M_s$ and nitrogen content determined by RBS, electron microprobe analysis and SIMS of ferromagnetic FeN films as a function of nitrogen flow rate in the sputtering chamber. Argon flow rate was constant at 75 sccm. Sputtering power was 16 W/cm^2 and $V_b = -100$ V.

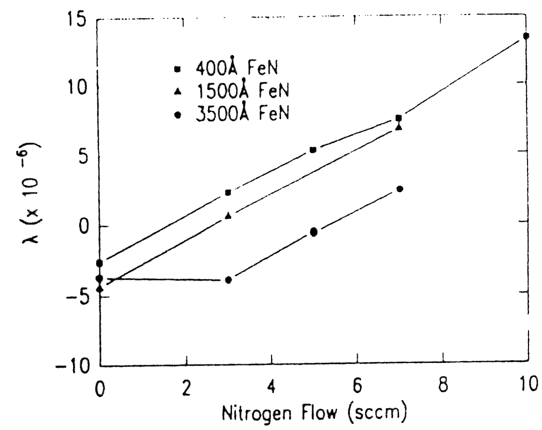

Fig. 2. λ_s as a function of nitrogen flow in the sputtering chamber and film thickness for ferromagnetic FeN films.

3870 IEEE TRANSACTIONS ON MAGNETICS, VOL. 30, NO. 6, NOVEMBER 1994

Writing Performance of Narrow Gap Heads Made with Sputtered Laminated FeN Materials on 3800 Oe Coercivity Media

(Ben) H.L. Hu, L. Vo, and Thao Nguyen
IBM Almaden Research Center, 650 Harry Road, San Jose, CA 95120

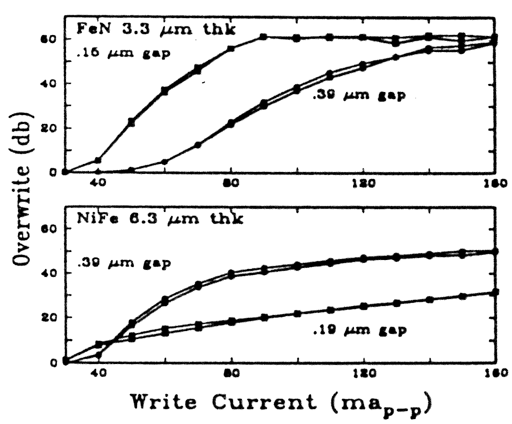

Fig.4. Overwrite (1000/1 fc/mm) as a function of write currents for FeN and NiFe heads.

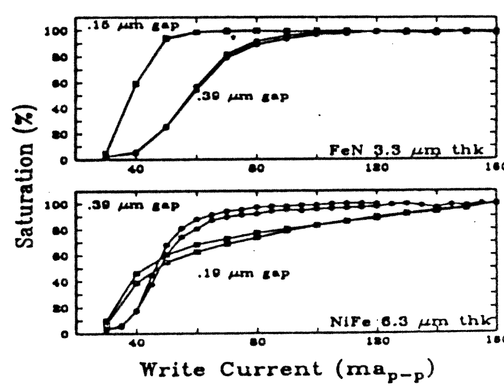

Fig.3. Media saturation as a function of write currents for FeN and NiFe heads.

X-ray Diffraction and Magnetic Properties of Rapid Thermal Annealed Sendust Films.

M.I. Ullah, K.R. Coffey, M.A. Parker and J. Kent Howard
IBM - Storage System Division, San Jose, CA.95193

sendust

Magnetic Parameters	RTA Anneal (500°C/10min)	Conventional Anneal (500°C/18hrs)
Easy-axis:		
Br_e/Bs_e	0.81	0.84
Hc_e	0.22 Oe	0.24 Oe
Hard-axis:		
Br_h/Bs_h	0.50	0.43
Hc_h	0.14 Oe	0.12 Oe
μ_i (initial)	> 4000	> 4000

$Fe_{85}Si_9Al_6$

Table 1. Comparison of soft magnetic parameters for RTA and conventionally annealed sendust films. (μ_i and μ_r measured at 10 Hz).

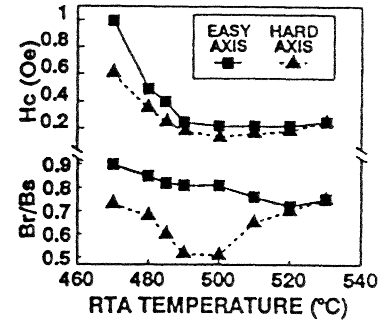

Fig. 1. Effect of annealing temperatures on film coercivity, Hc and (Br/Bs) ratio for RTA sendust films. Annealing time kept constant at 10 minutes.

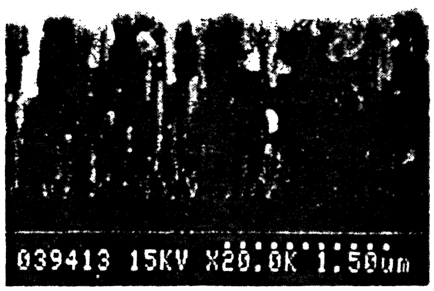

Fig.5. SEM image of a cross section of RTA sendust film showing columnar grain morphology.

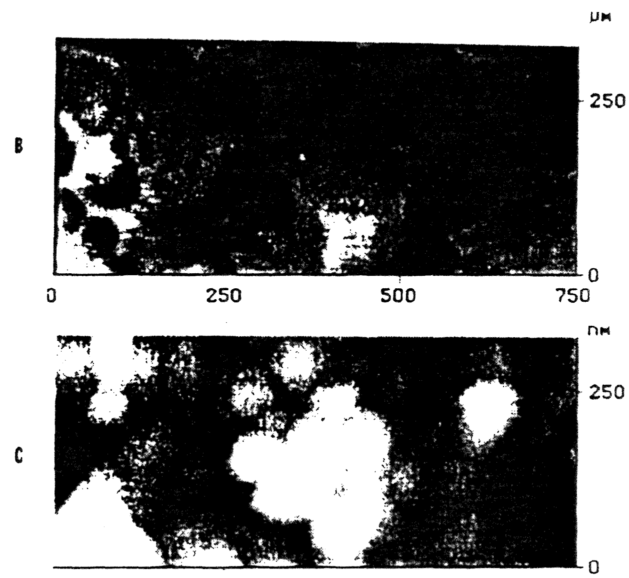

Fig.6. AFM images showing, a) cross section of a RTA sendust film while b) and c) compares the surface morphologies of long annealed and rapid annealed sendust films, respectively.

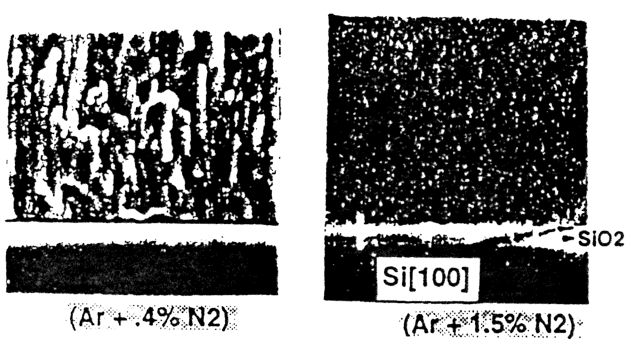

Fig.2 - SEM cross-sections of annealed 6 µm thick Sendust films on 0.5 µm SiO_2 / Si substrates:
a) colomnar structure and non-adherence of films grown in (Ar + 0.4 % N_2) atmosphere.
b) fine structure and adherence of films grown in (Ar + 1.5 % N_2) atm.

IEEE TRANSACTIONS ON MAGNETICS, VOL. 30, NO. 6, NOVEMBER 1994

Thick and Stress-Free Sendust Films on Silicon for Recording Head Cores.

J. Daval, B. Béchevet, J. Arroyo, B. Valon, MF. Armand and H. Joisten
LETI (CEA-Technologies Avancées) DMEL-CENG
17 Rue des Martyrs
38054 GRENOBE CEDEX 9 FRANCE 3930

IBM Almaden Research Center

Bruce A. Gurney

FeMO soft films

High resistive nanocrystalline Fe-M-O (M=Hf, Zr, rare-earth metals) soft magnetic films for high-frequency applications (invited)

Y. Hayakawa and A. Makino
Central Research Laboratory, Alps Electric Co., Ltd., 1-3-5 Higashi-Takami, Nagaoka 940, Japan

H. Fujimori and A. Inoue
Institute for Materials Research, Tohoku University, 2-1-1 Katahira, Sendai 980-77, Japan

Microstructure, soft magnetic properties, and applications of high resistive Fe-M-O (M=Hf, Zr, rare-earth metals) were studied. The Fe-M-O films are composed of bcc nanograins and amorphous phases with larger amounts of M and O elements which chemically combine each other. Consequently, the amorphous phases have high electrical resistivity. The compositional dependence of magnetic properties, electrical resistivity, and structure have been almost clarified. For example, the high magnetization of 1.3 T, high permeability of 1400 at 100 MHz and the high electrical resistivity of 4.1 $\mu\Omega$ m are simultaneously obtained for as-deposited $Fe_{62}Hf_{11}O_{27}$ nanostructured film fabricated by rf reactive sputtering in a static magnetic field. Furthermore, Co addition to Fe-M-O films improves the frequency characteristics mainly by the increase in the crystalline anisotropy of the nanograins. The $Co_{44.3}Fe_{19.1}Hf_{14.5}O_{22.1}$ film exhibits the quality factor ($Q = \mu'/\mu''$) of 61 and the μ' of 170 at 100 MHz as well as the high Is of 1.1 T. This frequency characteristics is considered to be superior to the other films already reported. The films also exhibit high corrosion resistance in an isotonic sodium chloride solution. Therefore, these films enable us to realize the high-frequency magnetic devices, such as thin-film ind[illegible] microswitching converters and ultrahigh-density recording heads. ©
Physics [illegible]

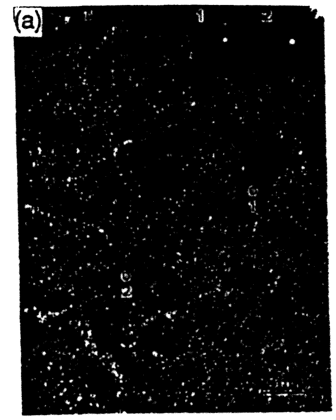

TABLE I. Magnetic properties, electrical resistivity (ρ), and film structure for as-deposited Fe-M-O films.

	I_s(T)	H_c (Am^{-1})	ρ ($\mu\Omega$ m)	Structure
$Fe_{56}Ti_{15}O_{29}$	1.2	1040	6.4	bcc
$Fe_{65}Zr_9O_{26}$	1.3	211	6.6	amo.+bcc
$Fe_{55}Hf_{11}O_{34}$	1.2	154	9.1	amo.+bcc
$Fe_{59}V_{15}O_{26}$	1.2	···	5.6	bcc
$Fe_{64}Nb_{12}O_{24}$	1.3	168	4.1	amo.+bcc
$Fe_{64}Ta_{13}O_{23}$	1.3	658	4.7	bcc
$Fe_{67}W_{13}O_{20}$	1.3	···	8.3	bcc
$Fe_{68}Y_{22}O_{10}$	0.9	207	22.6	amo.+bcc
$Fe_{75}Ce_{15}O_{10}$	1.2	116	5.9	amo.+bcc
$Fe_{81}Nd_{10}O_9$	1.4	286	5.2	amo.+bcc
$Fe_{67}Dy_7O_{26}$	1.3	322	9.3	amo.+bcc

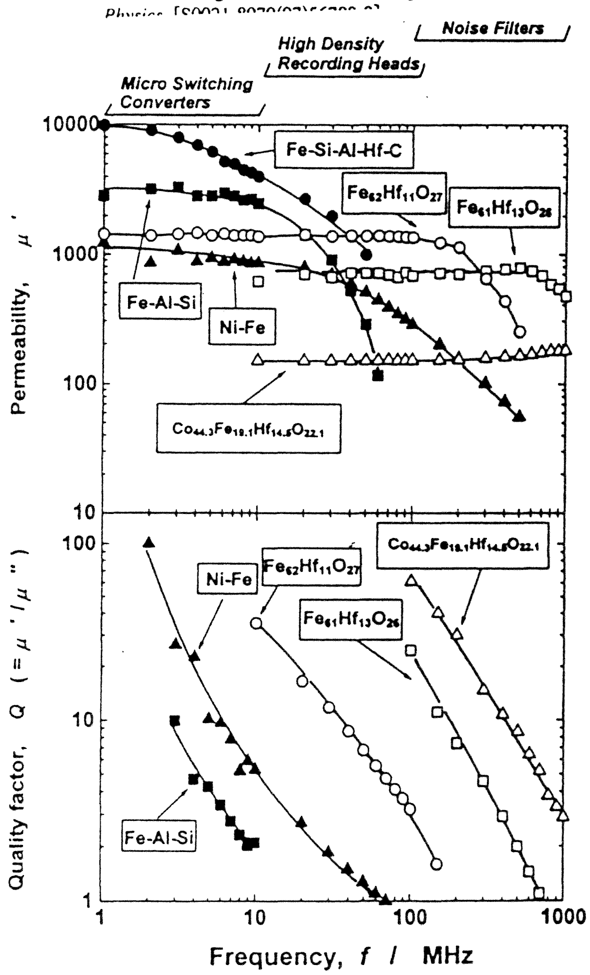

FIG. 7. Frequency dependence of the real part of initial permeability μ' and the quality factor $Q(=\mu'/\mu'')$ for an $Fe_{62}Hf_{11}O_{27}$ film (as-deposited), $Fe_{61}Hf_{13}O_{26}$ film (UFA) at 673 K for 10.8 ks, and $Co_{44.3}Fe_{19.1}Hf_{14.3}O_{22.1}$ film (as-deposited) compared with the other soft magnetic films have ever been reported.

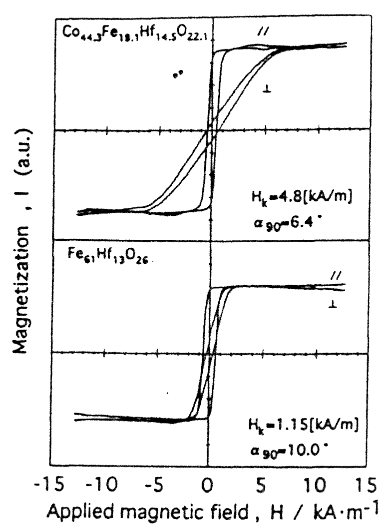

FIG. 6. Magnetization curves for an as-deposited $Co_{44.3}Fe_{19.2}Hf_{14.5}O_{22.1}$ film and an $Fe_{61}Hf_{13}O_{26}$ film after UFA at 673 K for 10.8 ks.

Fe/Co and $Fe/CoFe$

Magnetic properties of ion-beam-sputtered Fe/Co and Fe/CoFe multilayer films

672 Appl. Phys. Lett. 52 (8), 22 February 1988

Masakatsu Senda and Yasuhiro Nagai
NTT Applied Electronics Laboratories, Musashino, Tokyo 180, Japan

FIG. 2. Fe layer thickness dependence of coercivity. Circles represent a 2-nm-thick Co layer, and triangles represent a 0.5-nm-thick Co layer.

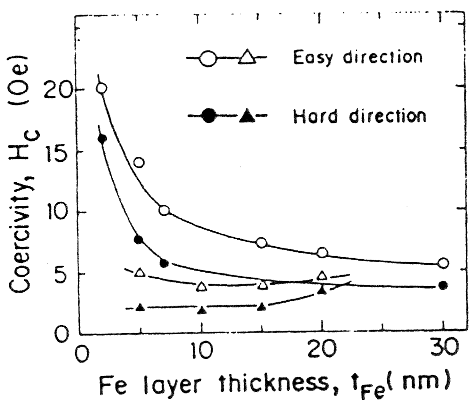

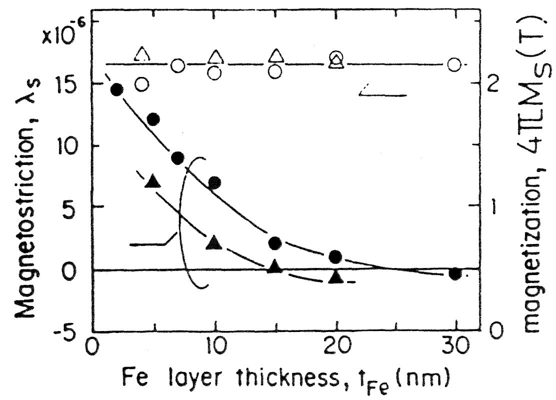

FIG. 1. Fe layer thickness dependence of magnetostriction and magnetization. Circles represent a 2-nm-thick Co layer, and triangles represent a 0.5-nm-thick Co layer.

FIG. 4. Hard-axis coercivity and magnetostriction as a function of annealing temperature. Circles represent Fe/Co films consisting of 20/2 nm, and triangles represent Fe/Co consisting of 10/0.5 nm. Squares are the Fe/CoFe films consisting of 10/0.5 nm.

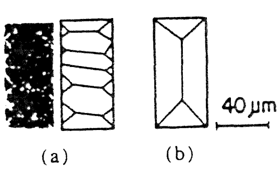

FIG. 5. Magnetic domain structure of Fe/Co multilayer films. (a) is the practical and (b) is the model domain patterns for films with negative magnetostriction. The thickness of the Fe layer is 14 nm, and the thickness of the Co layer is 0.5 nm. The 14 nm Fe layer is located on the top surface. The magnetostriction is $+6\times10^{-7}$, and the film stress is compressive.

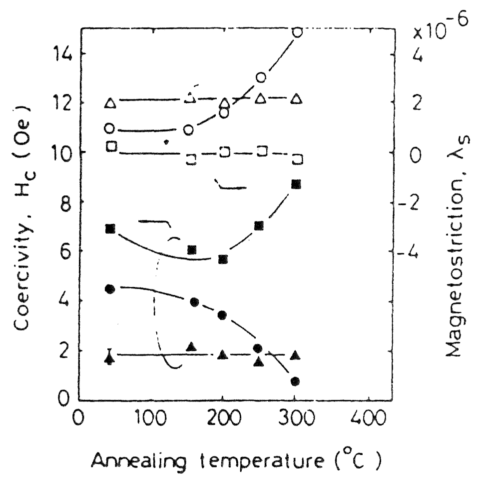

magnetostriction (λ)

origin: spin orbit coupling ($\vec{L} \bullet \vec{S}$)
definition:
$\lambda = \Delta L/L$ usually defined from the demagnetized state to a saturated state.

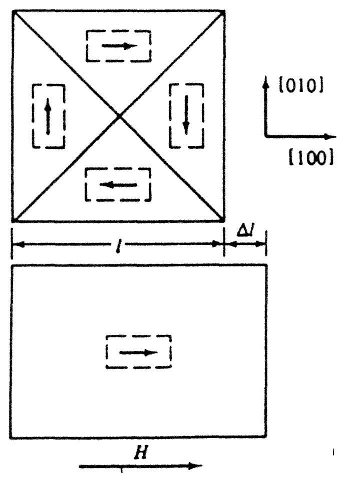

cubic: $\lambda_s = \lambda_{100} + 3(\lambda_{111} - \lambda_{100})(\alpha_1^2\alpha_2^2 + \alpha_2^2\alpha_3^2 + \alpha_3^2\alpha_1^2)$
α_i are direction cosines

isotropic: $\lambda_s = (3/2)\lambda_0(cos^2\theta - 1)$
θ is angle from magnetization direction

cantilever measurement of λ

cantilever deflection[10] can measure $\lambda < 10^{-7}$ for $t \leq 300$ Å

$$d = \lambda \frac{3 t_f l^2}{t_s^2} \frac{E_f (1 - \nu_s)}{E_s (1 + \nu_f)}$$

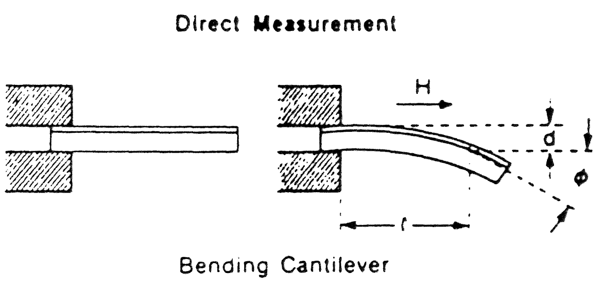

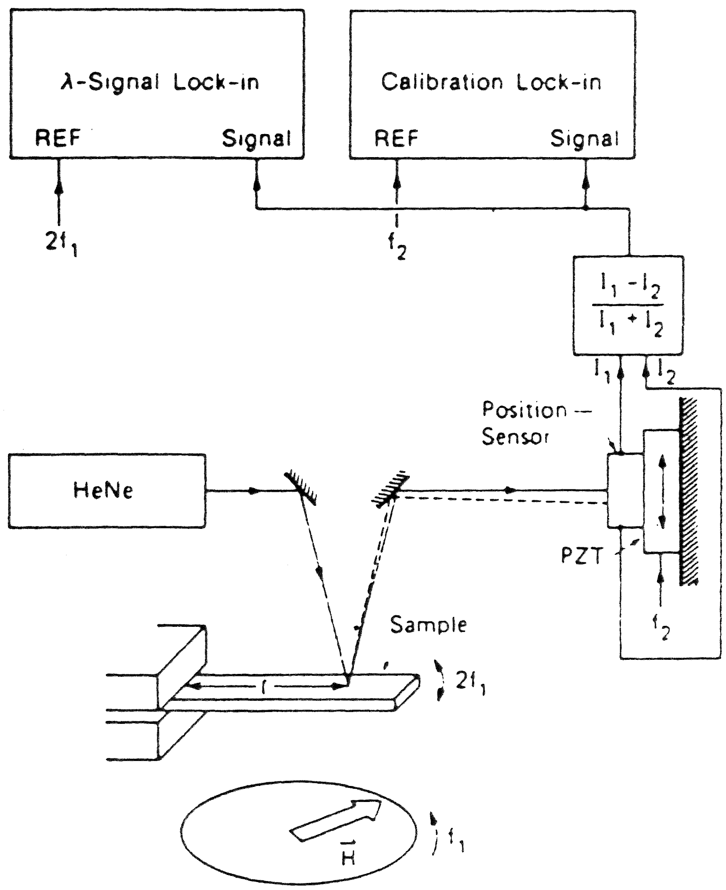

---

[10] A. Tam and H. Schroeder, IEEE Trans. Magnetics MAG-25, 2629 (1989)

rise time of write head reversal

Current dependence of the magnetization rise time in thin film heads

M. R. Freeman, A. Y. Elezzabi, and J. A. H. Stotz
Department of Physics, University of Alberta, Edmonton, Canada T6G 2J1

Time-domain optical measurements of magnetization dynamics can now be performed with sufficient resolution to reveal the intrinsic speed of many structures relevant to magnetic recording. Here we describe the behavior of the magnetization rise time at the air-bearing surface of a thin film recording head, as a function of the amplitude of current pulses in the write coil. The spatial profile of the magnetization on both sides of the gap is also examined through time-resolved, current dependent measurements. Spatial resolution enhancement via a solid immersion lens allows domain features to be discerned in the data.
[S0021-8979(97)23608-X]

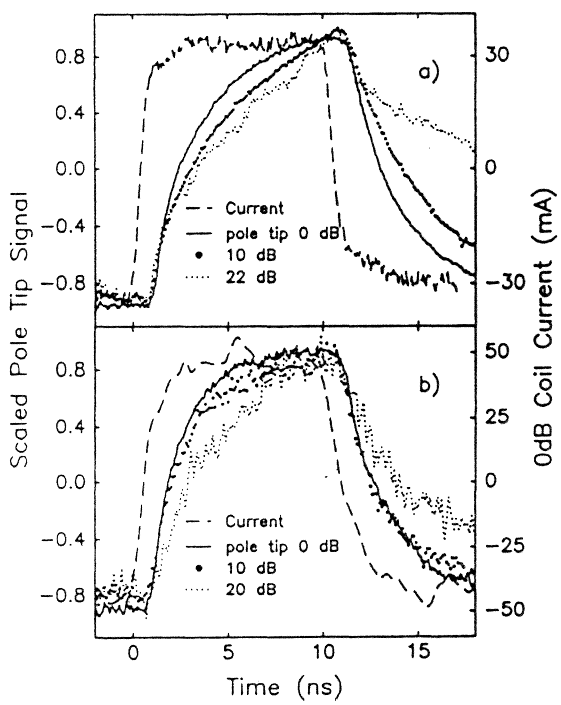

FIG. 4. "Spot" measurements of the time-dependent magnetic response on $P2$ near the gap (close to the peak of the magnetization) for three different current levels on each of two different recording heads. (a) 0.5 μm gap permalloy head, courtesy IBM Corp. (b) 0.25 μm gap permalloy head, courtesy Hewlett Packard Co.

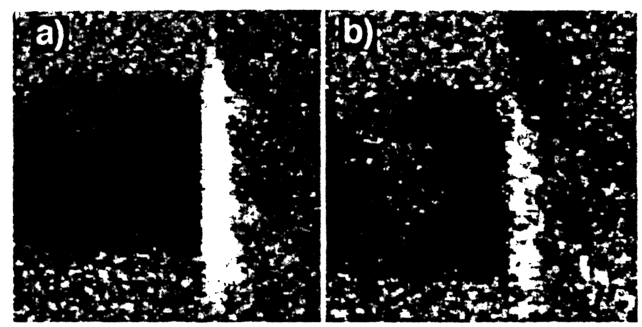

FIG. 5. Stroboscopic scanned Kerr images showing dynamic domain behavior on the head of Fig. 4(b) at the 0 dB level of current, (a) 1.6 ns and (b) 1.85 ns, after the onset of current reversal. The imaged areas are 7.5 μm on a side. Light and dark shadings reflect opposite polarities of the magnetization.

4516 J. Appl. Phys. **81** (8), 15 April 1997

'fastest' switching time

Following an instantaneous application of a 1 kOe field the magnetization precesses and rotates about $\vec{H}$

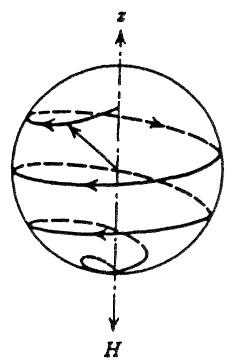

Estimate the time of reversal from Landau-Lifshitz eq. with

$$\vec{M}(t) = \vec{M}_o e^{i\omega t}$$

then

$$d\vec{M}/dt \sim i\omega\vec{M} = -\gamma\vec{M} \times \vec{H} \sim -\gamma\vec{M}H$$

so

$$w \sim \gamma H = 1.8 \times 10^{10}\ s^{-1}$$
$$\tau \sim 2\pi/\omega \sim 0.4\ ns$$

MAGNETICS AND MICROSTRUCTURE OF SPUTTERED $Ni_{80}Fe_{20}/SiO_2$ MULTILAYER FILMS

Michael A. Russak, Christopher V. Jahnes, Mark E. Re,
Bucknell C. Webb and S. Mohamaad Mirzamaani

$NiFe/SiO_2$

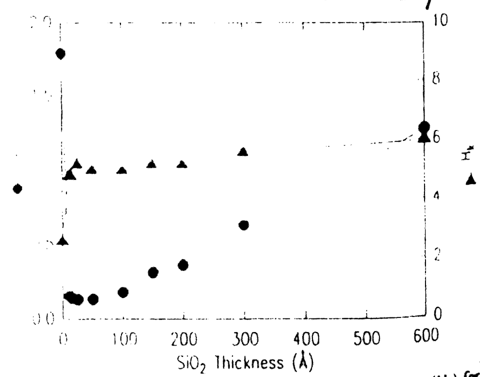

Figure 1. Easy axis coercivity (H_c) and anisotropy field (H_k) for laminated $Ni_{80}Fe_{20}$ films as a function of SiO_2 spacer thickness.

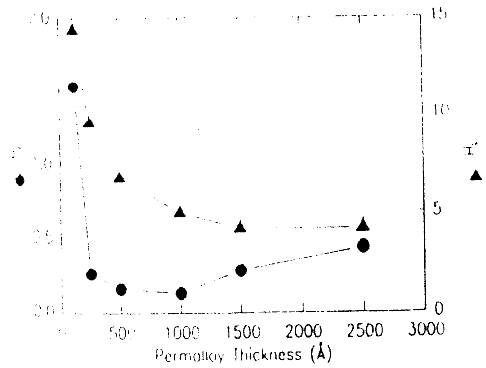

Figure 2. H_c and H_k as a function of $Ni_{80}Fe_{20}$ layer thickness for a constant SiO_2 spacer thickness of 50Å. The $Ni_{80}Fe_{20}$ layers were deposited without substrate bias.

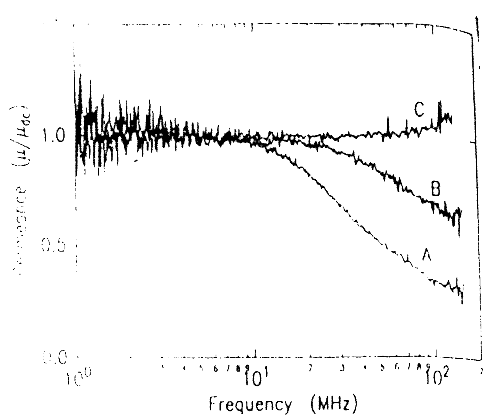

Figure 3. Frequency response of permeance for (A) monolithic $Ni_{80}Fe_{20}$ 1.5μm thick, (B) laminated $Ni_{80}Fe_{20}$ consisting of fifteen 1000 Å $Ni_{80}Fe_{20}$ layers separated by fourteen 100 Å Zr layers and (C) laminated $Ni_{80}Fe_{20}$ consisting of fifteen 1000 Å layers separated by fourteen 100 Å SiO_2 layers.

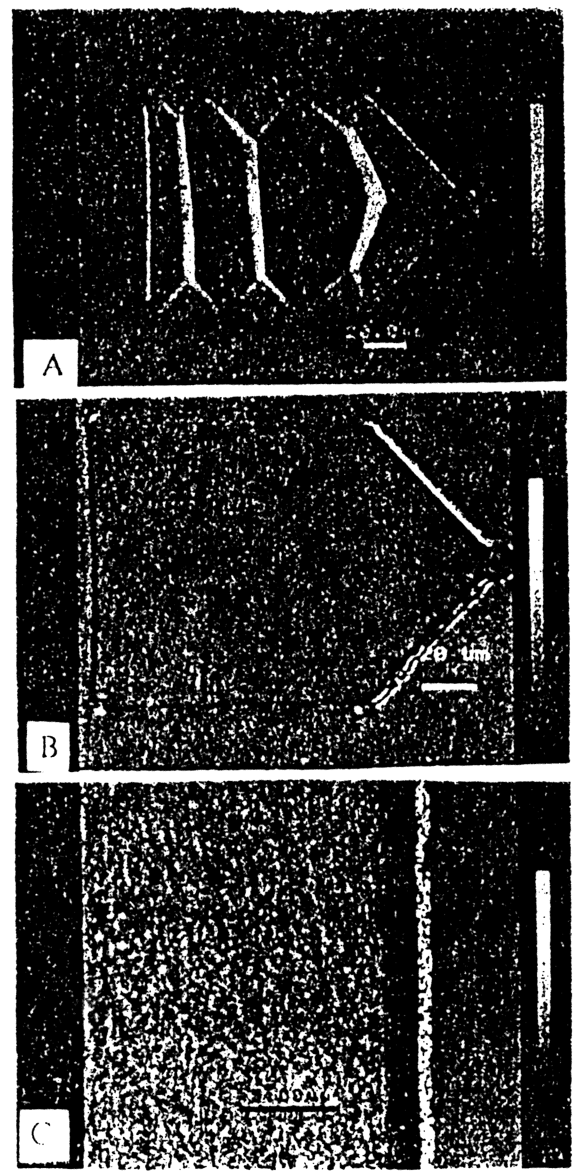

Figure 4. Domain contrast images [illegible] of A) a 1000 Å thick unlaminated $Ni_{80}Fe_{20}$ [illegible] consisting of two 1000 Å thick $Ni_{80}Fe_{20}$ [illegible] SiO_2 and C) a higher magnification view [illegible] trilayer film. The dark area at the sample [illegible] wall ≈ 2μm wide.

IBM Almaden Research Center

Bruce A. Gurney

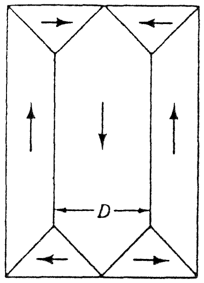

types of domain walls

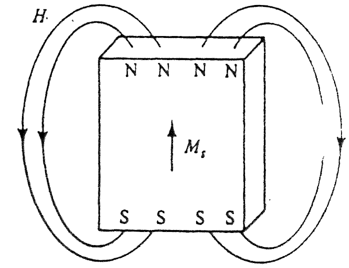

Domains reduce the total energy of magnetostatic fields.

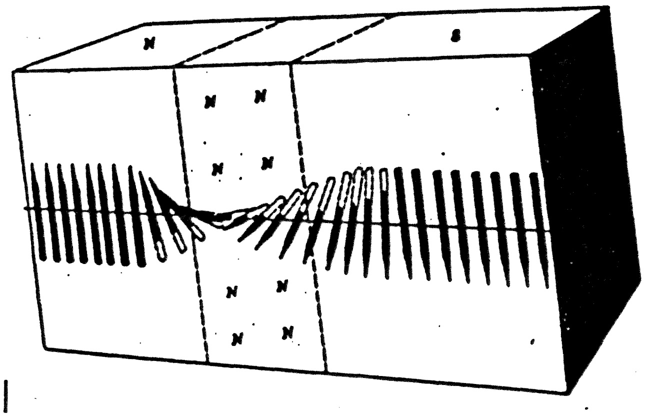

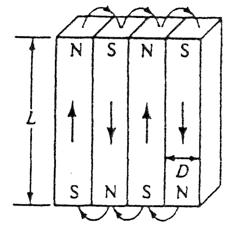

Bloch wall

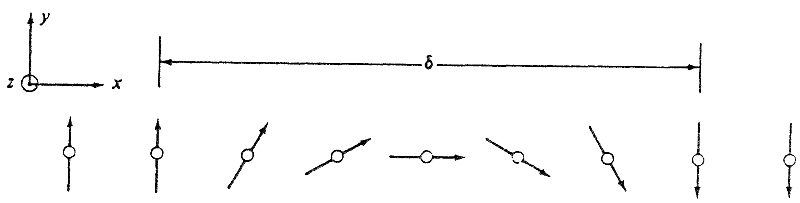

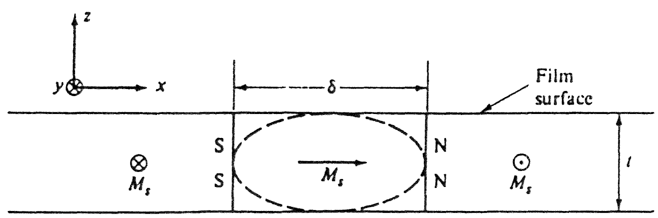

Neel wall

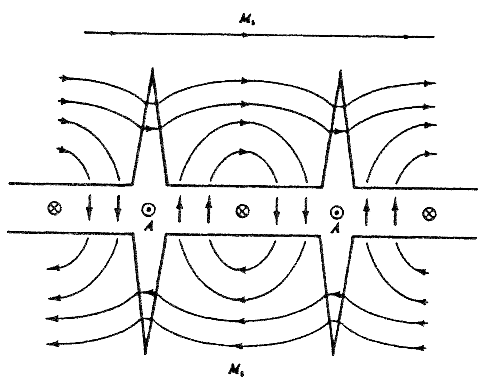

Cross-tie wall

domain wall width

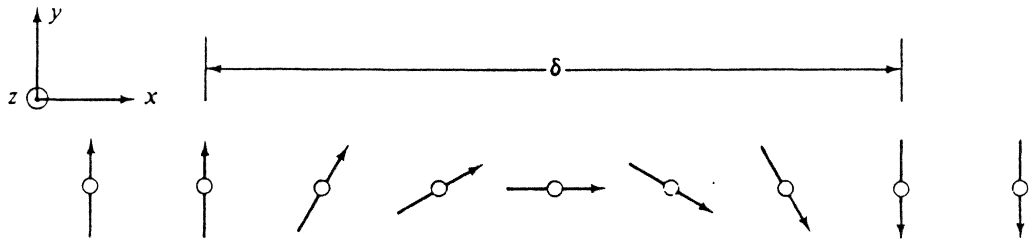

exchange energy in a wall:

$$\begin{aligned} \mathcal{E}_{ex} &= -2JS^2\cos\phi \approx 2JS^2\phi^2 \qquad \phi \approx \pi/N \\ \gamma &= \mathcal{E}_{ex}N/a^2 \approx 2\pi^2 JS^2 N/a^2 \sim \pi^2 A/\delta a \end{aligned}$$

anisotropy energy in a wall:

$$\mathcal{E}_K \approx K\delta$$

minimize the total energy to find equillibrium:

$$\begin{aligned} \gamma &\approx K\delta + 2\pi^2 A/a\delta \\ 0 &\approx K - 2A\pi^2/a\delta^2 \\ \rightarrow \delta &\approx \pi\sqrt{2A/aK} \end{aligned}$$

Micromagnetics of Laminated Permalloy Films

JOHN C. SLONCZEWSKI, BOJAN PETEK, AND BERNELL E. ARGYLE

laminated head

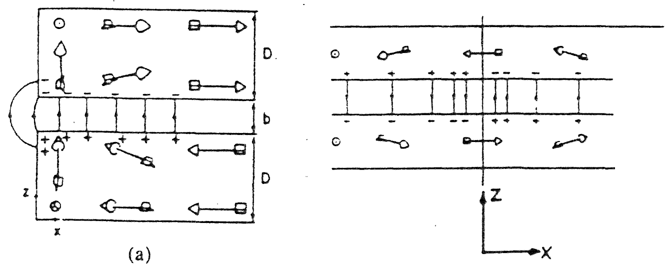

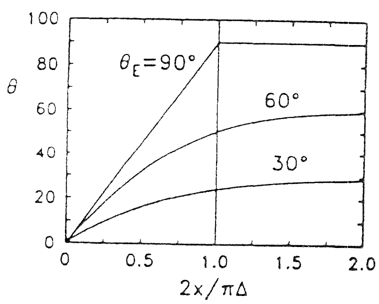

Fig. 5. Edge curling wall (ECW). (a) Schematic configuration for case of easy anisotropy angle $\theta_E = 90°$. Inclination of M out of film plane indicated by some arrows is exaggerated for sake of clarity. (b) Profile of ECW for three values of θ_E.

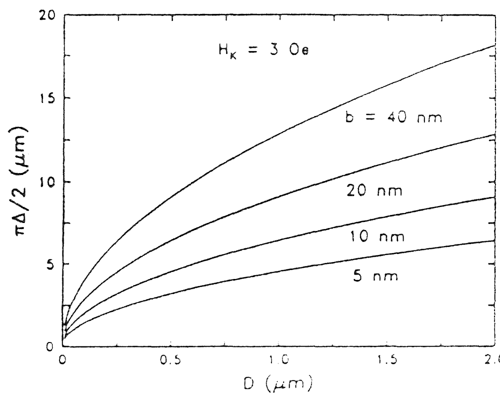

Fig. 6. Theoretical edge-curling wall width $\pi\Delta/2$ versus laminated-film thickness.

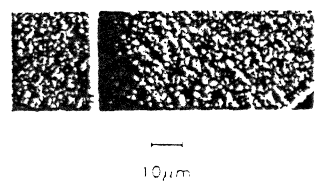

Fig. 7. Photomicrograph of edge curling wall in double Permalloy. Bright vertical line represents film edge, while faint line in the corner is image of a 180° Bloch wall parallel to the film easy axis.

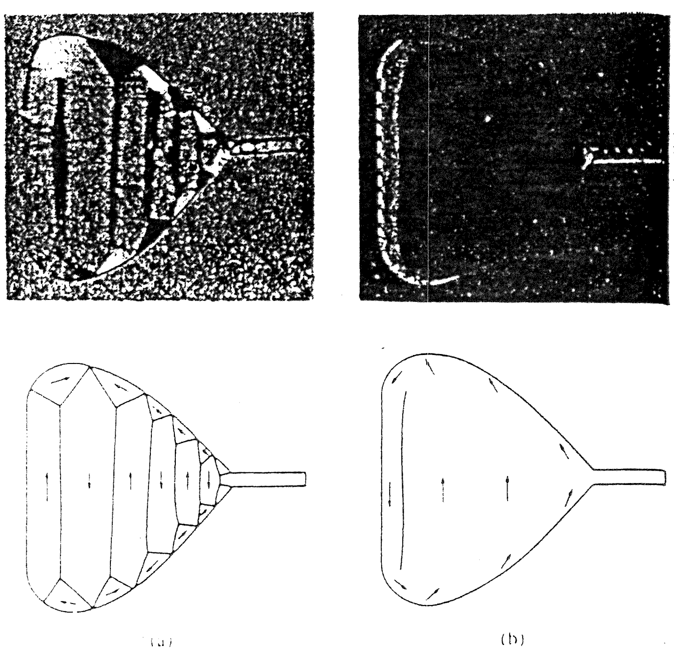

Fig. 12. Photomicrograph of Permalloy-film structure. (a) Single Permalloy film with $D = 3.2$ μm. (b) Similar structure in which yoke was laminated using two films, with $D = 1.6$ μm, $b = 12$ nm.

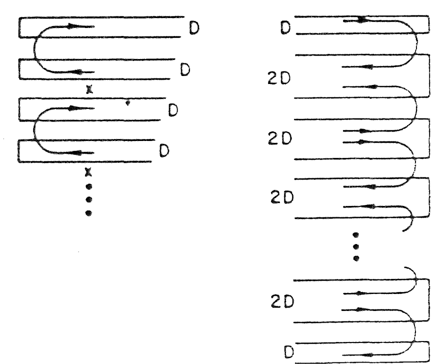

Fig. 16. Two schemes for flux closure in laminations with more than two magnetic sublayers.

IBM Almaden Research Center

Bruce A. Gurney

spin valve vs AMR head

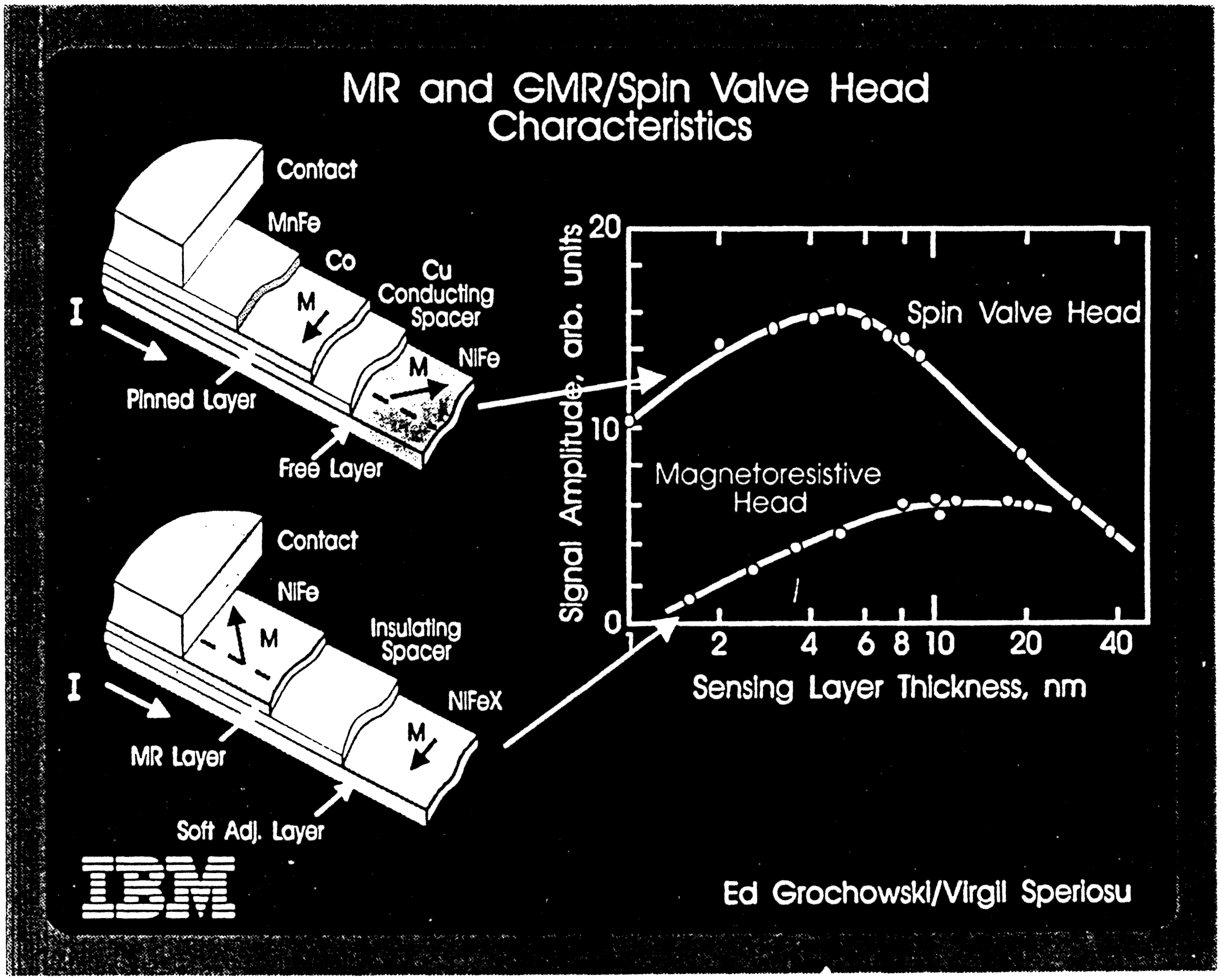

AMR vs GMR

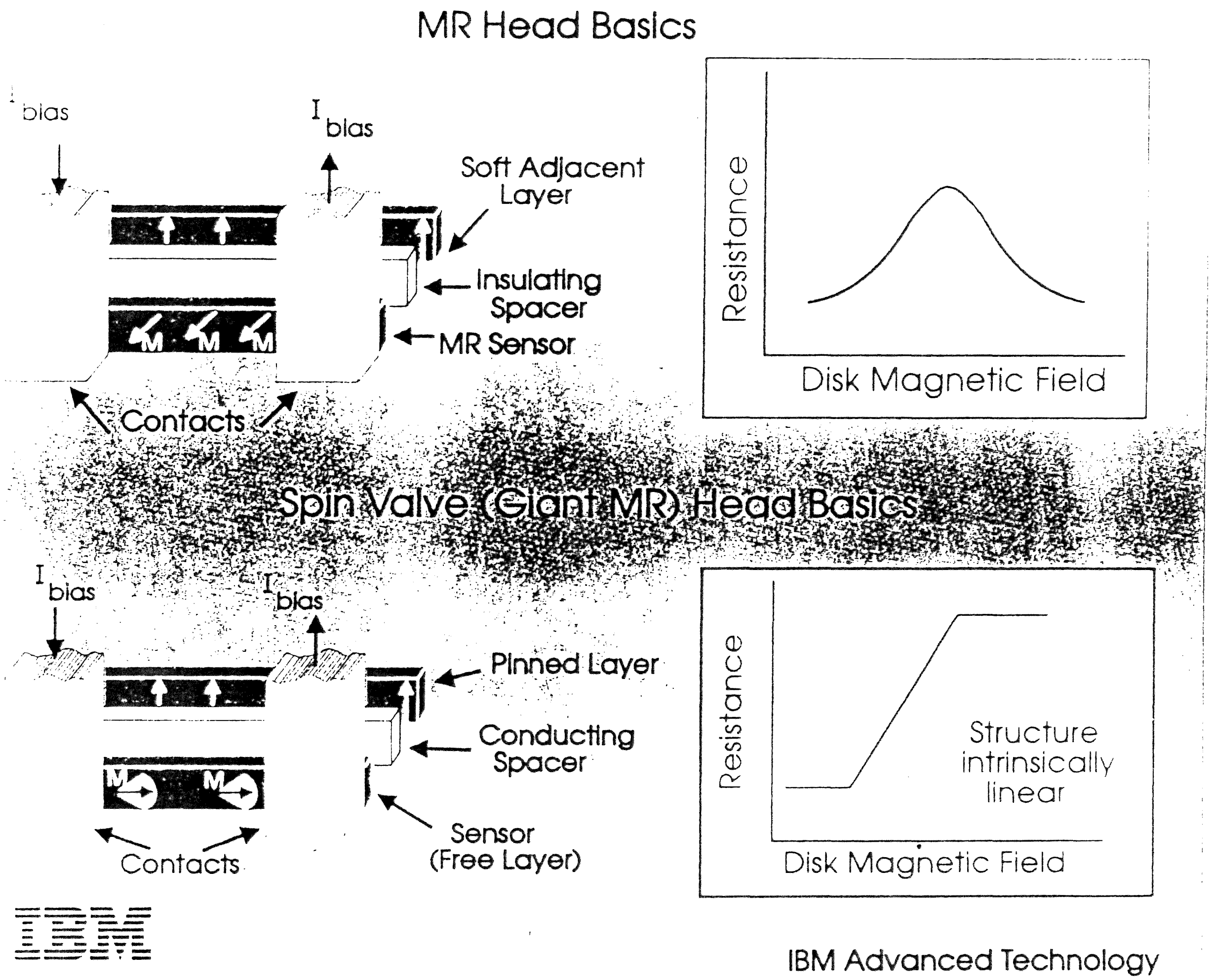
MR Head Basics
I bias
I bias
Soft Adjacent Layer
Insulating Spacer
MR Sensor
M M M
Contacts
Resistance
Disk Magnetic Field
Spin Valve (Giant MR) Head Basics
I bias
I bias
Pinned Layer
Conducting Spacer
M M
Sensor (Free Layer)
Contacts
Resistance
Structure intrinsically linear
Disk Magnetic Field
IBM
IBM Advanced Technology

GMR vs AMR in Ni-Fe-Co ternary alloys

Comparison between giant magnetoresistance in Fe–Co–Ni/Cu multilayers and anisotropic magnetoresistance in the ternary alloys

T. Miyazaki, J. Kondo, and H. Kubota
Department of Applied Physics, Faculty of Engineering, Tohoku University, Sendai 980-77, Japan

J. Inoue
Department of Applied Physics, Nagoya University, Nagoya 464-01, Japan

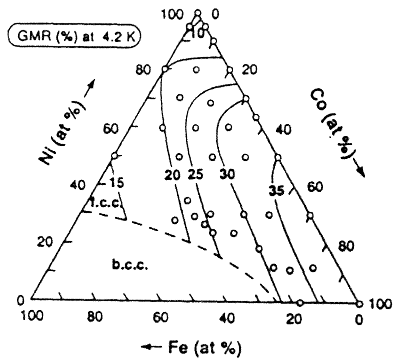

FIG. 1. Concentration dependence of the GMR ratio at the second peak at 4.2 K in (15 Å Fe–Co–Ni/Cu)$_{30}$ multilayers.

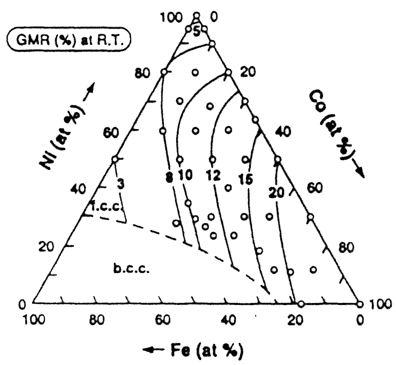

FIG. 2. Concentration dependence of the GMR ratio at the second peak at RT in (15 Å Fe–Co–Ni/Cu)$_{30}$ multilayers.

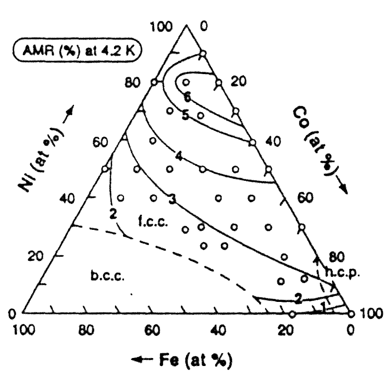

FIG. 3. Concentration dependence of the AMR ratio at 4.2 K in Fe–Co–Ni ternary alloy films.

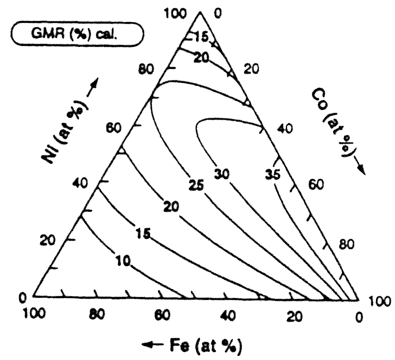

FIG. 6. Concentration dependence of the GMR ratio calculated by taking account of the spin-dependent interface and bulk scattering as well as the spin-independent scattering.

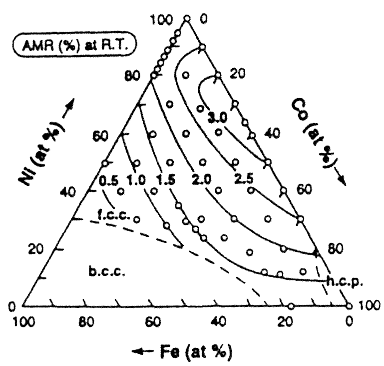

FIG. 4. Concentration dependence of the AMR ratio at RT in Fe–Co–Ni ternary alloy films.

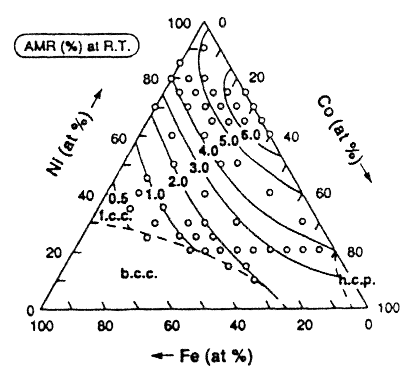

FIG. 5. Concentration dependence of the AMR ratio at RT in Fe–Co–Ni ternary alloy ribbons.

Exchange Anisotropy

Exchange anisotropy[9][10] is the shift in magnetization loop of a ferromagnetic layer in contact with an antiferromagnet:

$$H_{ex} = \frac{K_s}{M_s t}$$

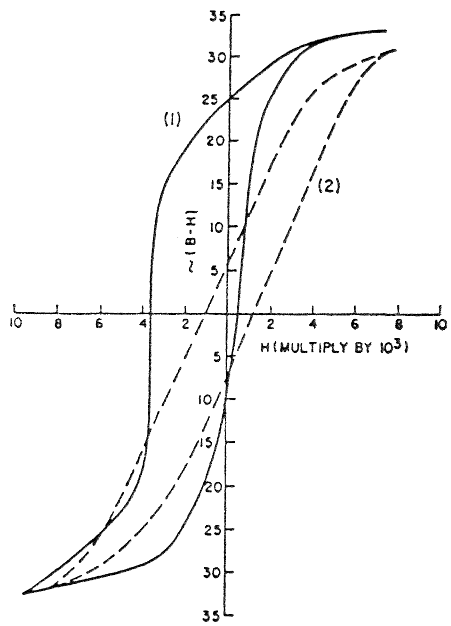

FIG. 1. Hysteresis loops at 77°K of oxide-coated cobalt particles. Solid line curve results from cooling the material in a 10 000 oersted field. The dashed line curve shows the loop when cooled in zero field.

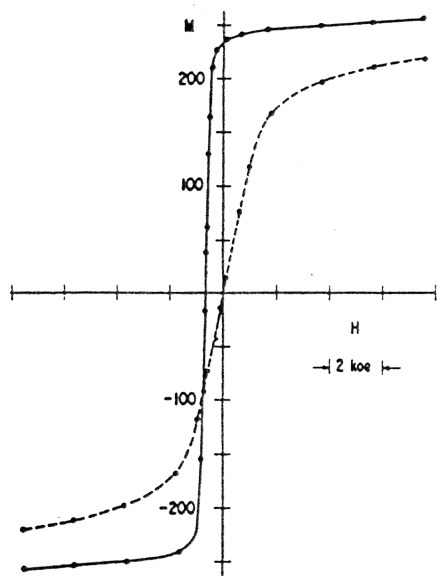

FIG. 1. Hysteresis loops measured at 4.2°K for 18.9 atomic % Fe in $(Ni,Fe)_3Mn$. Specimen cooled in +5-koe field (solid curves) or in zero field (dashed curve) (after Kouvel).

---

[9] W.H. Meiklejohn, et al. Phys. Rev. 105, 904 (1957)
[10] W.H. Meiklejohn, J. Appl. Phys. 33, 1328 (1962)

exchange anisotropy systems

A variety of systems exhibit exchange anisotropy, including

couple	structure	K_s † erg/cm^2	temp. $^\circ K$	ref.
$NiFe/FeMn$	poly	0.1	300	6
$NiFe/\alpha - Fe_2O_3$	poly	0.04	300	6
$NiFeMo/\alpha - TbFe$	poly/amorph	0.25	300	7
NiO/Ni	single	1.75	300	8
Co/CoO	single	1.4	98	9
$Co_xNi_{1-x}O/NiFe$	poly	0.1	300	10
$NiOCoO/NiFe$	multilayer	0.1	300	11
$NiMn/NiFe$	poly	0.25	300	12

† cf. $E_{ex} \sim 8A/a^2 = 133\ erg/cm^2$ for Fe.

[11] R.D. Hempstead et al., IEEE Trans. Magn. MAG-14, 521 (1978)

[12] F. Hellman, et. al. (1987)

[13] A.E. Berkowitz, et al. 1965

[14] D. Paccard et al., Phys. Stat. Solidi 16, 301 (1966)

[15] M.J. Carey et al., Appl. Phys. Lett. 60, 3060 (1992)

[16] M.J. Carey et al., J. Appl. Phys. 73, 6892 (1993)

[17] T. Lin, et al., Appl. Phys. Lett. 65, 1183 (1994)

temperature dependence

Typically a linear behavior is observed, very different from the expected sublattice magnetization[18 19 20] with $H_{ex} \rightarrow 0$ at $T_b < T_N$.

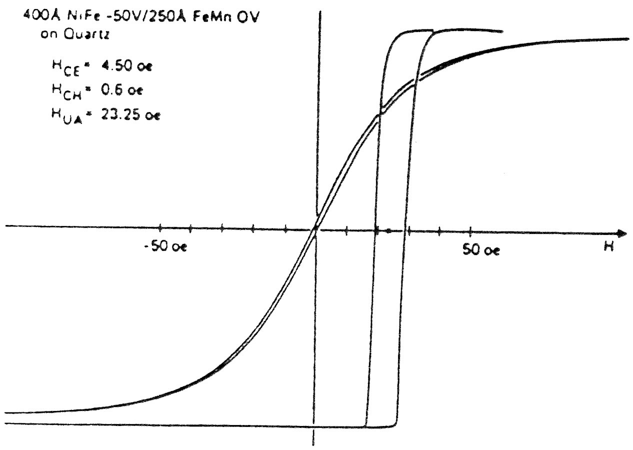

Figure 1. B-H Loop of an Exchange-Biased Film

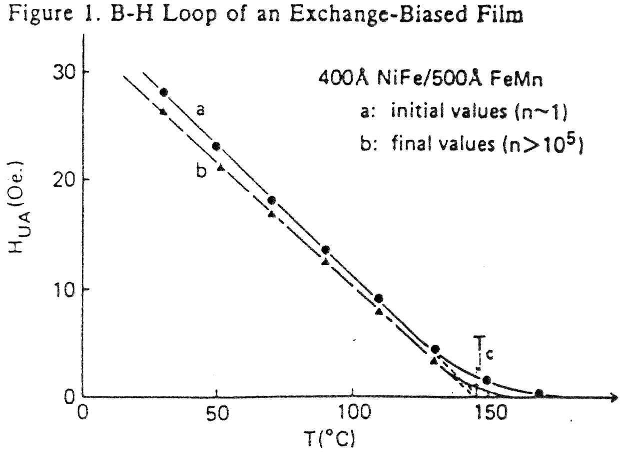

Figure 2. H_{UA}(T) for the standard permalloy/FeMn film

Si/100Å Cu/60Å NiFe/ t_{AF} FeMn/100Å Cu

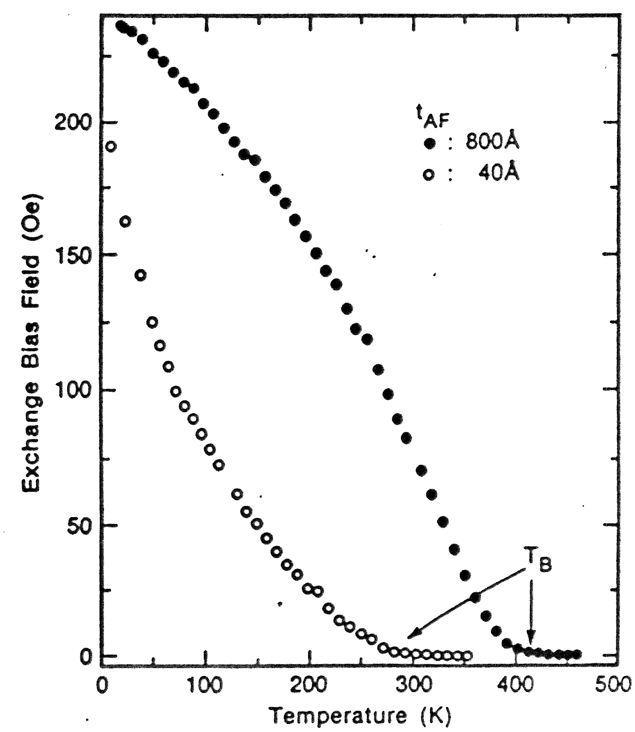

[18] C. Tsang, et al., J. Appl. Phys. 53, 2605 (1982)

[19] Y. Endoh, et al., J. Phys. Soc. Jpn. 30, 1614 (1971)

[20] V.S. Speriosu, et al. IBM J. of Research and Deleopment 34, 884 (1990)

thickness dependence

Typically exchange persists to thicknesses of a few nanometers, then drops to zero.[21]

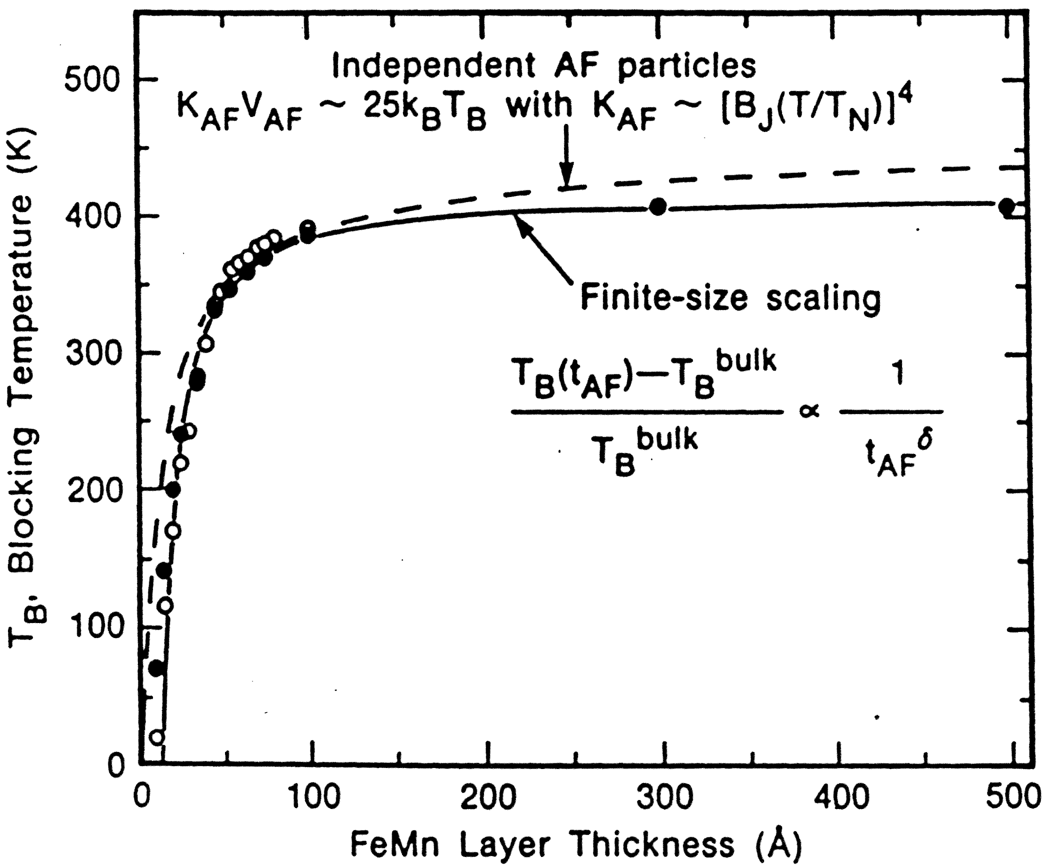

---

[21] S.S.P. Parkin and V.S. Speriosu, '*Magnetic Properties of Low Dimensional Systems II*, Springer Proceedings in Physics vol. 50, L.M. Falicov, Ed. Springer-Verlag, Berlin (1990)

models of exchange anisotropy I

Formation of a domain wall in the antiferromagnet parallel to the interface.[22]

$$\overset{energy}{\mathcal{E}} = \overbrace{2\sqrt{AK}(1-\cos\alpha)}^{wall\ energy} + \underbrace{K_f t \cos^2\beta}_{ferro\ anisotropy} + \overbrace{A_{12}/\xi\ [1-\cos(\alpha-\beta)]}^{interface\ energy} + \underbrace{HMt(1-\cos\beta)}_{Zeeman\ energy}$$

$$\Rightarrow \qquad MtH_{ex} = \begin{array}{ll} -[A_{12}/\xi], & A_{12}/2\xi\sqrt{AK} \ll 1 \\ -2\sqrt{AK}, & A_{12}/2\xi\sqrt{AK} \gg 1 \end{array}$$

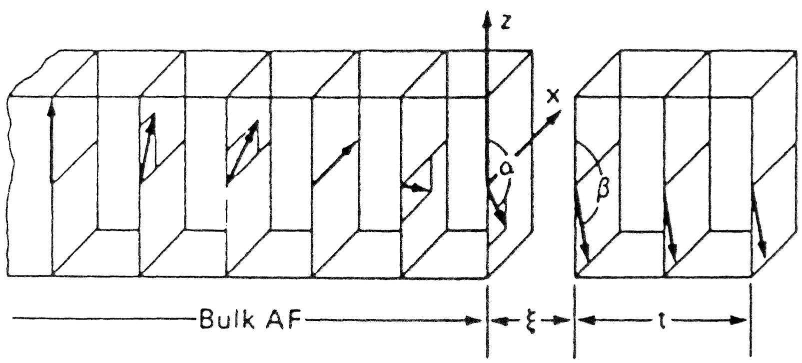

FIG. 1. Magnetic model for the interface of a thin ferromagnetic film on a thick antiferromagnetic substrate. The uniaxial anisotropy of the antiferromagnet is along the z axis. The figure depicts a situation in which an external magnetic field is applied opposite to z and in which the exchange coupling across the interface with thickness ξ is positive. The spins of only one sublattice of the antiferromagnet are shown.

[22] D. Mauri, et al. J. Appl. Phys. 62, 3047 (1987)

interdiffusion at the interface

Annealed $FeMn/NiFe$ couples show increased exchange and a blocking temperature above the Neel temperature of bulk $FeMn$ due to the formation of a $NiFeMn$ alloy at the interface.[23]

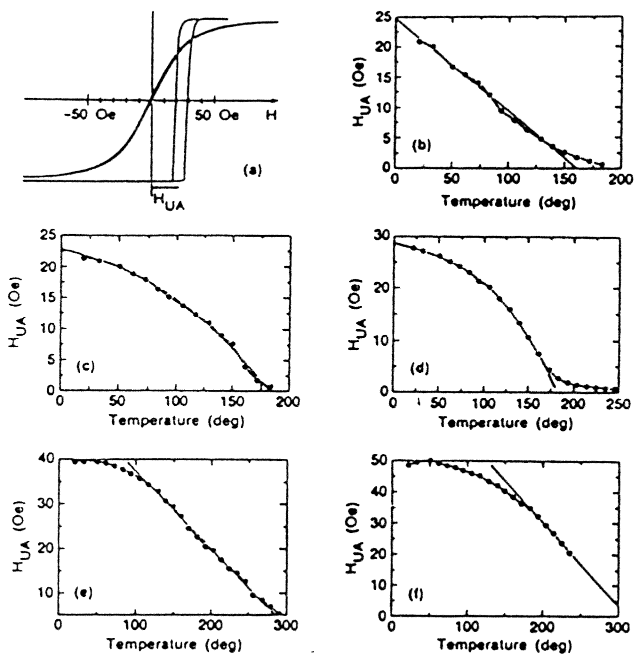

FIG. 1. Temperature dependence of the exchange-bias field, $H_{UA}(T)$. (a) Typical B–H loop for NiFe/FeMn. (b) As-deposited NiFe/FeMn films. (c) NiFe/FeMn film annealed at 245 °C for seven cycles and 260 °C for five cycles. (d) NiFe/FeMn film annealed at 245 °C for seven cycles and 19 hours at 270 °C. (e) NiFe/FeMn film annealed 40 hours at 270 °C. (f) NiFe/FeMn film annealed 60 hours at 270 °C.

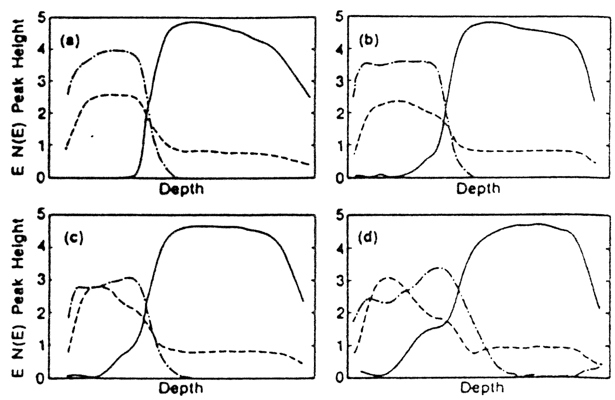

FIG. 2. Crater edge depth profiles of FeMn/NiFe region of samples. Ni is shown by the solid lines, Fe by the dashed lines, and Mn by the dot-dashed lines. The crater edge depth profile data are normalized so the Ni signal in the NiFe is the same for all the films. Any differences in signals from Fe and Mn result because the data are recorded in N(E) (integral) mode, so slight spectrometer misalignment will change the magnitude of signal. (a) As deposited. (b) Annealed at 245 °C for seven cycles. (c) Annealed at 245 °C for seven cycles and 260 °C for five cycles. (d) Continuously annealed at 270 °C for 40 hours.

---

[23] M. Toney, et al., J. Appl. Phys. 70 6228 (1991)

models of exchange anisotropy II

Formation of domain walls in the antiferromagnet perpendicular to the interface that arise from random averaging of steps.[24]

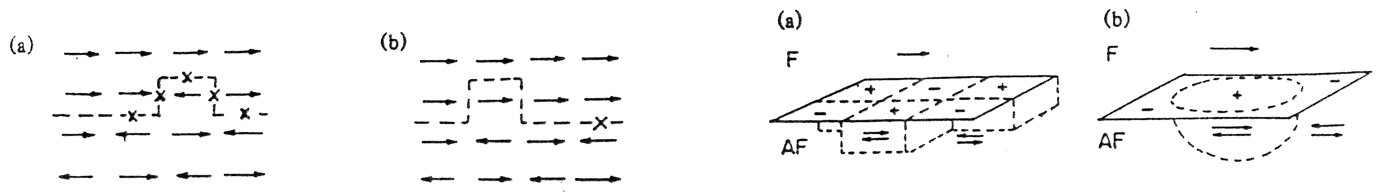

This model considers an interface whose exchange energy $J_i \approx fJ$ is a fraction f of the exchange in the bulk $J \sim A/a$. For an interfacial area L^2 with $N = L^2/a$ atoms the average random field energy per unit area is

$$\mathcal{E} \approx -fJ/a^2\sqrt{N} = -fJ/aL$$

The averaging takes place over L about the length of a domain wall, i.e. $L \sim \pi\sqrt{A/K}$. Thus

$$MtH_{ex} = 2\mathcal{E} \approx -2f\sqrt{AK}$$

i.e. the domain wall energy.

[24] A.P. Malozemoff, J. Appl. Phys. 63, 3874 (1988)

distribution of blocking temperatures in FeMn

Net anisotropy energy is a convolution[25] of the density of regions with a given blocking temperature $\rho(T_b)$ with the temperature dependence of the energy density $f(T;T_b)$:

$$K_s(T) \approx \int f(T;T_b)\ \rho(T_b)\ dT_b$$

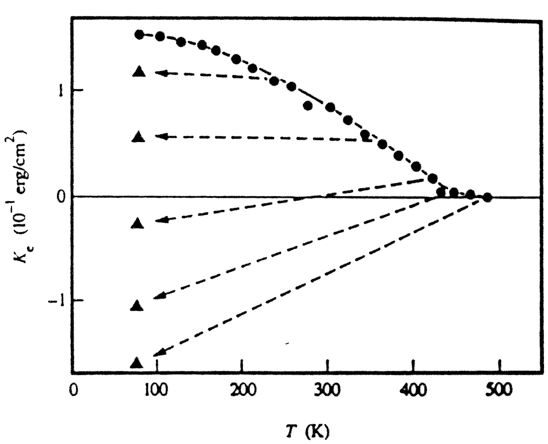

IBM J. RES. DEVELOP. VOL. 34 NO. 6 NOVEMBER 1990

Field Cooling Along Hard Direction

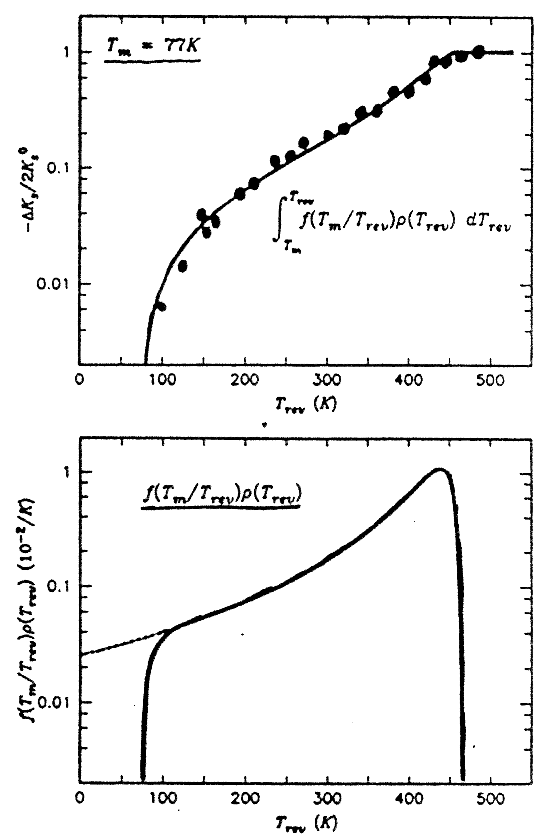

[25] L. Neel, Ann. Phys. 2, 61 (1968)

independent 'particles' in FeMn

Independent-particle model

- Distribution of local blocking temperature, T_{bl}

- Net exchange anisotropy, $\vec{K_s}$, is vector sum of local components:

local $\vec{k_i}$

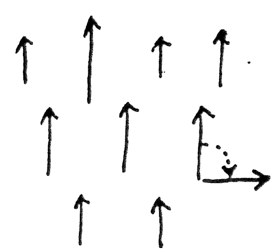

$\vec{K_s} = \Sigma\vec{k_i}$

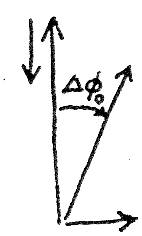

- Change easy direction $\Delta\phi_0$ by field cooling

- If particles are rotating independenlty, K_s and $\Delta\phi_0$ are uniquely related.

(VSS)

independent 'particles' in FeMn

test of independent particle picture in $FeMn$ by field cooling in different directions[26]

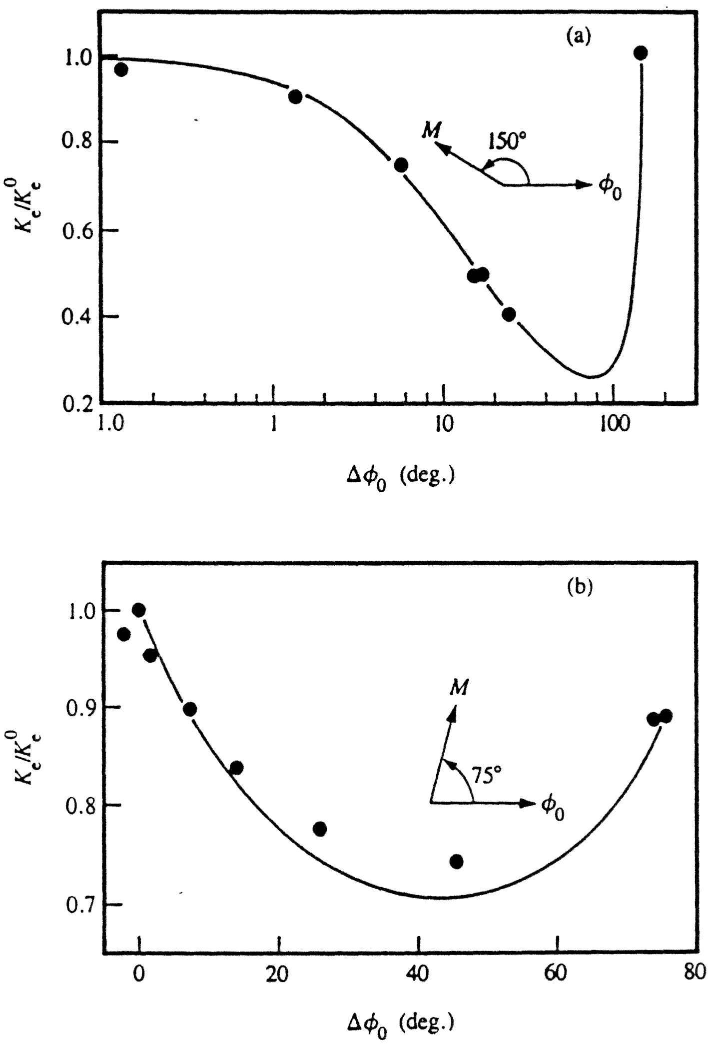

Comparison between measured (solid circles) and calculated lines of exchange anisotropy versus the change in easy direction for field cooling at (a) 150° and (b) 75° to the initial easy direction.

---

[26] V.S. Speriosu et al., *Technical Digest, Magnetic Recording Conference,* IEEE (1990)

distribution of local anisotropy

For a broad distribution of activation energies E_a kinetics yields a $\ln(time)$ dependence:

$$\Delta\phi = const. + \frac{\pi k_B T}{2E_a^{max}} \ln \tau$$

$$E_a^{max} = V_A^{max}(K_A^{max} - \frac{K_s}{t_A})$$

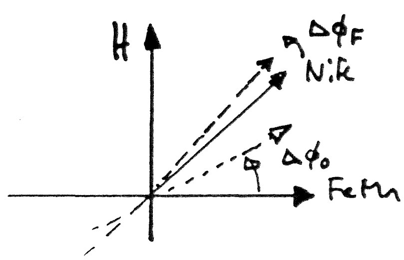

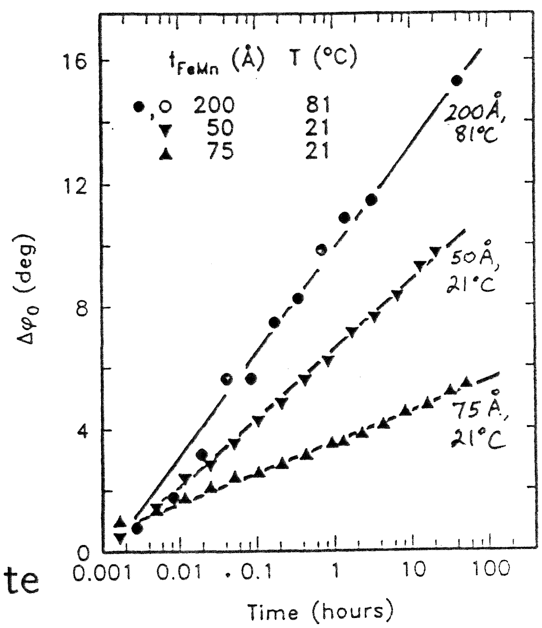

Results[27] for $FeMn$ at 300K indicate

$$\begin{array}{lcccll} 2\times10^{-18} & \le & V_A^{max} & \le & 2\times10^{-17} & cm^3 \\ 7\times10^{5} & \le & K_A^{max} & \le & 7\times10^{6} & erg/cm^3 \end{array}$$

[27] V. Speriosu, *private communication*

$Co_x Ni_{1-x} O$

Exchange anisotropy in coupled films of $Ni_{81}Fe_{19}$ with NiO and $Co_xNi_{1-x}O$

M. J. Carey and A. E. Berkowitz
Department of Physics and Center for Magnetic Recording Research, University of California San Diego, La Jolla, California 92093-0401

(Received 15 July 1991; accepted for publication 29 March 1992)

Shifted hysteresis loops were used to investigate exchange anisotropy in 500 Å $Co_xNi_{1-x}O$/300 Å $Ni_{81}Fe_{19}$ polycrystalline bilayer couples. Bilayers of $Ni_{81}Fe_{19}$ with NiO have a room-temperature exchange field, H_e, of 30 Oe in the as-deposited state. A maximum in the exchange field at room temperature was observed near $x = 0.4$, indicating an optimal alloying of the properties of the high anisotropy CoO and the high Néel temperature NiO. The blocking temperatures of the exchange couples vary linearly with x, suggesting a linear dependence of the oxide Néel temperature with x.

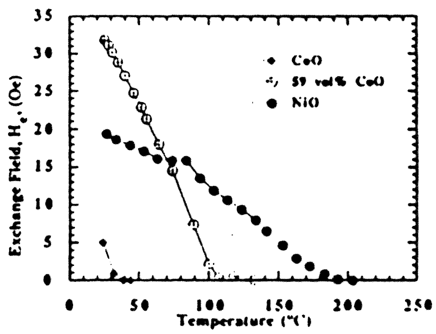

FIG. 1. Exchange field, H_e, as a function of temperature for 300 Å $Ni_{81}Fe_{19}$ on 500 Å antiferromagnetic oxides: CoO, $Co_{0.59}Ni_{0.41}O$, and NiO. These samples were cooled from above their blocking temperatures in a 3 kOe field.

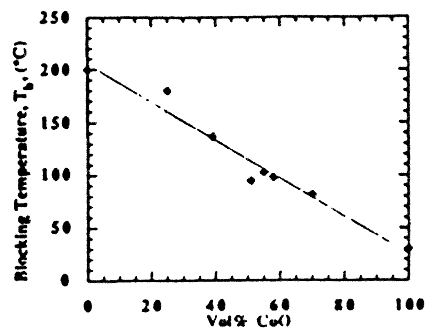

FIG. 3. Blocking temperature, T_b, as a function of the CoO concentration in $Co_xNi_{1-x}O/Ni_{81}Fe_{19}$ couples. The best linear fit is shown

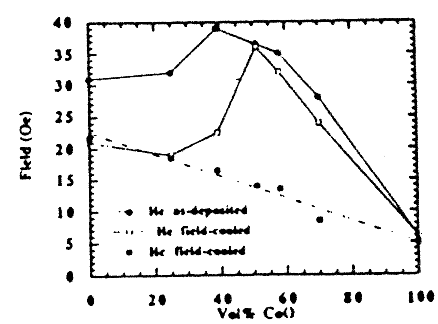

FIG. 2. Room-temperature exchange field, H_e, for samples in the as-deposited and field-cooled states and coercive force, H_c, for samples in the field-cooled state. Data are shown for $Co_xNi_{1-x}O/Ni_{81}Fe_{19}$ couples as a function of x.

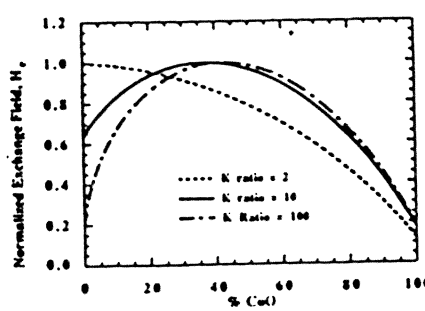

FIG. 4. Calculated dependence of the room-temperature exchange field on the CoO concentration. Model discussed in text.

IBM Almaden Research Center

Bruce A. Gurney

nanostructure of NiO/Co pinned layer spin valves

Nanostructure, interfaces, and magnetic properties in giant magnetoresistive NiO-Co-Cu-based spin valves

Harsh Deep Chopra[a)]
National Institute of Standards & Technology, Gaithersburg, Maryland 20899; and Department of Materials and Nuclear Engineering, The University of Maryland, College Park, Maryland 20742-2115

B. J. Hockey, P. J. Chen, R. D. McMichael, and W. F. Egelhoff, Jr.
National Institute of Standards & Technology, Gaithersburg, Maryland 20899

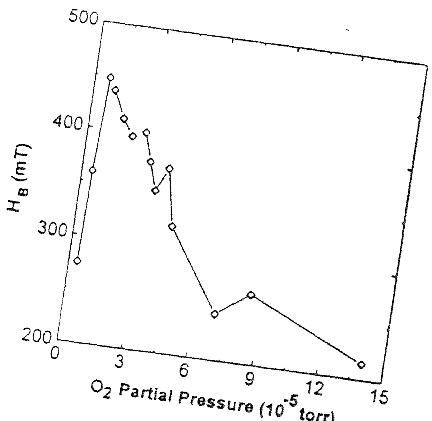

FIG. 1. Effect of $p(O_2)$ on pinning strength, H_B, in NiO-Co-Cu-based top spin valves.

J. Appl. Phys., Vol. 81, No. 8, 15 April 1997

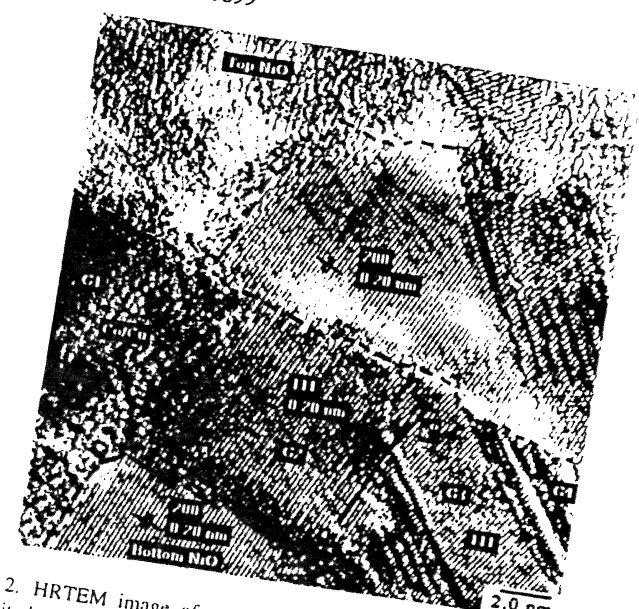

FIG. 2. HRTEM image of a symmetric spin valve, with top NiO layer deposited at 2.5×10^{-5} Torr.

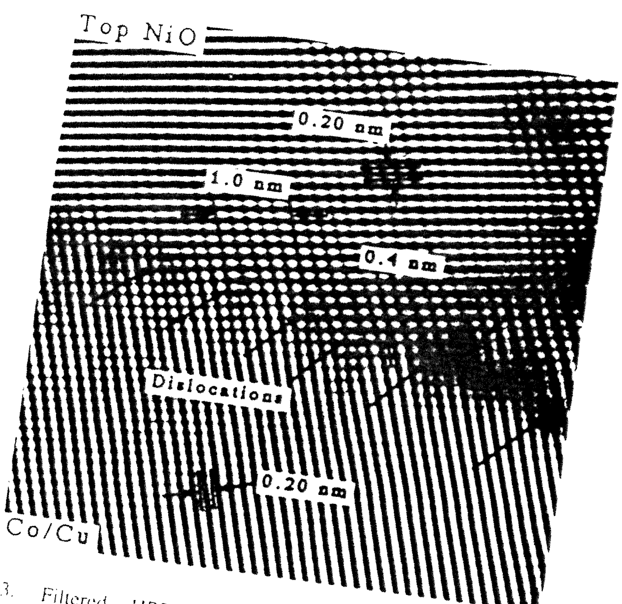

FIG. 3. Filtered HRTEM image of a symmetric spin valve [$p(O_2)=2.5\times10^{-5}$ Torr] showing steps in a crystallographically well-defined top NiO-Co interface.

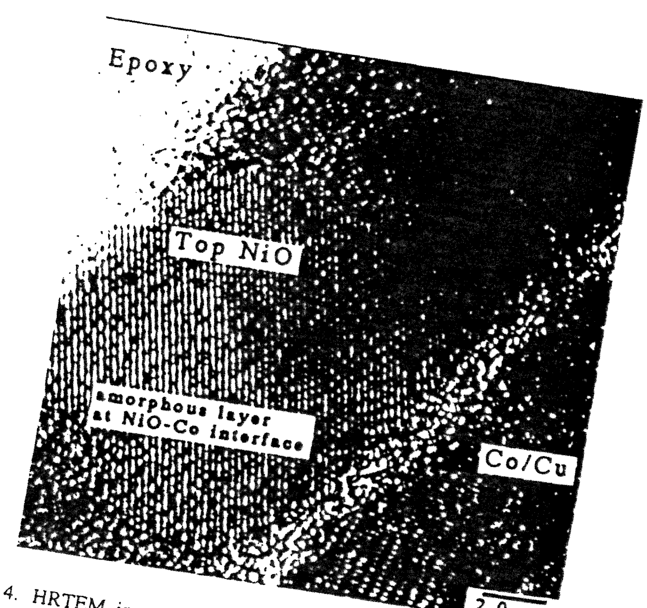

FIG. 4. HRTEM image of a symmetric spin valve, with top NiO layer deposited at 13.0×10^{-5} Torr. An amorphous film has formed at the top NiO-Co interface.

IBM Almaden Research Center

Bruce A. Gurney

Stress and NiO/NiFe

Stress effects on exchange coupling field, coercivity, and uniaxial anisotropy field of NiO/NiFe bilayer thin film for spin valves

De-Hua Han, Jian-Gang Zhu, Jack H. Judy, and John M. Sivertsen[a)]
The Center for Micromagnetics and Information Technologies (MINT), Department of Electrical Engineering, University of Minnesota, Minneapolis, Minnesota 55455

The effects of uniaxial stress on the exchange coupling field, H_{ex}, coercivity, H_c, and uniaxial anisotropy field, H_K, in NiO/NiFe bilayers were experimentally studied. The NiO/NiFe bilayers were deposited onto a Si(100) wafer using radio frequency reactive sputtering. Samples of the bilayers were externally and constantly uniaxial stressed (either tensile or compressed) using a specially designed sample holder with a fixed radius of curvature. The hysteresis loops of the stressed NiO/NiFe bilayer samples were measured *in situ* along the easy and hard axes of the NiFe films using a vibrating sample magnetometer. The composition of the NiFe film in the NiO/NiFe bilayer was characterized as $Ni_{80.2}Fe_{19.8}$ using x-ray photoelectron spectroscopy. The H_c and H_K of the bilayers were significantly affected by the stress, while the H_{ex} was apparently not changed by the same stress. The large changes in the coercivity in the stressed NiO/NiFe bilayer were produced by the change of the effective uniaxial anisotropy field of the bilayer. We conclude that the control and reduction of both intrinsic and external stress are very important in the fabrication of spin-valve giant magnetoresonance heads and sensors.
[S0021-8979(97)18108-7]

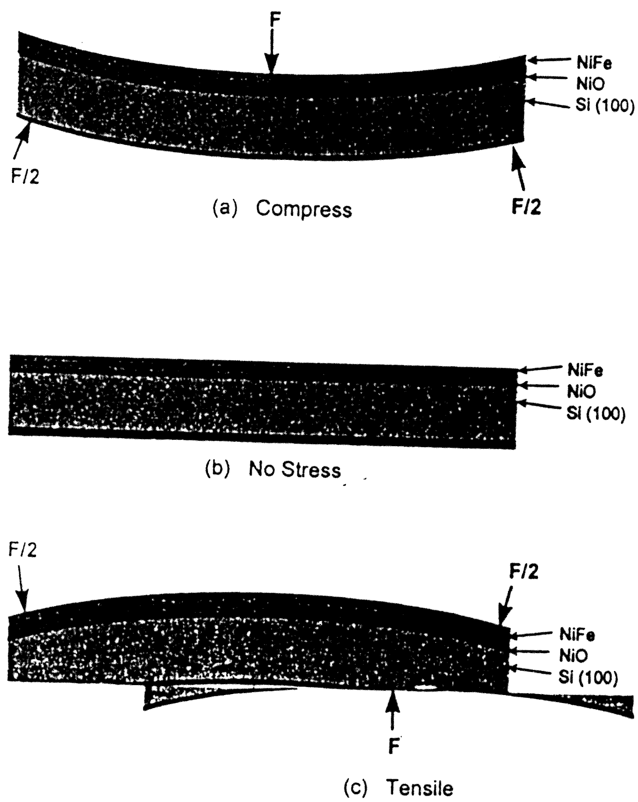

FIG. 1. Schematic of the externally and constantly stressed samples. The NiO/NiFe bilayer can be (a) compressive stressed, (b) nonstressed, or (c) tensile stressed (c). In the compressive-stressed state, stress $\sigma<0$; in the nonstressed state, $\sigma=0$; in the tensile-stressed state, $\sigma>0$.

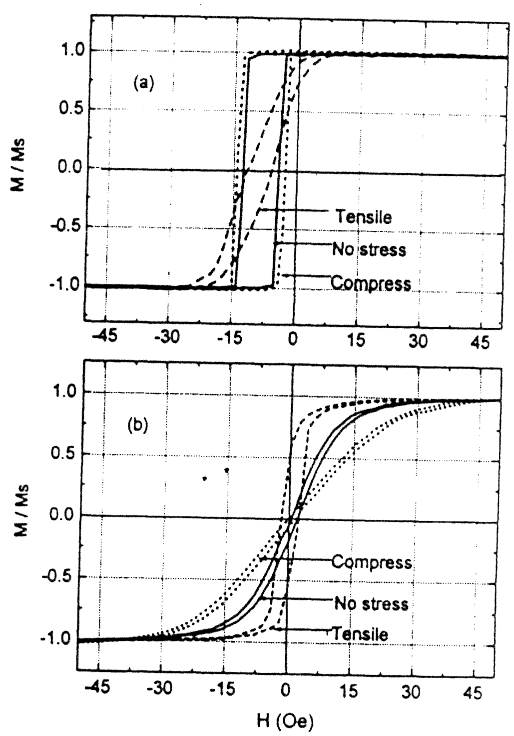

FIG. 2. Typical results of the easy- (a) and hard-axis (b) hysteresis loops of NiO/NiFe bilayers measured at compressive-stressed, nonstressed, and tensile-stressed states, and the direction of the stress parallel to the easy axis of the NiO/NiFe bilayer.

stress induced anisotropy

$$H_\sigma = 3\lambda\sigma/M = 3\lambda E\epsilon_b/M(1+\nu)$$

where σ is stress, E is Young's modulus, ϵ_b is the bending strain, and ν is Poisson's ratio.[11]

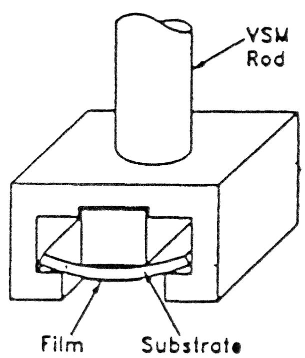

Figure 1: Sample holder with variable bending strain.

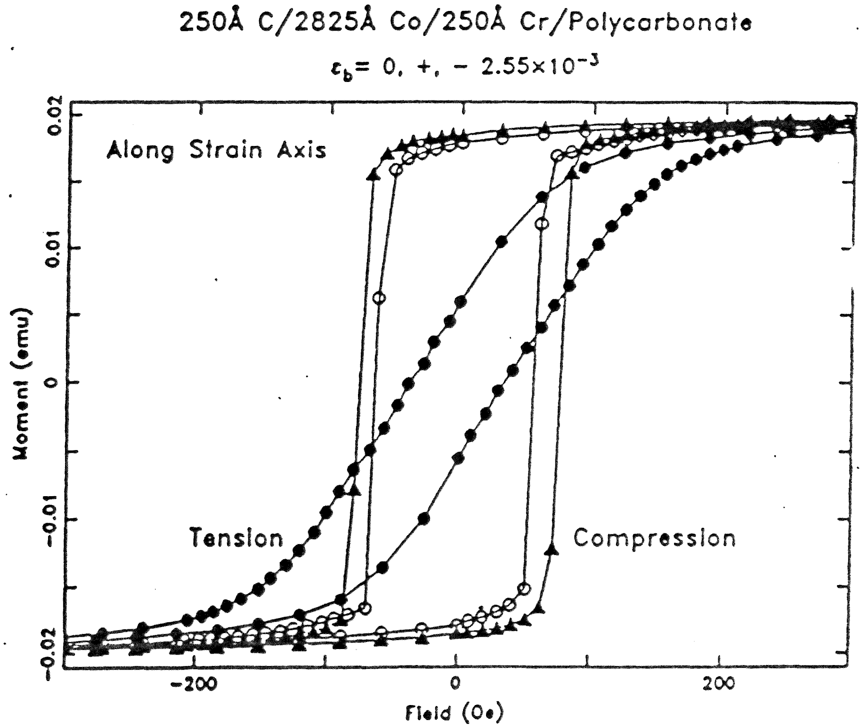

[11] D. Mauri et al., IEEE Trans. Magnetics MAG-26, 1584 (1990)

Improved exchange coupling between ferromagnetic Ni-Fe and antiferromagnetic Ni-Mn-based films

Tsann Lin, Daniele Mauri, Norbert Staud, Cherngye Hwang, and J. Kent Howard
IBM Storage Systems Division, San Jose, California 95193

NiMn

Appl. Phys. Lett. 65 (9), 29 August 1994 1185

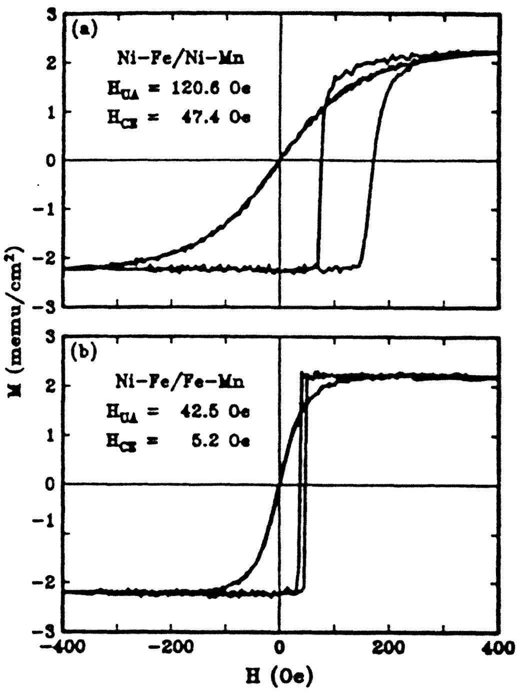

FIG. 1. Easy- and hard-axis hysteresis loops of (a) Ni-Fe (28.5 nm)/Ni-Mn (25.2 nm) and (b) Ni-Fe (28.5 nm)/Fe-Mn (8.4 nm) films with 22.0-nm-thick Ta underlayers after five annealing cycles.

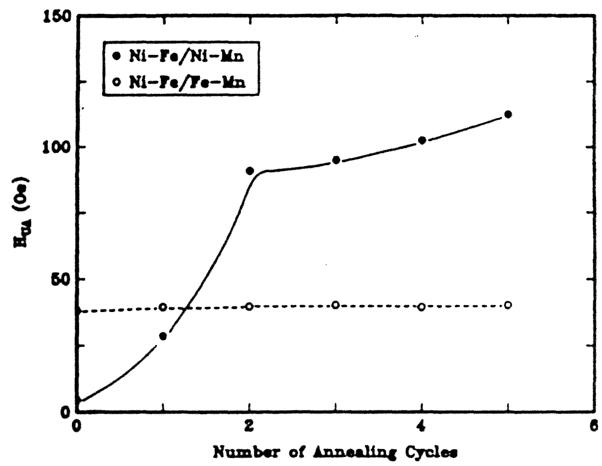

FIG. 3. H_{UA} vs annealing cycles for 50.4 nm thick Ni-Mn and 12.6-nm-thick Fe-Mn films deposited on 28.5-nm-thick Ni-Fe films.

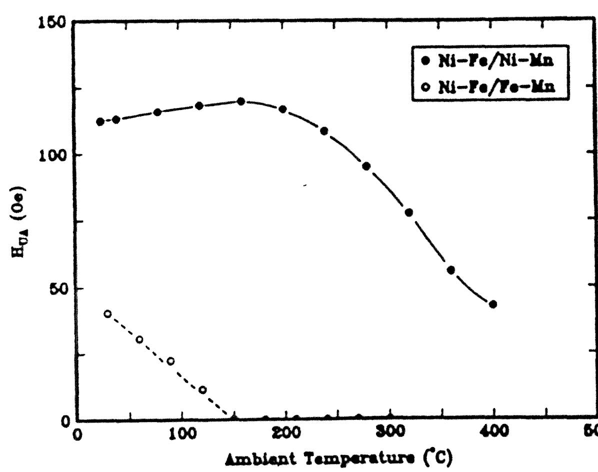

FIG. 4. H_{UA} vs temperature for 50.4 nm thick Ni-Mn and 12.6 nm thick Fe-Mn films deposited on 28.5 nm-thick Ni-Fe films.

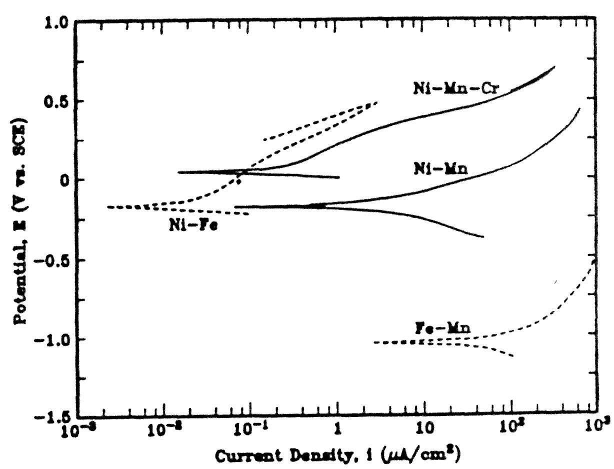

FIG. 5. Potentiodynamic scans of as-deposited 53.3Ni-46.7Mn, 49.5Ni-44.1Mn-6.4Cr, 50Fe-50Mn, and 81Ni-19Fe films in an aerated 0.1 N sodium sulfate electrolyte.

PdPtMn[1]

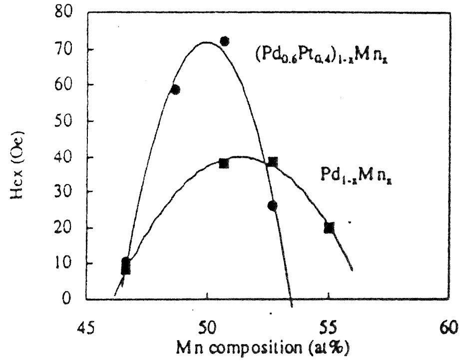

Fig. 1. He dependence on Mn composition of Ni-Fe (20 nm)/Pd-Pt-Mn and Pd-Mn (25 nm each) films annealed 230℃.

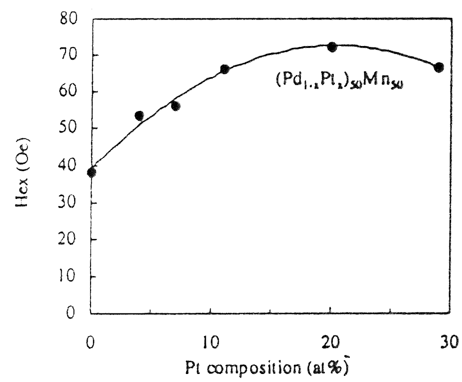

Fig. 2. He dependence on Pt composition of Ni-Fe (20 nm)/Pd-Pt-Mn(25 nm) films annealed 230℃.

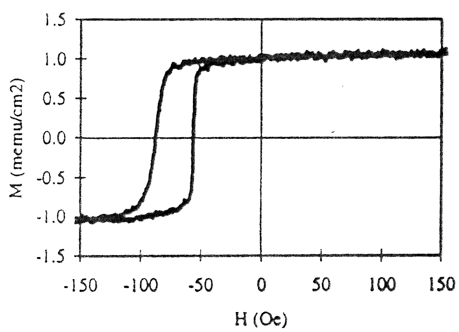

Fig. 3. Hysteresis loop of Ni-Fe (20 nm)/30Pd-20Pt-50Mn (25 nm) film annealed at 230℃.

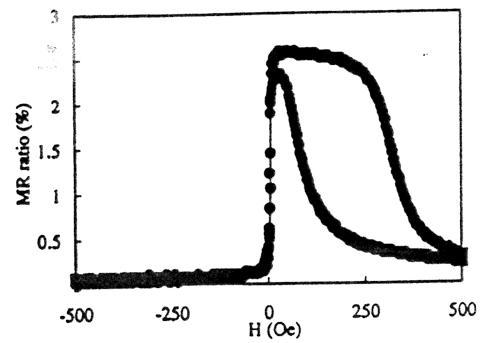

Fig. 8. ρ-H loop for spin-valve film structured Ta (5 nm)/Ni-Fe (9 nm)/Cu (2.5 nm)/Ni-Fe (4 nm)/30Pd-20Pt-50Mn (25 nm)/Ta (10 nm) annealed at 230℃.

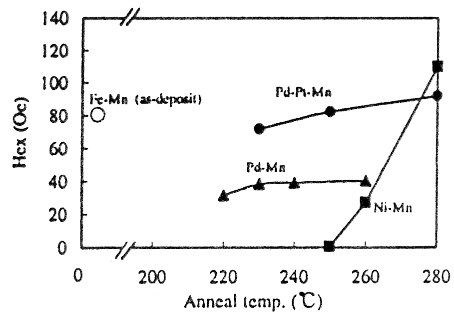

Fig. 4. He dependence on annealing temperature of Ni-Fe(20 nm)/30Pd-20Pt-50Mn, Pd-Mn and Ni-Mn (25 nm each) films.

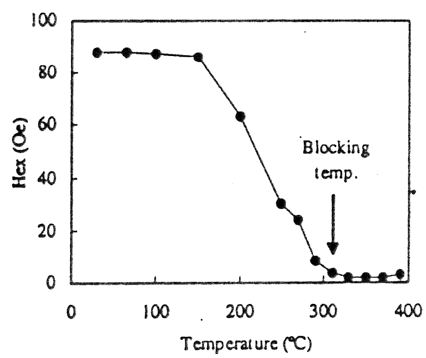

Fig.5. He dependence on temperature of Ni-Fe (20 nm)/30Pd-20Pt-50Mn (25nm) films

[1] H. Kishi, et al., IEEE Trans. Mag. 32, 3380 (1996)

spin valve with IrMn in pinned layer

Spin-valve giant magnetoresistive films with antiferromagnetic Ir-Mn layers

Hiromi Niu Fuke, Kazuhiro Saito, Yuzo Kamiguchi, Hiroshi Iwasaki, and Masashi Sahashi
Materials and Devices Research Laboratories, Research and Development Center, Toshiba Corporation, 72, Horikawa-cho, Saiwai-ku, Kawasaki 210, Japan

We succeeded in developing CoFe spin valves with an antiferromagnetic Ir-Mn film. Ir-Mn single-layer films and spin valves of Ta(5 nm)/Ir-Mn(8 or 9 nm)/$Co_{90}Fe_{10}$(x nm)/Cu(3 nm)/$Co_{90}Fe_{10}$(3 nm)/NiFe(2 nm)/CoZrNb(10 nm)/ (x = 2, 2.3, 2.6 nm), prepared by the sputtering method, showed the crystal structure of a fcc (111) preferred orientation. As-deposited CoFe spin valves with Ir-Mn exhibited an interfacial exchange coupling energy of J = 0.192 erg/cm^2 (H_{ua} ~ 640 Oe at t_{CoFe} = 2 nm), that was the highest ever reported for as-deposited antiferromagnetic films, such as NiO, NiMn, and FeMn. Furthermore, CoFe spin valves with Ir-Mn exhibited a higher blocking temperature of 260 °C, and a higher MR ratio of 6.37% than the spin valves with FeMn film. After annealing, the MR ratio increased to 7.82%. On the other hand, the H_{ua} decreased about 100 Oe after annealing. The H_{ua}-T curve was, however, improved and the H_{ua} at 100 °C increased to 400 Oe. The decrease in H_{ua} was not observed after second annealing and seems to be stabilized by first annealing. [S0021-8979(97)68008-1]

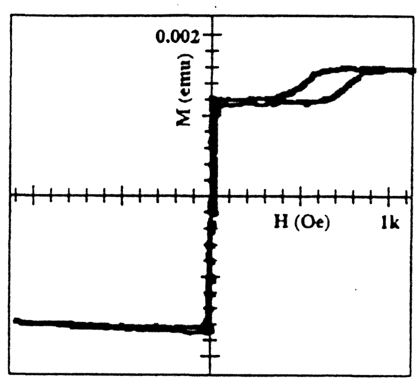

4004 J. Appl. Phys. **81** (8), 15 April 1997

FIG. 3. Magnetization curve of as-deposited Ta(5 nm)/Ir-Mn(8 nm)/$Co_{90}Fe_{10}$(2 nm)/Cu(3 nm)/$Co_{90}Fe_{10}$(3 nm)/NiFe(2 nm)/CoZrNb(10 nm) film on AlO_x-coated Si(100) substrate.

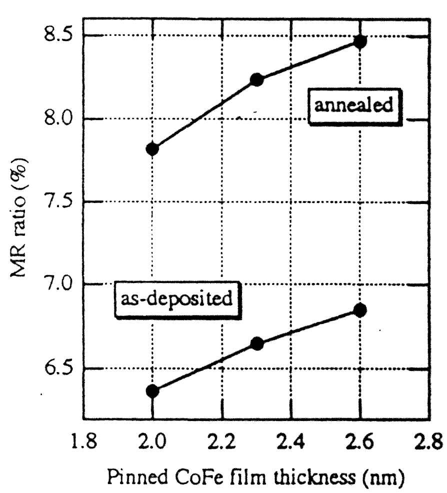

FIG. 5. Dependence of magnetoresistance (MR) ratio on pinned CoFe film thickness for as-deposited and annealed Ta(5 nm)/Ir-Mn(9 nm)/$Co_{90}Fe_{10}$(2 nm)/Cu(3 nm)/$Co_{90}Fe_{10}$(3 nm)/NiFe(2 nm)/CoZrNb(10 nm) films on AlO_x-coated Si(100) substrates.

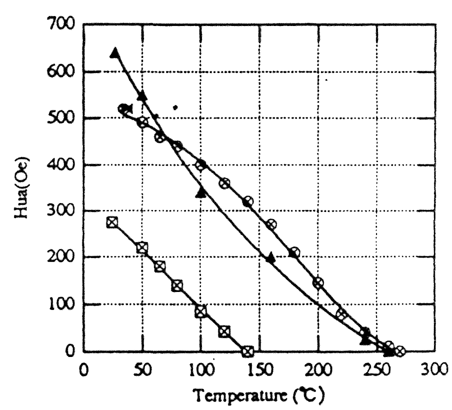

FIG. 6. Temperature dependence of unidirectional anisotropy (H_{ua}) for as-deposited and annealed Ta(5 nm)/Ir-Mn(8 nm)/$Co_{90}Fe_{10}$(2 nm)/Cu(3 nm)/$Co_{90}Fe_{10}$(3 nm)/NiFe(2 nm)/CoZrNb(10 nm) films on AlO_x-coated Si(100) substrates and for as-deposited Ta(5 nm)/FeMn(15 nm)/$Co_{90}Fe_{10}$(2 nm)/Cu(3 nm)/$Co_{90}Fe_{10}$(3 nm)/NiFe(2 nm)/CoZrNb(10 nm) film on AlO_x-coated Si(100) substrate. H_{ua} at room temperature of reannealed spin valves with Ir-Mn film. ▲: As-deposited spin valve with Ir-Mn film, ⊗: Annealed spin valve with Ir-Mn film, ⧓: Reannealed spin valve with Ir-Mn film, ⊠: As-deposited spin valve with Fe-Mn film.

Orientational dependence of the exchange biasing in molecular-beam-epitaxy-grown $Ni_{80}Fe_{20}/Fe_{50}Mn_{50}$ bilayers (invited)
R. Jungblut, R. Coehoorn, M. T. Johnson, J. aan de Stegge, and A. Reinders
Philips Research Laboratories, Prof. Holstlaan 4, 5656 AA Eindhoven, The Netherlands

crystallographic effects

6662 J. Appl. Phys., Vol. 75, No. 10, 15 May 1994

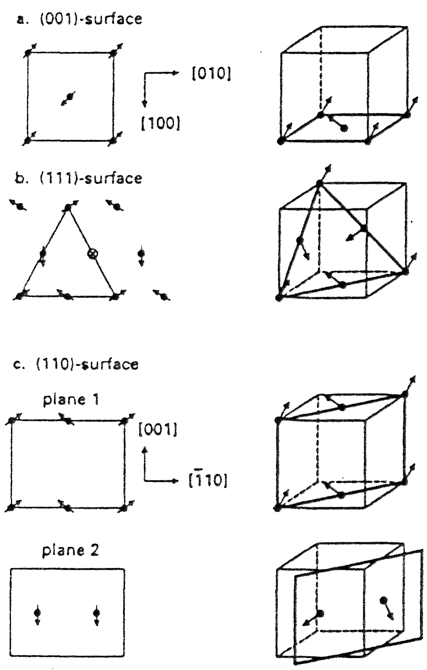

FIG. 1. Spin structure in the ⟨111⟩ model for the different orientations.

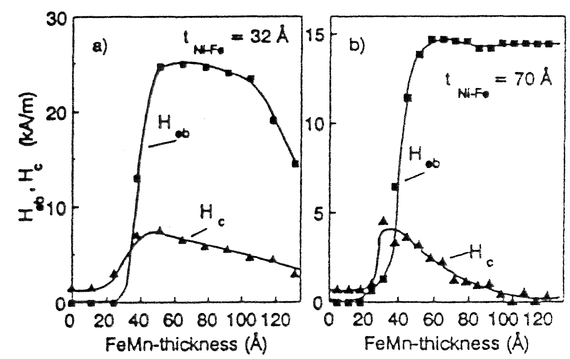

FIG. 5. $H_{eb}(t_{FeMn})$ and $H_c(t_{FeMn})$ for the [111] oriented sample for 32 and 70 Å $Ni_{79}Fe_{21}$.

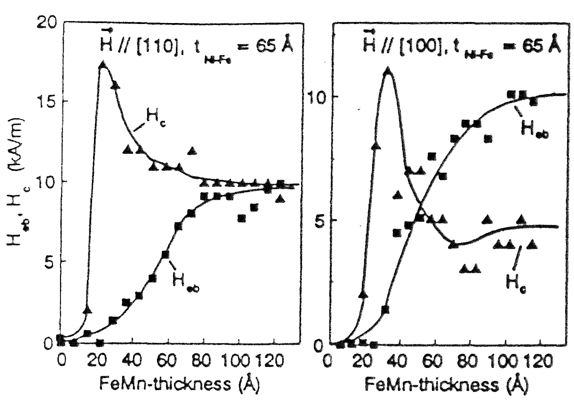

FIG. 6. $H_{eb}(t_{FeMn})$ and $H_c(t_{FeMn})$ for the [001] oriented samples grown and measured with $H \parallel [110]$ and $H \parallel [100]$.

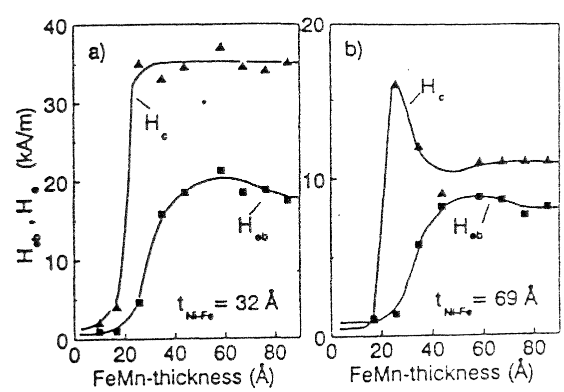

FIG. 8. $H_{eb}(t_{FeMn})$, $H_c(t_{FeMn})$ for the [011] oriented sample for 32 and 69 Å $Ni_{80}Fe_{20}$.

Advanced Materials for Magnetoresistive Recording Readback Sensors

Bruce A. Gurney
IBM Almaden Research Center
gurney@almaden.ibm.com

Giant Magnetoresistance

- a little history
- GMR structures
- GMR and interlayer coupling
- models of GMR
- mean free paths and interfacial scattering
- distribution of current
- heads, field sensors, and memories

VOLUME 61, NUMBER 21 PHYSICAL REVIEW LETTERS 21 NOVEMBER 1988

2472

Giant Magnetoresistance of (001)Fe/(001)Cr Magnetic Superlattices

M. N. Baibich,[a] J. M. Broto, A. Fert, F. Nguyen Van Dau, and F. Petroff
Laboratoire de Physique des Solides, Université Paris-Sud, F-91405 Orsay, France

Fe/Cr multilayers

First reports[1] of a new magnetoresistance phenomenon in layered structures showed substantial amplitude in high fields.

We have studied the magnetoresistance of (001)Fe/(001)Cr superlattices prepared by molecular-beam epitaxy. A huge magnetoresistance is found in superlattices with thin Cr layers: For example, with $t_{Cr} = 9$ Å, at $T = 4.2$ K, the resistivity is lowered by almost a factor of 2 in a magnetic field of 2 T. We ascribe this giant magnetoresistance to spin-dependent transmission of the conduction electrons between Fe layers through Cr layers.

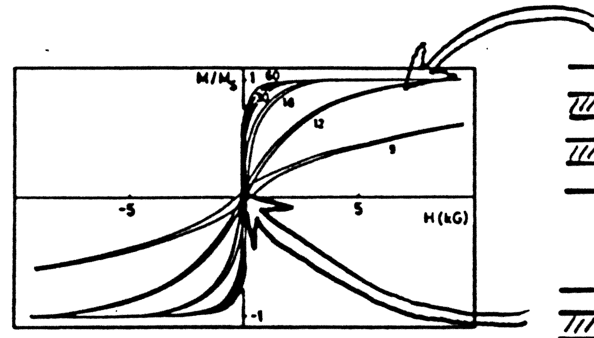

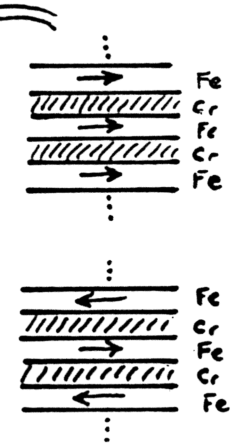

FIG. 1. Hysteresis loops at 4.2 K with an applied field along [110] in the layer plane for several (001)Fe/(001)Cr superlattices: [(Fe 60 Å)/(Cr 60 Å)]$_5$, [(Fe 30 Å)/(Cr 30 Å)]$_{10}$, [(Fe 30 Å)/(Cr 18 Å)]$_{30}$, [(Fe 30 Å)/(Cr 12 Å)]$_{40}$, [(Fe 30 Å)/(Cr 9 Å)]$_{40}$, where the subscripts indicate the number of bilayers in each sample. The number beside each curve represents the thickness of the Cr layers.

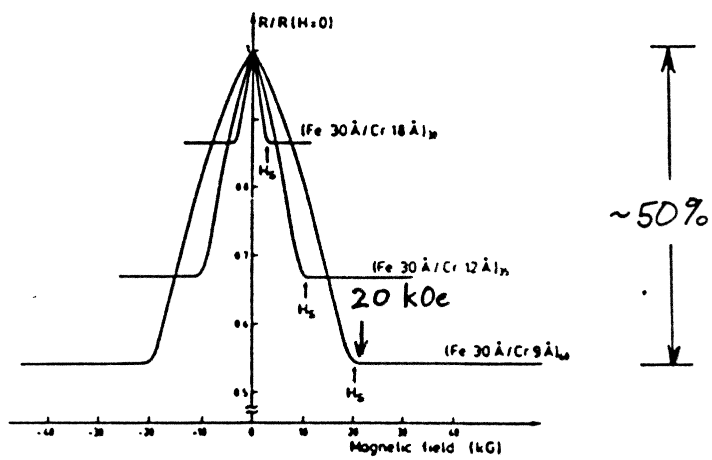

FIG. 3. Magnetoresistance of three Fe/Cr superlattices at 4.2 K. The current and the applied field are along the same [110] axis in the plane of the layers.

---

[1] see also pg. IV.29, G. Binash, et al., Phys. Rev. B. rapid commun. 39, 4829

an expanding field

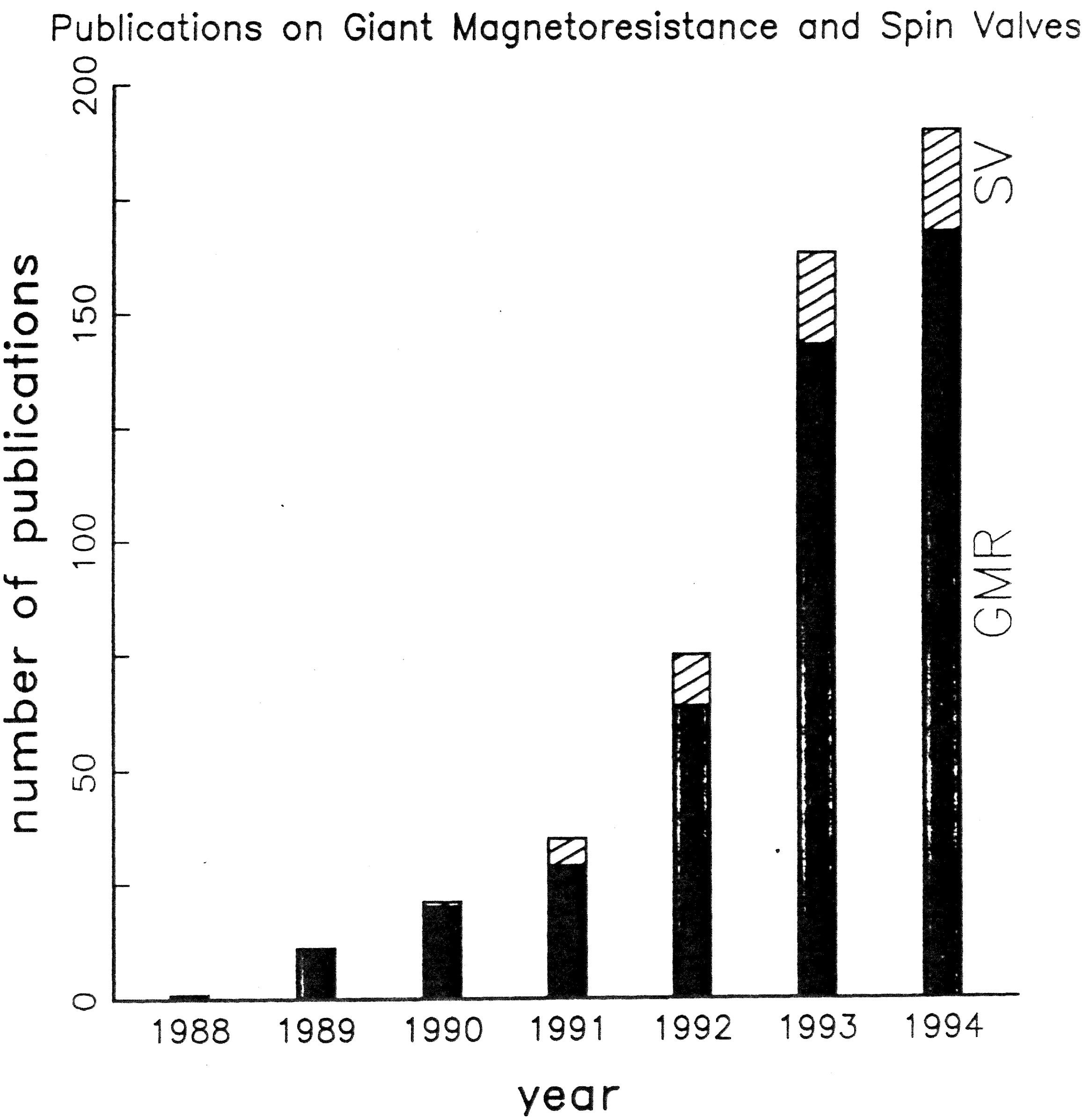

basic mechanism

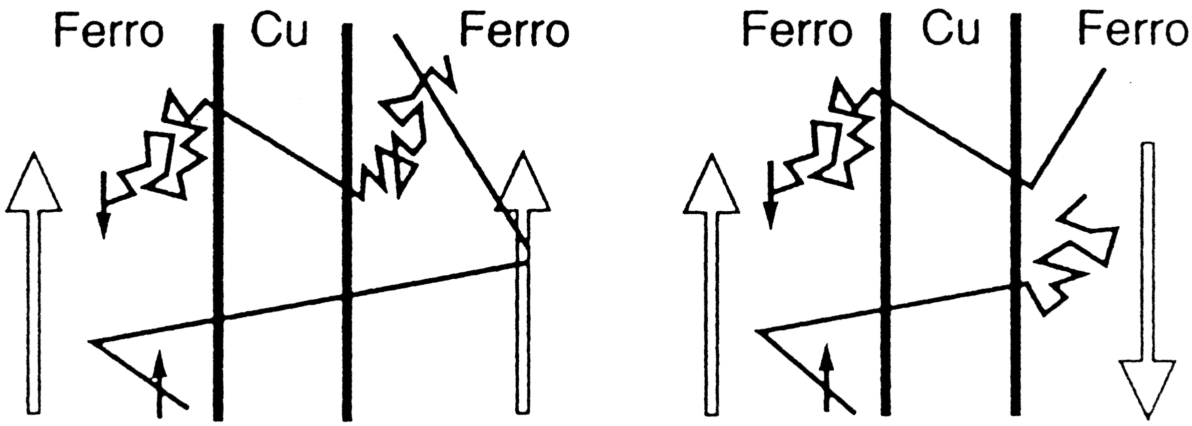

(a) Short circuit by ↑ electrons
Low R

(b) Both species of electrons
are strongly scattered
High R

spin valves

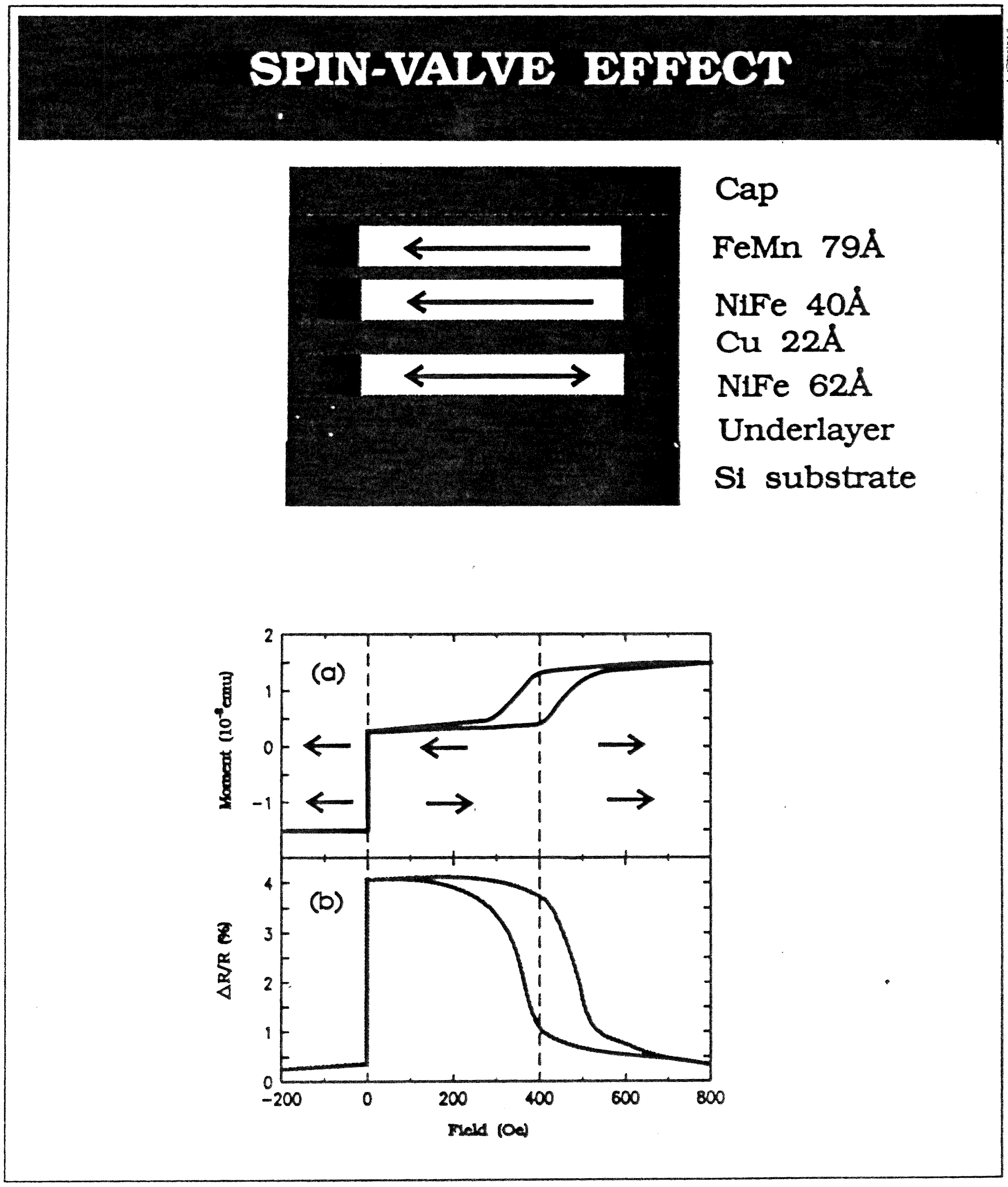

[2]e.g. Dieny, et al. J. Appl. Phys. 69, 4774 (1991)

some spin valves investigated at IBM

F1	NM	F2/FeMn	largest $\Delta R/R$ at room T	Minimum t_{NM} for decoupling
Co	Cu	Co	9.5%	$t_{Cu} \geq 16Å$
$Ni_{80}Fe_{20}$	Cu	$Ni_{80}Fe_{20}$	5%	$t_{Cu} \geq 18Å$
Ni	Cu	Ni	2.5%	$t_{Cu} \geq 20Å$
Fe	Cu	$Ni_{80}Fe_{20}$	2.5%	$t_{Cu} \geq 18Å$
Gd	Cu	$Ni_{80}Fe_{20}$	0 % at 77K	$t_{Cu} \geq 20Å$
Nd	Cu	$Ni_{80}Fe_{20}$	0 % at 77K	$t_{Cu} \geq 20Å$
Co	Cu	$Ni_{80}Fe_{20}$	6.5%	$t_{Cu} \geq 16Å$
Co	Ag	$Ni_{80}Fe_{20}$	1.5%	$t_{Ag} \geq 50Å$
$Ni_{80}Fe_{20}$	Ag	$Ni_{80}Fe_{20}$	1.2%	$t_{Ag} \geq 50Å$
Co	Au	$Ni_{80}Fe_{20}$	4.5%	$t_{Au} \geq 10Å$
$Ni_{80}Fe_{20}$	Pt	$Ni_{80}Fe_{20}$	0.3%	$t_{Pt} \geq 20Å$
$Ni_{80}Fe_{20}$	Pd	$Ni_{80}Fe_{20}$	0.2%	$t_{Pd} \geq 20Å$
$Ni_{80}Fe_{20}$	Al	$Ni_{80}Fe_{20}$	0 %	$t_{Al} \geq 20Å$
$Ni_{80}Fe_{20}$	V	$Ni_{80}Fe_{20}$	0 %	$t_{V} \geq 16$ Å
$Ni_{80}Fe_{20}$	Cr	$Ni_{80}Fe_{20}$	0 %	$t_{Cr} \geq 16$ Å
$Ni_{80}Fe_{20}$	Nb	$Ni_{80}Fe_{20}$	0 %	$t_{Nb} \geq 20Å$
$Ni_{80}Fe_{20}$	Ru	$Ni_{80}Fe_{20}$	0 %	$t_{Ru} \geq 15$ Å
$Ni_{80}Fe_{20}$	Ta	$Ni_{80}Fe_{20}$	0 %	$t_{Ta} \geq 15Å$
$Ni_{80}Fe_{20}$	W	$Ni_{80}Fe_{20}$	0 %	$t_{W} \geq 15$ Å

some other spin valves investigated

system	publications†	$\Delta R/R$ (%)‡
NiFe/Cu/NiFe	9	4.3
Ni/Cu/NiFe	1	1.5
NiFe/Cu/Co	6	6
NiFe/Ag/Co	1	1.5
NiFe/Au/Co	1	2.5
NiFe/Co/Cu/Co	1	7.6
Co/Cu/Co	2	8.7
Fe/Ag/CoFe	1	
Fe/Cu/Co	1	3.3
NiFeCo/Cu/NiFeCo	2	2.2

† approximate number

‡ representative

multilayers

Giant magnetoresistance in antiferromagnetic Co/Cu multilayers

S. S. P. Parkin
IBM Research Division, Almaden Research Center, 650 Harry Road, San Jose, California 95120-6099

Z. G. Li and David J. Smith[a]
Center for Solid State Science, Arizona State University, Tempe, Arizona 85280

(Received 20 February 1991; accepted for publication 22 March 1991)

We report giant values of saturation magnetoresistance in sputtered antiferromagnetic Co/Cu multilayers containing thin Co and Cu layers 8–10 Å thick. We discuss the key importance of the buffer layer in controlling the growth of flat Co and Cu layers. As shown by cross-section transmission electron microscopy high-quality structures are found for growth on Fe buffer layers. Such structures display saturation magnetoresistance at 300 K of more than 65% with saturation fields of ≈10 kOe. These values are several times larger than previously found for any magnetic material at room temperature.

2710 Appl. Phys. Lett. 58 (23), 10 June 1991 0003-6951/91/232710-04$02.00 2

65% at 295 K!

compare with 2% anisotropic magnetoresistance in $Ni_{80}Fe_{20}$

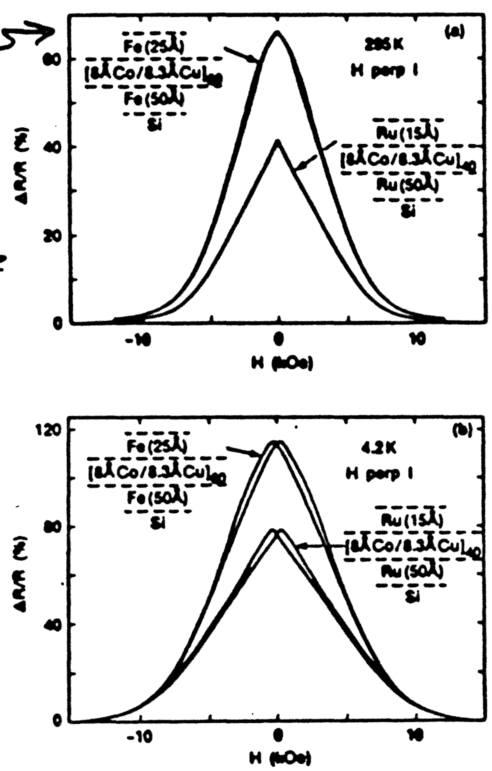

FIG. 4. Resistance vs field curves for two multilayers, Si(100)/30 Å Fe/[8 Å Co/8.3 Å Cu]$_{40}$/30 Å Cu and Si(100)/30 Å Ru/[9 Å Co/8.3 Å Cu]$_{40}$/15 Å Ru at (a) 300 and (b) 4.2 K.

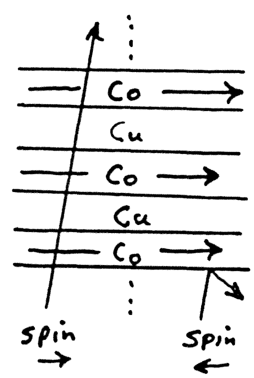

multilayers investigated

system	publications†	$\Delta R/R$ (%)‡
Co/Cu	52	72
CoFe/Cu	6	40
Co/Ag	16	41
NiFe/Co/Cu	1	17
Ni/Ag	1	28
NiCo/Cu	5	16
CoNiFe/Cu	6	35
NiFe/Cu	6	20
NiFe/Au	1	
NiFe/Ag	3	17
Ni80Co20/Cu	3	18
NiFe/Cu/Co	1	7
NiFeCo/Cu/Co	1	15
Fe/Cr	43	150 (4K)
Fe/Cu	5	
Fe/Pd	1	
NiFe/Cr	1	0

† approximate number

‡ representative

heterogeneous alloys

VOLUME 68, NUMBER 25 PHYSICAL REVIEW LETTERS 22 JUNE 1992

Giant Magnetoresistance in Heterogeneous Cu-Co Alloys

A. E. Berkowitz,[1,2] J. R. Mitchell,[1,2] M. J. Carey,[1,2] A. P. Young,[1,2] S. Zhang,[3] F. E. Spada,[2] F. T. Parker,[2] A. Hutten,[4] and G. Thomas[4]

[1]Department of Physics, University of California at San Diego, La Jolla, California 92093
[2]Center for Magnetic Recording Research, University of California at San Diego, La Jolla, California 92093
[3]Department of Physics, New York University, 4 Washington Place, New York, New York 10003
[4]Department of Materials Science and Mineral Engineering and National Center for Electron Microscopy, Lawrence Berkeley Laboratory, University of California at Berkeley, Berkeley, California 94720

(Received 20 February 1992)

We have observed giant magnetoresistance in heterogeneous thin film Cu-Co alloys consisting of ultrafine Co-rich precipitate particles in a Cu-rich matrix. The magnetoresistance scales inversely with the average particle diameter. This behavior is modeled by including spin-dependent scattering at the interfaces between the particles and the matrix, as well as the spin-dependent scattering in the Co-rich particles.

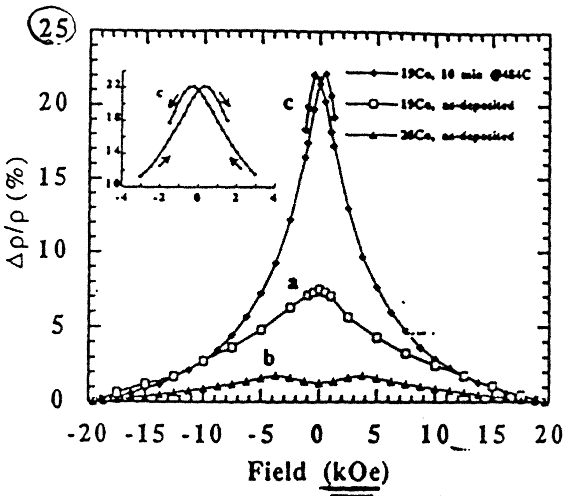

FIG. 2. Field dependence of $\Delta\rho/\rho = (\rho_{H_c} - \rho_{H=20\,\mathrm{kOe}})/\rho_{H=20\,\mathrm{kOe}}$ for the three types of curves obtained. Inset: Details of curve c. Curves a and b measured at $T=100$ K; curve c measured at 10 K. Sense current parallel to field.

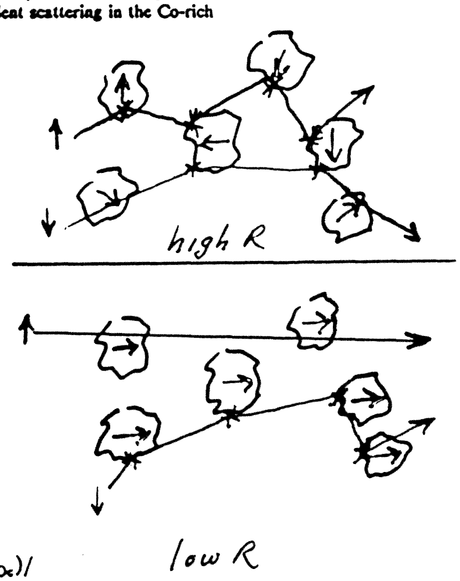

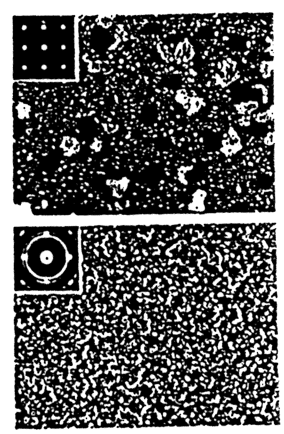

Giant magnetoresistance and microstructural characteristics of epitaxial Fe-Ag and Co-Ag granular thin films

N. Thangaraj, C. Echer, and Kannan M. Krishnan
Materials Sciences Division, Lawrence Berkeley Laboratory, University of California, Berkeley, California 94720

R. F. C. Farrow, R. F. Marks, and S. S. P. Parkin
IBM Research Division, Almaden Research Center, 650 Harry Road, San Jose, California 95120-6099

6900 J. Appl. Phys. 75 (10), 15 May 1994

heterogeneous alloys investigated

system	publications†	$\Delta R/R$ (%)‡
Co-Ag	33	25
Fe-Ag	16	25
CoFe-Ag	4	14
NiFe-Ag	8	7
NiFeCo-Ag	1	11
Co-Fe Cu	5	3
CoMn-Cu	1	
Fe-Cu	1	
Co-Cu	15	20
Co-Au	1	
Fe-Au	3	

† approximate number

‡ representative

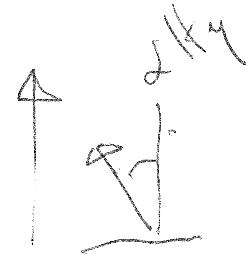

Exchange coupling in magnetic heterostructures

M. D. Stiles
National Institute of Standards and Technology, Gaithersburg, Maryland 20899

48 7238

mechansim of coupling

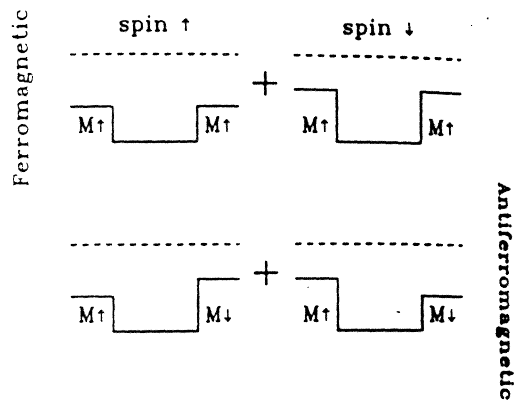

FIG. 5. Quantum wells for exchange coupling. The top left (right) quantum well shows the potential seen by spin-up (-down) electrons in a ferromagnetically aligned quantum-well structure. The bottom left (right) quantum well shows the potential seen by spin-up (-down) electrons in an antiferromagnetically aligned quantum-well structure.

$$\frac{J_\infty(t)}{A} = -\left[\frac{\hbar}{2\pi^2}\kappa_{ij}v_{Fij}\right]\left[|R_\uparrow^\uparrow|^2 + |R_\downarrow^\uparrow|^2 - 2|R_\uparrow^\uparrow R_\downarrow^\uparrow|\right] \times \frac{1}{t^2}\sin(2k_F t + \phi). \quad (13)$$

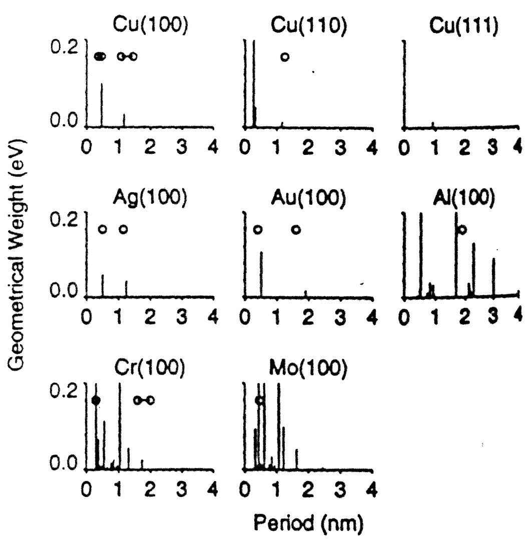

FIG. 8. Comparison between periods measured on samples grown by MBE and calculated extremal spanning vectors. The experimental data are shown as circles with an arbitrary y coordinate.

$$\frac{E_\infty(t)}{A} = -\left[\frac{\hbar}{2\pi^2}\kappa_{ij}v_{Fij}\right]|R_{ij}|^2\frac{1}{t^2}\sin(2k_F t + \phi). \quad (12)$$

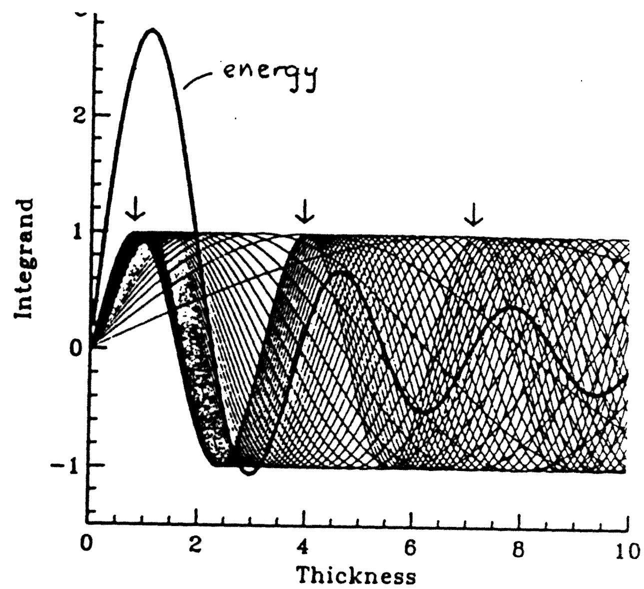

FIG. 6. Integration over parallel momentum. The integrand (20 thin lines) and result (heavy line) in Eq. (8) illustrate the cancellation of the the multiple oscillations in the integrand leaving only the oscillation due to the extrema.

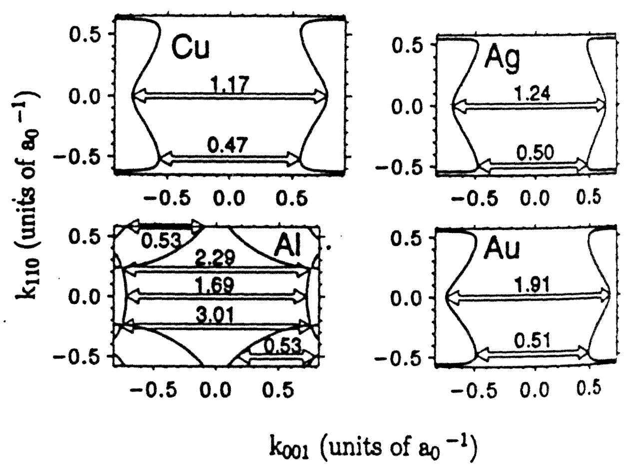

FIG. 10. Extremal spanning vectors for fcc(100) interfaces. Slices though the Fermi surface (heavy lines) in the interface adapted bulk Brillouin zone are shown for the noble metals and Al. Selected extremal spanning vectors (arrows) are labeled by the period in nm that would arise from the coupling of these parts of the Fermi surface.

biquadratic coupling

coupling exhibits[3] higher order terms:

$$\overbrace{J_{12}}^{coupling} = \overbrace{J_a \cos(\theta_1 - \theta_2)}^{biaxial} + \overbrace{J_b \cos^2(\theta_1 - \theta_2)}^{biquadratic} + \cdots$$

日本応用磁気学会誌 16, 313-318 (1992)

$(Co_xFe_{1-x}/Cu)_n$ 人工格子膜の巨大磁気抵抗効果

Giant Magnetoresistance in $(Co_xFe_{1-x}/Cu)_n$ Multilayers

斉藤好昭・橋本 進・奥野志保・柚須圭一郎・猪俣浩一郎
東芝総合研究所，川崎市幸区小向東芝町 1 番地 (〒210)

Y. Saito, S. Hashimoto, S. N. Okuno, K. Yusu and K. Inomata
Toshiba Research and Development Center, *1, Komukai Toshiba-cho, Saiwai-ku, Kawasaki 210*

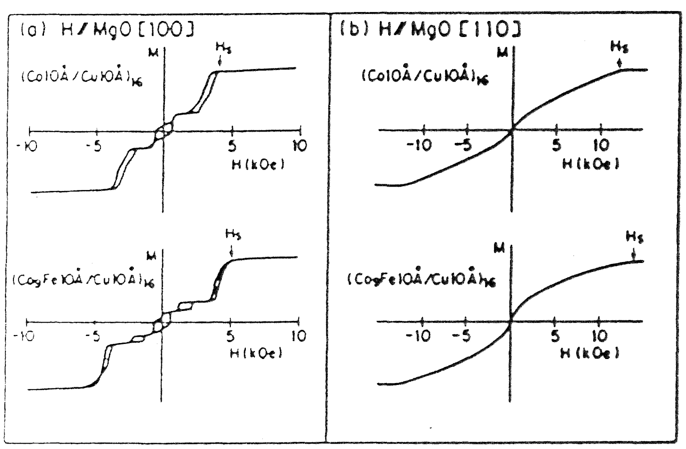

Fig. 3 In-plane magnetization *versus* field at room temperature for the samples (1) and (2) in Fig. 2. Magnetic field was applied to (a) the easy axis and (b) the hard axis of the films.

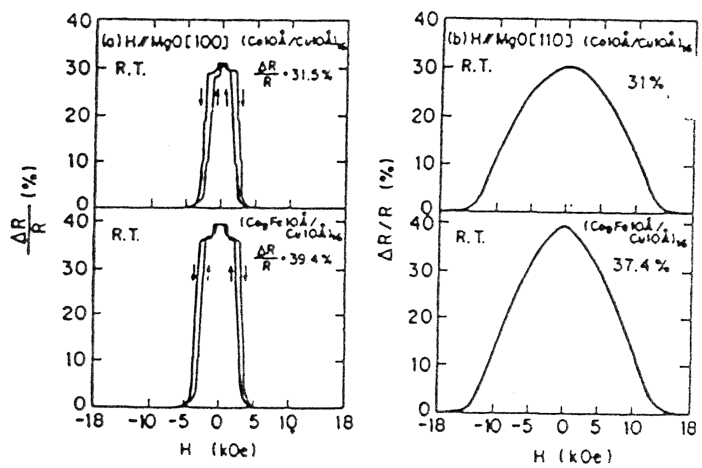

Fig. 4 Resistance *versus* magnetic field curves at room temperature for the samples (1) and (2) in Fig. 2. Magnetic field was applied to (a) the easy axis and (b) the hard axis of the films.

[3] for modeling see J. Slonczewski, J. Appl. Phys. 73, 5957 (1993).

PHYSICAL REVIEW B VOLUME 44, NUMBER 10 1 SEPTEMBER 1991-II

Nonoscillatory magnetoresistance in Co/Cu/Co layered structures with oscillatory coupling

5358

V. S. Speriosu, B. Dieny,* P. Humbert,† B. A. Gurney, and H. Lefakis
IBM Research Division, Almaden Research Center, 650 Harry Road, San Jose, California 95120-6099

no oscillation in GMR amplitude

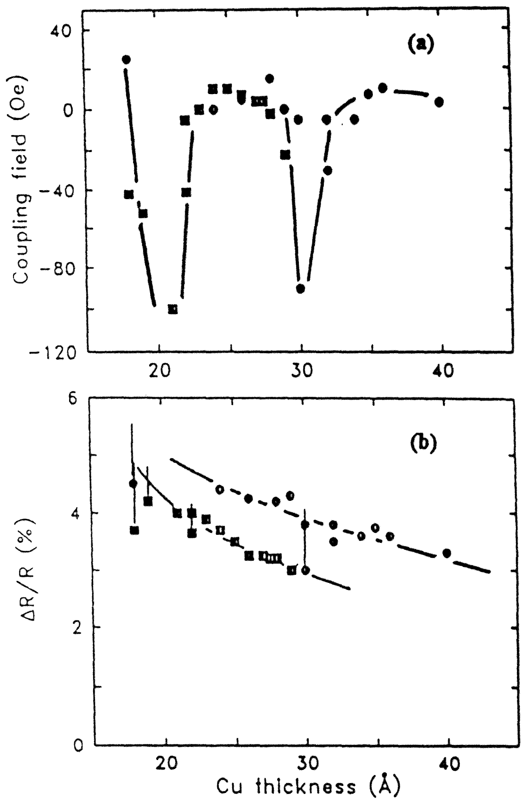

FIG. 4. (a) Coupling field and (b) magnetoresistance vs Cu-layer thickness. The two sets of points correspond to different underlayer thicknesses, giving different shunting. Oscillations in coupling are observed, but the slow, monotonic decrease of magnetoresistance demonstrates that the two phenomena are not fundamentally linked.

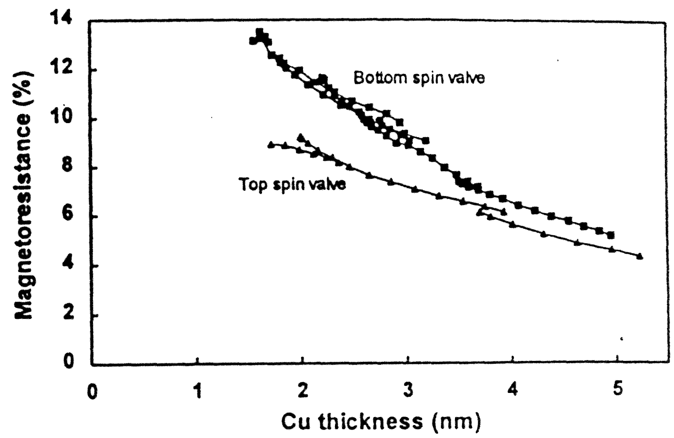

Fig. 1. Magnetoresistance of bottom and top spin valves as a function of Cu spacer layer thickness. Data series connected by lines were collected from samples from the same graded Cu thickness deposition.

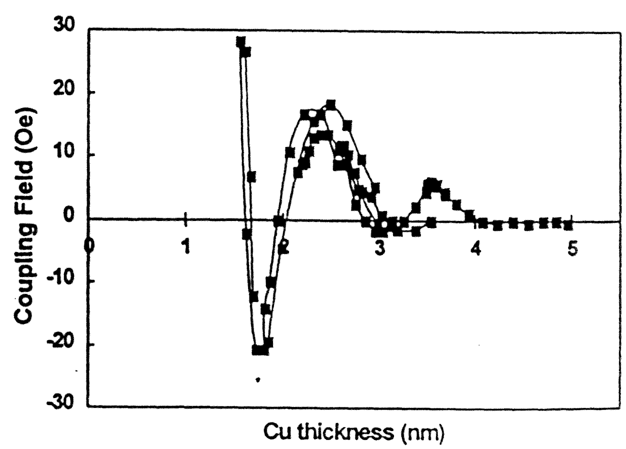

Fig. 2. Dependence of interlayer coupling field in bottom spin valves on Cu spacer thickness. Data series connected by lines were collected from samples from the same graded Cu thickness deposition.

IEEE TRANSACTIONS ON MAGNETICS, VOL. 30, NO. 6, NOVEMBER 1994 3819

Magnetoresistance of Symmetric Spin Valve Structures

Thomas C. Anthony and James A. Brug
Hewlett-Packard Laboratories, 1501 Page Mill Road, Palo Alto, CA 94304

electrical conductivity in metals

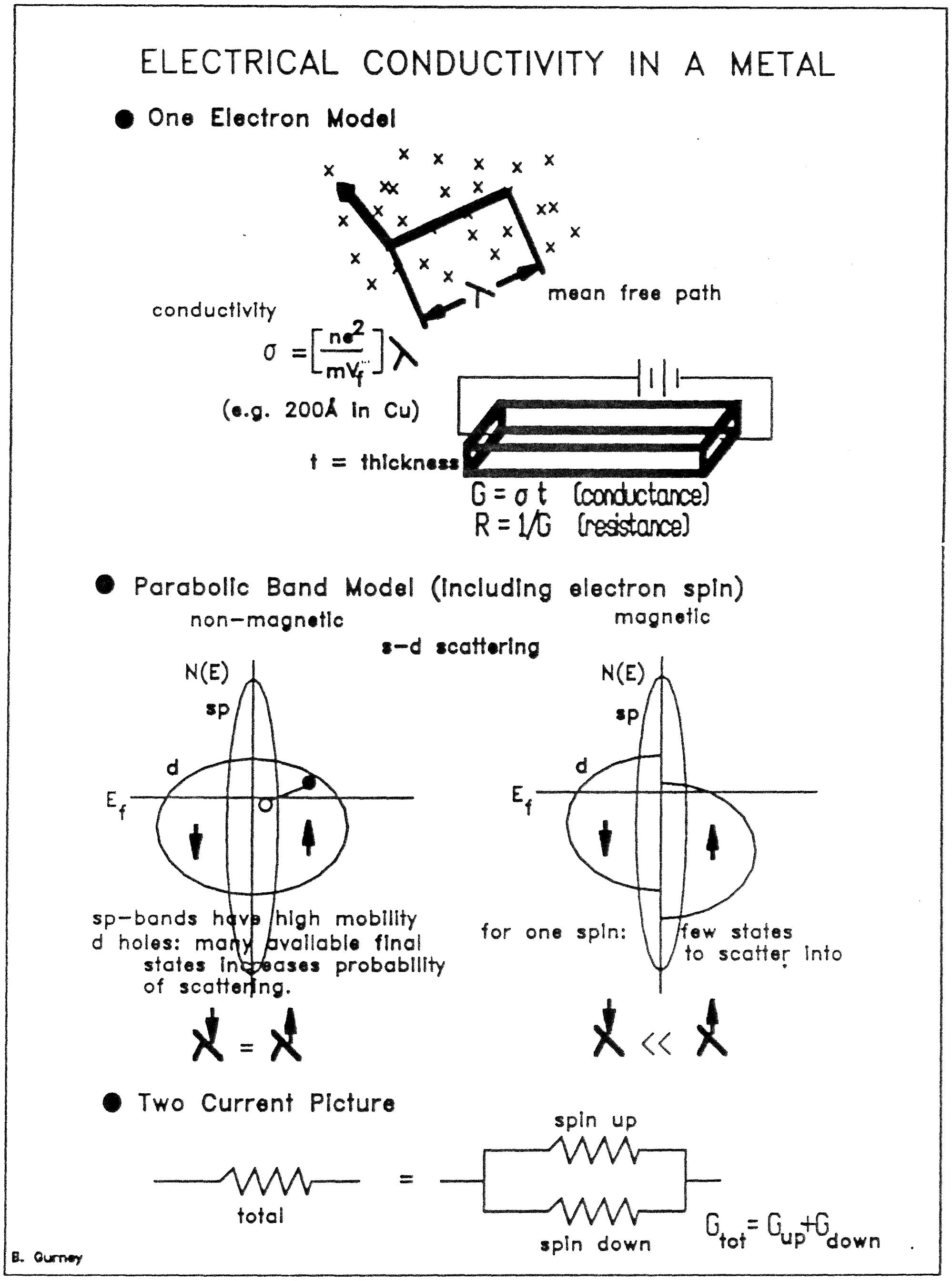

spin dependent impurity scattering

SPIN DEPENDENT SCATTERING IN DILUTE ALLOYS

- Campbell and Fert, Ferromagnetic Mater. 3, 747 (1982)

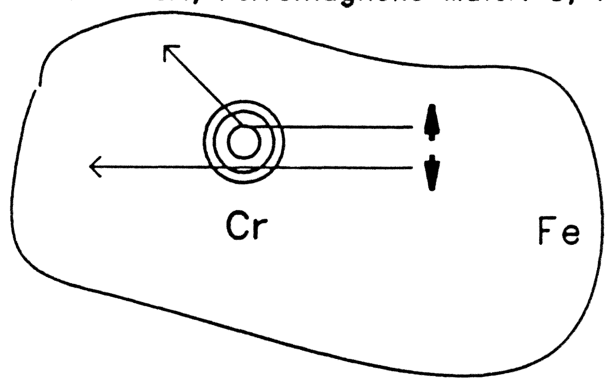

From binary and ternary alloys were able to obatin the contribution to resistivity,

$\rho^{\uparrow}$ and $\rho^{\downarrow}$ per % of impurity

e.g.

	$\rho^{\downarrow}$	$\rho^{\uparrow}$	α
Cr in Fe	2.8	12.5	.16
Ni in Fe	2.4	12	.2

- What about spin dependent MEAN FREE PATHS?
- WHat about spin dependent scattering in PURE ELEMENTS?
- What about spin dependent scattering in CONCENTRATED ALLOYS?

B. Gurney 6/93

shared electrons lead to GMR

Spin Valve Magnetoresistance

Electrons shared by ferromagnetic layers across a non-magnetic conducting layer.

Spin valve magnetoresistance depends on the distance of penetration before scattering of spin-up and spin-down electrons emanating from one ferromagnetic layer into the other ferromagnetic layer.

the question: "how many" go "how far"

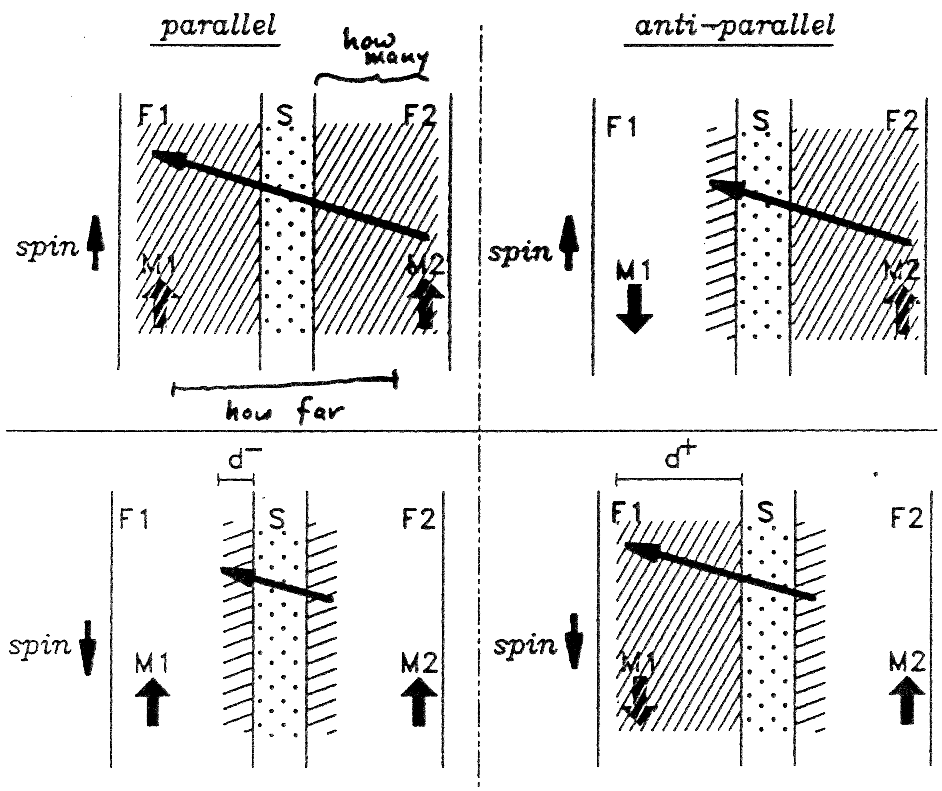

GMR models

- **spin dependent interface scattering**
  basics: essentiall phenomenological, a spin dependent transmission/reflection coefficient is ascribed to each interface. Can include spin dependent bulk mean free paths.
  limitations: no bands, no potentials
  example: Barnas, et al., Phys. Rev. B 42, 8110 (1990)
- **random potential scattering**
  basics: due to intermixing the potential barrier seen by electrons at the interface is random leading to scartering that is spin dependent just like the potentials.
  limitations does not include bulk scattering
  example: H. Itoh, et al. Phys. Rev. B 47, 5809 (1993).
- **Kubo formalism**
  basisc: quantum statistical solution of the linear response to electrons whose energies are given by a model Hamiltonian that includes potentials and spin dependent scattering.
  limitations: does not include band structure.
  examples: P. Levy, Solid State Physics.
- **(semi-)classical transport**
  basics:relaxation time approximation (i.e. spin dependent local mean free path) withing each of the layers to solve Boltzmann eq. ·
  limitations: includes no quantum effects , bands, or potentials.
  examples: R. Hood et al, Phys. Rev. B 46, 8287 (1992); B. Dieny, Europhys. Lett. 17, 261 (1992); A. Barthelemy et al., Phys. Rev. B 43, 13124 (1991).

fundamental observable: ΔG

Absolute Change in the SHEET CONDUCTANCE
is the Fundamental Measure of Spin Valve MR

- $\Delta R/R$, ΔR, or ΔG?
  - From the relaxation time Boltzmann equation

$$\frac{\partial g^{\sigma}(z,v)}{\partial z} + \frac{g^{\sigma}(z,v)}{\tau^{\sigma}\, v_z} = \frac{eE}{mv_z}\frac{\partial f_0^{\sigma}(v)}{\partial v_x}$$

$$\Rightarrow \Delta G = \sum_{\sigma=\uparrow\downarrow}\int v_x d^3v \int \frac{\Delta g^{\sigma}(v_z, z)}{E}\,dz$$

- ΔG is directly connected to the changes in the Fermi surface that results from the scattering leading to GMR

- $\Delta R/R$ and ΔR are partially determined by the scattering leading to GMR, but also include all other scattering

Appl. Phys. Lett. 61, 2111 (1992).

ΔG in experiments

The relative change in sheet resistance from antiparallel to parallel alignment of the magnetizations.

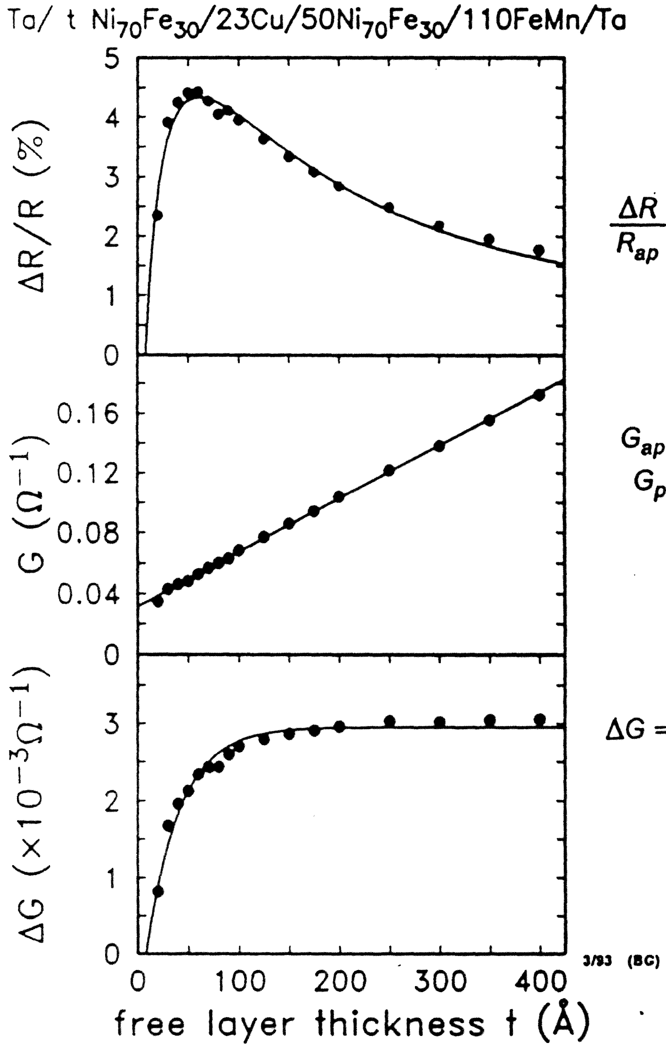

$$\frac{\Delta R}{R_{ap}} = \frac{\Delta G}{G_p}$$

$$G_{ap} = 1/R_{ap}$$
$$G_p = 1/R_p$$

$$\Delta G = \frac{\Delta R}{R_p\, R_{ap}}$$

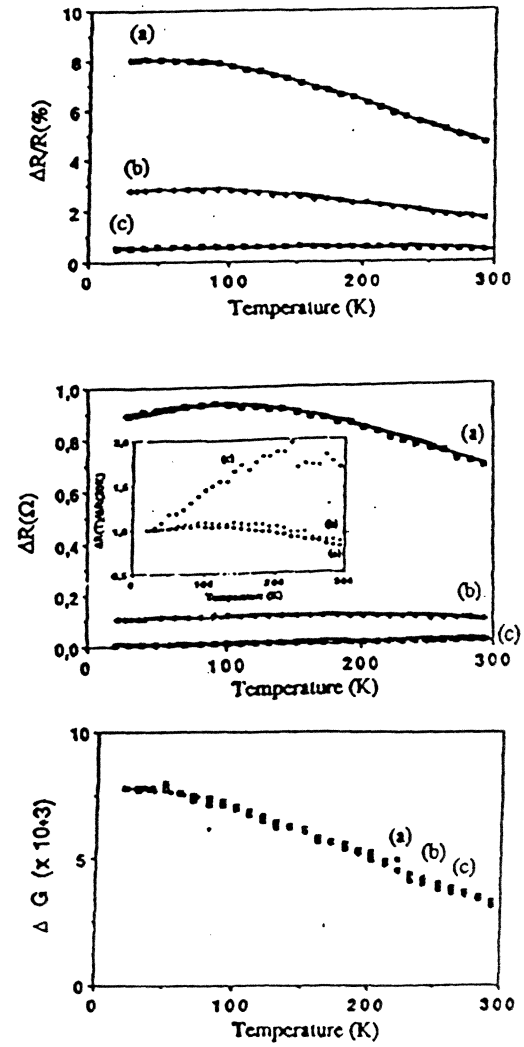

□ Si/(80Å)Co/(25Å)Cu/(50Å)NiFe/(90Å)FeMn/(50Å)Ta/CAP

— (a) CAP = (50Å)Ta

— (b) CAP = (100Å)Cu/(50Å)Ta

— (c) CAP = (300Å)Cu/(50Å)Ta

classical model basics

PATH INTEGRAL SOLUTION (relaxation time)

<u>CURRENT DENSITY $\propto$ LOCAL MEAN FREE PATH</u>

$$\underline{\underline{j^s(\vec{r})}} = -e\int \frac{d\vec{k}}{4\pi^3} V(\vec{k})g^s(\vec{r},\vec{k}) = \sigma^s E = \vec{E}\,\frac{ne^2}{m^* V_F}\,\underline{\underline{\lambda^s(\vec{r})}}$$

$$= -e\int \frac{d\vec{k}}{4\pi^3} V(\vec{k})\delta g^s(\vec{r},\vec{k}) \quad \text{where } g^s(\vec{r},\vec{k}) = g_o^s + \delta g^s$$

<u>SPECIALIZE TO LAYERED GEOMETRY (path integral)</u>

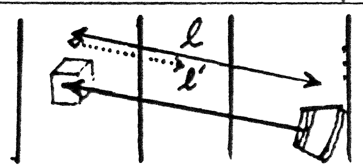

$$\delta g^s(\vec{r}) = \int_{-\infty}^{t} P^s(t,t')\,\vec{V} \bullet e\vec{E}\,dt' \quad \text{where } P^s = \text{probability unscattered}$$

$$= \frac{e}{V_F}\int_{-\infty}^{\infty}\left\{\left(\frac{\partial f}{\partial \varepsilon}\right)\vec{V}\bullet\vec{E}\ \exp\left[\int_{\ell}^{0}\frac{d\ell'}{\lambda^s(\ell')}\right]\right\}dv'$$

$$j^s(\vec{r}) = E\,\frac{ne^2}{V_F M^*}\int d\vec{\rho}'\ \exp\int_{\ell}^{0}\frac{d\ell'}{\lambda^s(\ell')}$$

total current density at $\vec{r}$

total flux: integrate over all $\vec{r}'$

probability that flux will arrive at $\vec{r}$ unscattered

1-D model

An Example: 1 Dimension

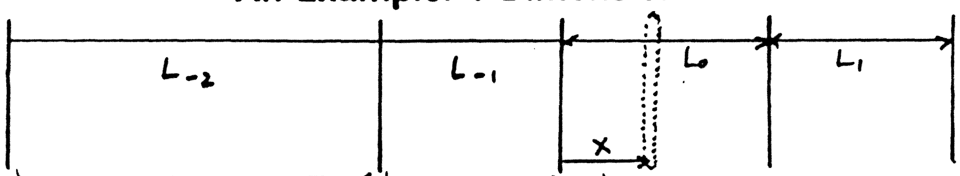

$$\underbrace{\lambda^s_{-2}\left[(1 - e^{-L_{-2}/\lambda^s_{-2}})\right]}_{\Lambda_{-2}} \times \underbrace{e^{-(L_{-1}/\lambda^s_{-1})}}_{e_{-1}} \times e^{(-x/\lambda^s_0)}$$

arriving at x from layer -2

Add from all layers to obtain $j^s(x)$

$$\begin{aligned} j^s(x) = \lambda^s_0\left[2 - e^{(-x/\lambda^s_0)} - e^{-(L_0 - x)/\lambda^s_0}\right] \\ + e^{(-x/\lambda^s_0)}[\Lambda_{-1} + e_{-1}\Lambda_{-2} + e_{-1}e_{-2}\Lambda_{-3} + \cdots] \\ + e^{(-(L_0 - x)/\lambda^s_0)}[\Lambda_1 + e_1\Lambda_2 + e_1e_2\Lambda_3 + \cdots] \end{aligned}$$

$\boxed{\text{Conductance:}}$ $G^s = \int_0^{L} j^s(x)\,dx$

$$= 2\lambda^s_i[L^s_i - \Lambda^s_i] + \Lambda^s_i\left[\Lambda^s_{i-1} + \sum_{j=1}^{-\infty}\left(\Lambda^s_{i+j-1}\prod_{k=0}^{j} e^s_{j+k}\right) + \Lambda^s_{i+1} + \sum_{j=1}^{\infty}\left(\Lambda^s_{i+j+1}\prod_{k=0}^{j} e^s_{j+k}\right)\right]$$

For a spin valve with two ferro layers (F1 and F2):

$$\Delta G = G^{\uparrow\uparrow} - G^{\uparrow\downarrow} = 2e_{sp}e_x^2\left[\Lambda^+_{F1} - \Lambda^-_{F1}\right]\left[\Lambda^+_{F2} - \Lambda^-_{F2}\right]$$

product of number of electrons emanating from one layer times the distance they travel in the second, reduced by scattering in spacer (sp) and intermixed interfaces (x).

GMR amplitude vs number of periods

classical solution to transport shows how multilayers compare to spin valves for the same interface and bulk properties:[5]

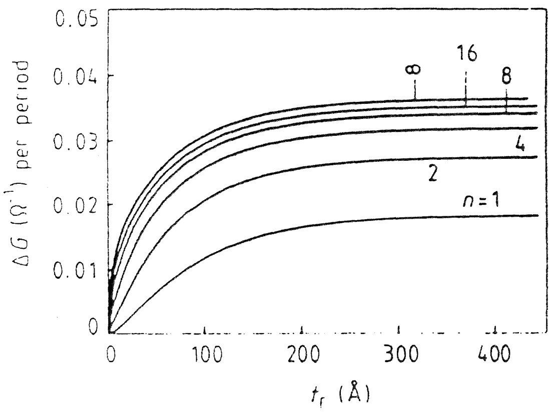

Figure 5. Magnetoresistance (absolute change of sheet conductance ΔG per period) versus thickness of the magnetic layer of a finite multilayer n (Ft_F/NM 10 Å/Ft_F/NM 10 Å) for different values of the number of periods n.

$\lambda_F^{\uparrow} = 114$ Å, $\lambda_F^{\downarrow} 12$ Å, $\lambda_{NM} = 205$ Å, $T^{\uparrow} = T^{\downarrow} = 1$ (only bulk spin-dependent scattering).

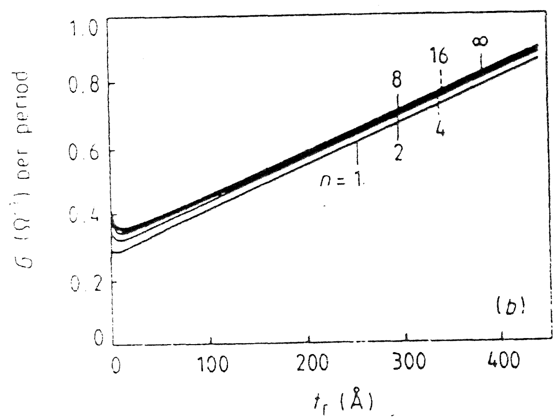

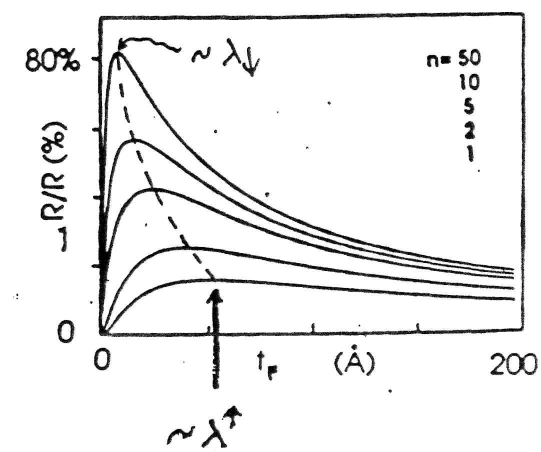

[5] B. Dieny, J. Phys. Condens. Matter 4, 8009 (1992), and B. Dieny, *private commun.*

spin dependendent scattering likely everywhere

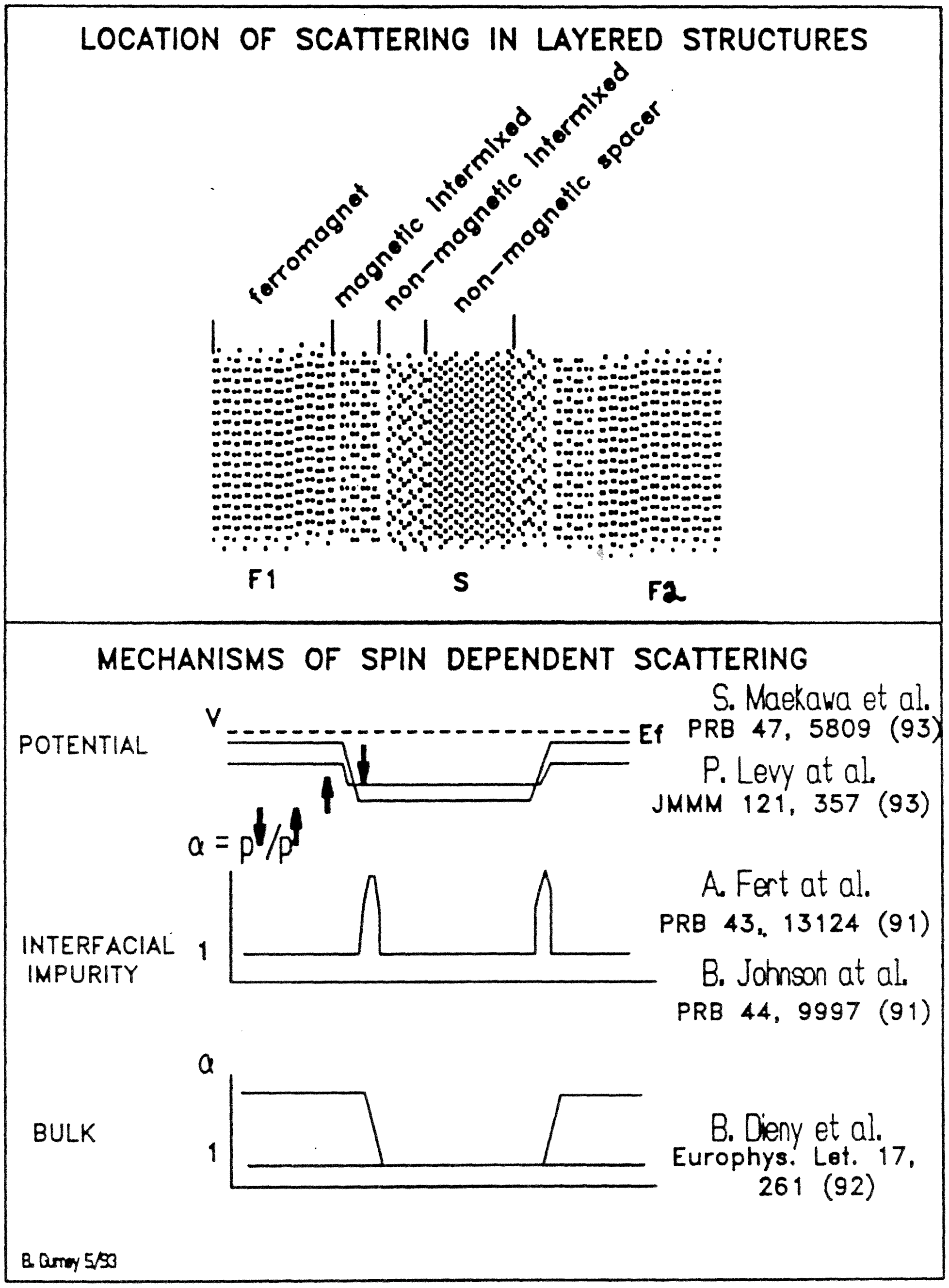

methods of probing scattering

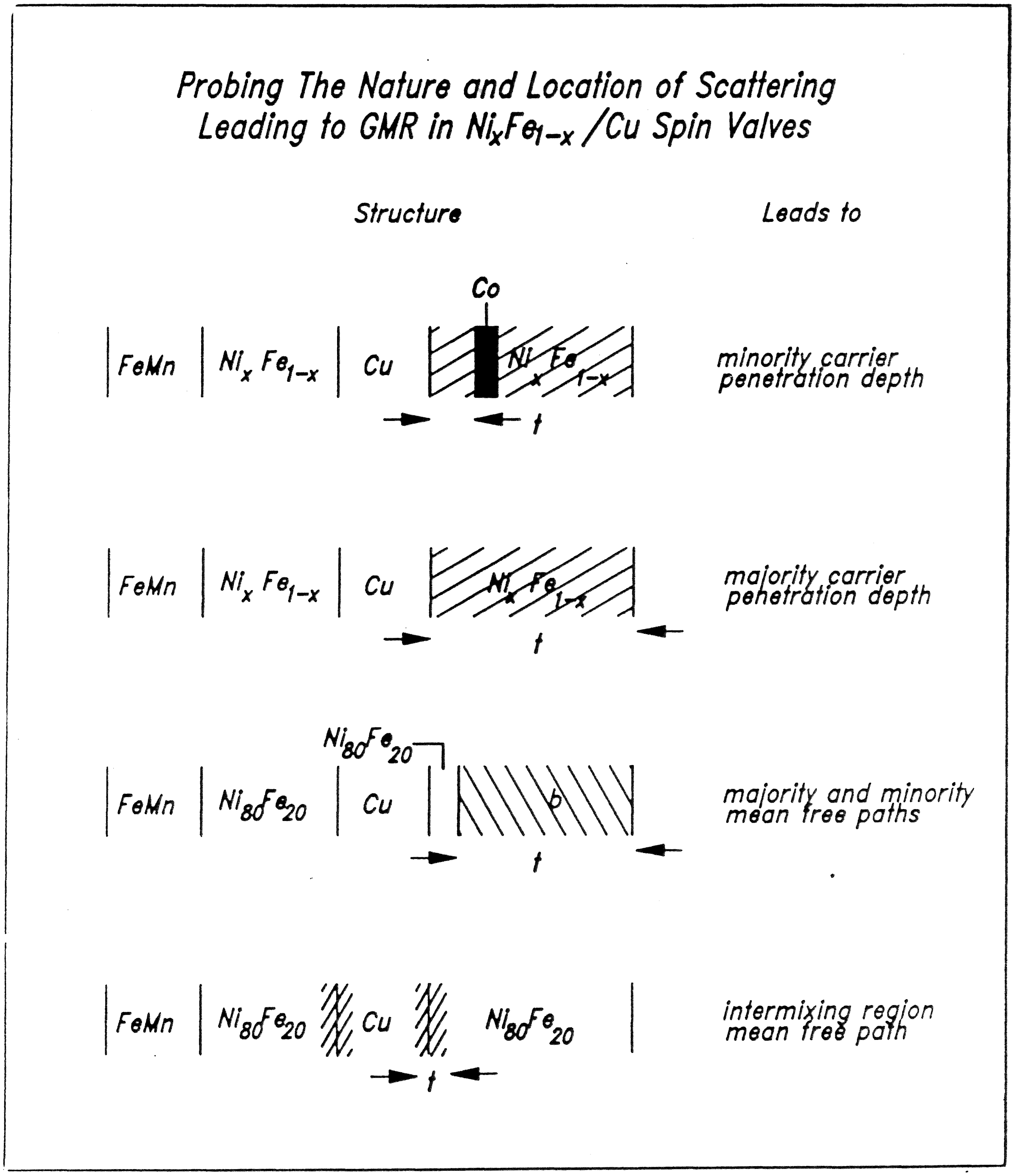

interfaces of $NiFe/Cu/NiFe$

Effect of annealing on the interfaces of giant-magnetoresistance spin-valve structures

T. C. Huang, J.-P. Nozieres,[a] V. S. Speriosu, B. A. Gurney, and H. Lefakis
IBM Research Division, Almaden Research Center, 650 Harry Road, San Jose, California 95120-6099

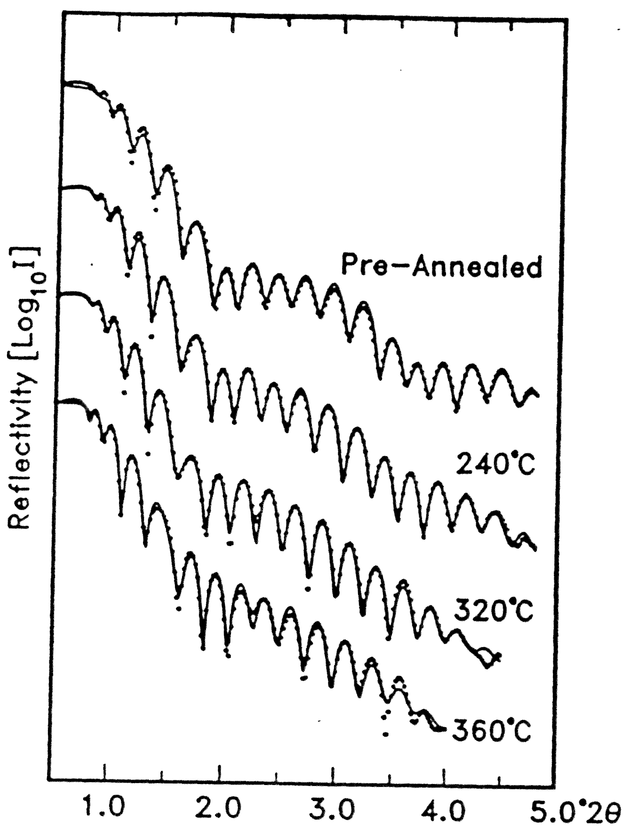

TABLE II. Interfacial widths (Å) of spin-valve samples.

	Annealing			
Interface	No.	240 °C	320 °C	360 °C
Ta_2O_5/air	10.2	11.2	10.1	11.3
Ta/Ta_2O_5	6.1	7.1	8.7	9.0
FeMn/Ta	10.1	11.0	11.5	10.9
NiFe/FeMn	7.1	9.7	14.7	16.5
Cu/NiFe	6.8	9.9	12.1	20.8
NiFe/Cu	6.7	9.3	11.6	24.3
Ta/NiFe	4.6	7.4	10.8	16.3
$TaSi_2$/Ta	6.3	6.3	7.2	14.5

non-mangetic intermixing

Non-Magnetic Layers in $Ta/Ni_xFe_{1-x}/Cu$ Sandwiches

- Some Ni and Fe atoms at the interface are non-magnetic at room temperature in sputtered $Ta/Ni_xFe_{1-x}/Cu$ sandwiches.
- The lost moment, when expressed as a thickness t_{nm} of Ni_xFe_{1-x}, is in agreement with about half the width of the intermixed region determined by x-ray reflectance measurements on samples whose intermixed regions were increased by annealing, suggesting the origin of t_{nm} is alloying (Appl. Phys. Lett. 60, 1573 (1992), Appl. Phys. Lett. March 29 (1993)).
- Magnetotransport is reduced by t_{nm}: for x=80 we find $\Delta G \sim \Delta G_0 \exp[-t_{nm}/(6.1 \pm 0.6\ \text{Å})]$.

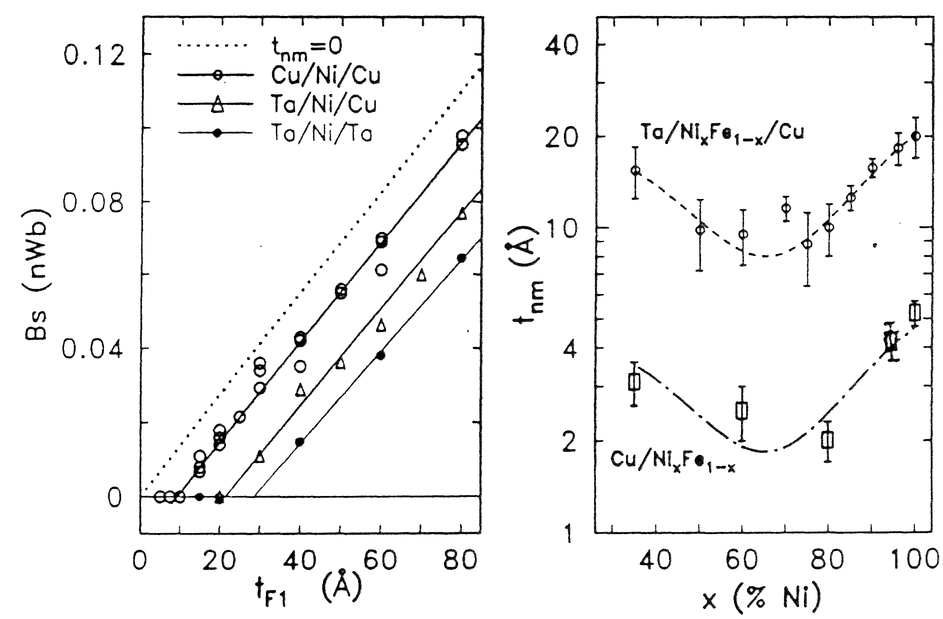

interfacial scattering in $NiFe/Cu/NiFe$

Si/50ÅTa/t NiFe/22.5ÅCu/50ÅNiFe/110ÅFeMn/50ÅTa

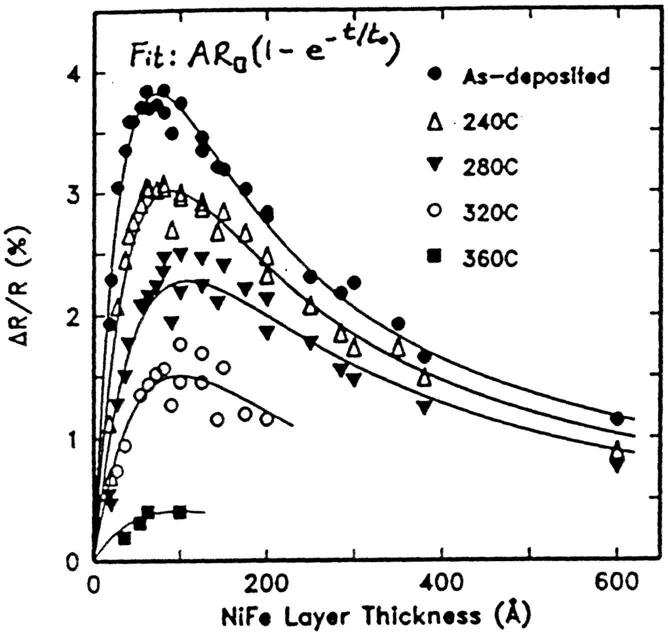

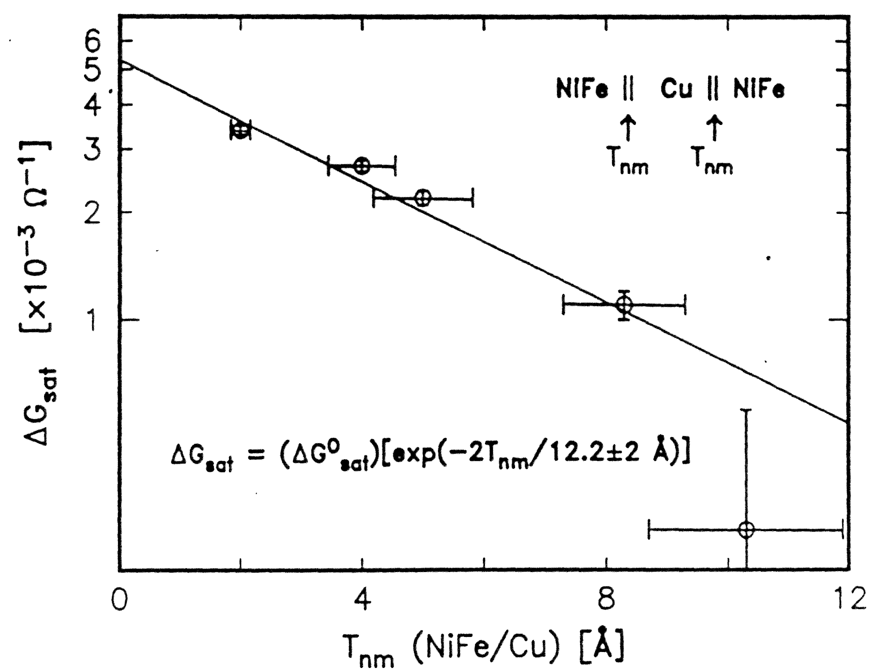

PHYSICAL REVIEW B VOLUME 47, NUMBER 17 1 MAY 1993-I

47 11 579

Role of interfacial mixing in giant magnetoresistance

V. S. Speriosu, J. P. Nozieres, and B. A. Gurney

IBM Research Division, Almaden Research Center, 650 Harry Road, San Jose, California 95120-6099

interfaces of $Fe/Cr/Fe$

VOLUME 68, NUMBER 6 PHYSICAL REVIEW LETTERS 10 FEBRUARY 1992

Roughness and Giant Magnetoresistance in Fe/Cr Superlattices

Eric E. Fullerton, David M. Kelly, J. Guimpel,[a] and Ivan K. Schuller
Physics Department, 0319, University of California, San Diego, La Jolla, California 92093-0319

Y. Bruynseraede
Laboratorium voor Vaste Stof Fysika en Magnetisme, Katholieke Universiteit Leuven, B-3001 Leuven, Belgium

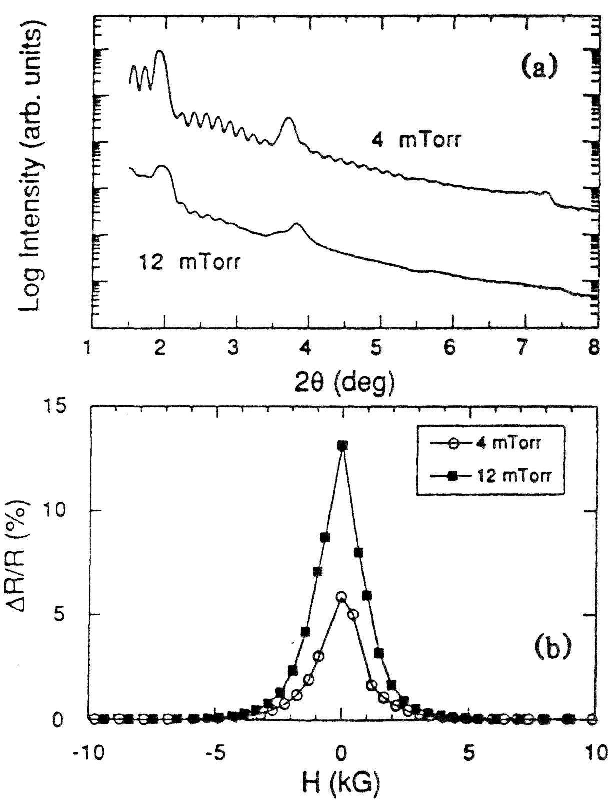

FIG. 1. (a) Low-angle θ-2θ x-ray-diffraction spectra and (b) $\Delta R/R$ vs applied field at 4 K for selected representative $[Fe(30\ Å)/Cr(18\ Å)]_{10}$ superlattices sputtered at various Ar pressures. X-ray spectra are offset by two decades for clarity. Saturation resistivities are 26 and 23 $\mu\Omega$ cm for the 4- and 12-mTorr samples, respectively.

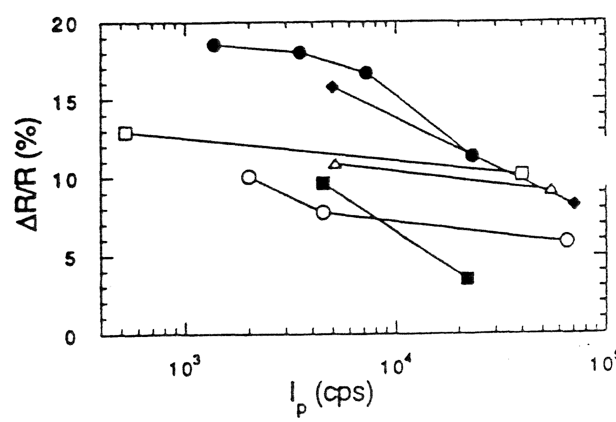

FIG. 2. Dependence of $\Delta R/R$ on the first superlattice Bragg peak intensity I_p for samples with $N=40$. I_p is a qualitative measure of the interfacial roughness (the background intensity has been subtracted). △, [Fe(30 Å)/Cr(13 Å)]; ◆, [Fe(30 Å)/Cr(15 Å)]; □, [Fe(30 Å)/Cr(16 Å)]; ●, [Fe(30 Å)/Cr(18 Å)]; ○, [Fe(30 Å)/Cr(20 Å)]; ■, [Fe(30 Å)/Cr(25 Å)].

interfacial scattering in $Fe/X/Cr/X/Fe$

The role of spin-dependent impurity scattering in Fe/Cr giant magnetoresistance multilayers

Peter Baumgart, Bruce A. Gurney, Dennis R. Wilhoit, Thao Nguyen, Bernard Dieny, and Virgil S. Speriosu
IBM Research Division, Almaden Research Center, 650 Harry Road, San Jose, California 95120-6099

4792 J. Appl. Phys. 69 (8), 15 April 1991 0021-8979/91/084792-03$03.00 © 1991 American Institute of Physics 4792

Giant magnetoresistance of Fe/Cr multilayers: Impurity scattering model of the influence of third elements deposited at the interfaces

Bruce A. Gurney, Peter Baumgart, Dennis R. Wilhoit, Bernard Dieny, and Virgil S. Speriosu
IBM Research Division, Almaden Research Center, 650 Harry Road, San Jose, California 95120-6099

5867 J. Appl. Phys. 70 (10), 15 November 1991 0021-8979/91/105867-03$03.00 © 1991 American Institute of Physics 5867

GOALS

- ☐ Demonstrate Spin Dependent Impurity Scattering (SDIS) is viable mechanism in giant MR films
- ☐ Demonstrate SDIS is responsible for giant MR in Fe/Cr

STRATEGY

test structure

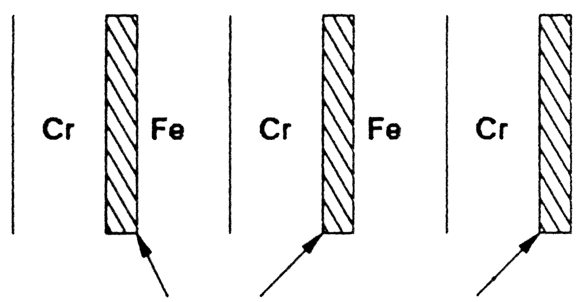

add third element with known scattering in alloys

$\alpha = \rho_\downarrow / \rho_\uparrow \gg 1$ for Al, Ir, Ge

$\ll 1$ for Cr, V, Mn

- ○ minimal perturbation of physical structure
- ○ no variation of Fe or Cr thickness
- ○ high absolute impurity resistivity

results for $Fe/X/Cr/X/Fe$

The role of spin-dependent impurity scattering in Fe/Cr giant magnetoresistance multilayers

Peter Baumgart, Bruce A. Gurney, Dennis R. Wilhoit, Thao Nguyen, Bernard Dieny, and Virgil S. Speriosu
IBM Research Division, Almaden Research Center, 650 Harry Road, San Jose, California 95120-6099

4792 J. Appl. Phys. 69 (8), 15 April 1991 4792

TABLE I. Spin-dependent resistivities and α of Cr, V, Mn, Al, Ir, and Ge when alloyed with Fe (from Ref. 10).

	Cr	V	Mn	Al	Ir	Ge
$\rho\downarrow$ ($\mu\Omega$ cm)	2.8 ± 0.2	1.3 ± 0.3	1.7 ± 0.2	48	20	49
$\rho\uparrow$ ($\mu\Omega$ cm)	12.5 ± 6	10.5 ± 3	13 ± 5	5.6	2.2	7.9
$\alpha=\rho\downarrow/\rho\uparrow$	0.17–0.37	0.12–0.13	0.09–0.17	8.6	9	6.2

Giant magnetoresistance of Fe/Cr multilayers: Impurity scattering model of the influence of third elements deposited at the interfaces

Bruce A. Gurney, Peter Baumgart, Dennis R. Wilhoit, Bernard Dieny, and Virgil S. Speriosu
IBM Research Division, Almaden Research Center, 650 Harry Road, San Jose, California 95120-6099

5867 J. Appl. Phys. 70 (10), 15 November 1991 5867

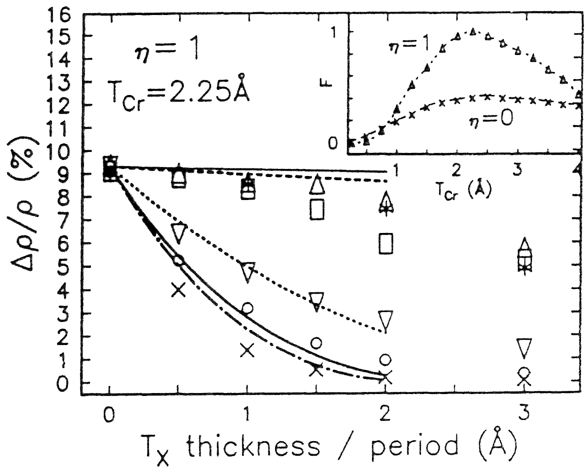

FIG. 1. Giant magnetoresistance vs thickness of deposited third-element X per Fe/Cr multilayer period (points, from Ref. 5) and best model fit (lines) for X = Mn(□—), V(Δ—), Cr(× same line as V), Ir(O-··-), Al(∇—), and Ge(×···); the best fit is obtained with an equivalent thickness of Fe/Cr scattering centers $t_{Cr} = 2.25$ Å and $\eta = 1$. Inset: Quality of fit F vs T_{Cr} for $\eta = 1$ (substitution of third-element scattering centers for Fe/Cr centers) and $\eta = 0$ (addition of third-element scattering centers to existing Fe/Cr centers).

PHYSICAL REVIEW B VOLUME 44, NUMBER 18 1 NOVEMBER 1991-II

Theory of giant magnetoresistance effects in Fe/Cr multilayers: Spin-dependent scattering from impurities

B. L. Johnson
Department of Physics, University of Colorado, Boulder, Colorado 80309-0390

R. E. Camley
Department of Physics, University of Colorado, Colorado Springs, Colorado 80933-7150

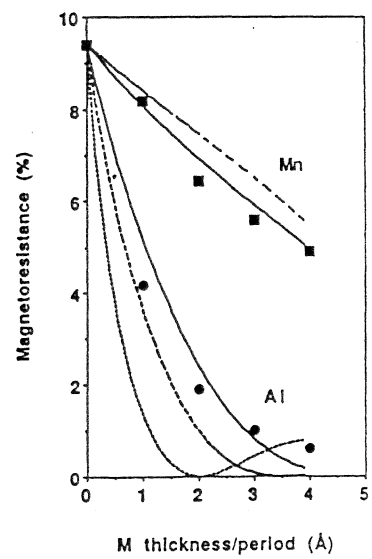

FIG. 2. The percent change in the magnetoresistance as a function of thickness per period of added impurity. The upper set of curves is for Mn impurities and the lower set is for Al impurities. The heavy squares are the experimental data for Mn, while the heavy dots are the experimental data for Al, both taken from Ref. 10. For Mn, the solid curve is calculated using the value for bulk scattering asymmetry $N_m=4$, while the dashed curved is calculated using $N_m=6.5$. For Al, the dashed line is obtained for $N_m=0.117$, the dotted line for $N_m=0.281$, and the solid line for $N_m=0.468$. Note that 0.468 is a *smaller* asymmetry than 0.117, as explained in the text.

minority carrier penetration depth

Minority Carrier Penetration Depth D⁻

- Using a structure introduced by Parkin et al., **D⁻** can be obtained from the change in transport as one varies the distance between the interface and an ultrathin scattering layer.
- Using a bulk scattering model Dieny et al. find $\lambda^{-} \simeq 10$Å for **x**=0.8 at 4K.
- We find at RT, **D⁻** = 4.1 ± 0.5Å, ***independent*** of **x**.

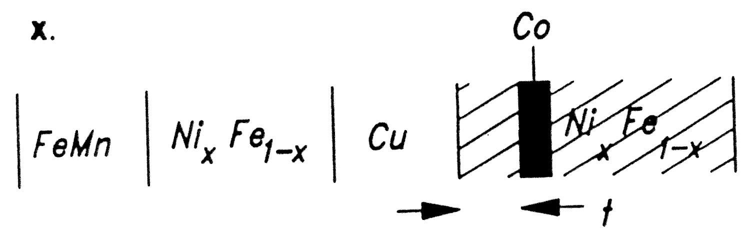

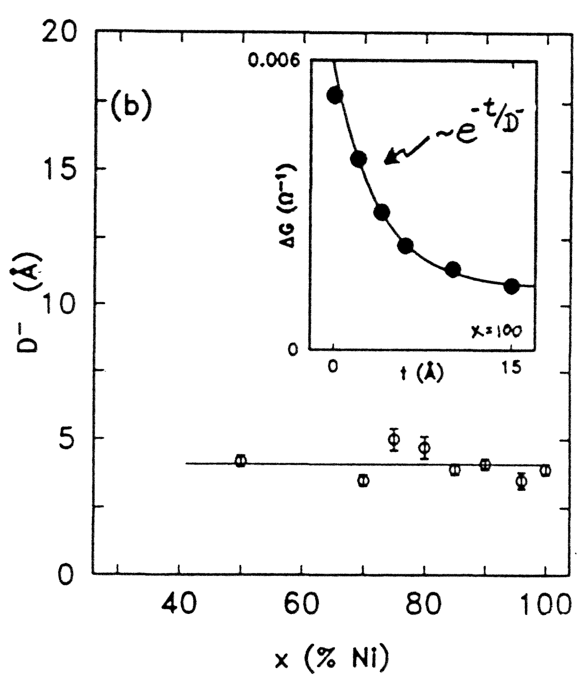

majority carrier penetration depth

- $\Delta\mathbf{G}$ rises with a characteristic length $\mathbf{D}_{\Delta G}$ to a saturation value $\Delta\mathbf{G}_{sat}$, i.e.

$$\Delta\mathbf{G} \simeq \Delta\mathbf{G}_{sat}[1 - \exp(-(\mathbf{t}_{F1} - \mathbf{t}_{nm})/\mathbf{D}_{\Delta G})]$$

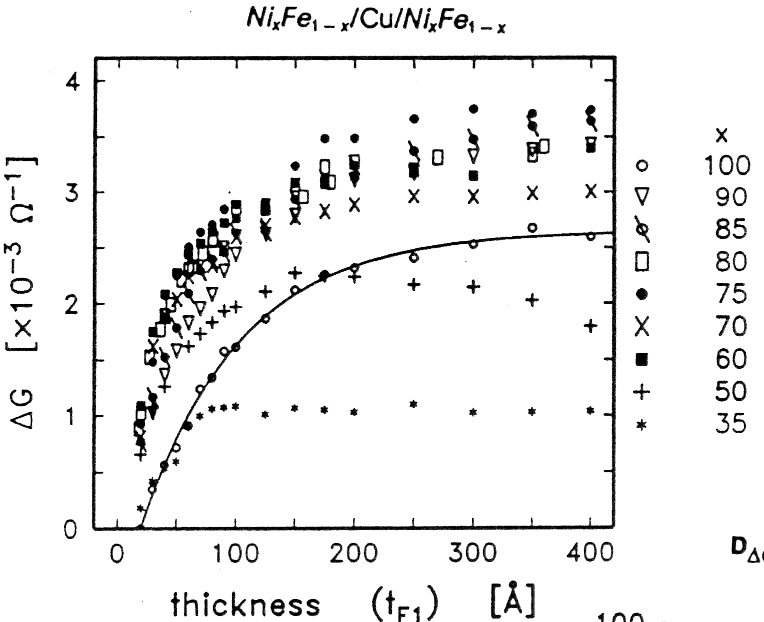

$\mathbf{D}_{\Delta G} = \beta\lambda^+$ ($\beta \cong 1$)

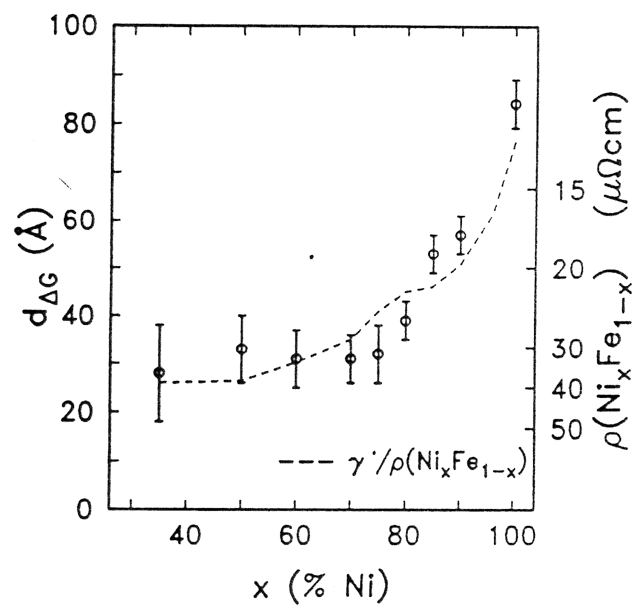

$Ni_xFe_{1-x}/Cu/Ni_xFe_{1-x}$ spin valves

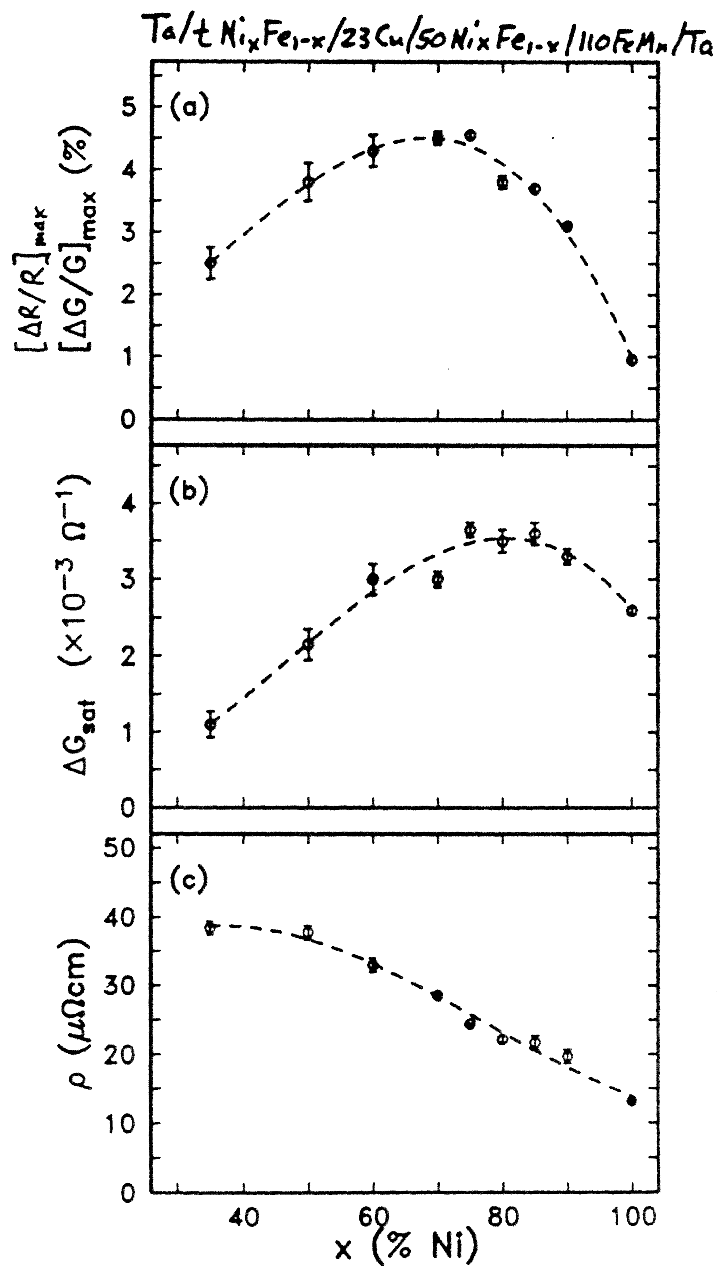

IBM Almaden Research Center

Bruce A. Gurney

using GMR to probe transport

BACKED SPIN VALVE STRUCTURE

- spin polarized conduction electron source
- directly measures the majority carrier mean free path

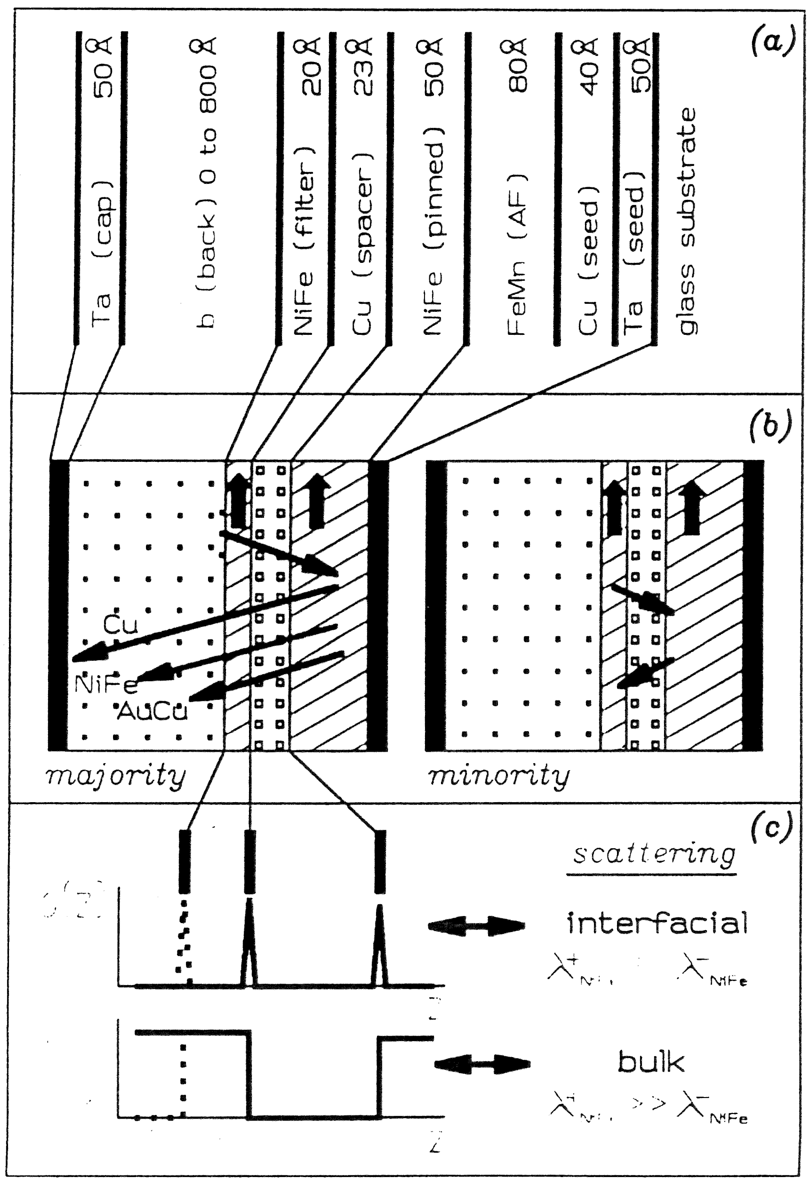

VOLUME 71, NUMBER 24 PHYSICAL REVIEW LETTERS 13 DECEMBER 1993

Direct Measurement of Spin-Dependent Conduction-Electron Mean Free Paths in Ferromagnetic Metals

4023

Bruce A. Gurney, Virgil S. Speriosu, Jean-Pierre Nozieres, Harry Lefakis, Dennis R. Wilhoit, and Omar U. Need
IBM Research Division, Almaden Research Center, 650 Harry Road, San Jose, California 95120-6099

backed spin theory

DIRECT MEASUREMENT OF MAJORITY CARRIER MEAN FREE PATH

Approximate solution to Boltzmann transport equation for backed spin valve with filter layer 'f' predicts

$$\Delta G \simeq \Delta G_f + \Delta g_0 \left[\lambda^+ e^{-\beta t_f/\lambda_f^+}\left\{1 - e^{-\beta[(t_d - t_x)/\lambda^+]}\right\} - \lambda^- \overbrace{e^{-\beta t_f/\lambda_f^-}}^{\approx 0}\left\{1 - e^{-\beta[(t_d - t_x)/\lambda^-]}\right\}\right]$$

$$\approx \underline{\Delta G_f} + \underline{\Delta G_b}\left[1 - e^{-\underline{\beta[(t_d - t_x)/\lambda^+]}}\right] \qquad (\lambda_f^- \ll \beta t_f)$$

magnetoconductance from filter layer	depends on b-layer material and filter, etc.	$\beta \simeq 1$ (XPT) $\beta \sim 2$ (theory) (average over solid angle)

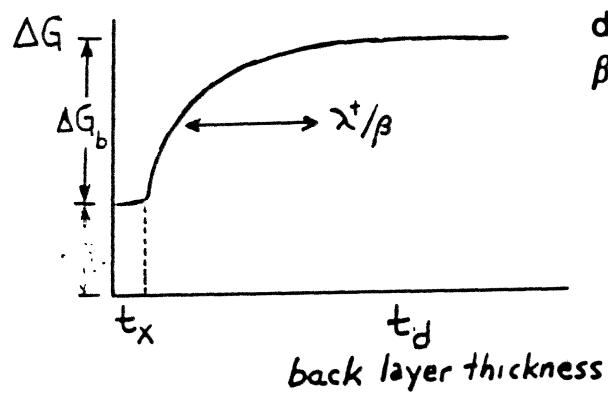

depends on β/λ^+ only

backed spin valve results

– λ^+ directly measured
– λ^- inferred from λ^+ and bulk resistivity

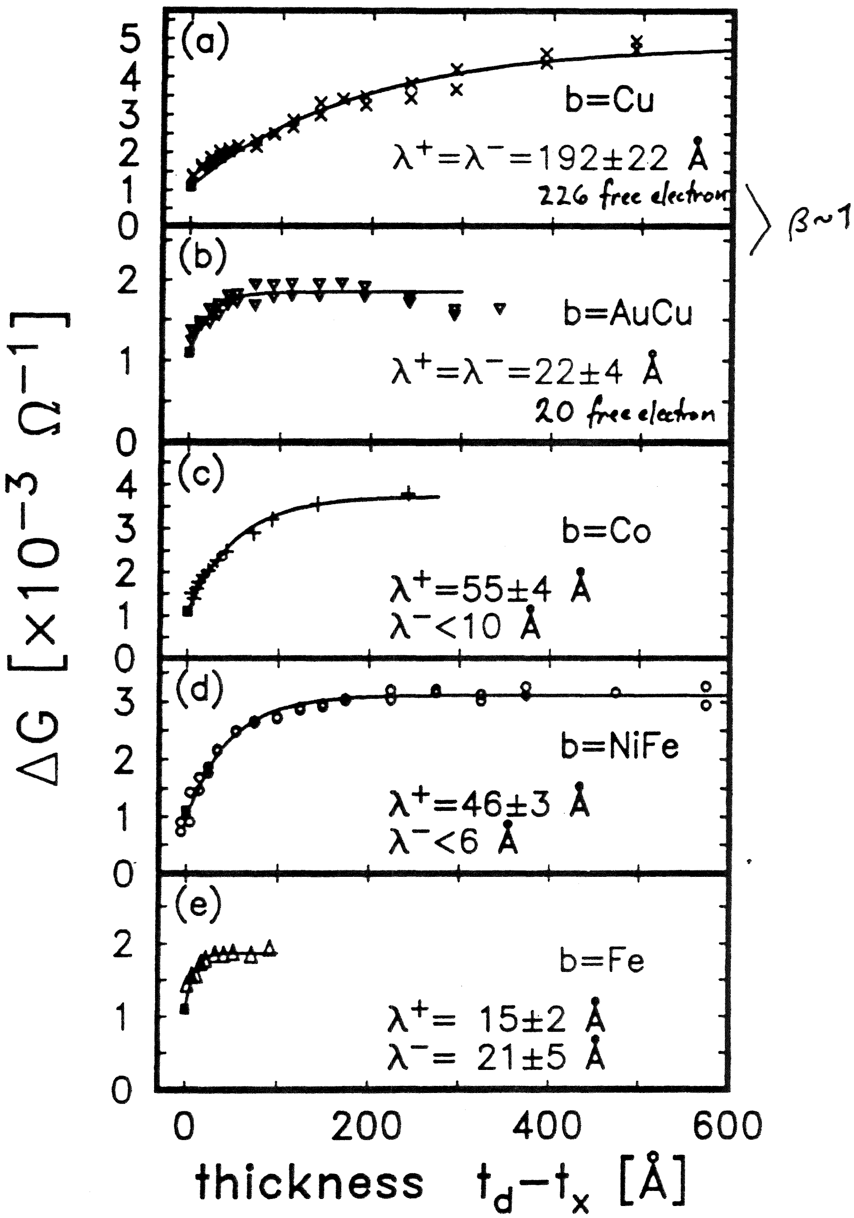

CIP vs CPP transport

Current perpendicular to the plane (CPP) yields a GMR amplitude two or more times larger than current in the plane (CIP), and can be used to measure spin dependent scattering.

PHYSICAL REVIEW LETTERS 10 JUNE 1991 VOLUME 66, NUMBER 23

Perpendicular Giant Magnetoresistances of Ag/Co Multilayers

W. P. Pratt, Jr., S.-F. Lee, J. M. Slaughter,[a] R. Loloee, P. A. Schroeder, and J. Bass
Department of Physics and Astronomy and Center for Fundamental Materials Research, Michigan State University, East Lansing, Michigan 48824
(Received 22 January 1991; revised manuscript received 11 April 1991)

$$\sqrt{(R^{(AP)} - R^{(P)})R^{(AP)}} = \beta \frac{t_F}{t_F + t_N}\rho_F^* L + 2\gamma r_b^* M$$

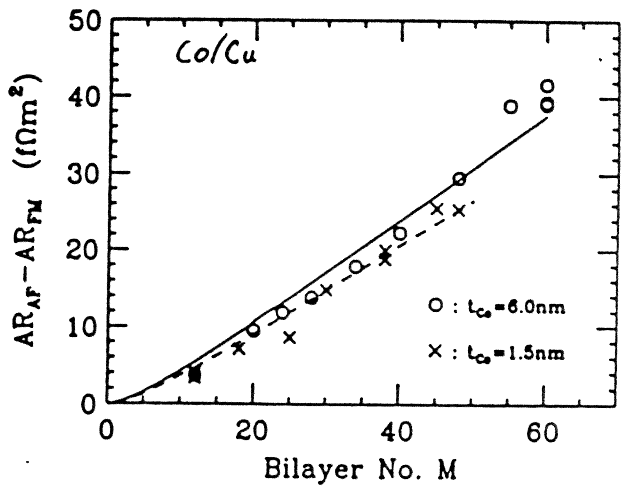

Figure 10. Plot of $AR_{AF} - AR_{FM}$ vs M for t_{Co} = 1.5 nm and 6 nm. The solid line represents the values expected from Eq. 9 for t_{Co} = 6 nm; the dashed line for t_{Co} = 1.5 nm.
From Nato Workshop on Magnetism in Reduced Dimensions, Cargère (1992)

Perpendicular giant magnetoresistance of microstructures in Fe/Cr and Co/Cu multilayers (invited)

M. A. M. Gijs, J. B. Giesbers, M. T. Johnson, J. B. F. aan de Stegge, and H. H. J. M. Janssen
Philips Research Laboratories, Prof. Holstlaan 4, 5656 AA Eindhoven, The Netherlands

J. Appl. Phys. 75 (10), 15 May 1994 6709

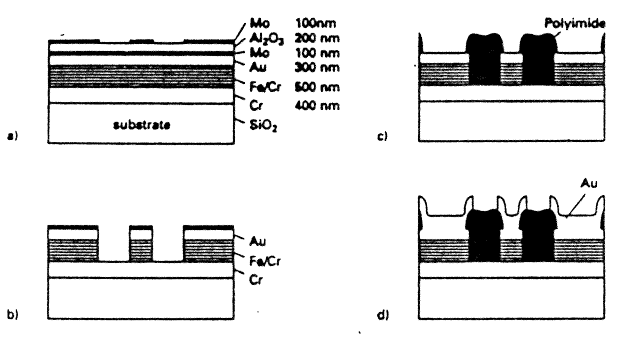

FIG. 1. Schematic diagram of different processing steps in the pillar structuring and contact fabrication.

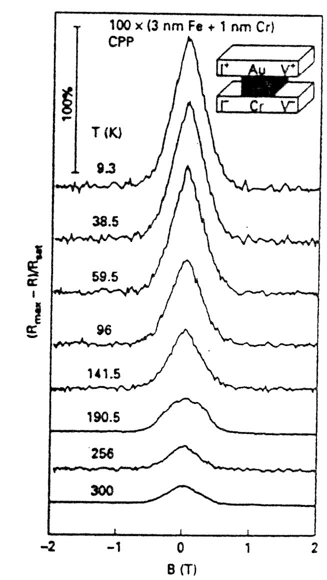

spin accumulation

Perpendicular magnetoresistance in magnetic multilayers: Theoretical model and discussion (invited)

Albert Fert
Laboratoire de Physique des Solides,[a] Université Paris-Sud, 91405 Orsay, France
J. Appl. Phys. 75 (10), 15 May 1994 6699

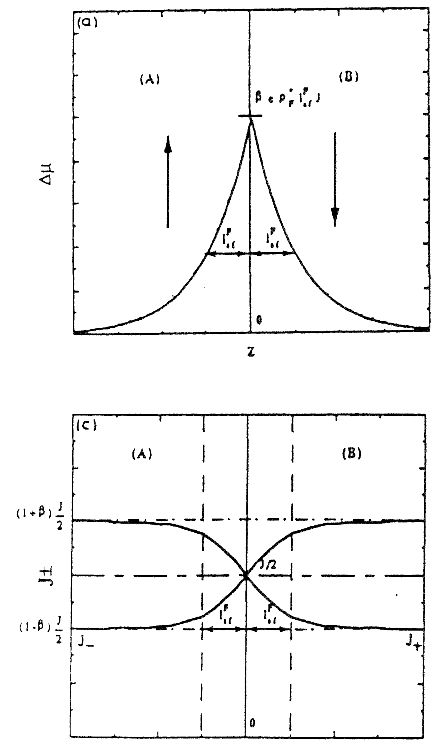

FIG. 1. Illustration of spin accumulation effects at the interface $z=0$ between two semi-infinite ferromagnetic regions with opposite magnetizations. The arrows indicate the majority spin direction in each region. The electrons flow from left- to right-hand side, and the spin + electrons are supposed to be weakly scattered at the left-hand side and strongly at the right-hand side. The change $\Delta\mu$ of the chemical potential of the spin + electrons (proportional to the out of equilibrium spin polarization), the absolute values of the current densities for spin + and spin − electrons, J_+ and J_-, respectively, and the absolute values of the electric field E are plotted vs z. See also Refs. 14 and 15.

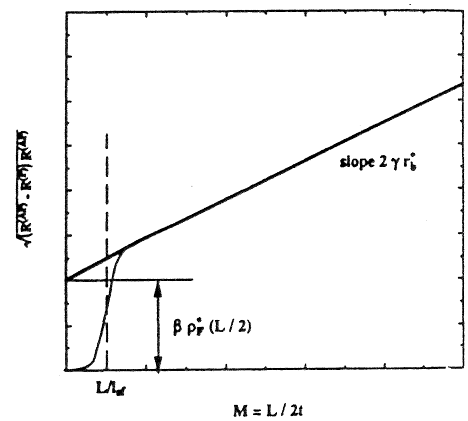

FIG. 3. $\sqrt{(R^{(AP)}-R^{(P)})R^{(AP)}}$ is plotted as a function of the number of bilayers M for a fixed total thickness L and the same individual thickness for the ferromagnetic and normal layer, $t_F=t_N=t=L/(2M)$. The solid line is the linear variation expected from Eq. (14) for the limit $t \ll l_{sf}$ or $M \ll L/l_{sf}$. For $M < L/l_{sf}$, Eq. (14) is no longer valid and $\sqrt{(R^{(AP)}-R^{(P)})R^{(AP)}}$ drops as $\exp(-t/4l_{sf}) \sim \exp(-L/2Ml_{sf})$ (see thin solid line).

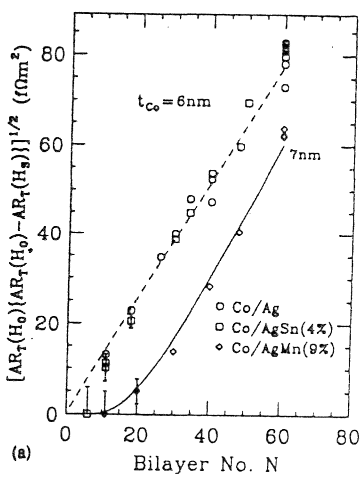

(a)

How to isolate effects of spin-flip scattering on giant magnetoresistance in magnetic multilayers (invited)

J. Bass, Q. Yang, S. F. Lee, P. Holody, R. Loloee, P. A. Schroeder, and W. P. Pratt, Jr.
Department of Physics and Astronomy and Center for Fundamental Materials Research, Michigan State University, East Lansing, Michigan 48824-1116
J. Appl. Phys., Vol. 75, No. 10, 15 May 1994

bipolar spin switch

Spin polarization of gold films via transported (invited)

Mark Johnson
Bellcore, 331 Newman Springs Rd., Red Bank, New Jersey 07701

6714 J. Appl. Phys. **75** (10), 15 May 1994

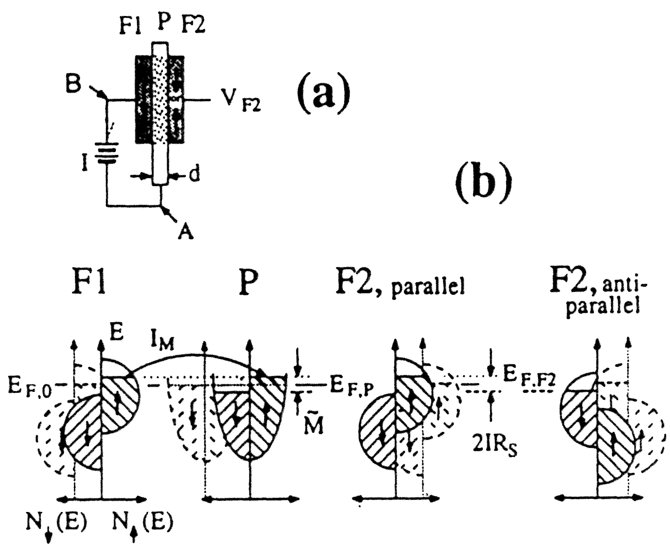

FIG. 1. (a) Pedagogical model of three-terminal device. Arrows in F1 and F2 refer to magnetization orientation as determined by majority spin subband. (b) Diagrams of the densities of state $N(E)$ as functions of energy E of the ferromagnet-paramagnet-ferromagnet system depicted in (a).

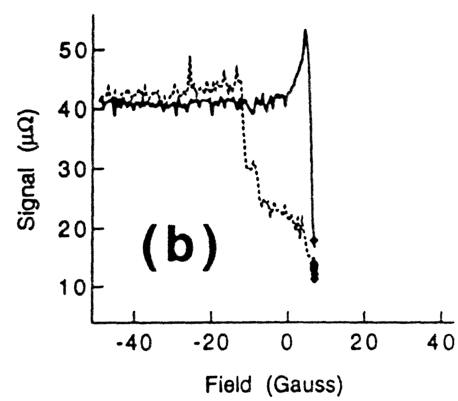

implications of $j(x)$ for sensors: spin valves

DISTRIBUTION OF CURRENT INFLUENCES THE BIAS POINT

three contributions to bias point

pinned layer demag field	interlayer coupling	current flow
$H_d = \pi^2 \frac{M_s t_p}{h}$	H_i	$H_j = Q\ 2\pi \frac{i[mA]}{h[\mu m]}$

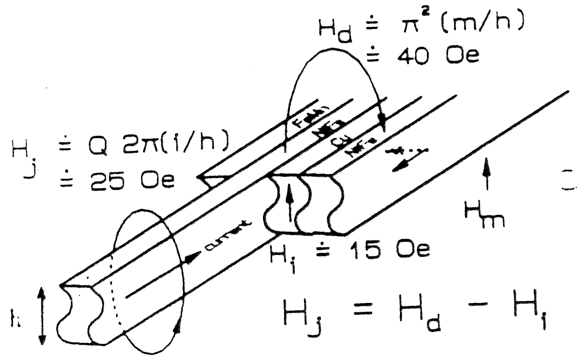

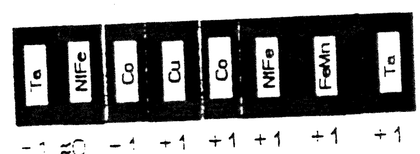

$$H_j = H_d - H_i \qquad Q = \left(\sum_i c_i\, j_i\right) / \left(\sum_i j_i\right)$$

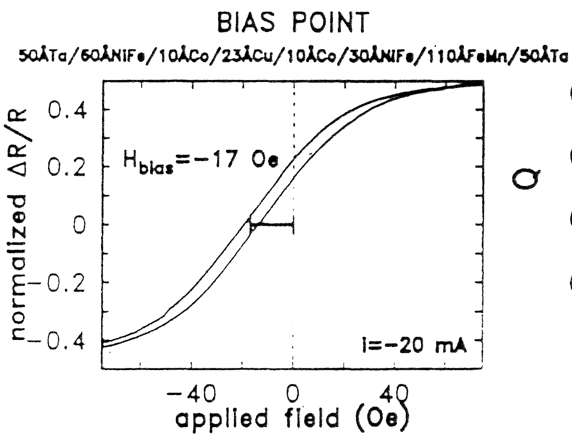

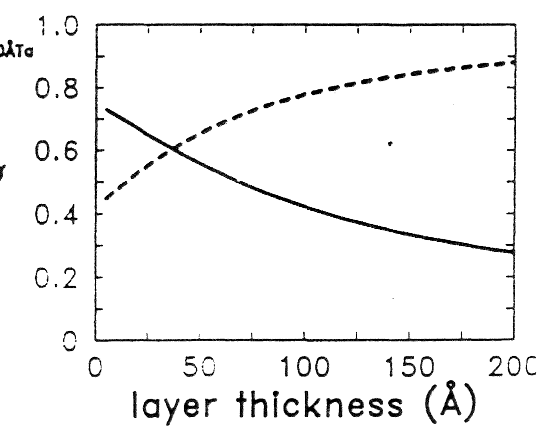

current distribution $j(x)$ in a spin valve

LOCAL CURRENT DENSITY

NiFe/Cu/NiFe spin valve using previously measured λ_i^s

50ÅTa/45ÅNiFe/22.5ÅCu/45ÅNiFe/110ÅFeMn/50ÅTa

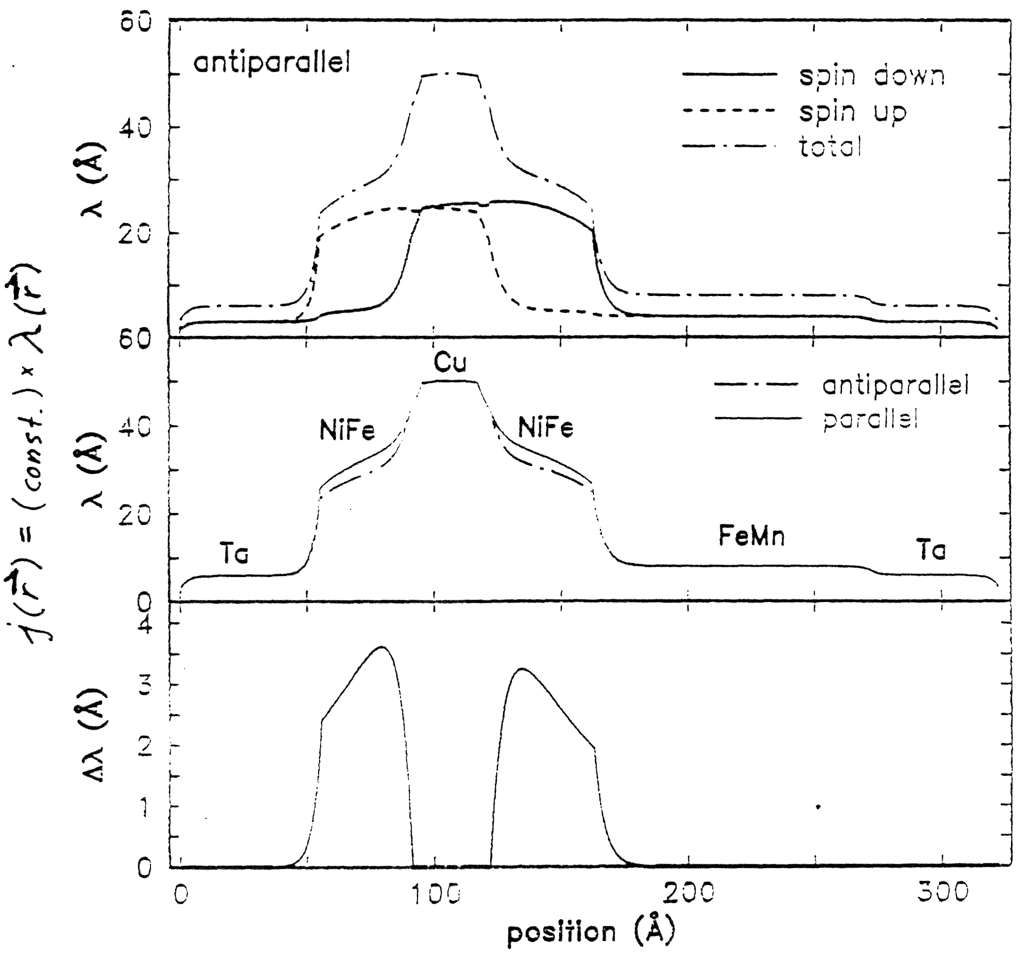

- △ illustrates how SDS leads to resistance change
- △ shows that current density change is in ferro layers
- △ current density much more uniform than parallel resistor model

path integral vs parallel resistor models

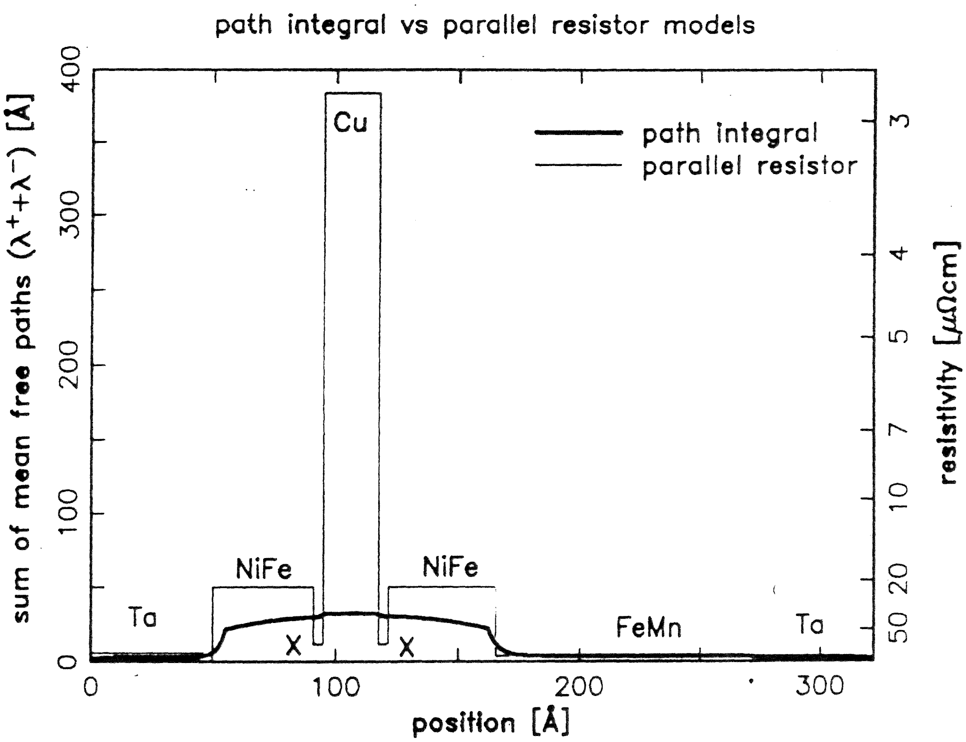

current bias: experimental results

MODEL PREDICTS BIAS POINT SHIFT

The transfer curve of a 10μm x 3.8μm stripe was measured vs sense current, and compared with the model prediction of bias point shift.

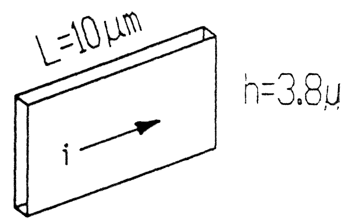

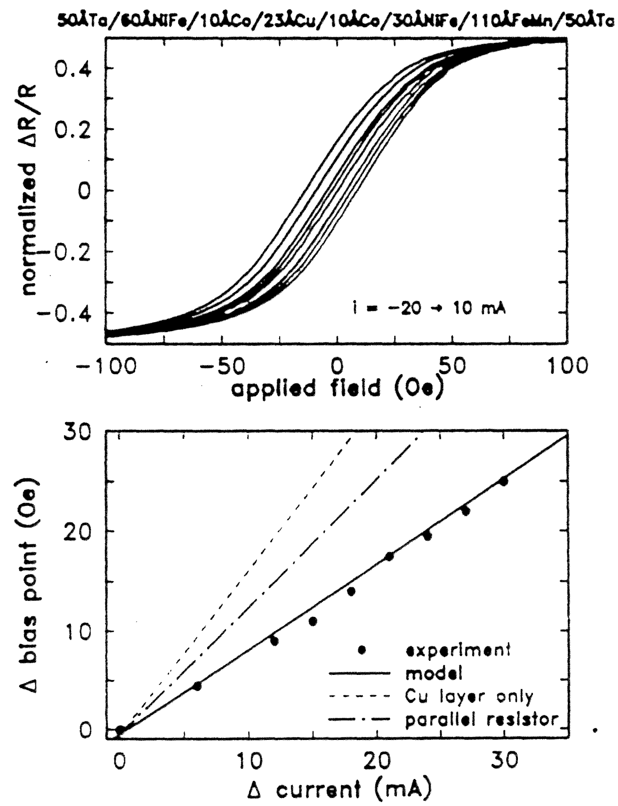

- △ model accurately predicts Q=0.52 for this structure
- △ implies higher current (more heating, electromigration) to achieve optimal bias than more simplistic current distributions.

recording constraints on MR heads

interplay of t, g, h, H_k

order of magnitude estimates [1] for:

t film thickness

g gap

h stripe height

H_k sensor film anisotropy

sensor moment — matched to flux from media:

$$\begin{aligned} M_r^{media}\delta &\approx M_s t \\ 10^{-3}[emu/cm^2] &\approx 800[G]125[\text{Å}] \end{aligned}$$

$$\Rightarrow t \approx 100 \text{ Å}$$

gap — follows from density

$PW_{50} \approx \sqrt{2}g$ FWHM of read back pulse, from transition

density ~ 1 [Gbit/in^2] $= 1.6 \times 10^8$ [bit/cm^2]

$= 1/(3 \times 10^{-4}$ [cm] $\cdot$ 2×10^{-5} [cm])

$$\Rightarrow g \approx 1.4 \times 10^{-5} \, [cm]$$

[1] see, e.g. N. Bertram, *Theory of Magnetic Recording. Cambridge. 1994*

recording constraints on MR heads

interplay of t, g, h, H_k

order of magnitude estimates for:

t film thickness

g gap

h stripe height

H_k sensor film anisotropy

h and H_k can be estimated from t, g, and considereations of maximum efficiency of flux propagation into the head, and maximizing the signal to noise:

maximum efficiency — $h \sim \lambda$ characteristic length of flux propagation. (tradeoff of h and H_k)

$$h \sim \lambda \approx \sqrt{\frac{2\pi M g t}{H_k}} \quad \Rightarrow \quad tg \approx \frac{h^2 H_k}{2\pi M}$$

signal to noise power (want large h for large signal)

$$\frac{S}{N} = \left(\frac{V_{sig}}{V_{noise}}\right)^2 = \frac{(\eta\,\Delta\rho\,J\,W)^2}{4\,kT\,R\,\Delta f} = \frac{\eta^2 J^2 \rho h W t}{4kT\Delta f}\left(\frac{\Delta\rho}{\rho}\right)^2.$$

practical compromise — $h \approx 1\mu m$

$$\Rightarrow H_k \approx \frac{2\pi M t g}{h^2} \approx 10\,[Oe]$$

sensor materials: low field multilayers

IEEE TRANSACTIONS ON MAGNETICS, VOL. 30, NO. 6, NOVEMBER 1994 3837

Highly Sensitive Giant Magnetoresistance in NiFe/(Ni/Fe/Cu)n/NiFe Thin Films

Akira Kouchiyama, Teiichi Miyauchi and Kenjiro Watanabe
Corporate Research Laboratories, Sony Corporation, 6-7-35 Kitashinagawa, Shinagawa-ku, Tokyo, 141, Japan

Abstract - GMR of 0 to 6.95% has been found in fields of 0 to 50 Oe at room temperature in NiFe(5nm)/[Ni(1.58nm)/Fe(0.42nm)/Cu(2.1nm)]$_8$/NiFe(7nm) thin films prepared by DC magnetron sputtering with extremely precise thickness control. The full width at half maximum (FWHM) of the GMR curve was 10.4 Oe. The top and bottom NiFe layers had antiferromagnetic coupling to adjacent Ni/Fe layers across the Cu layers and also maintained magnetically soft characteristics. The NiFe/(Ni/Fe/Cu)$_8$/NiFe sensor which was 40nm thick, 3.5 μm wide and 15 μm long showed a large output 4 times as large as NiFe/Al2O3/NiFe sensors.

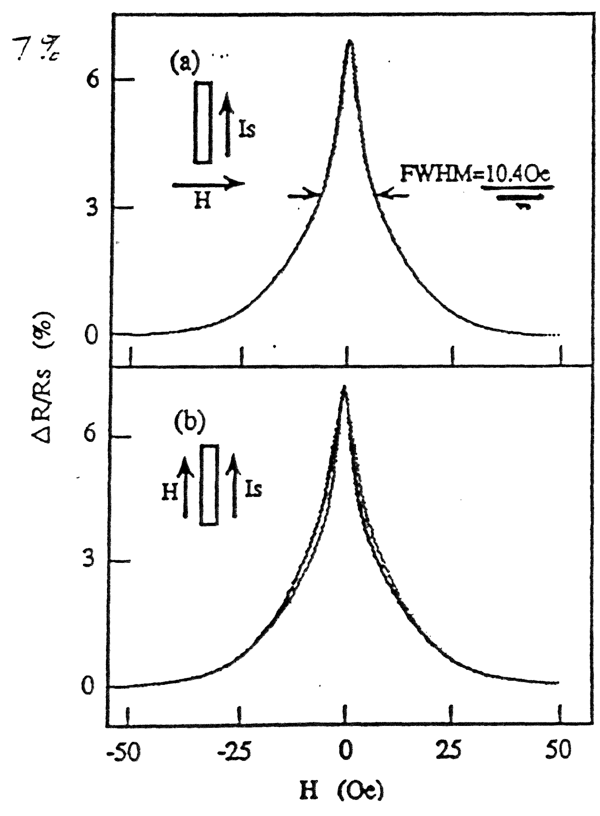

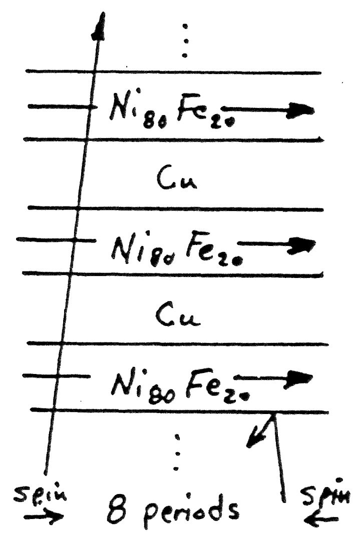

Fig. 2 MR curves for a NiFe(Ni/Fe/Cu)x/NiFe multilayer.

sensor materials: discontinuous multilayers

7058 J. Appl. Phys. 75 (10), 15 May 1994

Low field giant magnetoresistance in discontinuous magnetic multilayers

T. L. Hylton, K. R. Coffey, M. A. Parker, and J. K. Howard
IBM AdStar, San Jose, California 95193

Giant magnetoresistance of order 4%–6% has been observed in fields of 5–10 Oe at room temperature in annealed multilayers of $Ni_{80}Fe_{20}$/Ag prepared by magnetron sputtering. For a wide range of NiFe and Ag thicknesses, no giant magnetoresistance was observed in the unannealed films. We attribute the appearance of giant magnetoresistance to a magnetostatic interlayer interaction that promotes antiparallel order of the moments in adjacent layers fostered by a breakup of the NiFe layers. We discuss the effects of variations in the underlayers, spacer thickness, and the sputtering process on the magnetoresistance. Our results suggest that maximizing magnetoresistance and minimizing hysteresis require samples with continuous Ag layers that prevent contact between the NiFe layers and NiFe layers that are discontinuous but not too severly disrupted.

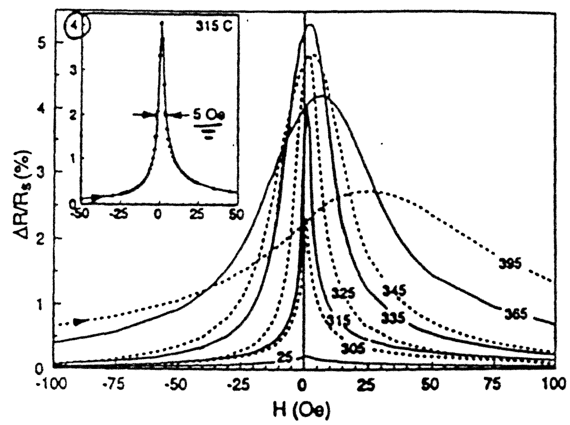

FIG. 1. $\Delta R/R_s$ vs H for a sample Ta(100 Å)/Ag(20 Å)/[NiFe(20 Å)/Ag(40 Å)]$_4$/NiFe(20 Å)/Ag(20 Å)/Ta(40 Å)/SiO2(700 Å)/Si. The field is in the plane of the sample and perpendicular to the current. Arrows indicate the ramping direction of the field. Unannealed samples show only a small AMR effect, but for annealing temperatures above 300 °C, a large GMR effect is evident. Large sensitivities of order 0.8%/Oe are achieved in the sample annealed at 315 °C (inset).

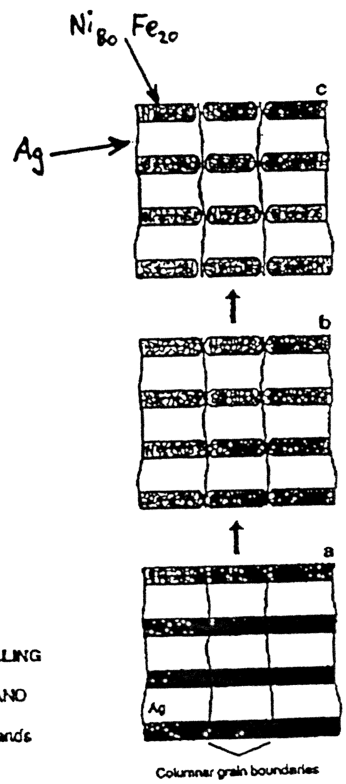

GIANT MAGNETORESISTANCE AND STRUCTURAL STUDY OF PERMALLOY/SILVER MULTILAYERS DURING RAPID THERMAL ANNEALING

F. ROOZEBOOM, L GIDEONSE*, J.P.W.B. DUCHATEAU, D.G. NEERINCK AND H.T. MUNSTERS
Philips Research, Professor Holstlaan 4, NL-5656 AA Eindhoven, The Netherlands
* University of Groningen, The Netherlands.

77
Mat. Res. Soc. Symp. Proc. Vol. 342. ©1994 Materials Research Society

sensor materials: spin valve

IEEE TRANSACTIONS ON MAGNETICS, VOL. 30, NO. 6, NOVEMBER 1994 3813

Application of Giant Magnetoresistive Elements in Thin Film Tape Heads

W. Folkerts, J.C.S. Kools, Th.G.S.M. Rijks, R. Coehoorn, M.C. de Nooijer,
G.H.J. Somers, J.J.M. Ruigrok and L. Postma
Philips Research, Prof. Holstlaan 4, 5656 AA Eindhoven, The Netherlands

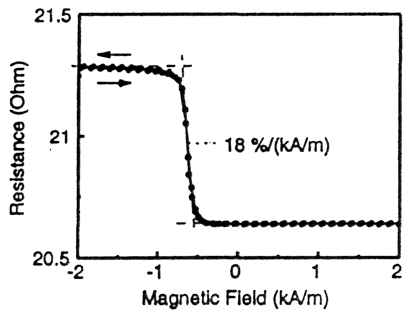

IEEE TRANSACTIONS ON MAGNETICS, VOL. 30, NO. 6, NOVEMBER 1994

Magnetoresistance of Symmetric Spin Valve Structures

3819

Thomas C. Anthony and James A. Brug
Hewlett-Packard Laboratories, 1501 Page Mill Road, Palo Alto, CA 94304

Shufeng Zhang
Department of Physics, New York University, 4 Washington Place, New York, NY 10003

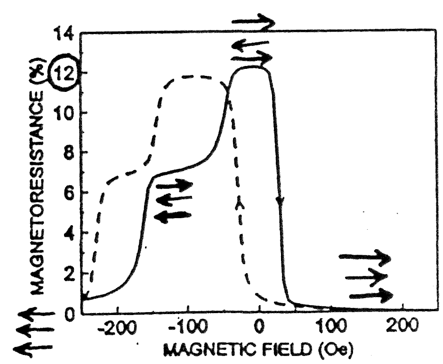

Fig. 5. R-H curve from NiO(75)/NiFe(30)/Co(20)/Cu(34)/Co(20)/NiFe(25)/Co(20)/Cu(24)/Co(20)/NiFe(30)/MnFe(150)/NiFe(20Å) symmetric spin valve with field applied parallel to easy axis.

IBM Almaden Research Center

Bruce A. Gurney

3822 IEEE TRANSACTIONS ON MAGNETICS, VOL. 30, NO. 6, NOVEMBER 1994

Micromagnetics of GMR Multilayer Sensors at High Current Densities

Neil Smith
Imaging Research and Development, San Diego Laboratories, Eastman Kodak Company, San Diego CA 92121

implications of $j(x)$ for sensors: multilayers

reduced signal at high (but necessary) current density

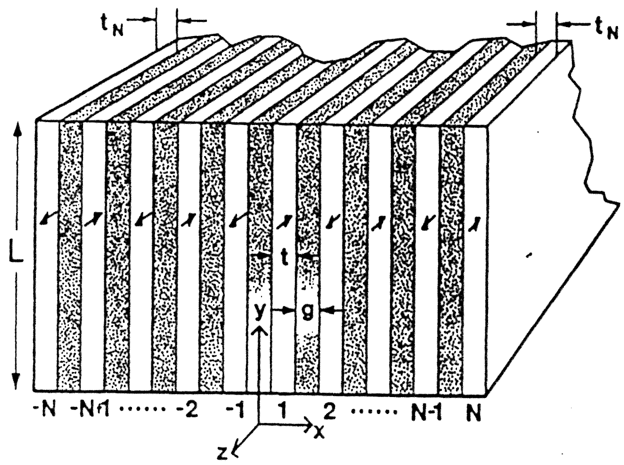

Fig. 1. Pictorialization of a GMR multilayer stripe in antiferromagnetic ground-state. Clear (shaded) are magnetic (nonmagnetic) conducting layers.

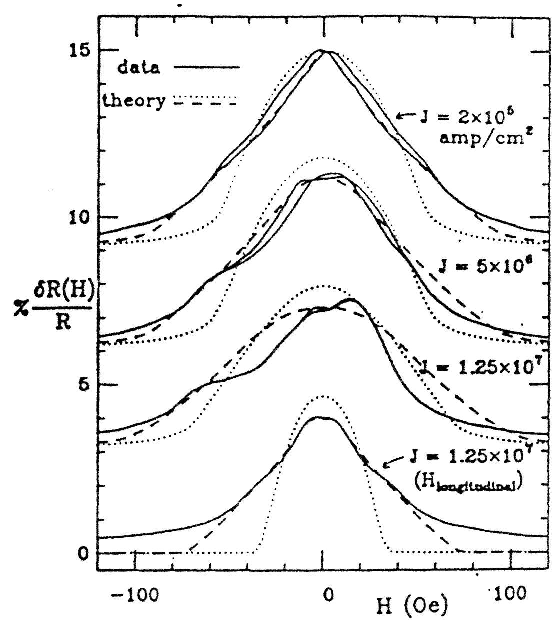

Fig. 3. Comparison of experimental (solid) and theoretical $\delta R(H)/R$ curves at current density, J, indicated. For theory, $H_{bqc} = 0$ (dotted), or $H_{bqc} = H_{afc}$ (dashed). Curves for each J are shifted vertically by 3% $\delta R/R$.

IEEE TRANSACTIONS ON MAGNETICS, VOL. 30, NO. 6, NOVEMBER 1994 3825

Size and Self-Field Effects in Giant Magnetoresistive Thin-Film Devices

R. William Cross, S. E. Russek, and S. C. Sanders, et al.
Electromagnetic Technology Division, National Institute of Standards and Technology
Boulder, Colorado 80303

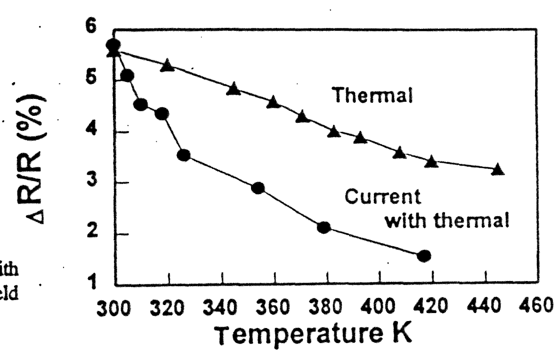

Fig. 4. Plots ΔR/R as a function of temperature for a NiCoFe/Cu device with a 6 × 6 μm active area. The difference between the curves is the self-field effect..

temperature effects in spin valves

Temperature dependence of magnetoresistance in spin valves with different thicknesses of NiO

Chih-Huang Lai, Thomas J. Regan,[a] and Robert L. White
Department of Materials Science and Engineering, Stanford University, Stanford, California 94305

Thomas C. Anthony
Hewlett Packard Research Laboratories, 1501 Page Mill Road, Palo Alto, California 94304

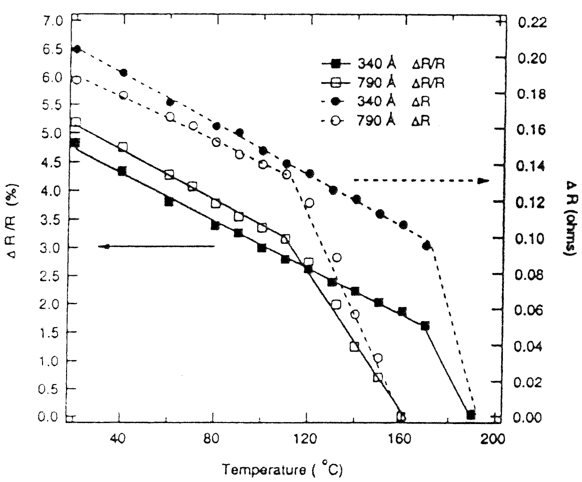

FIG. 1. Temperature dependence of $\Delta R/R$ and ΔR for spin valves with structure 340 and 790 Å NiO/60 Å NiFe/30 Å Cu/80 Å NiFe/50 Å Ta.

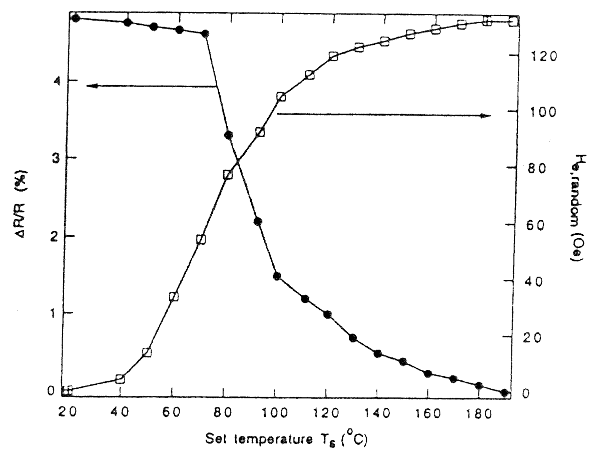

FIG. 3. Temperature dependence of $\Delta R/R$ and $H_{e,\mathrm{random}}$ for the 340 Å NiO sample, measured at room temperature after the samples were cooled in a perpendicular ac field from set temperatures T_s.

3990 J. Appl. Phys., Vol. 81, No. 8, 15 April 1997

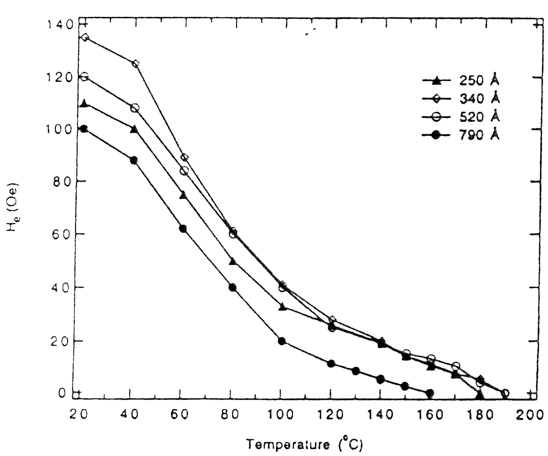

FIG. 2. Temperature dependence of the exchange field H_e for various thicknesses of NiO.

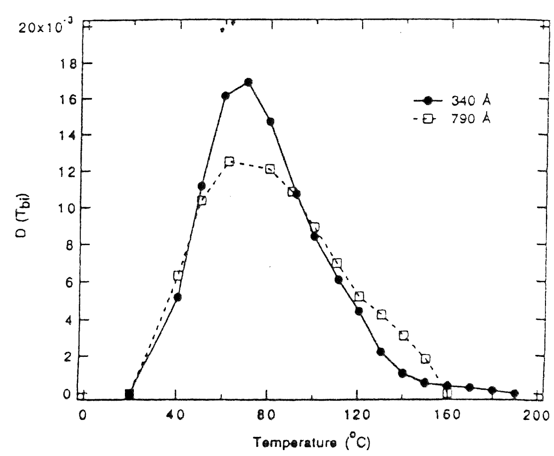

FIG. 4. The exchange path distribution, $D(T_{bi})$, of the 340 and 790 Å NiO samples.

can spin valves be reliably deposited?

Can spin valves be reliably deposited for magnetic recording applications? (invited)

Bruce A. Gurney, Virgil S. Speriosu, Dennis R. Wilhoit, Harry Lefakis,
Robert E. Fontana, Jr., David E. Heim,[a] and Moris Dovek
IBM Research Division, Almaden Research Center, 650 Harry Road, San Jose, California 95120

The tolerance of the expected read-back signal of spin valve giant magnetoresistance based structures to varying deposition and process conditions are described. We determine if spin valves can be produced reliably, and evaluate which thicknesses and properties are most critical. First, the dependence of spin valve properties on layer thickness are experimentally determined. Next, the variation of read-back signal and transfer curve characteristics with spin valve properties is calculated from micromagnetic modeling. Finally, these are convolved with the expected reproducibility of layer thickness to obtain an effective "yield" of structures within 10% of the mean amplitude. We find that spin valves can be reliably deposited, with "yields" well in excess of 90% likely. [S0021-8979(97)67908-6]

$$\Delta V = i\left(\frac{\Delta R}{R}\right)_0 R_\square \frac{L}{h} \frac{\langle\cos(\theta_{\text{free}} - \theta_{\text{pinned}}\rangle}{2}.$$

$$\frac{\partial(\widehat{\delta V})}{\partial \hat{t}_l} = \sum_k \left(\frac{\partial \hat{P}_k}{\partial \hat{t}_l}\right)_0 \left(\frac{\partial(\widehat{\delta V})}{\partial \hat{P}_k}\right)_0 \equiv \sum_k T_{kl} S_k.$$

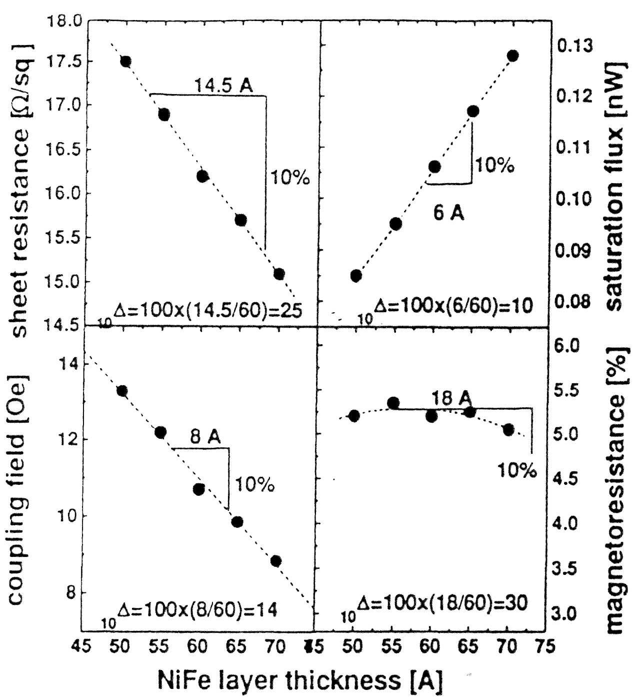

FIG. 3. Dependence of the magnetoresistance, sheet resistance, coupling field, and saturation flux on the free layer thickness for a 50 Å Ta/t NiFe/25 Å Cu/24 Å Co/150 Å FeMn/50 Å Ta spin valve.

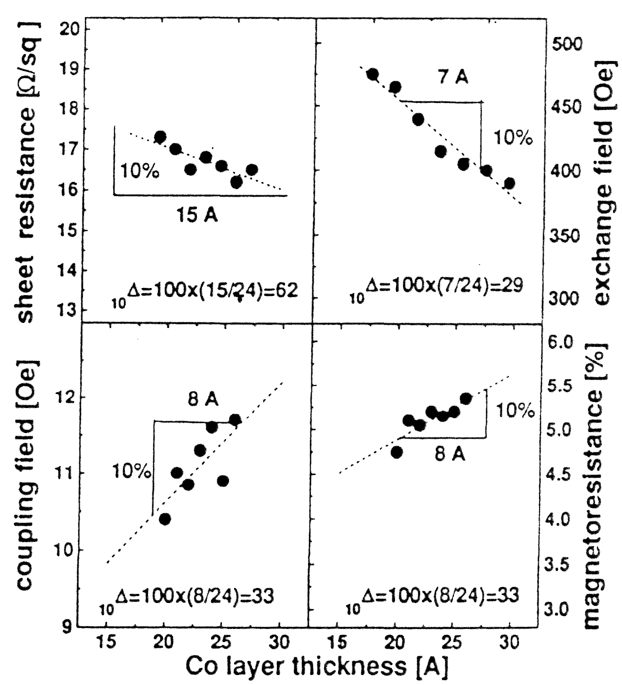

FIG. 4. Dependence of the magnetoresistance, coupling field, and exchange field on the pinned layer thickness for a 50 Å Ta/60 Å NiFe/25 Å Cu/t Co/150 Å FeMn/50 Å Ta spin valve.

can spin valves be reliably deposited?

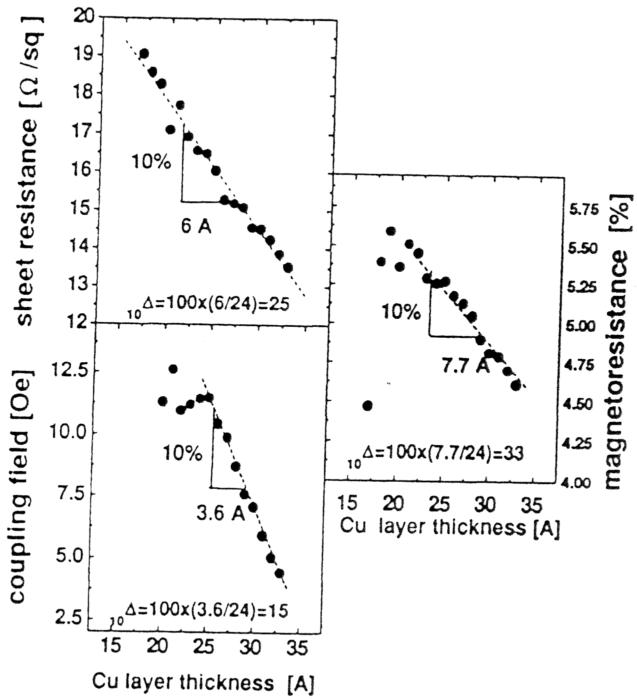

FIG. 5. Dependence of the magnetoresistance, coupling field, and sheet resistance on the spacer layer thickness for a 50 Å Ta/60 Å NiFe/t Cu/24 Å Co/150 Å FeMn/50 Å Ta spin valve.

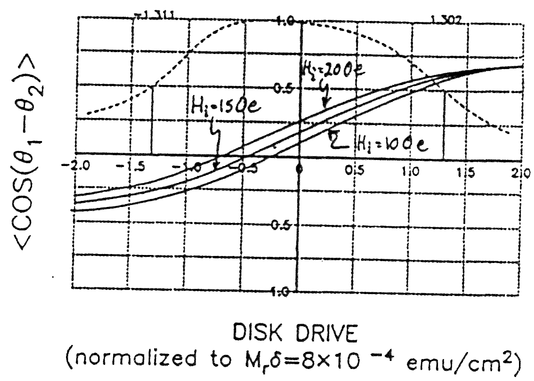

FIG. 6. Transfer curves calculated for different values of the interlayer coupling field.

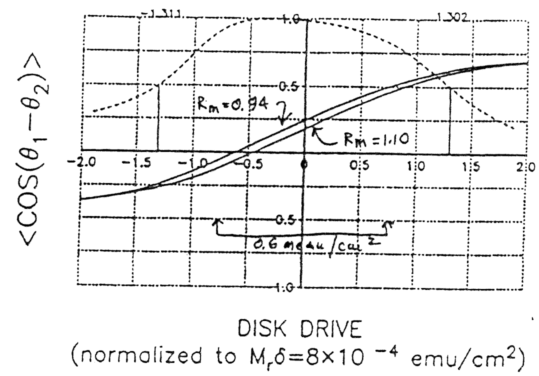

FIG. 7. Transfer curves calculated for different ratios of the pinned to free layer moment.

$$\sigma(\widehat{\delta V}) = \sqrt{\sum_l \left(\frac{\partial(\widehat{\delta V})}{\partial \hat{t}_l}\right)^2 (\sigma \hat{t}_l)^2}.$$

TABLE I. Process sensitivity $_{10}\Delta$ and signal sensitivity S for a spin valve. na=not applicable. † depends on strain in head.

Property P	Process sensitivity ($_{10}\Delta$) free	spacer	pinned	FeMn	Signal Sensitivity (S)	design criterion
Magnetostriction	8	na	na	na	0†	$0<\lambda_s<-2\times10^{-6}$
Magnetoresistance	−30	−33	33	−25	1	>3.5%
Resistance	−25	−25	−62	−33	1	⩾15 Ω/□
Free layer moment	10	na	na	na	−1	50 Å
pinned layer moment	na	na	10	na	0.25	50 Å
Coupling field	−14	−15	33	na	−0.15	$9<H_i<13$ Oe
Exchange bias field	na	na	−29	30	0.2	>200 Oe
Uniaxial anisotropy field	−20	na	na	na	−0.05	<5 Oe

$$_{10}\Delta_{kl} \equiv (10T_{kl})^{-1}$$

$$\sigma(\widehat{\delta V}) = 0.0331. \tag{12}$$

Taking as a quality criterion that a 10% or larger deviation from the mean signal amplitude would be considered an unsuccessful deposition these results suggest that over many runs 99.7% (corresponding to 3.0σ) of the spin valve depositions will yield high signal spin valve sensor materials.

recovery of spin valves from thermal destabilization

Improvement of thermal stability and magnetoresistance recovery of $Tb_{25}Co_{75}$ biased spin-valve heads

N. J. Oliveira,[a] J. L. Ferreira,[a] J. Pinheiro,[a] A. M. Fernandes, O. Redon, S. X. Li, P. ten Berge,[b] T. S. Plaskett, and P. P. Freitas[a]
INESC, R. Alves Redol 9-1, 1000 Lisboa, Portugal

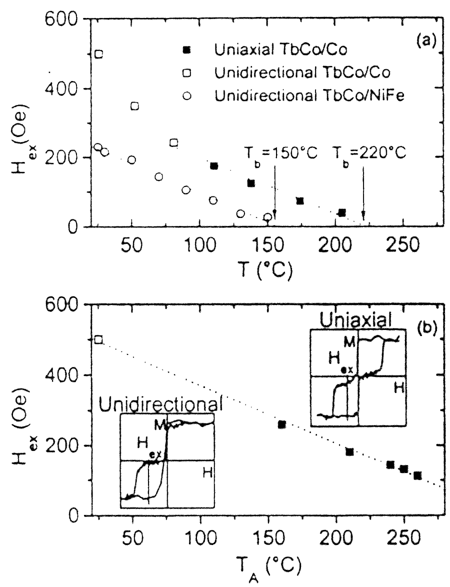

FIG. 1. H_{ex} as a function of temperature, (a) TbCo/Co and TbCo/NiFe measured at temperature, and (b) TbCo/Co measured at RT after annealing.

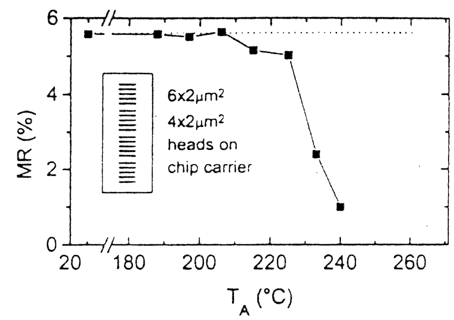

FIG. 2. Average MR of the unshielded sensors as a function of anneal temperature. The dashed line corresponds to a single domain micromagnetic model.

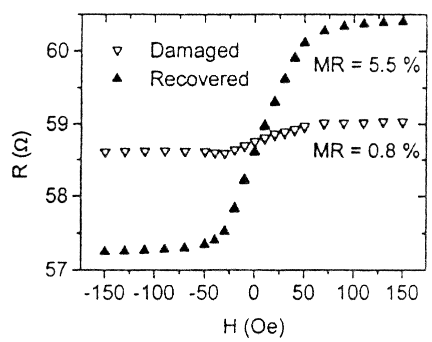

FIG. 3. Transfer curve of 6×2 μm^2 sensor during anneal/field recovery treatment.

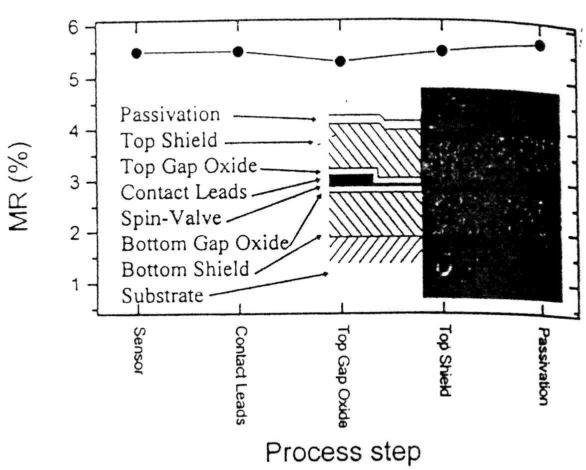

FIG. 4. The effect of wafer processing on the MR signal of test structures. Inset shows a schematic of the structures and SEM of the tape bearing surface.

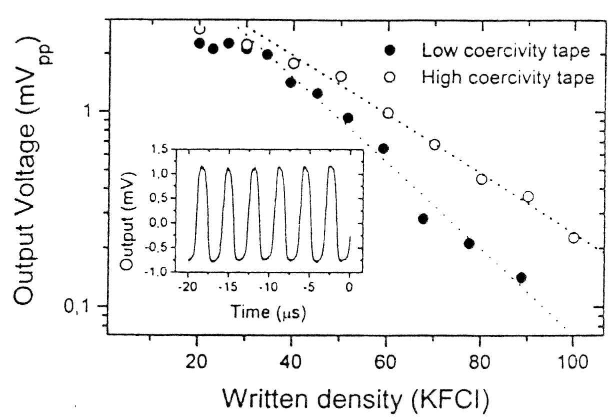

FIG. 5. Rolloff properties of a 10×2 μm^2 prototype head measured on 900 Oe tape. Inset shows the output voltage at 20 kfci.

electrostatic discharge and spin valves

Electrostatic discharge sensitivity of giant magnetoresistive recording heads

Albert J. Wallash[a)]
Quantum Corporation, 500 McCarthy Boulevard, Milpitas, California 95035

Young K. Kim[b)]
Quantum Corporation, 1450 Infinite Drive, Louisville, Colorado 80028

In this article electrostatic discharge (ESD) damage to giant magnetoresistive (GMR) recording heads is studied for the first time. The ESD failure threshold was measured using an extremely short duration (1 ns) metal contact ESD transient. The failure energy required to melt the GMR recording head was 2.3 nJ, about half of the 5 nJ of energy needed to melt a conventional anisotropic magnetoresistive (AMR) head design. Scanning electron microscope scans of ESD damaged AMR and GMR heads show localized melting of the sensors. It is concluded that recording heads with GMR sensors, planned for use in the near future, will have significantly lower ESD failure thresholds than AMR recording heads in use today. Finally, scaling arguments show that an AMR head design with the same reduced cross-sectional area of the GMR head has a comparable ESD failure threshold. [S0021-8979(97)33108-9]

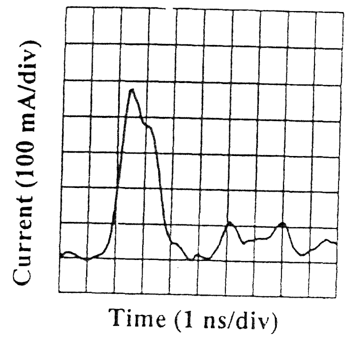

FIG. 2. ESD current transient when an MR input was grounded with a plate voltage of 150 V.

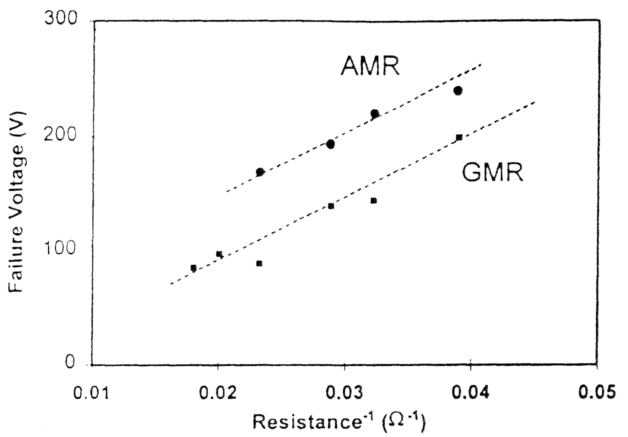

FIG. 4. Failure voltage as a function of inverse initial resistance. Note linear relationship between voltage and 1/resistance as predicted by Eq. (1).

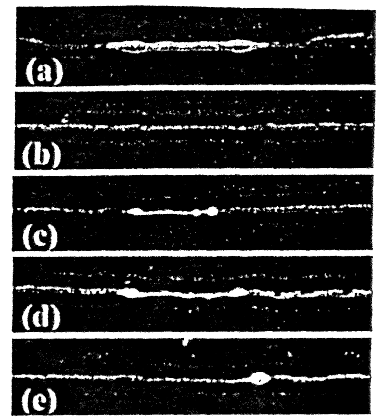

FIG. 5. SEM pictures of field-induced metal contact ESD damage to MR heads: (a) AMR head; (b)–(e) GMR heads.

$$I_{\text{melt}} = hd(C_p \rho_m \Delta T_m / \rho_e t)^{1/2},$$

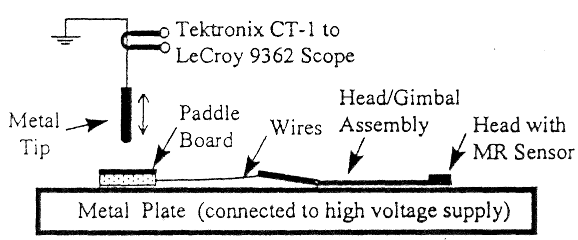

FIG. 1. Schematic representation of setup used to produce metal contact ESD transients.

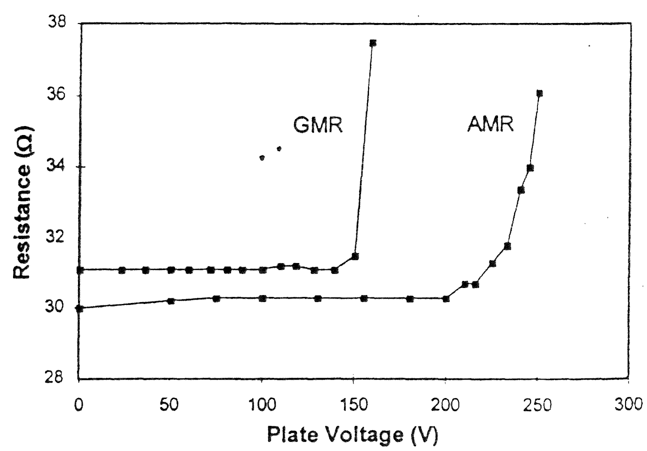

FIG. 3. Typical resistance behavior as a function of plate voltage for AMR and GMR heads.

corrosion and spin valves

Effect of corrosion on magnetic properties for FeMn and NiO spin valves

S. L. Burkett,[a] S. Kora, J. L. Bresowar,[b] J. C. Lusth, B. H. Pirkle,[c] and M. R. Parker[d]
The Center for Materials for Information Technology, The University of Alabama, Tuscaloosa Alabama 35487-0209

stored in a Tenney environmental chamber set at 60 °C and 90% relative humidity.

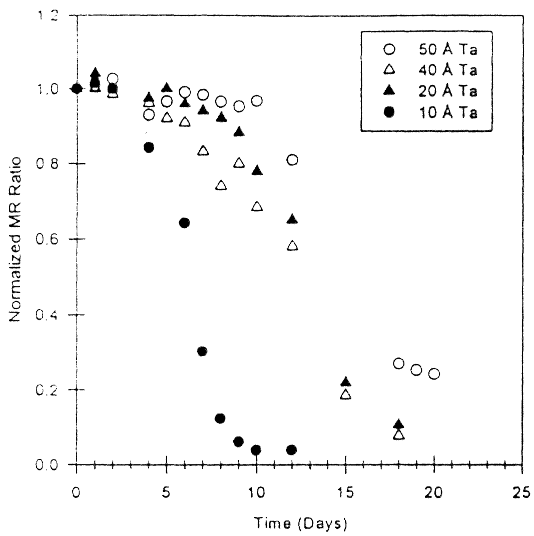

FIG. 1. Normalized MR ratio vs time in chamber for FeMn spin valves.

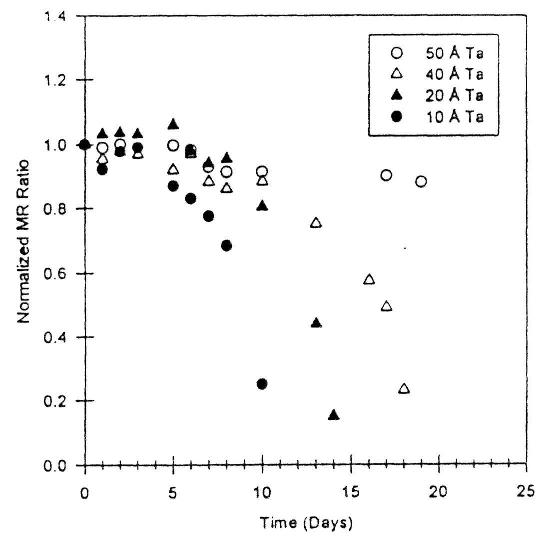

FIG. 3. MR ratio vs time in chamber for FeMn spin valves with epoxy coated edges.

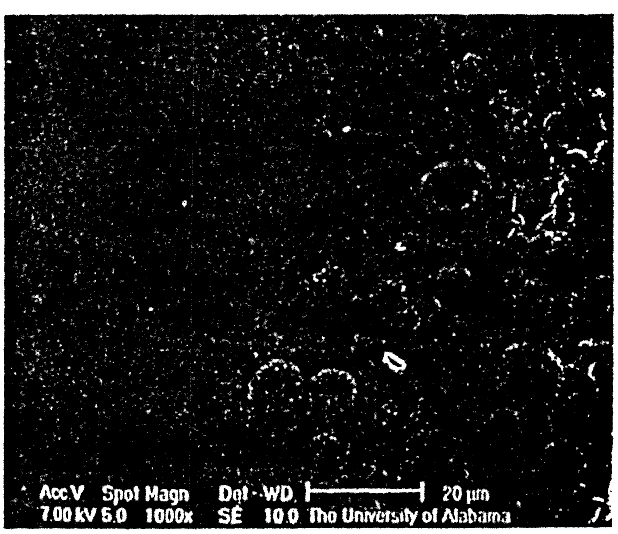

FIG. 4. SEM micrograph (spin-valve edge at far right) of FeMn after 4 days in chamber.

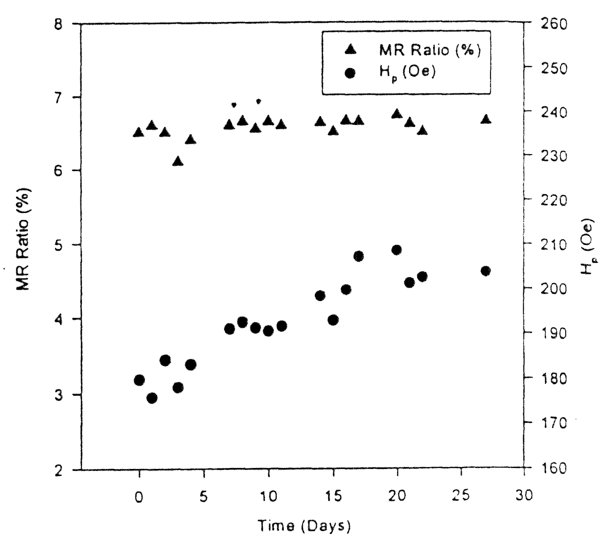

FIG. 6. MR ratio and H_p vs time in chamber for NiO spin valves.

4912 J. Appl. Phys. **81** (8), 15 April 1997

magnetic viscosity in spin valves

Magnetic viscosity effects in the giant magnetoresistance of NiO/Permalloy/Cu/Permalloy exchange-biased films

J. B. Restorff, M. Wun-Fogle, and S. F. Cheng
Carderock Division, Naval Surface Warfare Center, Code 684, 9500 MacArthur Boulevard, West Bethesda, Maryland 20817-5700

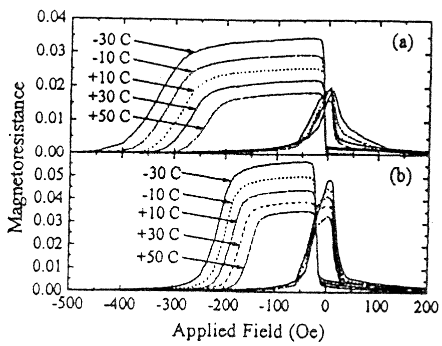

FIG. 1. Magnetoresistance as a function of field of the spin-valve structures: (a) NiO/Permalloy (45 Å)/Cu (45 Å)/Permalloy (45 Å) (sample A); (b) NiO/Permalloy (45 Å)/Co (6 Å)/Cu (45 Å)/Co (6 Å)/Permalloy (45 Å) (sample B). The data were taken by the stepped field method.

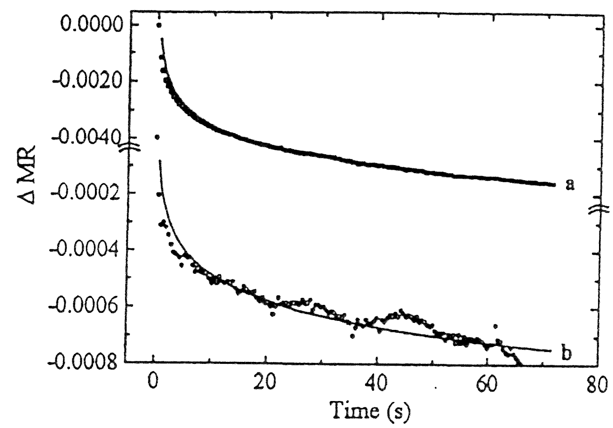

FIG. 3. An example of fits of the time dependent MR measurements to $C+S\ \ln(t)$. Curves a and b are for large ΔMR and small ΔMR, respectively. This data is for sample A; sample B is similar. The open symbols represent the data points and the solid lines represent the fits.

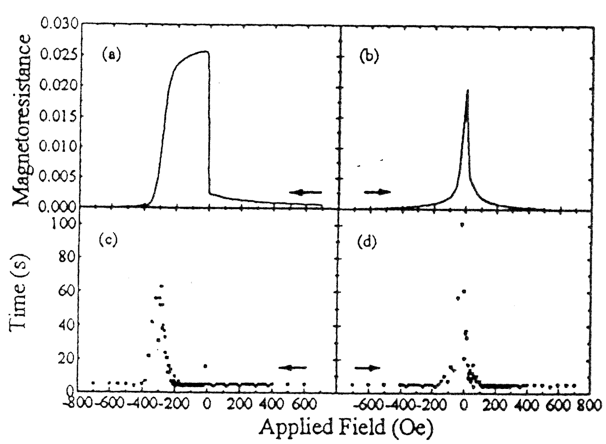

FIG. 2. Magnetoresistance and corresponding stabilization time vs field for NiO/Permalloy (45 Å)/Cu (45 Å)/Permalloy (45 Å) (sample A) at +10 °C. In (a) and (c) measurements were taken from +700 to −700 Oe and in (b) and (d) from −700 to +700 Oe. The data were taken by the stepped field method.

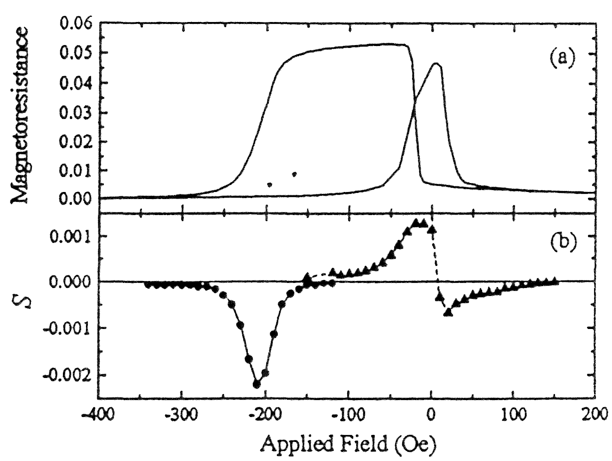

FIG. 4. Magnetoresistance vs H and coefficient of magnetic viscosity S vs H for sample B [NiO/Permalloy (45 Å)/Co (6 Å)/Cu (45 Å)/Co (6 Å)/Permalloy (45 Å)]. The S's associated with the broad maximum on the left are denoted by circles; the S's associated with the narrow maximum are denoted by triangles. The data were taken by the time-dependent method.

spin valve head

IEEE TRANSACTIONS ON MAGNETICS, VOL. 30, NO. 6, NOVEMBER 1994

Design, Fabrication & Testing of Spin-Valve Read Heads for High Density Recording

Ching Tsang, Robert E. Fontana, Tsann Lin*, D. E. Heim*,
Virgil S. Speriosu, Bruce A. Gurney & Mason L. Williams
IBM Research Division,
IBM Advanced Magnetic Recording Laboratory,
Almaden Research Center, 650 Harry Road, San Jose, CA 95120-6099
*IBM Storage Systems Division

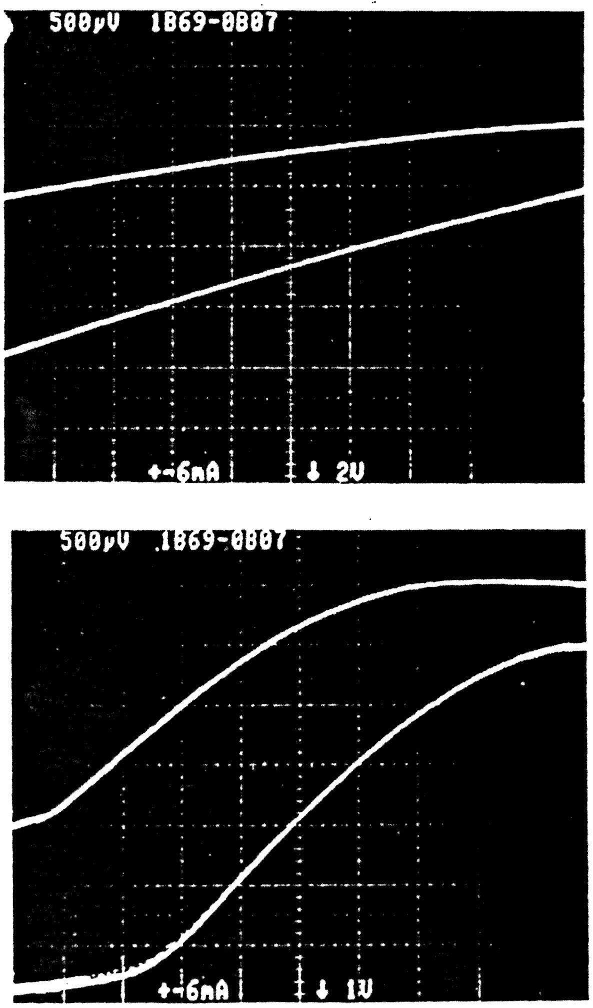

Fig. 5. Experimental low field (±100 Oe) and high field (±350 Oe) transfer curves of spin-valve read head.

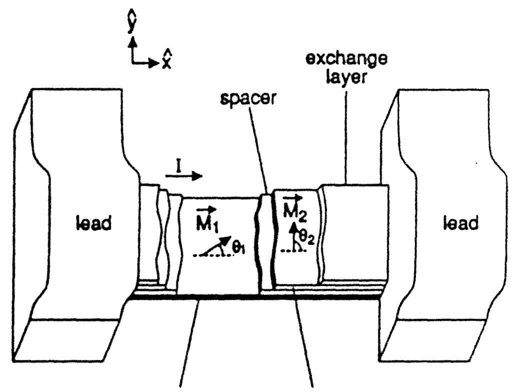

Fig. 1. Schematic of a spin-valve sensor (M: magnetic moment, θ: angle from the longitudinal direction).

4 Electronics Now, October 1994

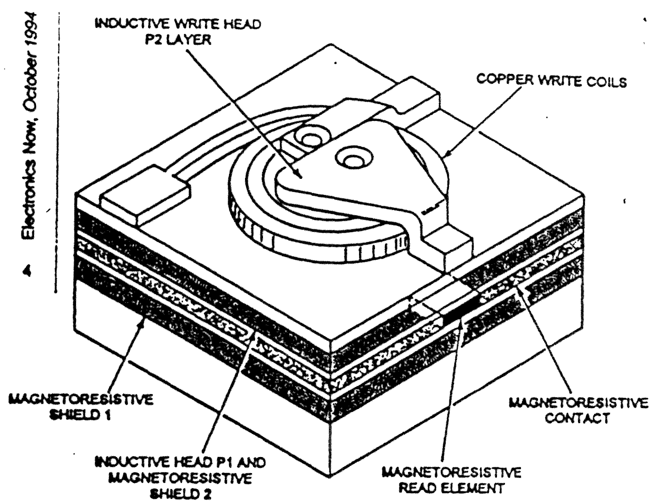

IBM's SPIN VALVE MAGNETORESISTIVE HEAD should permit disk drives with storage densities nearly 20 times what is possible today.

spin valve head

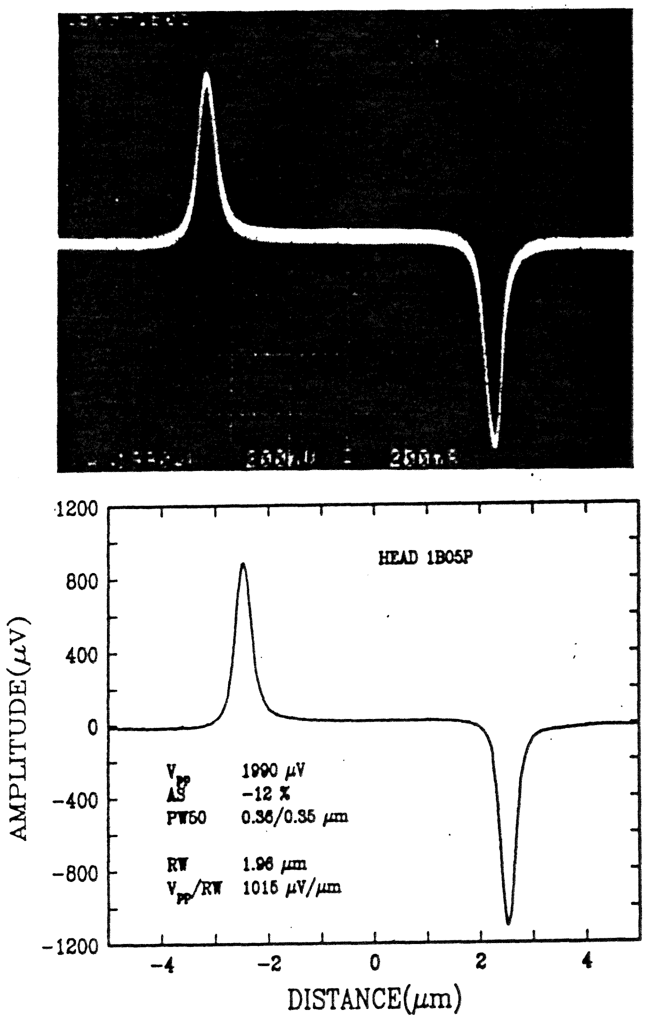

Fig. 6. Real-time (a) and Averaged (b) readback waveform of spin-valve head on CoCrPt disk.

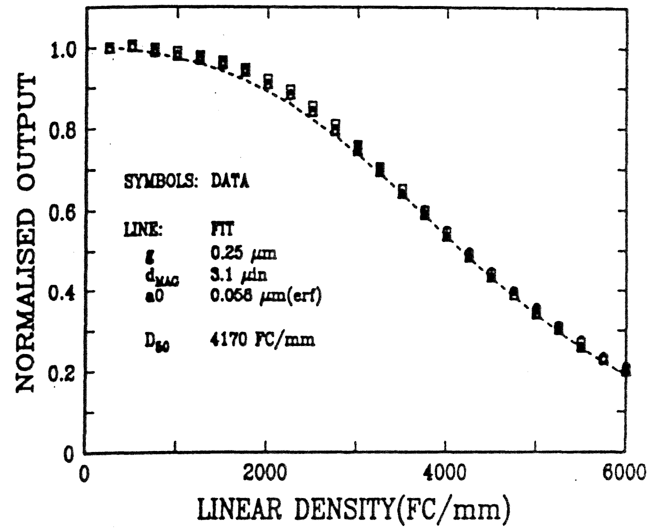

Fig. 8. Experimental and theoretical rolloff curves of the spin-valve read heads.

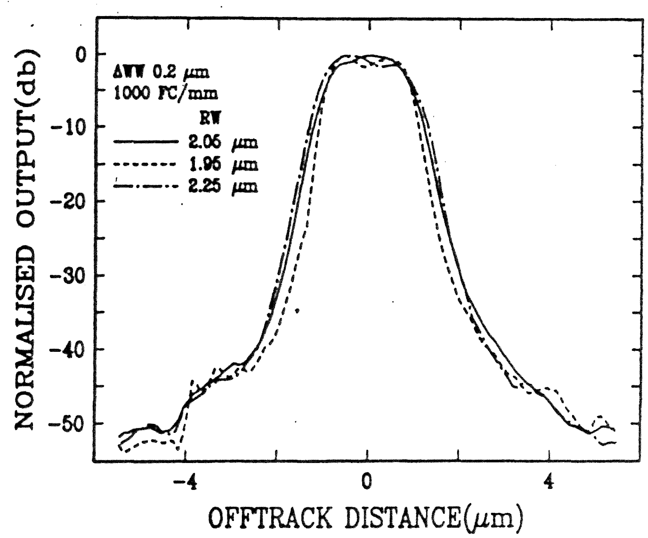

Fig. 9. Microtrack profiles of the spin-valve read heads.

Ultra-High Density Head Demonstrated[6]

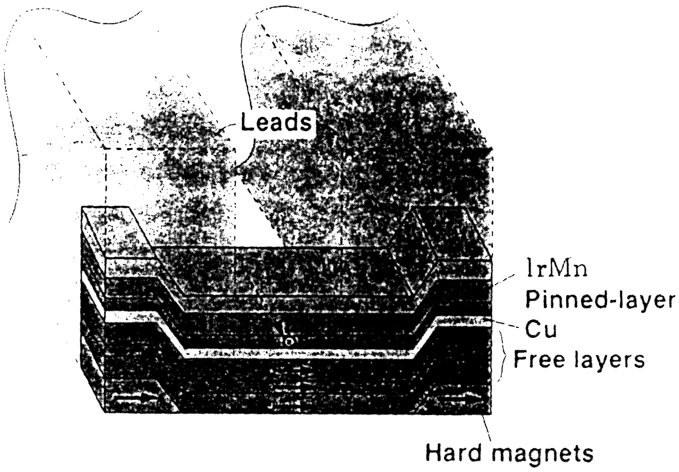

Fig. 1 Structure of the spin-valve element

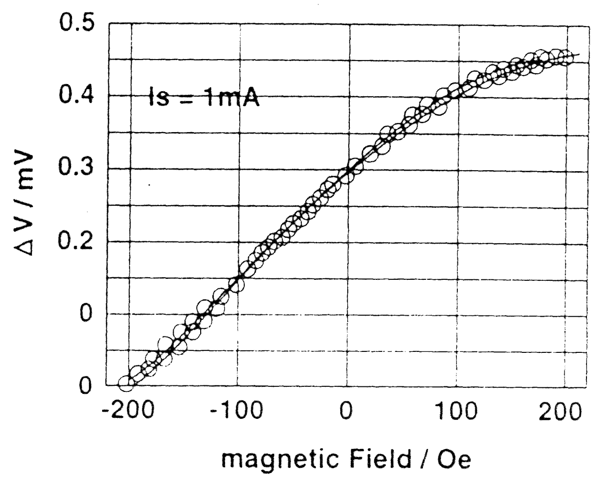

Fig. 3 Transfer curve

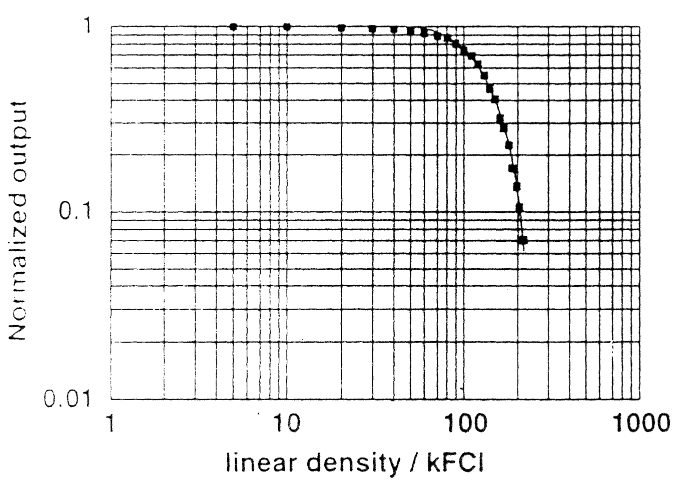

Fig. 9 Roll off curve

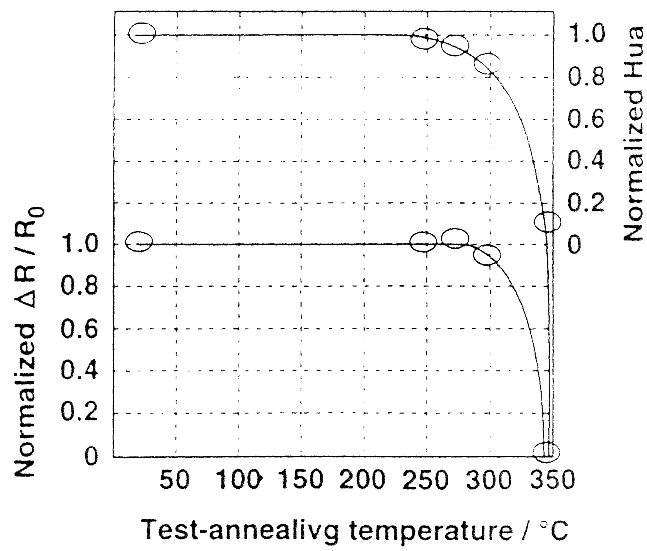

Fig. 4 Thermal Stability of CoFe Spin-valves

[6] H. Yoda, et al., IEEE Trans. Mag. 32, 3363 (1996)

GMR field sensors

GMR Materials for Low Field Applications

J. M. Daughton and Y. J. Chen
Nonvolatile Electronics, Inc.,
Plymouth, MN 55441, USA

IEEE TRANSACTIONS ON MAGNETICS, VOL. 29, NO. 6, NOVEMBER 1993

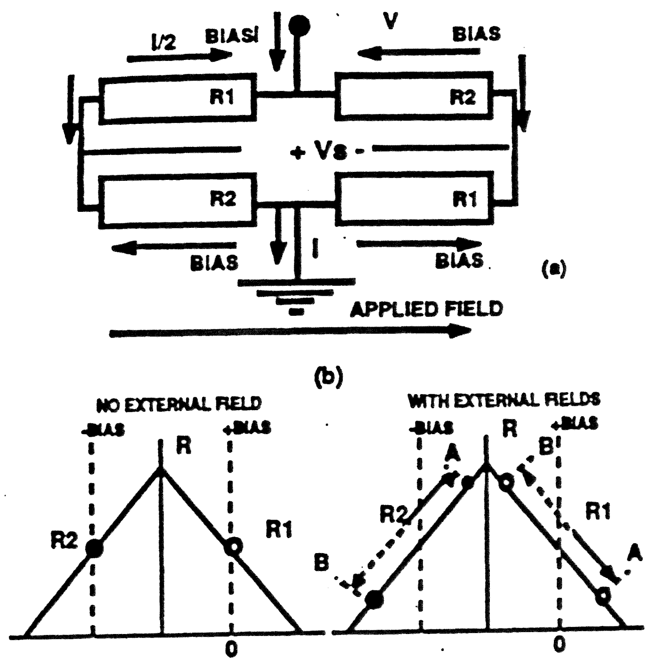

Fig. 3. GMR Bridge Field Sensor.

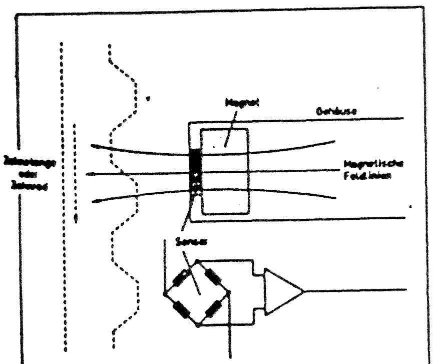

Bild 2. Die vorbeilaufenden Zähne verformen die magnetischen Feldlinien und verändern so die Flußdichte in der magnetoresistiven Schicht.

Dr. Volker Graeger
Dipl.-Phys. August Petersen

Magnetoresistiver Drehzahlsensor – zuverlässig und preiswert

Elektronik 24/1992

IBM Almaden Research Center

Bruce A. Gurney

GMR non-volatile memories

IEEE TRANSACTIONS ON MAGNETICS, VOL. 29, NO. 6, NOVEMBER 1993

GMR Materials for Low Field Applications

J. M. Daughton and Y. J. Chen
Nonvolatile Electronics, Inc.,
Plymouth, MN 55441, USA

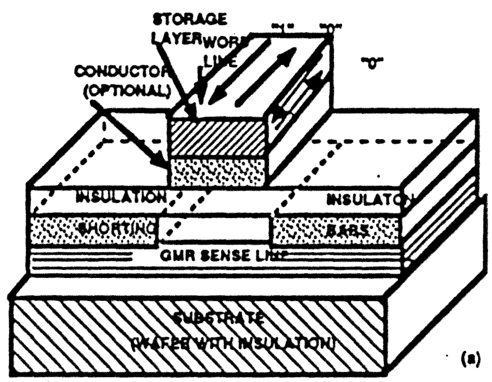

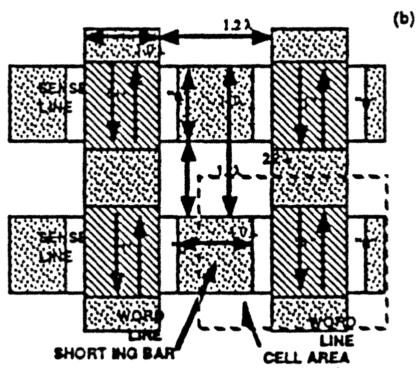

Fig. 5. Dense MRAM Cells.

Fig. 5(b) is an areal view of a 2x2 array of nanometer MRAM cells showing a cell area of 4.84 λ^2, where λ is the resolution limit of the lithography used to fabricate the memory cells. This compares with more than 10 λ^2 for minimum-size Dynamic Random Access Memory (DRAM) cells. MRAM potentially can be at least twice as dense, and will have an even greater density advantage as λ becomes smaller than 200 nm unless there is significant progress in capacitor technology used for DRAMs. With GMR materials for sensing, the read access times of MRAM will be comparable to semiconductor memories.

What's Hot: Colossal MR[8]

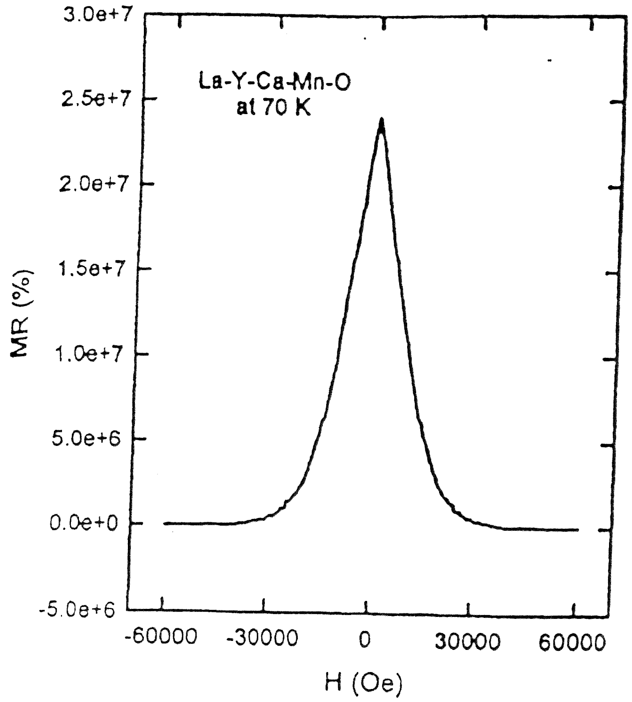

Fig. 1. Resistivity vs field curve for the La-Y-Mn-O film at 70 K (H_{max} = 6T).

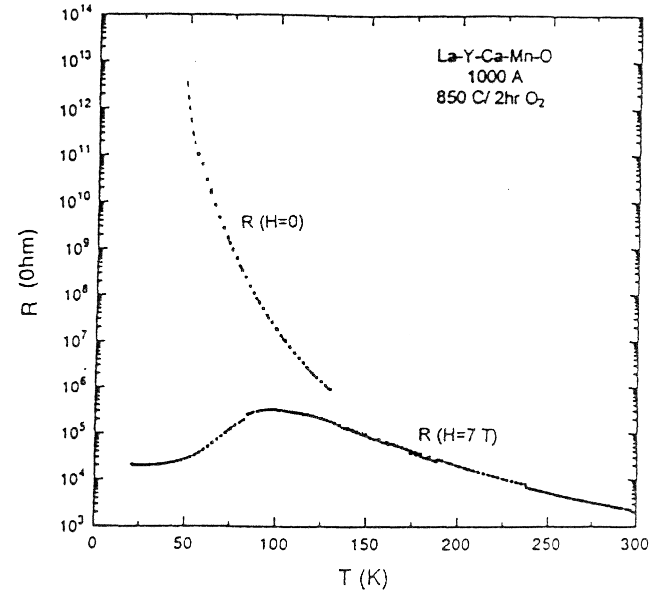

Fig. 2. Temperature dependence of resistance for the La-Y-Ca-Mn-O film at H = 0 and H = 7T, respectively.

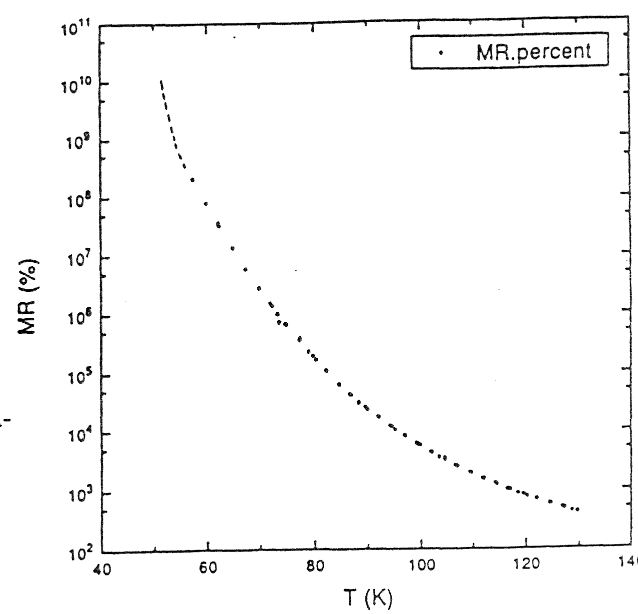

Fig. 3. MR value vs temperature curve for the La-Y-Ca-Mn-O film.

[8] T.H. Tiefel, et al., IEEE Trans. Mag. 32, 4692 (1996)

colossal magnetoresistance (CMR)

Magnetic field induced properties of manganite perovskites with colossal magnetoresistance (invited)

Gang Xiao, G. Q. Gong, and C. L. Canedy
Department of Physics, Brown University, Providence, Rhode Island 02912

E. J. McNiff, Jr.
Francis Bitter National Magnet Laboratory, Massachusetts Institute of Technology, Cambridge, Massachusetts 02139

A. Gupta
IBM T. J. Watson Research Center, Yorktown Heights, New York 10598

We present a systematic study of the magnetotransport and magnetic properties of the half-doped $La_{0.5}Ca_{0.5}MnO_{3+\delta}$ system. The solid is a metamagnet which undergoes a first-order antiferromagnet (AFM) to ferromagnet (FM) phase transition under a field or by changing temperature. Associated with the AFM–FM transition is an insulator to metal transition. A maximum 10^9-fold magnetoresistance ratio has been observed at 4.2 K between the least and the most conductive states. At low T ($\leq$50 K), we have also observed two additional metastable electronic states in the canted AFM state at certain fields. The resistivity of each state differs from one another by at least one order of magnitude. The existence of these multiple states may be related to the unique charge- and spin-ordered state of the half-doped manganite. © *1997 American Institute of Physics.* [S0021-8979(97)72008-5]

5324 J. Appl. Phys. 81 (8), 15 April 1997

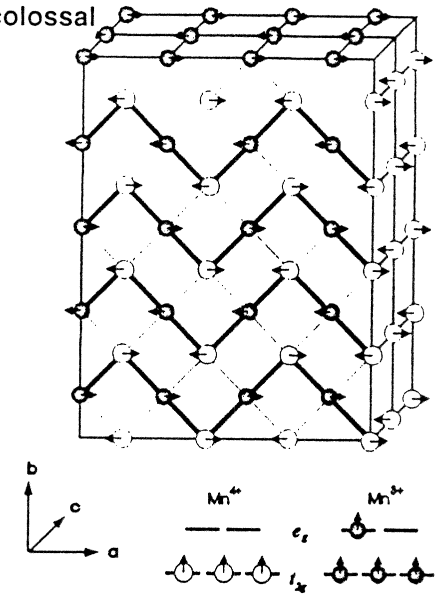

FIG. 3. The charge and spin ordering structure of $La_{0.5}Ca_{0.5}MnO_{3+\delta}$ ($a-b$ plane). Only the Mn^{3+} and Mn^{4+} ions are marked, O^{-2} ions are located midway between the shortest Mn^{3+}–Mn^{4+} pairs. The highlighted zigzag chains consist of alternating Mn^{3+} and Mn^{4+} ions whose spins are ordered ferromagnetically. The interchain coupling is of the antiferromagnetic type.

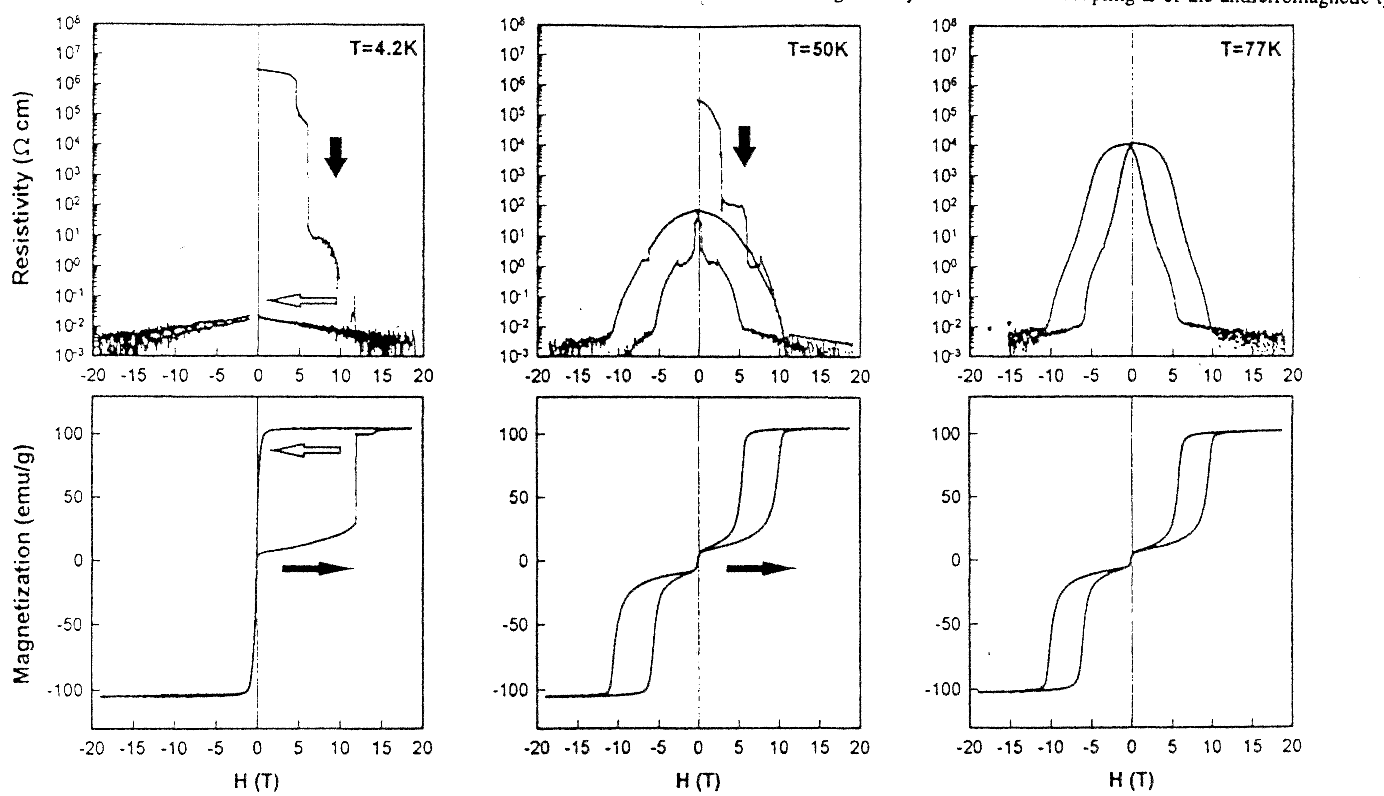

FIG. 2. Resistivity and magnetization of $La_{0.5}Ca_{0.5}MnO_{3+\delta}$ vs magnetic field at T=4.2, 50, and 77 K. For each run, the sample was cooled in zero field, and then subjected to a sweeping field sequence (see arrows): 0→19 T→0→−19 T→0→19 T.

colossal magnetoresistance (CMR)

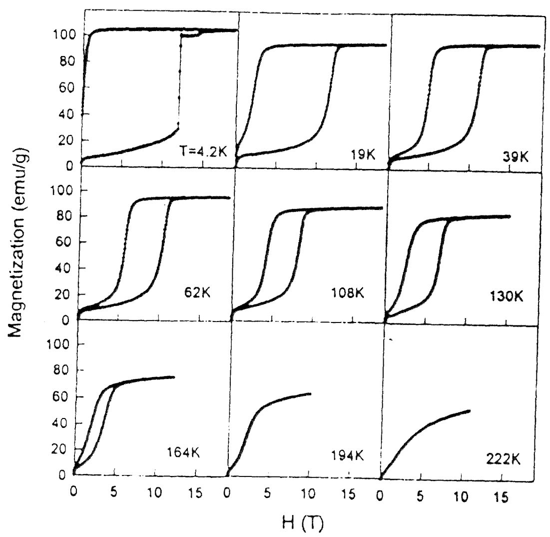

FIG. 4. Magnetization curves of $La_{0.5}Ca_{0.5}MnO_{3+\delta}$ measured at different temperatures.

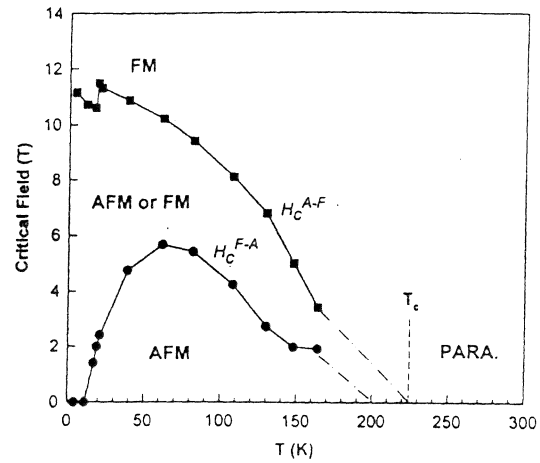

FIG. 5. Phase diagram of $La_{0.5}Ca_{0.5}MnO_{3+\delta}$ in the $H-T$ plane. H_c^{A-F} and H_c^{F-A} are critical fields for the AFM–FM and FM–AFM transitions, respectively. The magnetic transition temperature (T_c) was obtained from the susceptibility measurement.

Colossal magnetoresistance and charge order in $La_{1-x}Ca_xMnO_3$ (invited)

A. P. Ramirez and S.-W. Cheong
Bell Laboratories, Lucent Technologies, 600 Mountain Avenue, Murray Hill, New Jersey 07974

P. Schiffer
Physics Department, University of Notre Dame, Notre Dame, Indiana 46556

Double-exchange ferromagnets with their associated large magnetoresistance have recently been considered as candidates in magnetic storage applications. We review materials aspects of one compound family, $La_{1-x}Ca_xMnO_3$. There exist two distinct low temperature regimes; (i) ferromagnetic and metallic ($x<0.5$) and (ii) charge-ordered and semiconducting ($x>0.5$). We describe transport, magnetic, thermal and acoustic response in each regime. © *1997 American Institute of Physics.* [S0021-8979(97)72208-4]

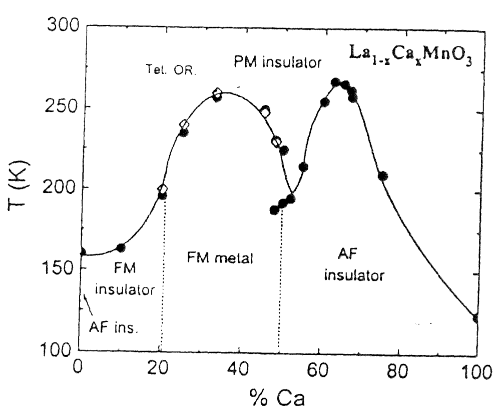

FIG. 1. The phase diagram of $La_{1-x}Ca_xMnO_3$. The transition temperatures are defined by inflection points of $M(T)$ (circles) and $\rho(T)$ (diamonds). Data for $x\approx0.5$ were taken on warming at $H=0.1$ T.

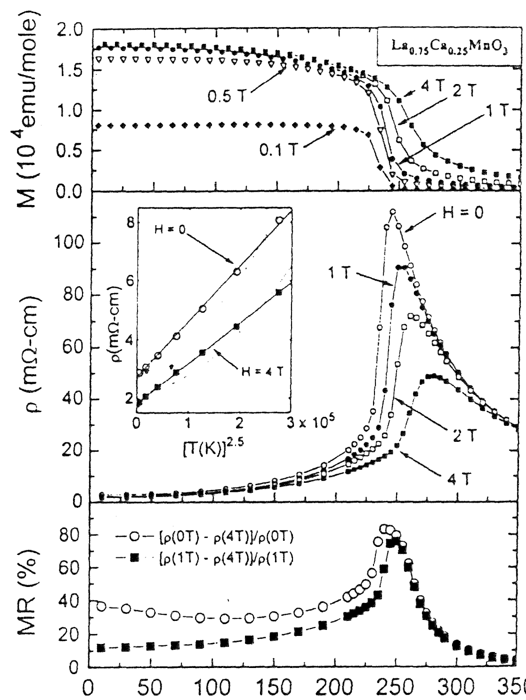

FIG. 2. The magnetization, resistivity, and magnetoresistance of $La_{0.75}Ca_{0.25}MnO_3$ as a function of temperature at various fields. Th[illegible] [illegible]set shows ρ at low temperatures; the lines are fits to the data as describ[illegible] [illegible]e text.

5338 J. Appl. Phys., Vol. 81, No. 8, 15 April 1997

What's Hot: Tunneling[7]

VOLUME 74, NUMBER 16 PHYSICAL REVIEW LETTERS 17 APRIL 1995

Large Magnetoresistance at Room Temperature in Ferromagnetic Thin Film Tunnel Junctions

J. S. Moodera, Lisa R. Kinder, Terrilyn M. Wong, and R. Meservey
Francis Bitter National Magnet Laboratory, Massachusetts Institute of Technology, Cambridge, Massachusetts 02139
(Received 29 November 1994)

Ferromagnetic-insulator-ferromagnetic tunneling has been measured in $CoFe/Al_2O_3/Co$ or NiFe junctions. At 295, 77, and 4.2 K the fractional change in junction resistance with magnetic field, $\Delta R/R$, is 11.8%, 20%, and 24%, respectively. The value at 4.2 K is consistent with Julliere's model based on the spin polarization of the conduction electrons of the magnetic films. $\Delta R/R$ changes little with a small voltage bias, whereas it decreases significantly at higher bias (>0.1 V), in qualitative agreement with Slonczewski's model. These junctions have potential use as low-power field sensors and memory elements.

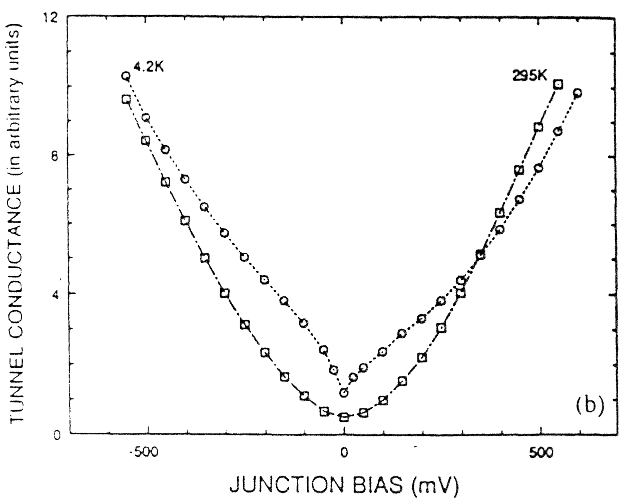

FIG. 1. Tunnel conductance plotted as a function of the applied dc bias for a $CoFe/Al_2O_3/NiFe$ tunnel junction at 4.2 and 295 K in zero field.

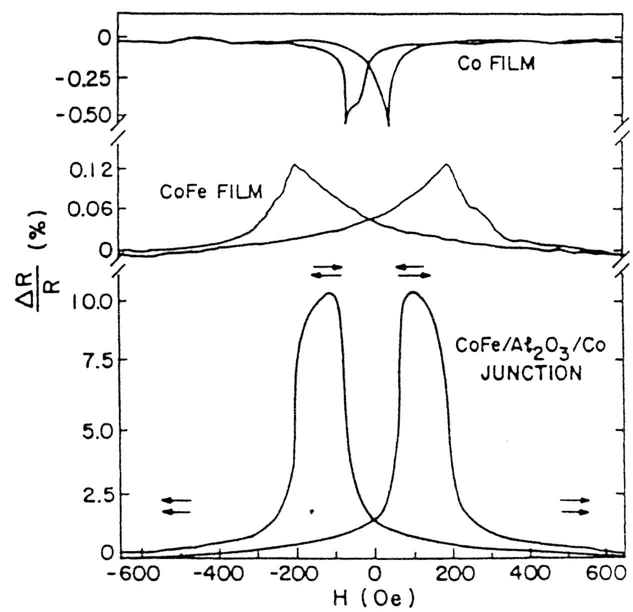

FIG. 2. Resistance of $CoFe/Al_2O_3/Co$ junction plotted as a function of H in the film plane, at 295 K. Also shown is the variation in the CoFe and Co film resistance. The arrows indicate the direction of M in the two films (see text).

[7] J.S. Moodera, et al., Phys. Rev. Lett. 74, 3273 (1995)

magnetic tunnel junction (MTJ)

Microstructured magnetic tunnel junctions (invited)

W. J. Gallagher
IBM Research Division, T. J. Watson Research Center, Yorktown Heights, New York 10698
S. S. P. Parkin
IBM Research Division, Almaden Research Center, Almaden, California 95120
Yu Lu
Physics Department, Brown University, Providence, Rhode Island 02912
X. P. Bian, A. Marley, and K. P. Roche
IBM Research Division, Almaden Research Center, Almaden, California 95120
R. A. Altman, S. A. Rishton, C. Jahnes, and T. M. Shaw
IBM Research Division, T. J. Watson Research Center, Yorktown Heights, New York 10698
Gang Xiao
Physics Department, Brown University, Providence, Rhode Island 02912

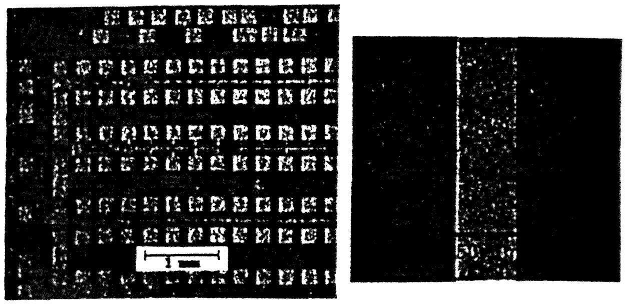

FIG. 1. Schematic of the patterning process for magnetic microtunneling junctions. The left and right panels are cross-sectional and plan spectively. The bottom optical micrographs show the layout o devices on a chip and a single tunneling junction with a rectang where both the bottom and the top leads are visible.

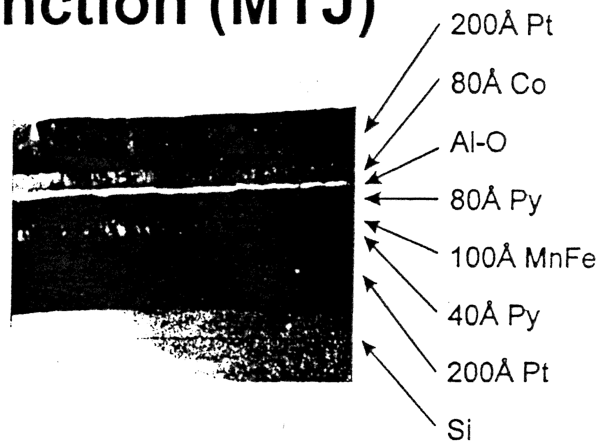

FIG. 3. Cross-sectional transmission electron micrograph of the layered structure of an MTJ with a Co-free layer. Each of the layers is indicated. The Pt layer contains an unexpected interface that may be due to silicide formation during the microscope sample preparation process.

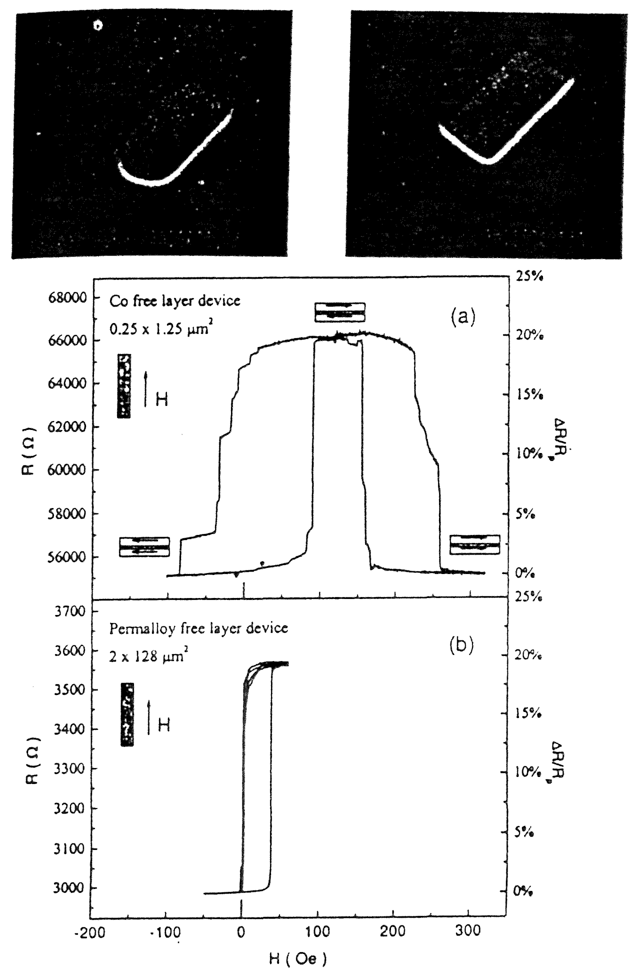

FIG. 5. Room-temperature tunneling resistance R, and magnetoresistance ratio $\Delta R/R_p$, vs magnetic field along the easy axis of two tunnel junctions: (a) a Co-free layer device with a rectangular 0.25×1.25 μm^2 top electrode, (b) a permalloy-free layer junction with top electrode dimensions of 2×128 μm^2. The orientation of the applied magnetic field relative to the junction shape anisotropy is indicated.

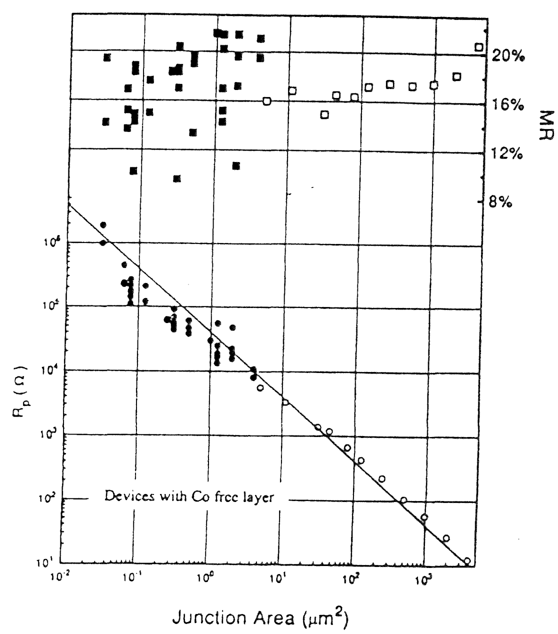

FIG. 6. Tunneling resistance vs nominal junction area at room temperature for MTJ devices with Co-free layers. The closed circles are data from samples fabricated using electron-beam lithography to define the junction area. Open circles are from samples patterned using optical lithography.

taking care of business

Science & Technology

PHYSICS

MAGNETIC FIELD OF DREAMS

Giant magnetoresistance may transform sensors and disk drives

Albert Fert had an inkling that he was on to something big. The University of Paris physicist knew that many metals exhibit a phenomenon called magnetoresistance (MR)—they show slight changes in electrical resistance when placed in a magnetic field. An expert in magnetism, Fert thought he could amplify the effect by designing materials made up of very thin layers of metals. In 1988, he tried—and the results were astonishing. The magnetoresistance in the material he used—chromium sandwiched between iron—was 10 times that of standard metals.

Along with similar results from Germany, Fert's find was dubbed "giant" magnetoresistance (GMR). Instantly, it became "the hot thing in physics," says Mark H. Kryder, director of the Data Storage Systems Center at Carnegie Mellon University. Many physicists put it on a par with high-temperature superconductivity, except for one thing: While the latter is still struggling to get out of the lab, in just six years, GMR has begun to have "a big impact on technology," says James Brug, manager for recording-head technology at Hewlett-Packard Co. Adds Kryder: "It's turning out to be useful much faster than I expected."

BRAKE KEYS. GMR has great commercial appeal, because if the right metal sandwiches are used, it can make them more sensitive (diagram). That lets them detect tiny external magnetic fields, an ability that's critical to lots of products. Each bit on a computer disk, for instance, is represented by a tiny magnetic field that is "read" by a magnetic sensor. Similar sensors are used to tell when car wheels stop turning and start skidding—the key to antilock brakes. In France, in fact, researchers at Thomson are testing GMR sensors in such brakes and to measure engine crankshaft speeds to help lower emissions or raise fuel economy. Startup Nonvolatile Electronics Inc. (NVE) in Eden Prairie, Minn., has even begun selling the first GMR product, a sensor aimed at everything from autos to hearing aids.

IBM and other disk-drive makers, meanwhile, are building GMR prototypes that promise leaps of up to seventeenfold in the amount of information that can be crammed onto drives. GMR also may enable memory chips to "remember" even after a computer's power is cut off. In short, GMR "may affect several billion-dollar businesses," says James M. Daughton, president of NVE.

Magnetoresistance was discovered by British physicist William Thomson, Lord Kelvin in 1856. But scientists couldn't explain it until the development of quantum mechanics in the 1920s. It turns out that holding a magnet near certain metals causes their atoms to "tilt"—and that tilted atoms are larger obstacles than untilted ones to electrons zipping by as electric current. The result is higher resistance. The "giant" phenomenon stems from the additional fact that there are two types of electrons—those that spin "up" or "down." The trick in changing resistance is constructing a material in which one of these electron types can get through more easily—aided by the external magnetic field. That's what Fert wanted to do with his miniature sandwich.

Today, the "bread" typically is an iron-nickel alloy, the "filling" nonmagnetic copper. Combined that way, each successive layer of iron-nickel is naturally magnetized in the opposite direction, much as the poles of bar magnets will always line up in opposite directions when one is held above the other. When electricity runs through such a sandwich, both up and down electrons in the current encounter many obstacles. Adding the external magnetic field changes things dramatically. It forces all the magnetism in the "bread" layers to line up in the same direction. Suddenly, the "down" electrons in the current skirt the obstacles. The result, says New York University physicist Peter M. Levy, "is a short-circuit effect"—a large drop in resistance.

Mount a chunk of this sandwich on a piece of silicon, suspend it above a disk drive, and each time a bit of magnetically encoded data swirls by, the sandwich experiences a big change in resistance—which tells the computer to put the data on your screen. Even before GMR, in fact, standard magnetoresistance was being used this way—mainly by IBM. Though GMR promised better performance. Fert's first devices had a flaw: "The initial material didn't look very

THE ATTRACTION OF GIANT MAGNETORESISTANCE

Discovered only six years ago, GMR is rapidly moving from lab to product development.

■ When no external magnetic field is present, the magnetic fields in a metal composed of copper (A) sandwiched between an iron-nickel alloy (B) face opposite directions. As a result, the metal's resistance to current (C) is high.

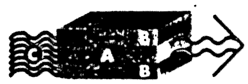

■ Applying an external magnetic field (D) causes the magnetic fields in all layers to line up in the same direction, so electrical resistance drops dramatically.

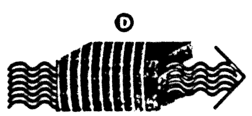

■ The lower resistance makes possible detection of very small external magnetic fields. That opens the door for use of the metal in designing:

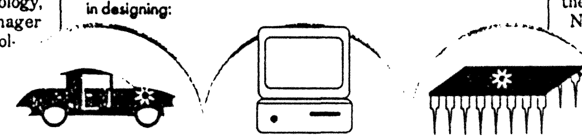

1. Automobile sensors that help better control engines, suspensions, brakes, and so on.
2. Computer disk drives that can hold 17 times the information of current ones.
3. Memory chips that "remember" even when the power is turned off.

LAUREL DAUNIS

AMR, GMR/SPIN VALVE READ HEADS

AND

WRITE HEADS

Edgar M. Williams

READ-RITE CORPORATION

Milpitas, California

This short course discusses recording characteristics of AMR and GMR/Spin Valve reading heads and advanced writing heads for application in high data rate, high areal density disk drives. Design considerations and process variances will be discussed to develop an appreciation for device impact on disk drive SNR and reliability issues. The course content is developed for non-specialists in the recording industry and for professionals wanting to follow recording head technology developments over the next few years.

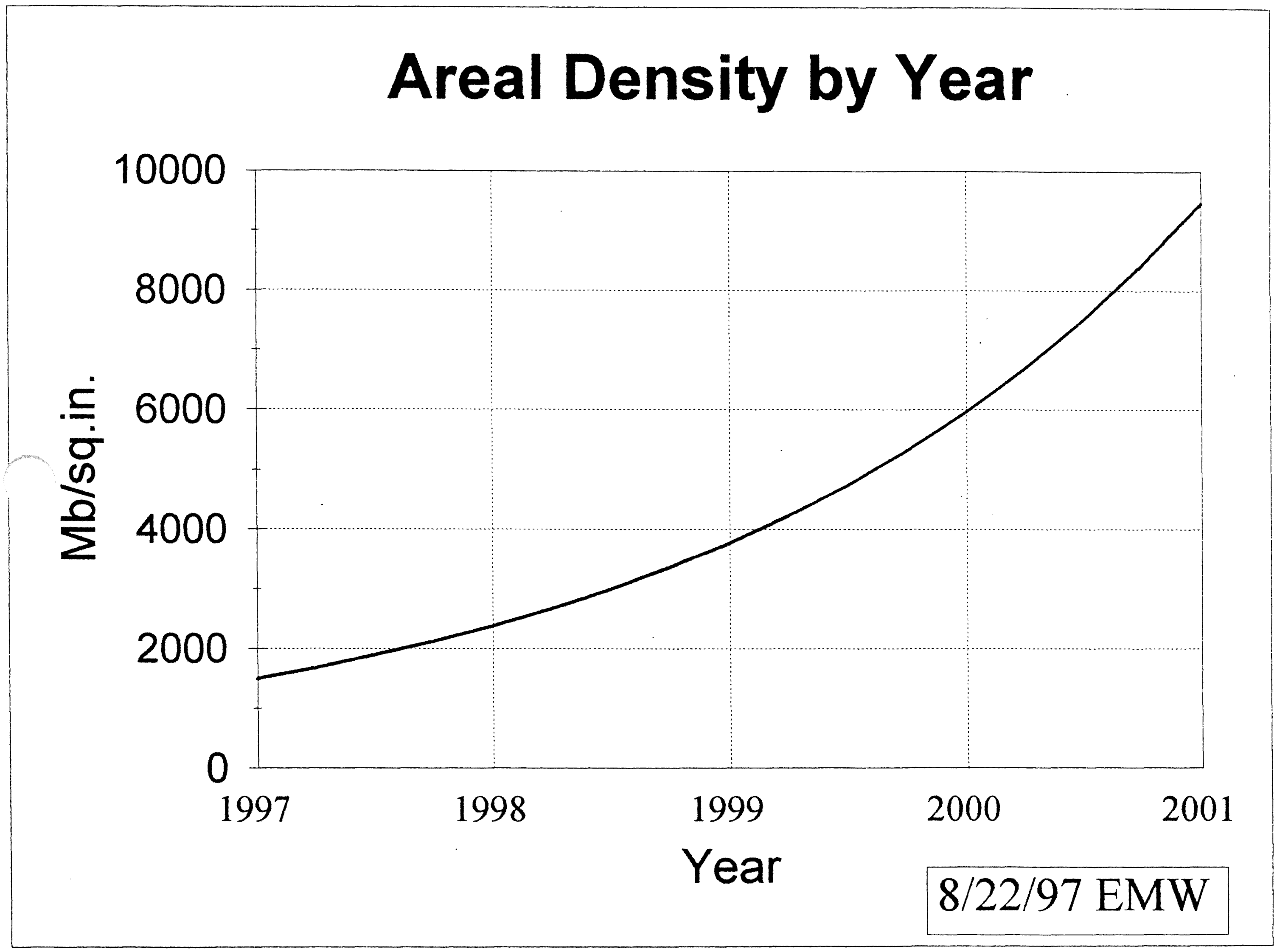

Areal Density by Year
10000
8000
6000
4000
2000
0
Mb/sq.in.
1997
1998
1999
2000
2001
Year
8/22/97 EMW

1

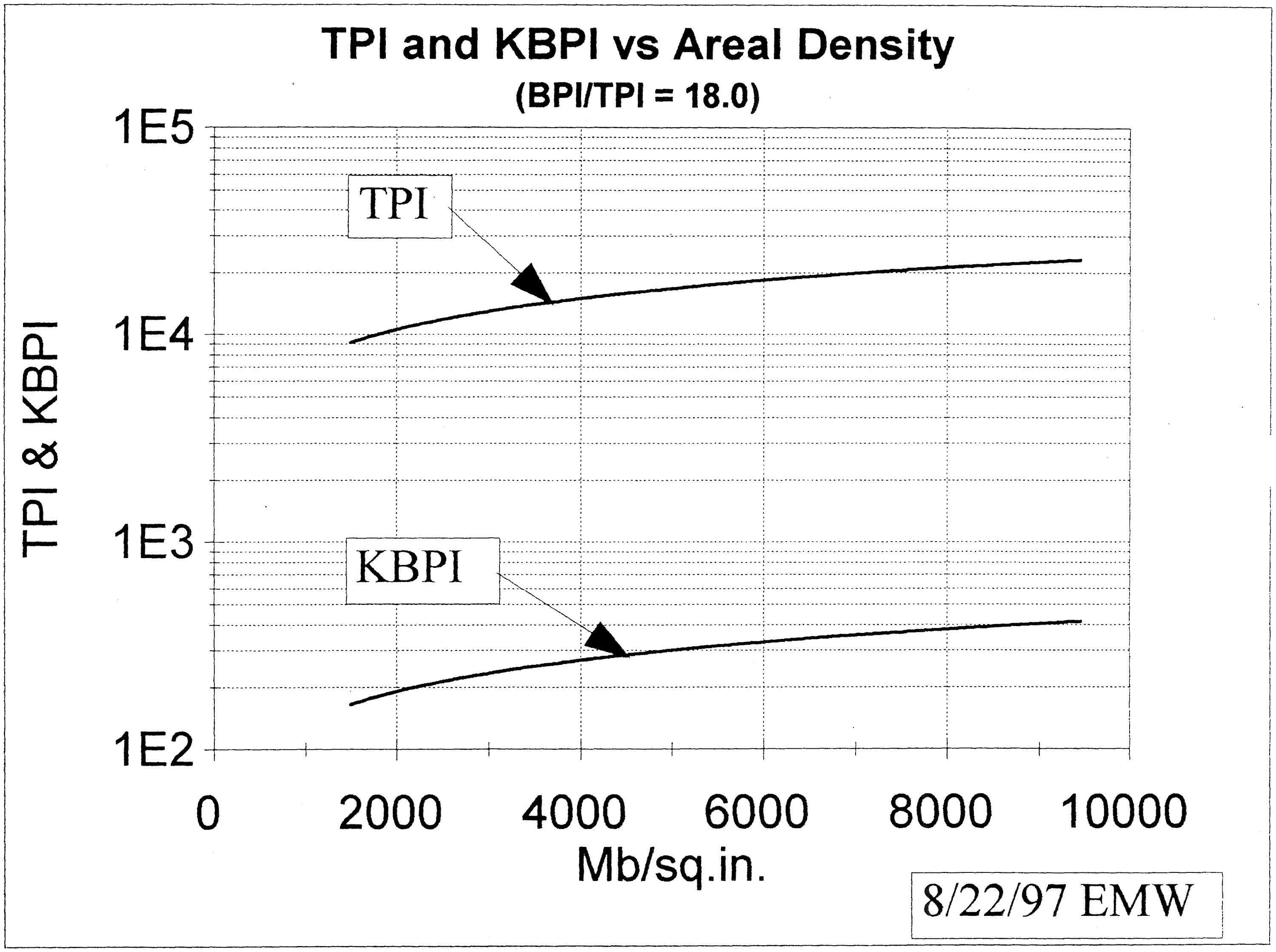
TPI and KBPI vs Areal Density
(BPI/TPI = 18.0)
1E5
1E4
1E3
1E2
TPI & KBPI
TPI
KBPI
0
2000
4000
6000
8000
10000
Mb/sq.in.
8/22/97 EMW

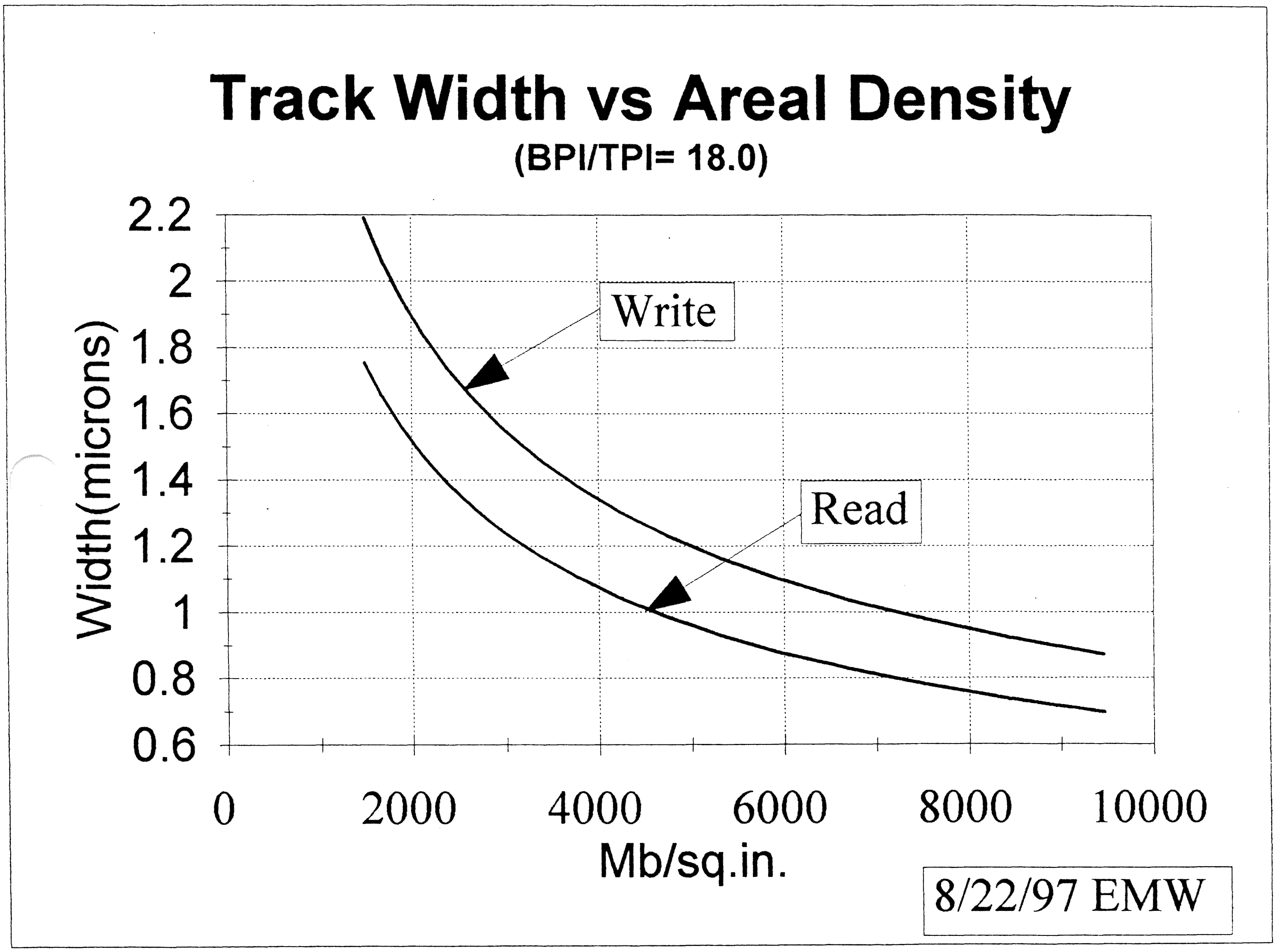
Track Width vs Areal Density
(BPI/TPI= 18.0)
Width(microns)
2.2
2
1.8
1.6
1.4
1.2
1
0.8
0.6
0
2000
4000
6000
8000
10000
Mb/sq.in.
Write
Read
8/22/97 EMW

(3)

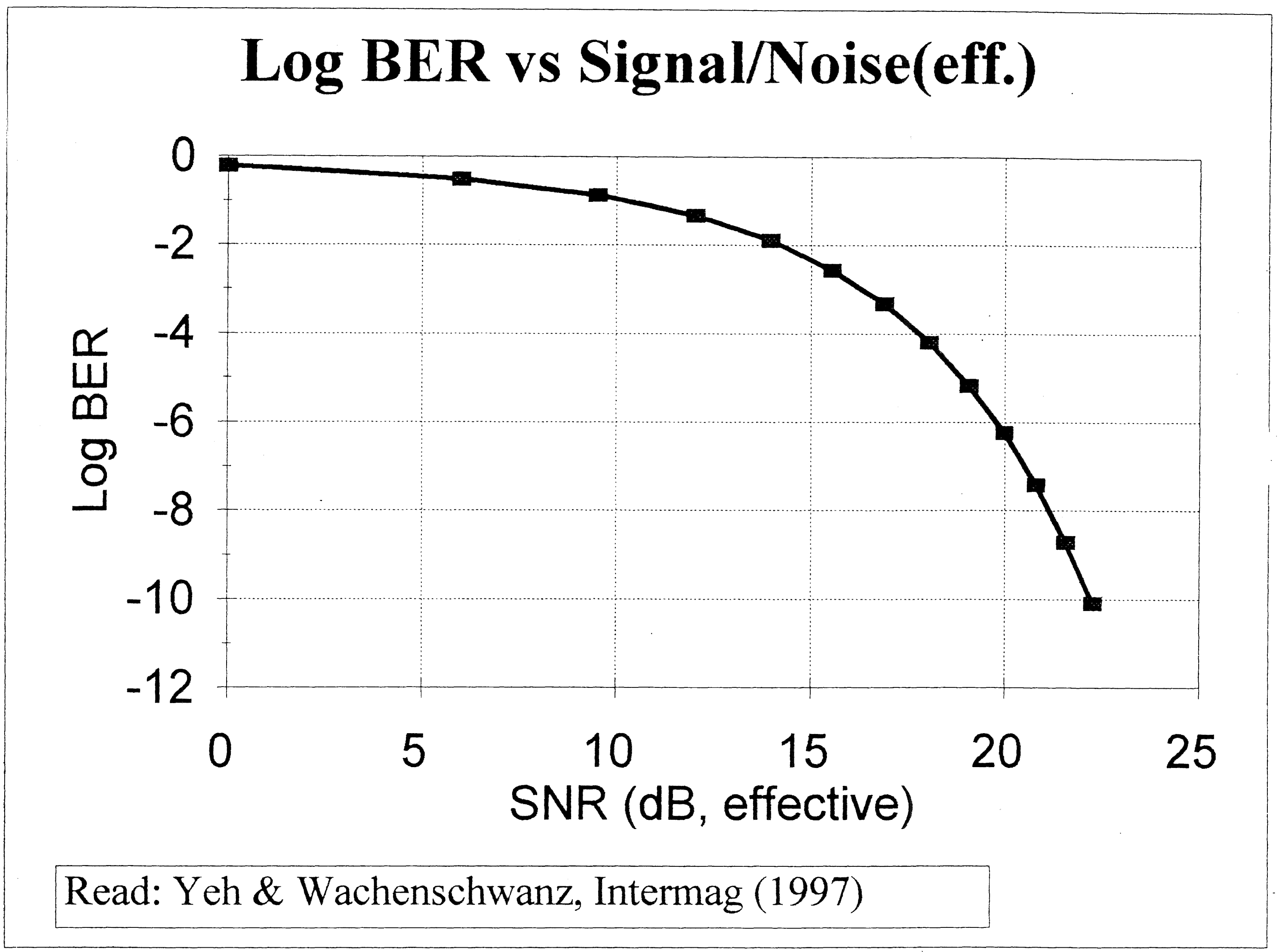
Log BER vs Signal/Noise(eff.)
Log BER
0
-2
-4
-6
-8
-10
-12
0
5
10
15
20
25
SNR (dB, effective)
Read: Yeh & Wachenschwanz, Intermag (1997)

Lorentzian Pulses:

$$V(t) = \frac{V_o}{1+(2vt/PW50)^2}$$

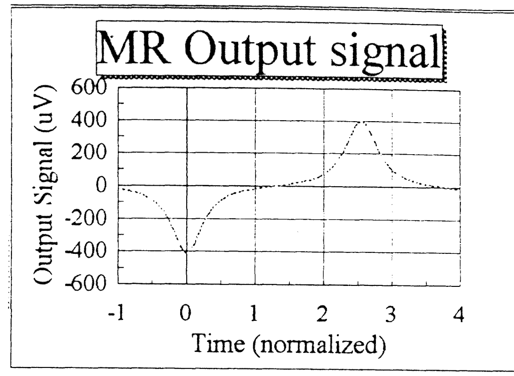

Infinite Sum of Alternating Polarity Lorentzians:

Refs: R.Comstock and M.Williams, IEEE Trans. Mag., **MAG-9**, 342(1973).
R.L. Smith, IEEE Trans. Mag., **MAG-27**, 4561 (1991).
H. N. Bertram, IEEE Trans. Magn., **MAG-31**, 2573(1995).

$$\Sigma = \frac{A \sinh A}{\cosh^2 A - 1} = \frac{A}{\sinh A}$$

$$where\ A = \frac{\pi}{2} PW50 \cdot Density;\ Isolated\ Pulse = 1.0$$

$$PW50 \cong \sqrt{\frac{G_{ss}^2 + t^2}{2} + 4(d+a+\delta/2)^2}$$

(5)

115T...

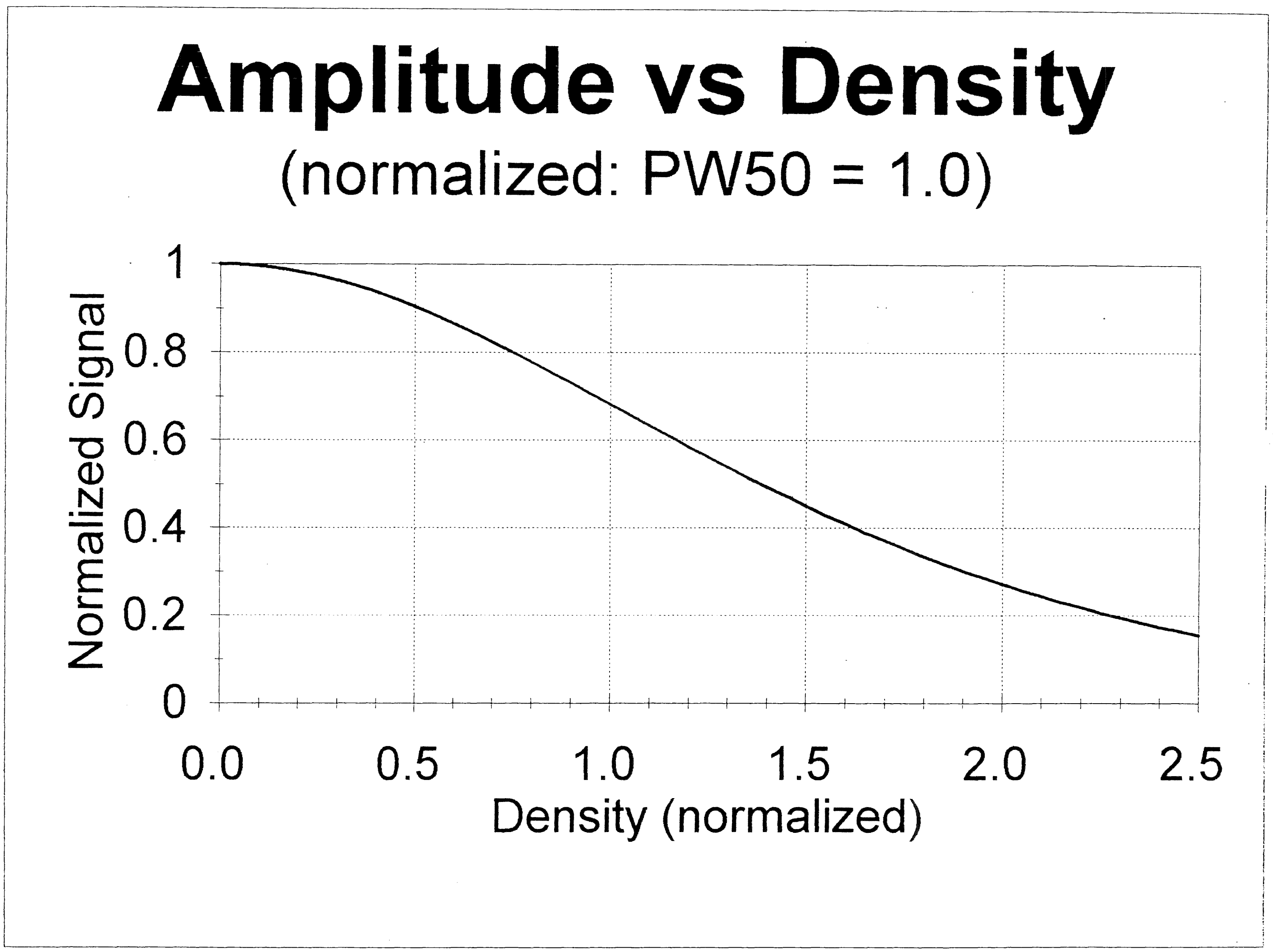

Amplitude vs Density
(normalized: PW50 = 1.0)
Normalized Signal
1
0.8
0.6
0.4
0.2
0
0.0
0.5
1.0
1.5
2.0
2.5
Density (normalized)

8/22/97 EMW

Anisotropic MR (AMR) Layer with Soft Adjacent Layer (SAL) Biasing:

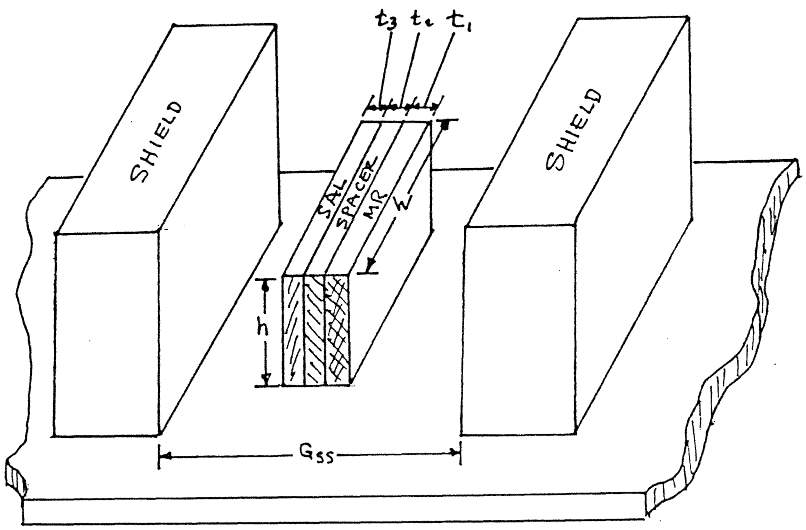

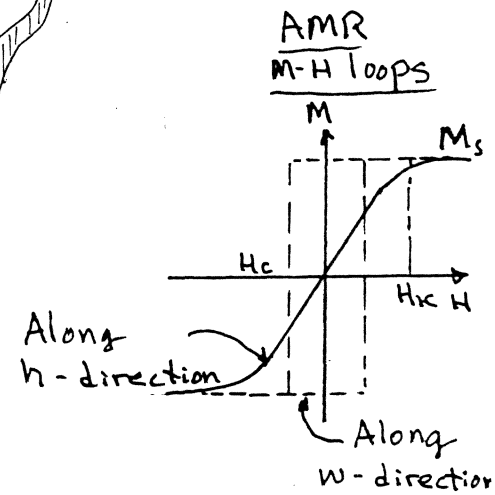

Trilayer Resistance:

$$R_t = \frac{R_1R_2R_3}{R_1R_2+R_1R_3+R_2R_3}$$

$$R_1=\frac{\rho_{MR}W}{t_{MR}h};\ R_2=\frac{\rho_{spacer}W}{t_{spacer}h};\ R_3=\frac{\rho_{sal}W}{t_{sal}h}.$$

Film resistivity in (ohm-cm), thickness in (cm), width in (cm), stripe height in (cm).

Current splitting among the films:

$$\frac{I_i}{I_t} = \frac{R_t}{R_i}$$

BIAS FIELD AND FILM COUPLING

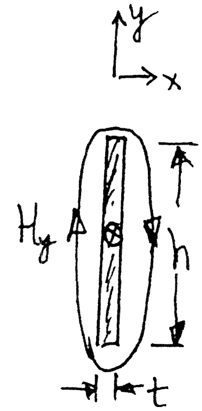

Field Outside a Thin Conducting Layer:

$$H_y \cong \frac{\pi I}{5h} \quad [Oe,\ for\ I(amp),\ h(cm)]$$

Magnetizing Behavior of a Thin Magnetic Film

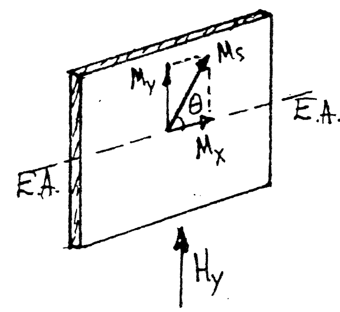

$$M_y = \frac{H_y}{H_d + H_k};\ H_d \cong \frac{4\pi M_s t}{h+t}$$

(Hd $\approx$ 150 Oe; Hk $\approx$ 4 Oe)

Coupling Equations for Unsaturated SAL and MR Layers

$$\frac{M_y^{MR}}{M_s^{MR}} = \sin\theta_{MR} = f_1(H,\alpha) = \frac{H_{sig}\alpha + H_y^{sal} + H_y^{MR}(1-\alpha)}{2\alpha H_d^{MR}}$$

$$\frac{M_y^{sal}}{M_s^{sal}} = \sin\theta_{sal} = f_2(H,\alpha) = \frac{-H_{sig}\alpha + H_y^{MR} + H_y^{sal}(1-\alpha)}{2\alpha H_d^{sal}}$$

(α much smaller than 1.0; terms in α^2 ignored.)

Ref: N. Bertram, "Theory of Magnetic Recording," Chap. 7, Cambridge(1994).

Saturation Behavior of Real Films is Gradual

$$\frac{M_y^{MR}}{M_s^{MR}} \simeq \tanh[f_1(H,\alpha)]; \quad \frac{M_y^{sal}}{M_s^{sal}} \simeq \tanh[f_2(H,\alpha)]$$

Ref: S. Middlehoek, "Ferromagnetic Domains in Thin NiFe Films."

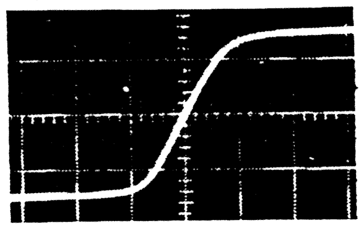

MR Bias With Saturated SAL

Optimal MR bias at $\theta_{MR} \simeq 45°$ *with* $\theta_{sal} = 90°$.

$$\frac{H_d^{sal}}{H_d^{MR}} = \frac{1}{\sqrt{2}} \cdot \frac{H_y^{MR} + H_y^{sal}(1-\alpha)}{H_y^{MR}(1-\alpha) + H_y^{sal}}$$

$$\frac{H_d^{sal}}{H_d^{MR}} \simeq \frac{M_s^{sal} t_{sal}}{M_s^{MR} t_{MR}} \approx \frac{1}{\sqrt{2}}.$$

NOTES:
t_0 = SAL thickness
t_1 = MR "
L = stripe height
I_s flows in MR only
g = distance between SAL & MR films

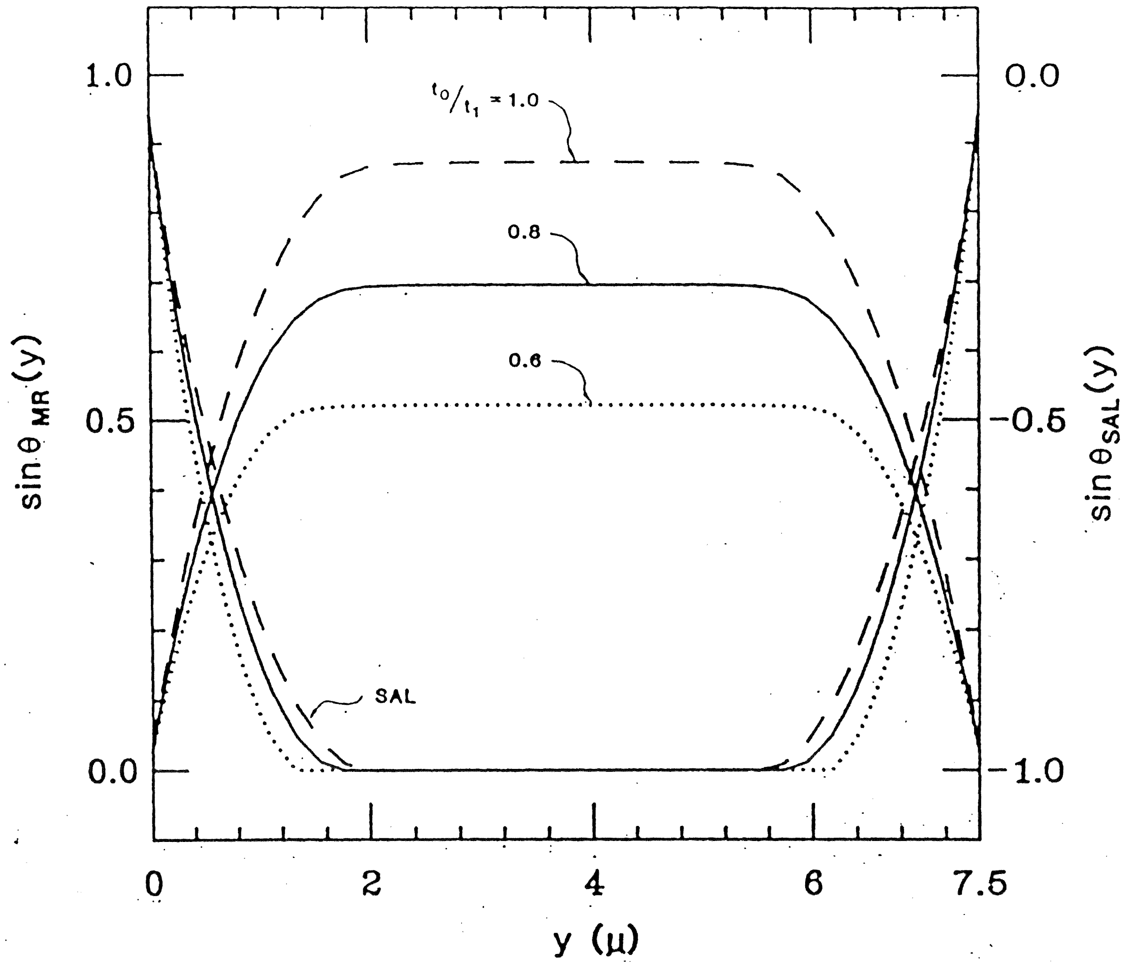

Fig. 6. Computed MR and SAL bias magnetization distributions as function of SAL/MR thickness ratio t_0/t_1 for fixed $J_s = 10^7$ A/cm^2 or $I_s = 0.03$ A, $L = 7.5$ μm, $g = 1000$ Å, and $t_1 = 400$ Å. Dotted, solid, and dashed curves correspond to values $t_0/t_1 = 0.6$, 0.8, and 1.0, respectively.

Ref: N. Smith, IEEE Trans. Mag., MAG-23, 259 (1987).

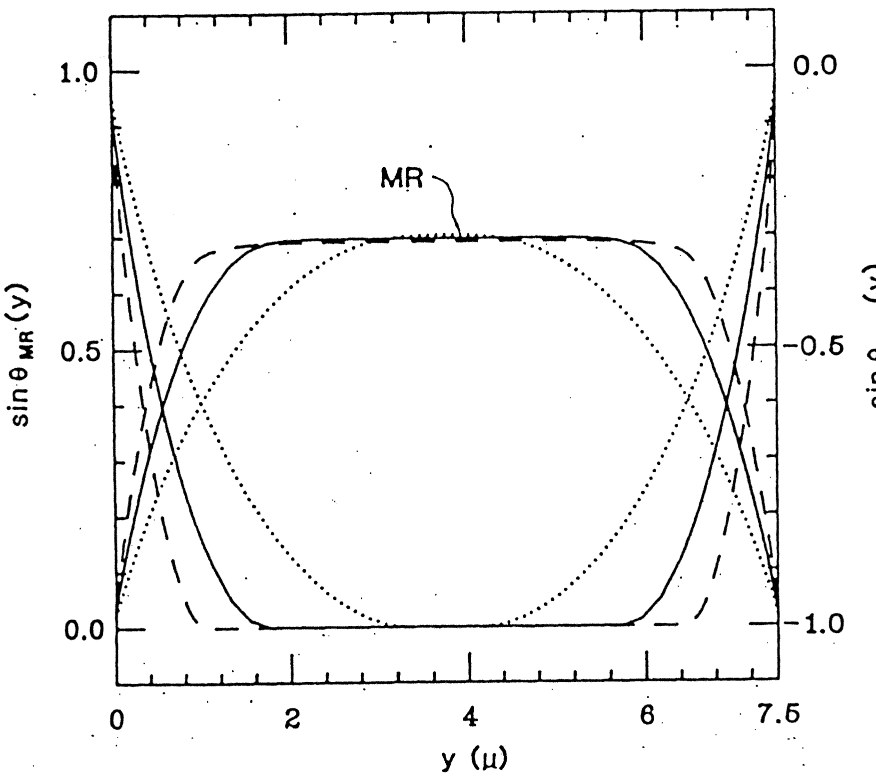

Fig. 7. Computed MR and SAL bias magnetization distributions as function of current density J_s for fixed thickness ratio $t_0/t_1 = 0.8$. $L = 7.5$ μm, $g = 1000$ Å, and $t_1 = 400$ Å. Dotted, solid, and dashed curves correspond to values $J_s = 0.5$, 1.0, and 2.0×10^7 A/cm^2, respectively.

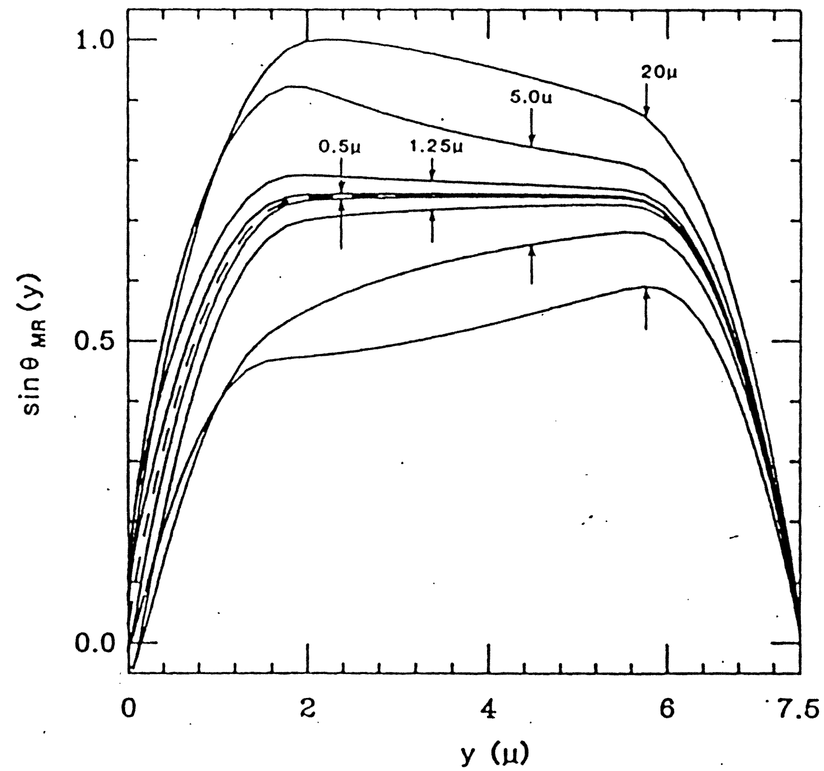

Fig. 13. Computed MR magnetization distribution changes in response to tape-media signal fields for sinewave recorded media (as previously considered in Figs. 9–11) for selected wavelengths λ as indicated. Shown are approximately maximum positive and negative excursions from bias distribution (dashed curve) for each wavelength; see text for further details. $L = 7.5$ μm; other parameters as given in Figs. 8 and 9.

(17)

Efficiency of Shielded MR Sensor

$$E_{MR} = \frac{\cosh(\beta h) - 1}{\beta h \cdot \sinh(\beta h)}, \ where\ \beta = \sqrt{4/(\mu t_{MR} G_{ss})}$$

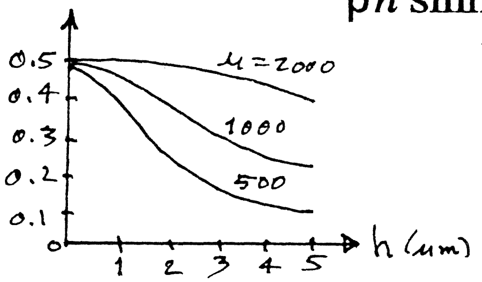

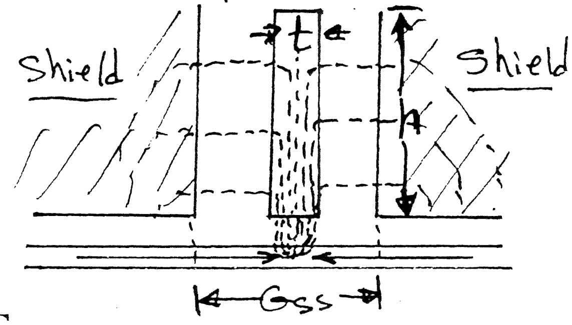

MAGNETORESISTANCE EFFECT

$$\frac{\Delta\rho}{\rho} \propto \cos^2\theta_{MR} = 1 - \sin^2\theta_{MR} = 1 - \tanh^2[f_1(H,\alpha)] = sech^2[f_1(H,\alpha)]$$

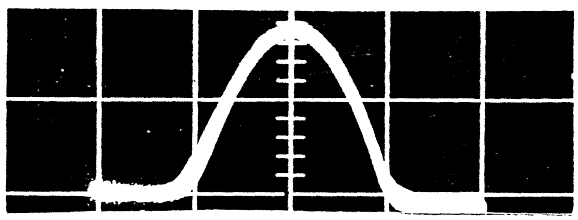

$$MR\ Signal \simeq E_{MR} \cdot I_{MR} \cdot \Delta R \cdot sech^2[f_1(H,\alpha)],$$

$$where\ \Delta R = \frac{\Delta\rho W}{t_{MR} h}$$

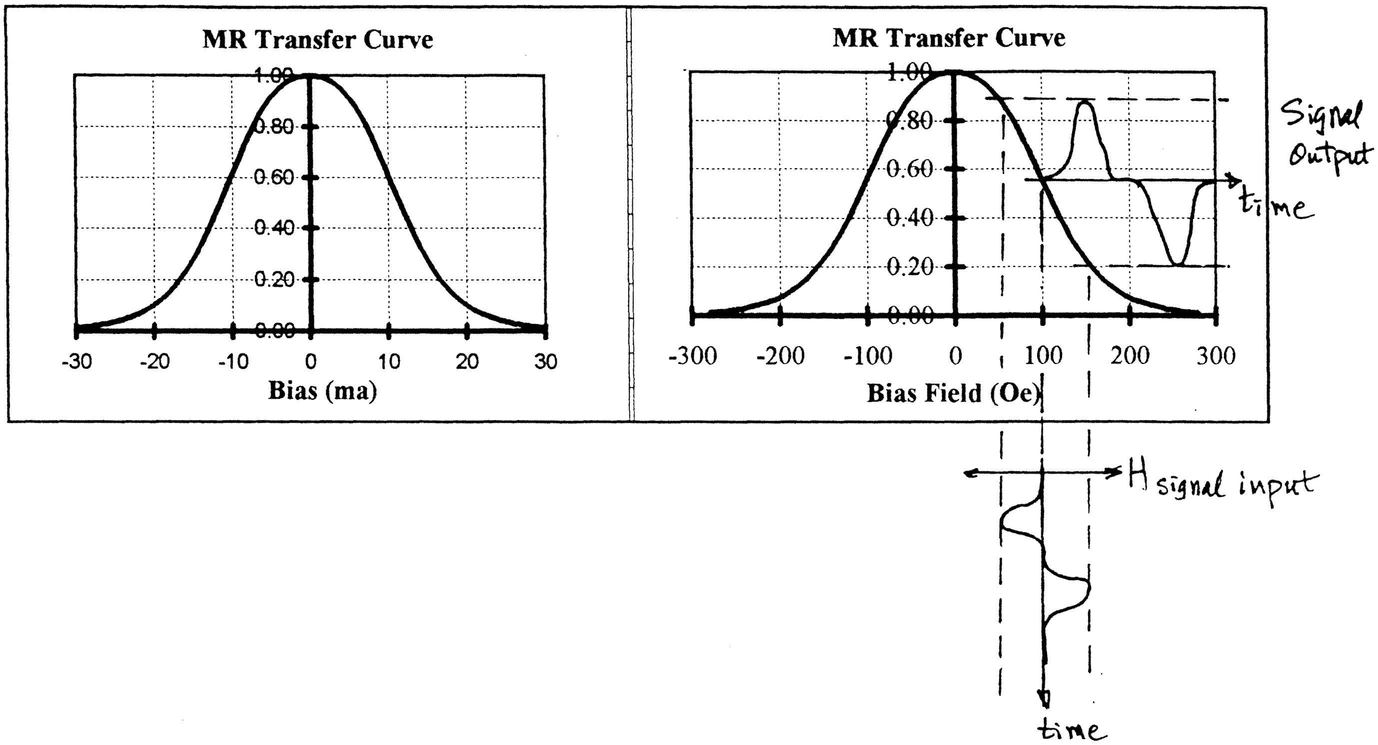

- Normally, the useful range for "linear output" is about 40%-50% of the full $\Delta R/R$ Transfer Curve.

- "Amplitude Asymmetry" = $\dfrac{|Pos| - |Neg|}{|Pos| + |Neg|} \times 100\%$

- Design for $0 \pm (10-15)\%$ at fixed bias current.

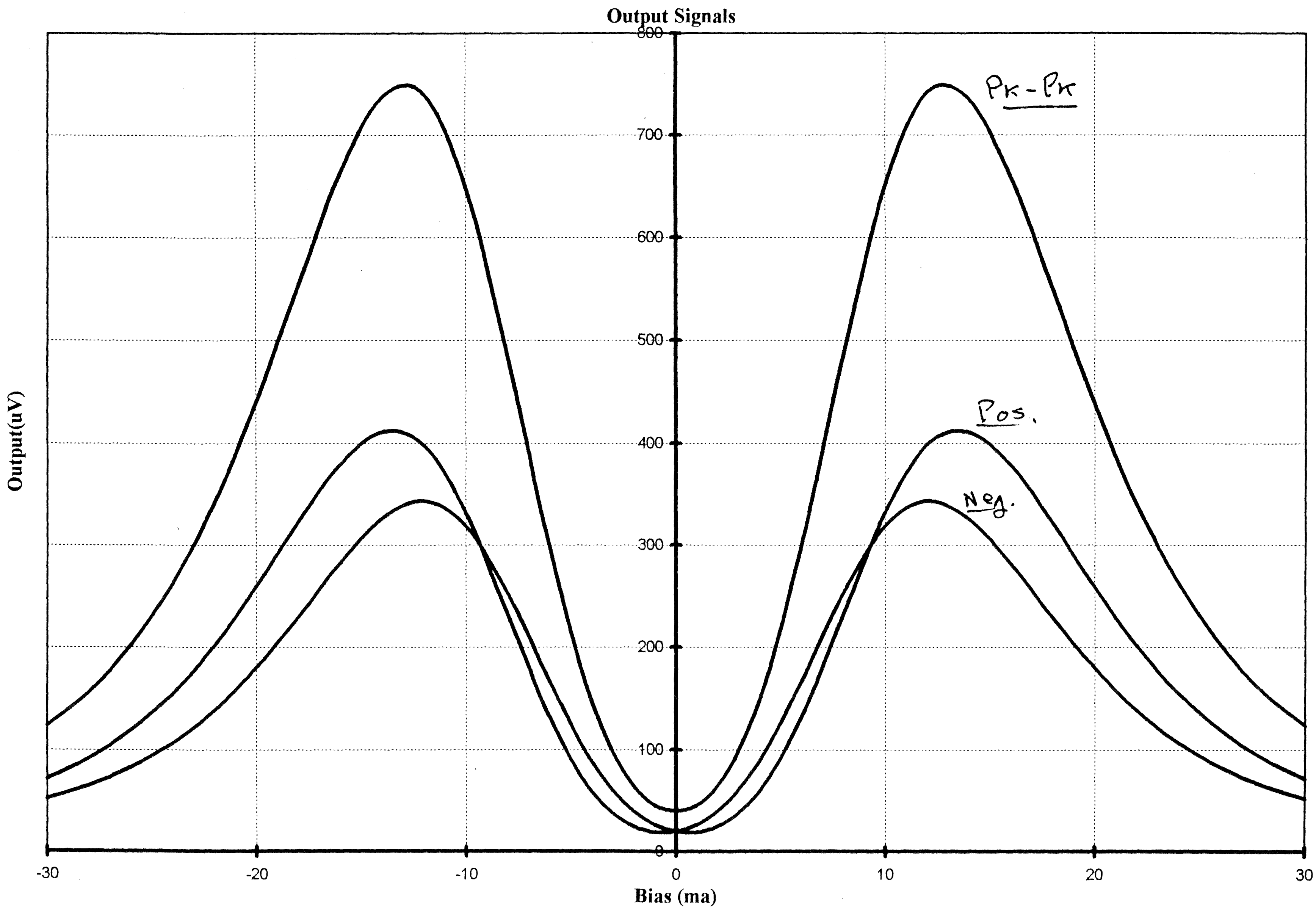
Output Signals
Output(uV)
800
700
600
500
400
300
200
100
0
-30
-20
-10
0
10
20
30
Bias (ma)
Pk-Pk
Pos.
Neg.

14

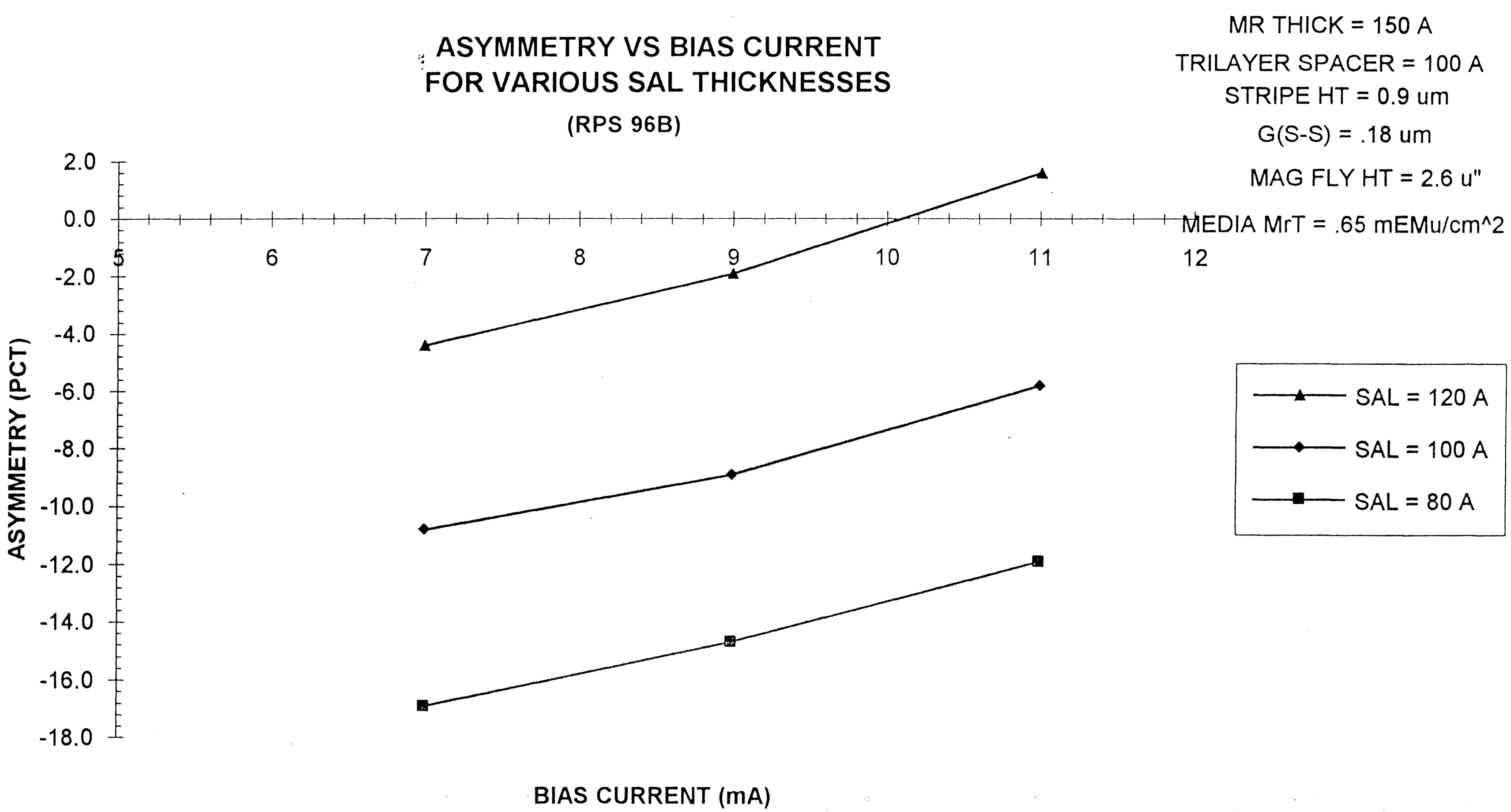

E KATZ

8/13/97

(15)

<u>Sample Calculations for 1.5 Gb/sq.in. Case</u>:

If bpi/tpi = 18.0, then Areal Density = (18.0 tpi)x(tpi)

and tpi = 9100; Kbpi = 164.

Write Width (industry average) = 0.80/tpi = 88 microinches

WW = 2.2 microns

MR Width (industry average) = 0.80WW

therefore MRW = W = 1.8 microns.

<u>Trilayer Design:</u>

80/20 NiFe with $\Delta R/R = 0.02$

$t_{MR} = 20$ nm

$t_{spacer} = 12$ nm

$t_{sal} = 14$ nm

$h = 1.2$ microns

Estimate of Signal for SAL-Biased Shielded AMR Head

A.D. = 1.5 Gb/sq.in.

Read Width = 1.8 microns

MR thickness = 20 nm

Spacer = 12 nm

SAL = 14 nm

Stripe Height = 1.2 microns

Tri-layer sheeet resistance = 10 ohms/square x 1.5 squares = 15 ohms

$\Delta R/R$ (MR layer) = 0.02 or ΔR = 0.42 ohm

I_{MR}/I_t = 0.69; Mr current = 6.9 ma for total bias of 10 ma

Shielded MR Sensor Efficiency = 0.48

$$\text{MR signal} = E_{MR}\, I_{MR}\, \Delta R\, \mathrm{sech}^2\,[f_1(H,a)]$$

$\cong$ 590 microvolts (p-p) at 27.3 Kbpi (30.8 Kfci)

$\cong$ 449 " " 82.0 " (82.0 Kfci)

$\cong$ 194 " " 164 " (184.5 Kfci)

Maximum useful range of MR transfer curve is about 0.4

at low densities (high input field strength from medium.)

AMR HEADS AT 3.0 Gb/sq.in.

Nominal Case (design center):

MR Width = 1.2 μm

Stripe Height = 0.8 μm

t_{MR} = 12.0 nm

t_{sal} = 8.6 nm

$\delta R/R$ = 0.02

Bias = 7.0 ma (4.8 ma in MR layer)

J_{MR} = 5.0×10^7 amp/cm^2

Output Signal (130 Kfci) = 580 μV (p-p)

" " (260 Kfci) = 240 μV (p-p)

PW50 = 0.21 μm

"3-sigma" Case:

MR Width = 1.1 μm

Stripe Height = 1.2 μm

t_{MR} = 13.2 nm

J_{MR} = 3.1×10^7 amp/cm$_2$

Output Signal (130 Kfci) = 310 μV (p-p)

" " (260 Kfci) = 110 μV (p-p)

PW50 = 0.25 μm

NOISE SOURCES: Johnson Noise of Heads and Preamps

$$e_n = \sqrt{4k_B \cdot T \cdot R \cdot BW} \;\; volt(rms)$$

where k_B = Boltzmann's Constant

T = temperature (K) of resistance

BW = bandwidth (Hz) of circuit

Sample Calculation:

T = 300 K; BW = 70 MHz; R_{MR} = 30 Ω; R_{preamp} = 15 Ω

e_n(MR) = 5.9 μV(rms) or 0.71 nV/√Hz

e_n(preamp) = 4.2 μV(rms) or 0.50 nV/√Hz

MR head and preamp are independent sources,

$$e_n(MR+Preamp) = \sqrt{5.9\mu V^2 + 4.2\mu V^2} = 7.24 \;\; \mu V(rms)$$

MEDIUM NOISE: Transition Jitter

Refs: Tarnopolsky and Pitts, #EB-07, 3M Conf. (1966)
Xing and Bertram, #AB-08, INTERMAG (1997).

$$Transition\ Noise = V_o \sigma_j \sqrt{\frac{\pi}{2 \cdot B \cdot PW50}} \;\; (volt,rms)$$

where V_o=Iso-Pulse amplitude; σ_j=jitter (nm,rms); B=distance between transitions ("bit length.")
Sample Calculation: 400 μV amplitude; 30 Å jitter; PW50 = 2500Å
B = 980 Å (260 Kfci):

e_j = 9.6 μV (rms)

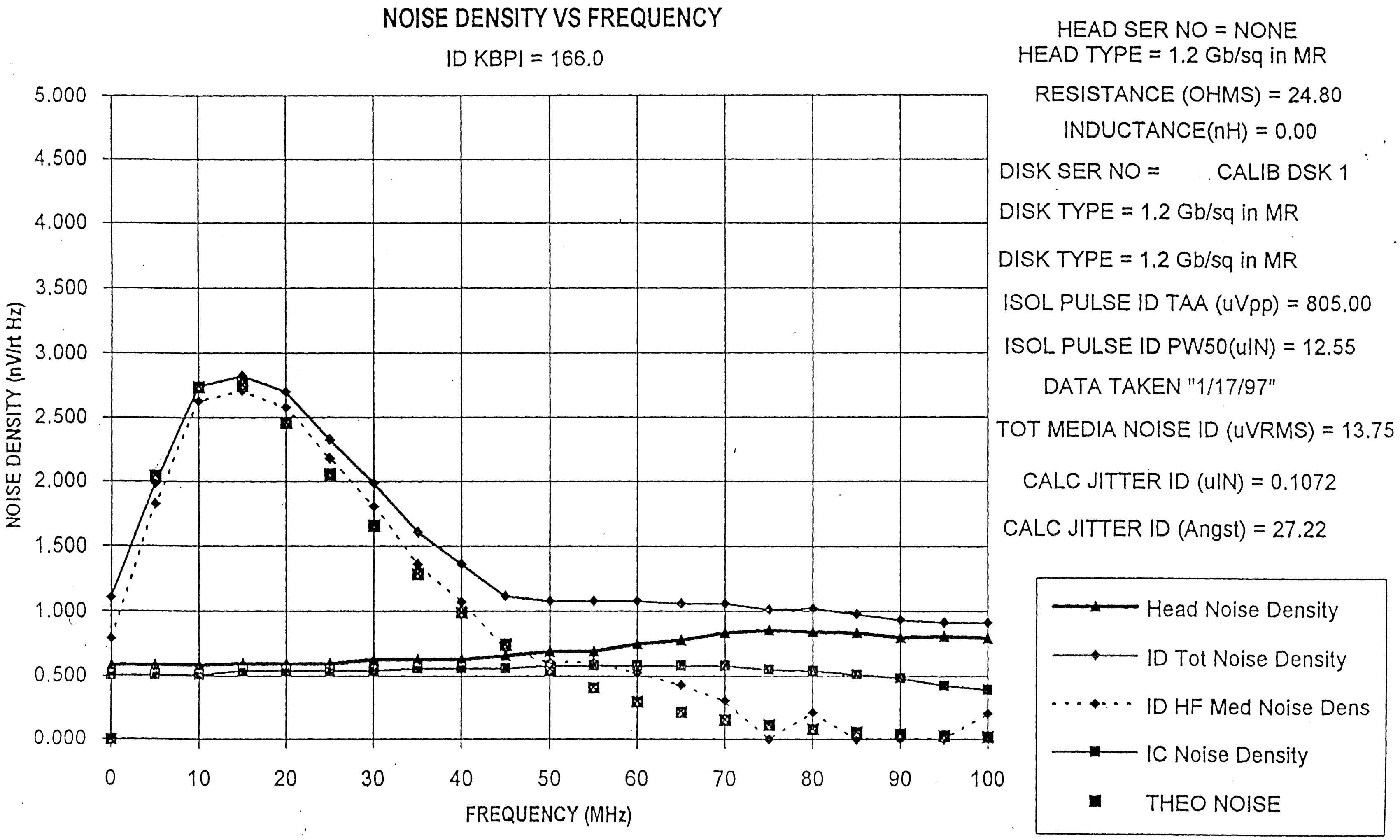

HEAD ID =MR-4

HEAD SER NO = NONE

HEAD TYPE = 1.2 Gb/sq in MR

RESISTANCE (OHMS) = 24.80

INDUCTANCE(nH) = 0.00

DISK SER NO = CALIB DSK 1

DISK TYPE = 1.2 Gb/sq in MR

DISK TYPE = 1.2 Gb/sq in MR

ISOL PULSE ID TAA (uVpp) = 805.00

ISOL PULSE ID PW50(uIN) = 12.55

DATA TAKEN "1/17/97"

TOT MEDIA NOISE ID (uVRMS) = 13.75

CALC JITTER ID (uIN) = 0.1072

CALC JITTER ID (Angst) = 27.22

Electronic Noise ≃ 7.24uV(rms)
Medium Noise ≃ 13.75uV(rms) : Dominant Noise Source!
Total Noise ≃ 15.5uV(rms)

E KATZ 1/26/97 8:26

Signal-to-Noise Estimates:

Nominal AMR Head at high current Density:

Electronic + Medium Noise: 12.0 μV(rms)

Isolated Pulse: 400 μV (0-p)

Signal at 130 Kfci: 290 μV (0-p) or SNR = 27.7 dB

" " 260 " : 120 μV (0-p) or SNR = 20.0 dB

At lower current densities signal drops accordingly, so there is a motivation for transducers with improved signal output.

SPIN VALVE/GMR Sensors!!

Issues With Increased Sense/Bias Current

- Temperature Rise of MR Trilayer

$$\Delta T = \frac{L}{K_T A} I^2 R; \quad R = \frac{R_o}{1 - \alpha \frac{L}{K_T A} I^2 R_o}$$

L = Thickness of gap material (element-shield)

K_T = Thermal conductivity of gap material [Al_2O_3 = 1.0 watt/(C°-meter)]

A = Area of heat dissipation [Stripe Height x (width of leads+trilayer)x2]

a = Temperature coefficient of trilayer sandwich (2.3 x 10^{-3} /°C)

Estimate of Temperature Rise/Watt:

$$\Delta T/Watt = \frac{10^{-7} m}{1.0 \frac{watt}{C^{\circ}\text{-}m} 1.5 \cdot 10^{-11} m^2} \simeq 6{,}670 \frac{C^{\circ}}{Watt}$$

- Electromigration and Head Longevity:

Black's Equation

$$Lifetime \propto A J^{-n} \exp\left[\frac{E_a}{k_B T}\right]$$

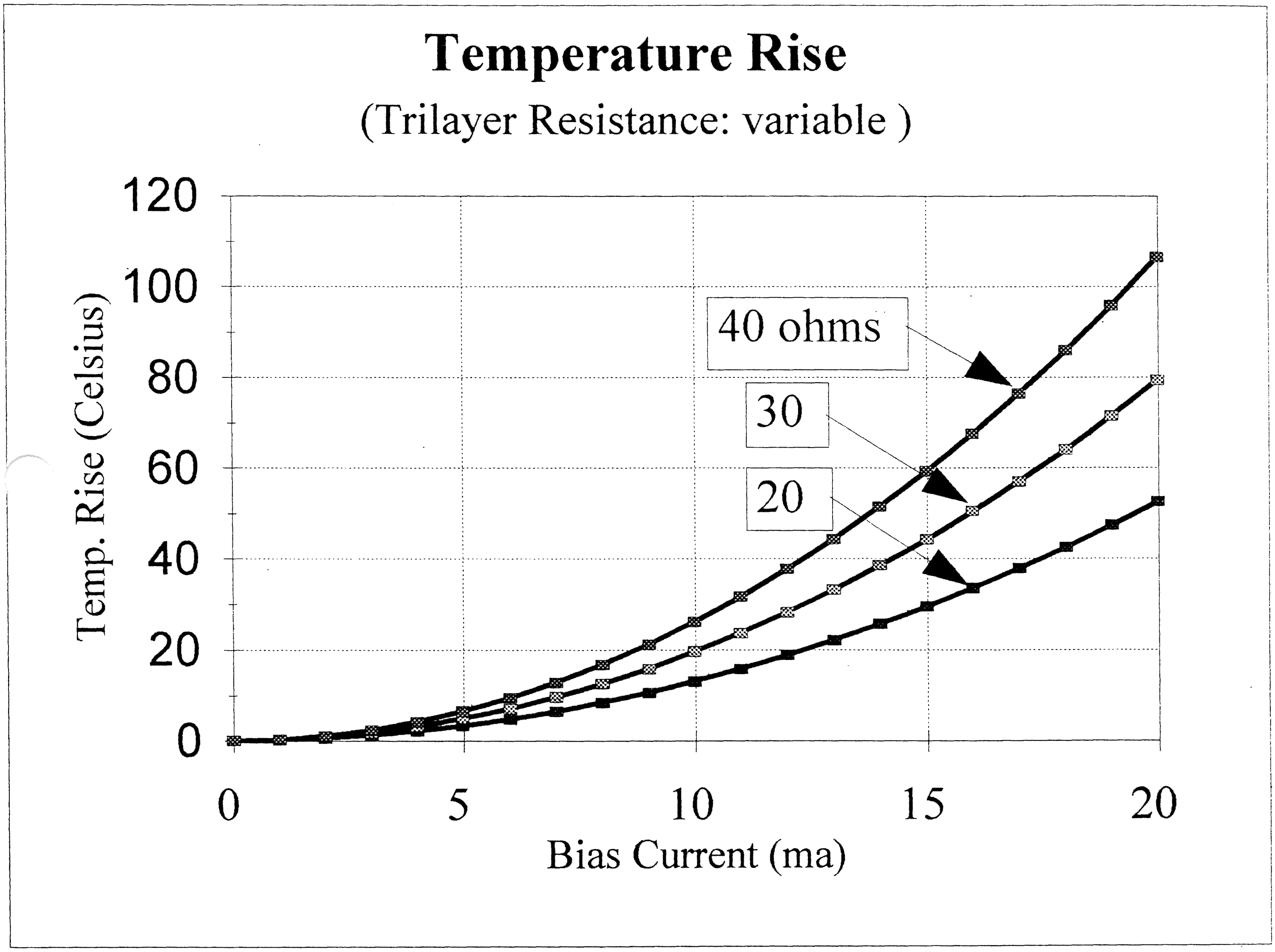

Temperature Rise
(Trilayer Resistance: variable)
Temp. Rise (Celsius)
120
100
80
60
40
20
0
40 ohms
30
20
0
5
10
15
20
Bias Current (ma)

8/22/97 EMW

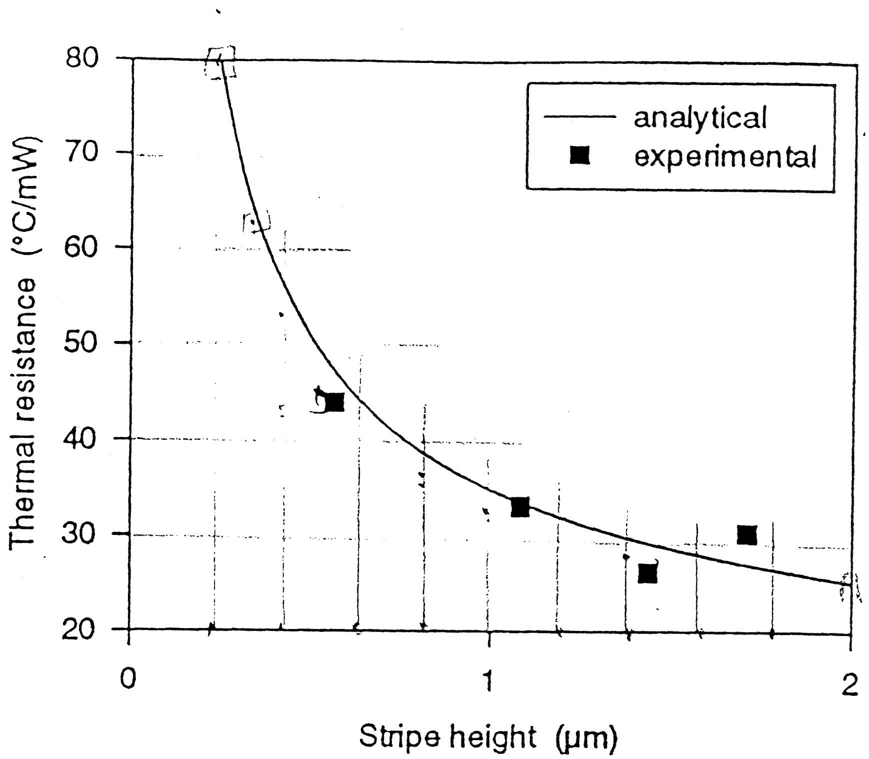

Fig. 5. Model predictions for the thermal resistance of heads as a function of MR stripe height compared to experimental data.

Ref: Jander, Indeck, Brug and Wicke
"A Model for Predicting Heating of MR Heads.
(to be published).

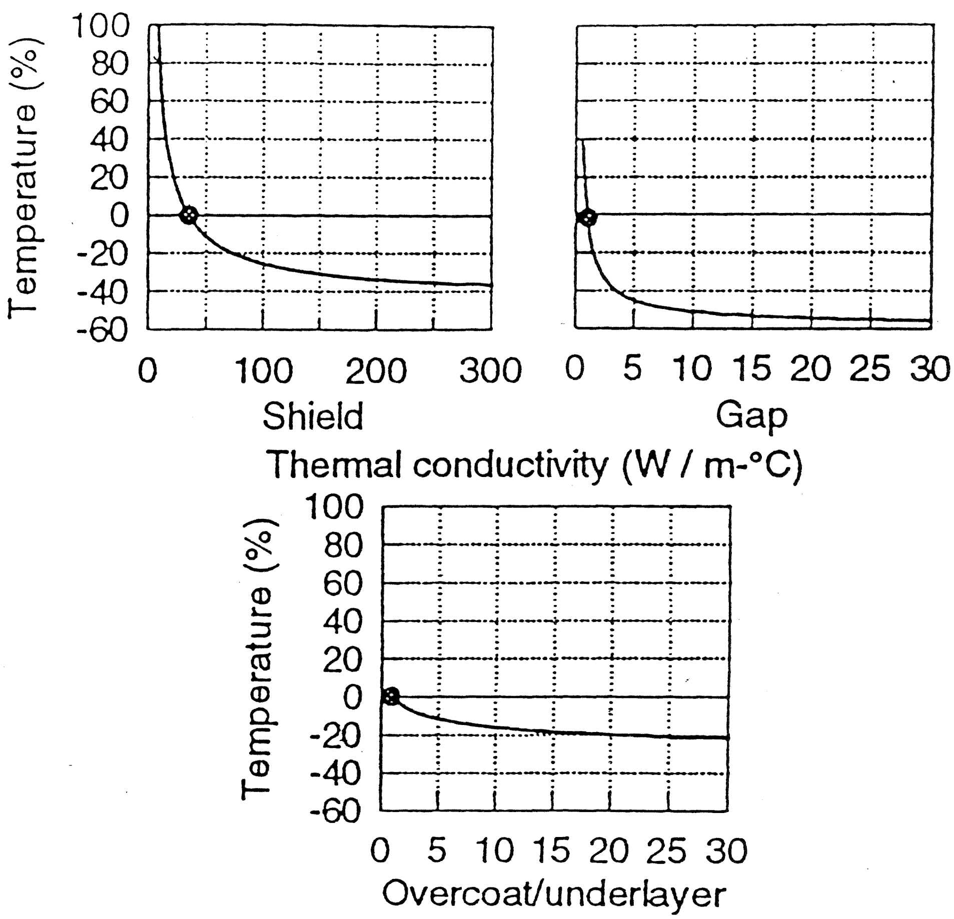

Fig. 4. Percent change in maximum temperature as thermal conductivities are varied from a standard head design.

Electrical & Thermal Longevity

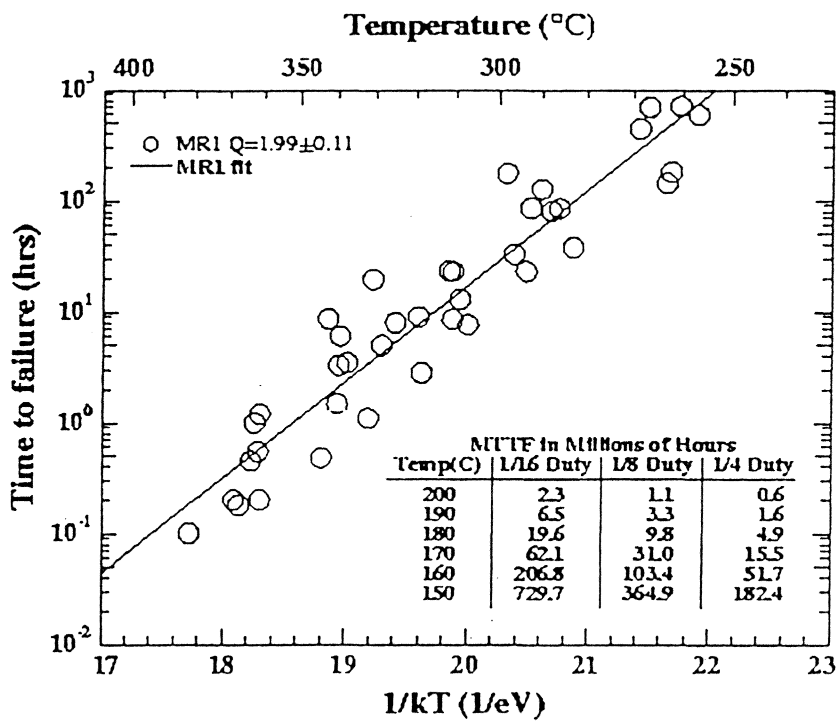

MTTF in Millions of Hours

Temp(C)	1/16 Duty	1/8 Duty	1/4 Duty
200	2.3	1.1	0.6
190	6.5	3.3	1.6
180	19.6	9.8	4.9
170	62.1	31.0	15.5
160	206.8	103.4	51.7
150	729.7	364.9	182.4

HEADWAY TECHNOLOGIES, INC

Ref: Kochan Ju (1996)

Ref: Kochan Ju (Headway Technologies)

Ju0294

Dual Stripe MR Head

Thermal Asperity Sensitivity

MR1

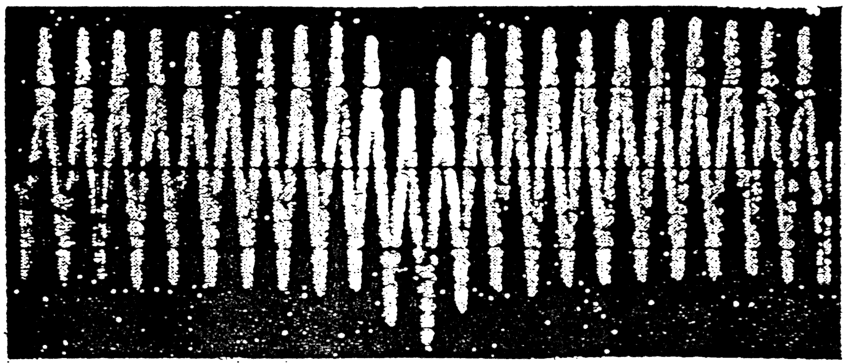

MR2

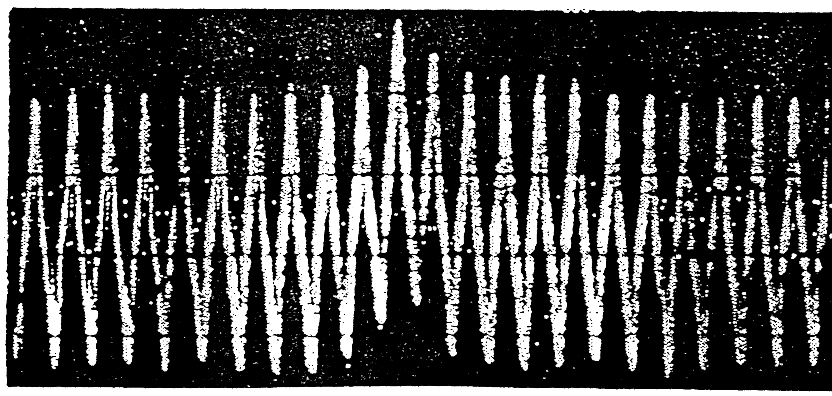

Dual Stripe

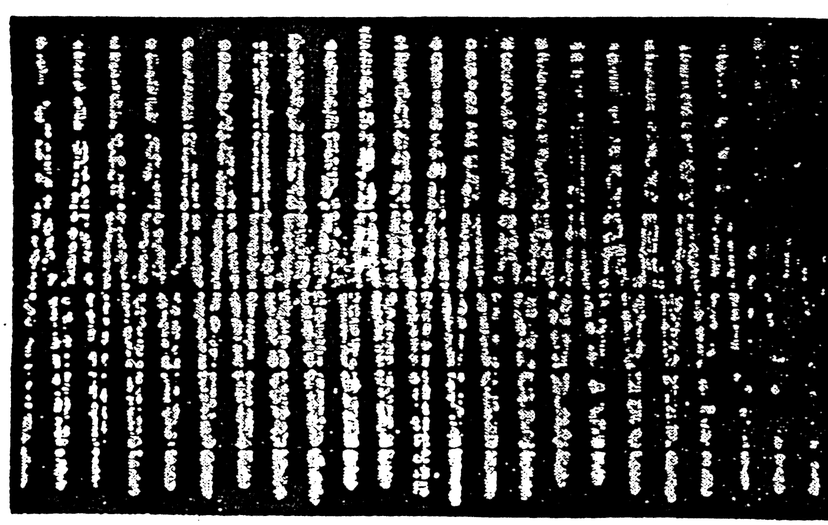

Ref: K. Ju

Track Profiles of MR1, MR2 and Dual-element

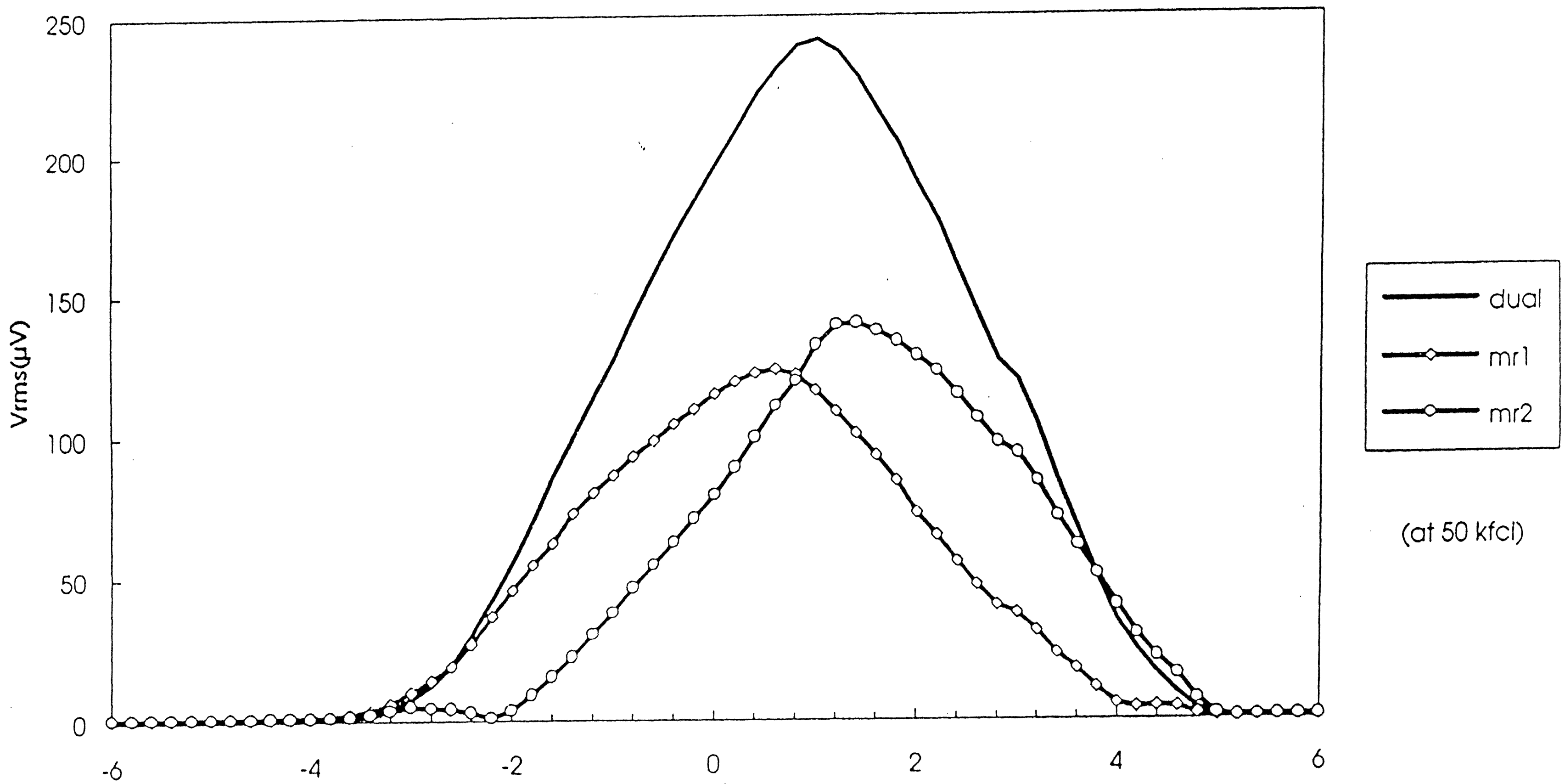

Approximate Formula

- **R. Smith has shown that the PW50 for a SAL/MR head can be approximately expressed as follows:**

$$PW50 \approx \sqrt{G^2 / 2 + 4(a+d)(a+d+\delta)}$$

- **Following R. Smith's method, one can prove that the PW50 for a DSMR head can be approximately calculated by:**

$$PW50 \approx \sqrt{(G^2 + (D+2t)^2) / 2 + 4(a+d)(a+d+\delta)}$$

Ref: K. Ju (Headway Technologies)

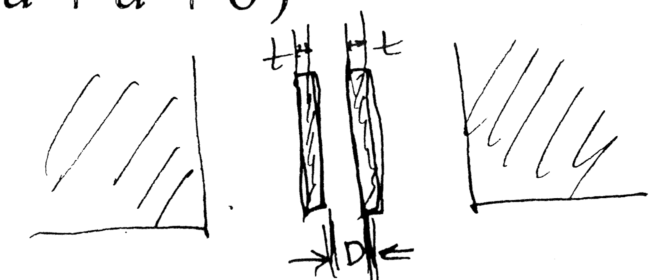

D = spacing between dual stripes

DESIGN AND OPERATION OF SPIN VALVE SENSORS

D. E. Heim
IBM Storage Systems Division, 5600 Cottle Rd., San Jose, CA 95193

R. E. Fontana, Jr., C. Tsang, V. S. Speriosu, B. A. Gurney, M. L. Williams
IBM Research Division, Almaden Research Center, 650 Harry Rd., San Jose, CA 95120

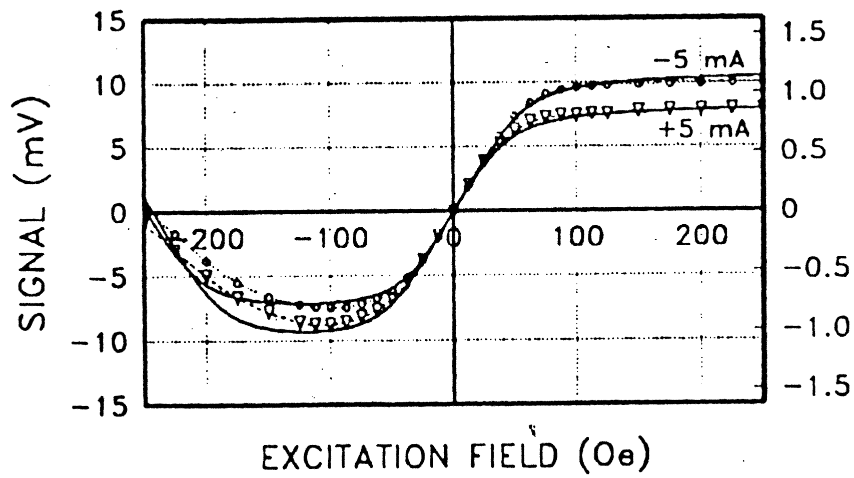

Fig. 5. Experimental transfer curve for the 2 μm high nano-layered spin valve sensor for +5 mA and -5 mA sense current. The solid lines are the computed transfer curves.

$$\Delta R \simeq \frac{\Delta R}{R} R_{\square\uparrow\uparrow} \frac{W}{h} \frac{<\cos(\theta_1 - \theta_2)>}{2} \tag{1}$$

where $\Delta R/R = (R_{\uparrow\downarrow} - R_{\uparrow\uparrow})/R_{\uparrow\uparrow}$ is the intrinsic magnetoresistance of the spin valve as measured on infinite samples, and $R_{\square\uparrow\uparrow}$ is the sheet resistance measured in the parallel magnetic state. W is the length of the sensor active region between the leads, and the notation $<\cdots>$ denotes averaging over the sensor height, h.

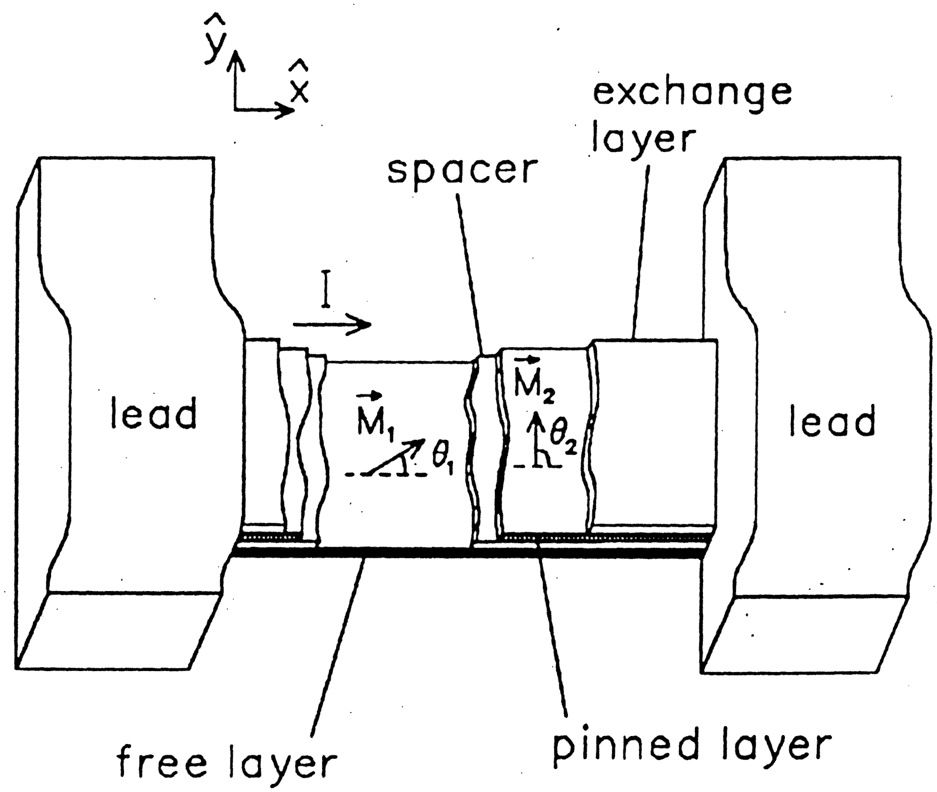

Fig. 1. Unshielded spin valve sensor.

$\frac{\Delta R}{R} \simeq 6\%$; $R \simeq 26\Omega$
$R_s \simeq 15\Omega/\square$ (h≃ ...)

29

Ref: Dieny, Humbert, Speriosu, Metin, Gurney, Baumgart, and Lefakis, Phys. Rev. B., 45, 806–813, Jan (1992).

TABLE I. Characteristic MR parameter A and "active" layer thickness t_0 for three series of samples of structure glass/$M(1)$(t Å)/Cu (22 Å)/NiFe (50 Å)/FeMn (80 Å)/Cu (15 Å), with $M(1)$=Co, NiFe, or Ni. The third row lists the values of $G_{rest}\rho_{M(1)}$ corresponding to the shunting by the rest of the structure.

Ferromagnet	A (%)	t_0(Å)	$G_{rest}\rho_{M(1)}$(Å)
Co	14.5	72	65
$Ni_{80}Fe_{20}$	9.6	72	85
Ni	5.1	85	65

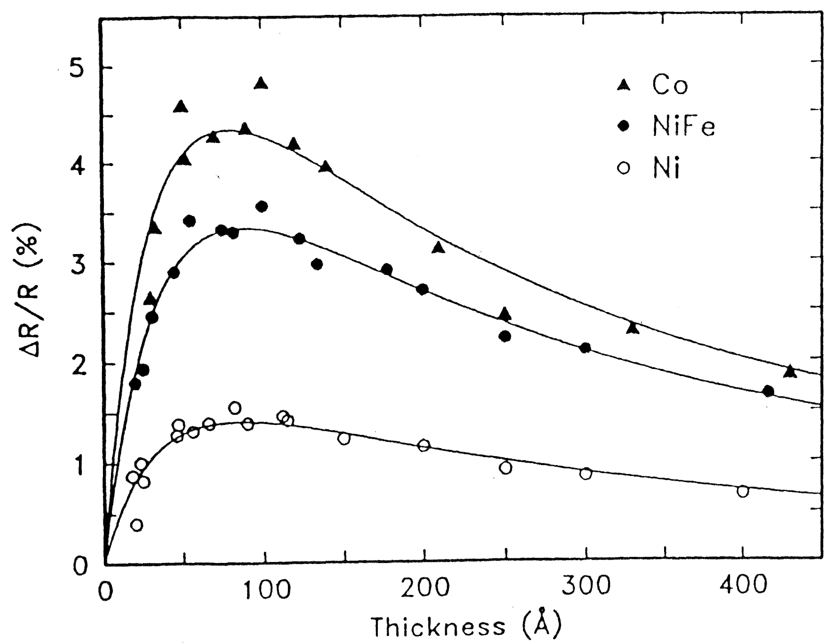

FIG. 9. Variation of the magnetoresistance versus the thickness of the "free" ferromagnetic layer $M(1)$, with $M(1)$=Co, NiFe, or Ni, at room temperature. The lines are two-parameter fits a' ding to Eq. (7).

$$\frac{\Delta R}{R}(t_{M(1)}) = A\frac{[1-\exp(-t_{M(1)}/t_0)]}{[1+(t_{M(1)}/G_{rest}\rho_{M(1)})]} \tag{7}$$

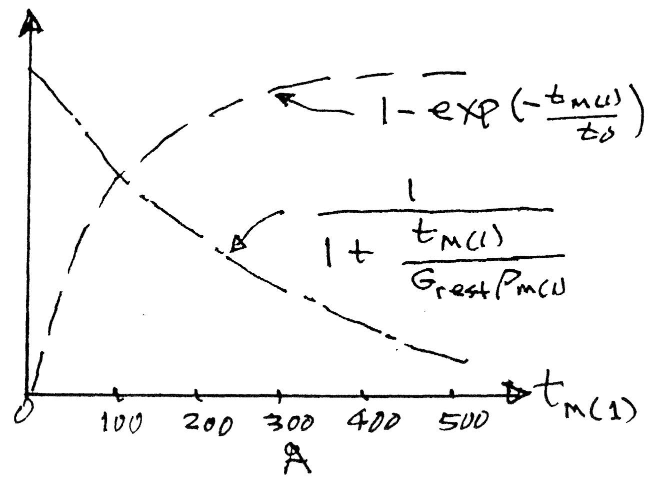

t_0 = thickness of "active" part of free layer $M(1)$. (at 0°K).

"Inactive" part of $M(1)$ has a resistance independent of orientation of magnetization in free layer.

30

Signal Estimates for Spin Valve/GMR Sensors:

$$Signal = I\Delta R \simeq I\,\frac{\Delta R}{R}\,R_s\frac{W}{h}\,\frac{\langle\cos(\theta_1-\theta_2)\rangle}{2}$$

Useful range of transfer curve is about +/- 0.5, or about half of the total (+/- 1.0). This preserves signal linearity, reduces amplitude asymmetry, and pulse broadening (second harmonic distortion.)

Sample calculation (unshielded SPV):

I = 5 ma; $\Delta R/R$ = 0.06; R_S = 15 ohms/square; W/h = 1.5

Signal = 3.38 mV (0-p)

Shielding reduces the amplitude by roughly 50% relative to the above number; this arises from flux leakage out of the SPV structure to the shields. That is, the effective ΔR (averaged over the stripe height) is more nearly equal to 3%. Thus, the signal in a shielded SPV/GMR head would be closer to 1.2 mV (0-p).

Resistance of Spin Valve Sensors is comparable to AMR sensors, thus electrical noise is about the same. Connection metallurgy and design may cause greater device resistance (increased electrical noise), but overall SNR is significantly improved (about7+dB). This is the gateway to higher areal densities.

Beyond Spin Valves: Multilayer GMR and Spin Tunneling Devices

Multilayer GMR Sensors: $\Delta R/R$ greater than 10%

- **May extend head technolgy beyond 10 Gb/sq.in.**
- **Significant process control issues (track width, etc.)**
- **Cip vs Cpp modes (signal vs track width control)**

Spin-Dependent Tunneling (SDT) Devices:

- **Very high resistances (10K-100K ohms) today**
- **RC time constant (bandwidth) issues to overcome**

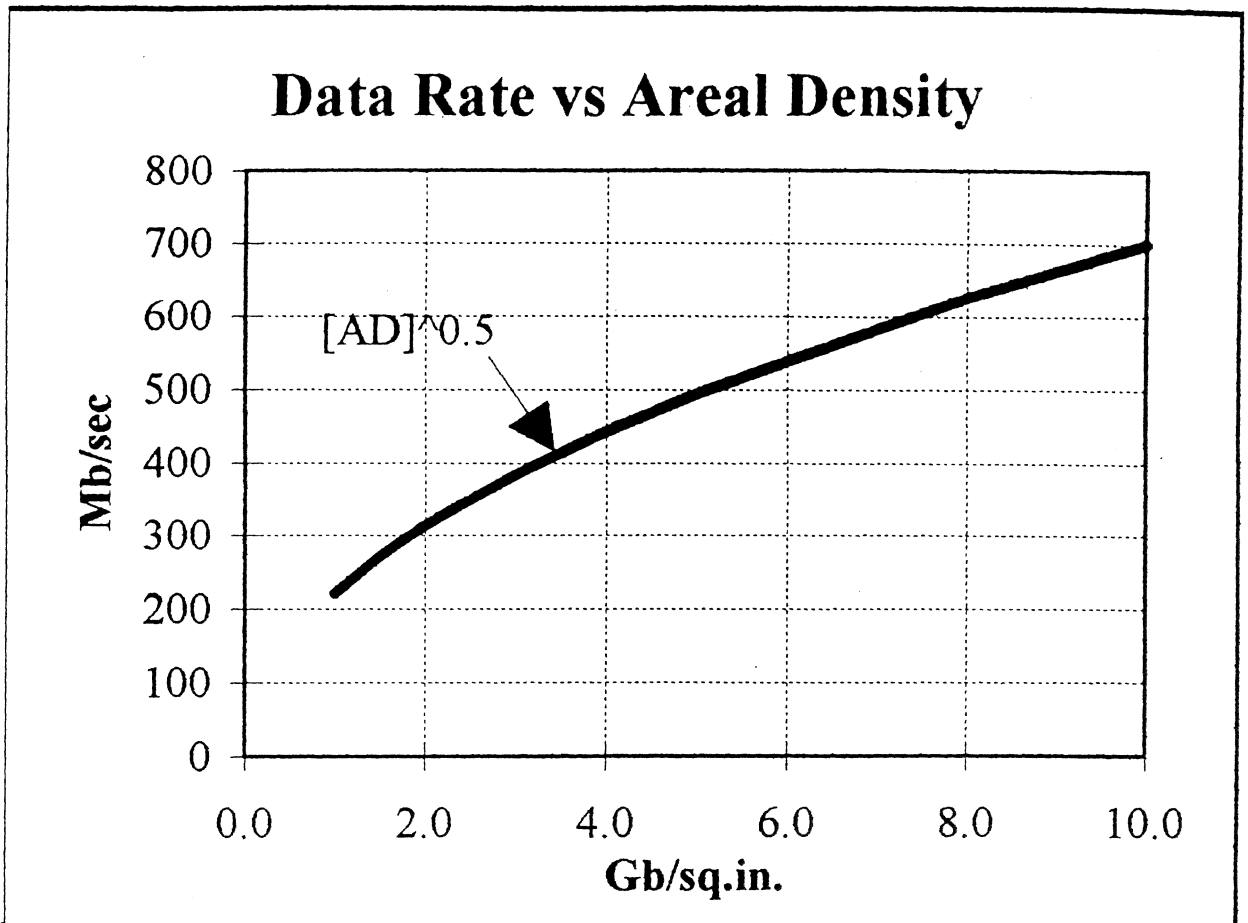
Data Rate vs Areal Density
800
700
600
500
400
300
200
100
0
Mb/sec
[AD]^0.5
0.0
2.0
4.0
6.0
8.0
10.0
Gb/sq.in.

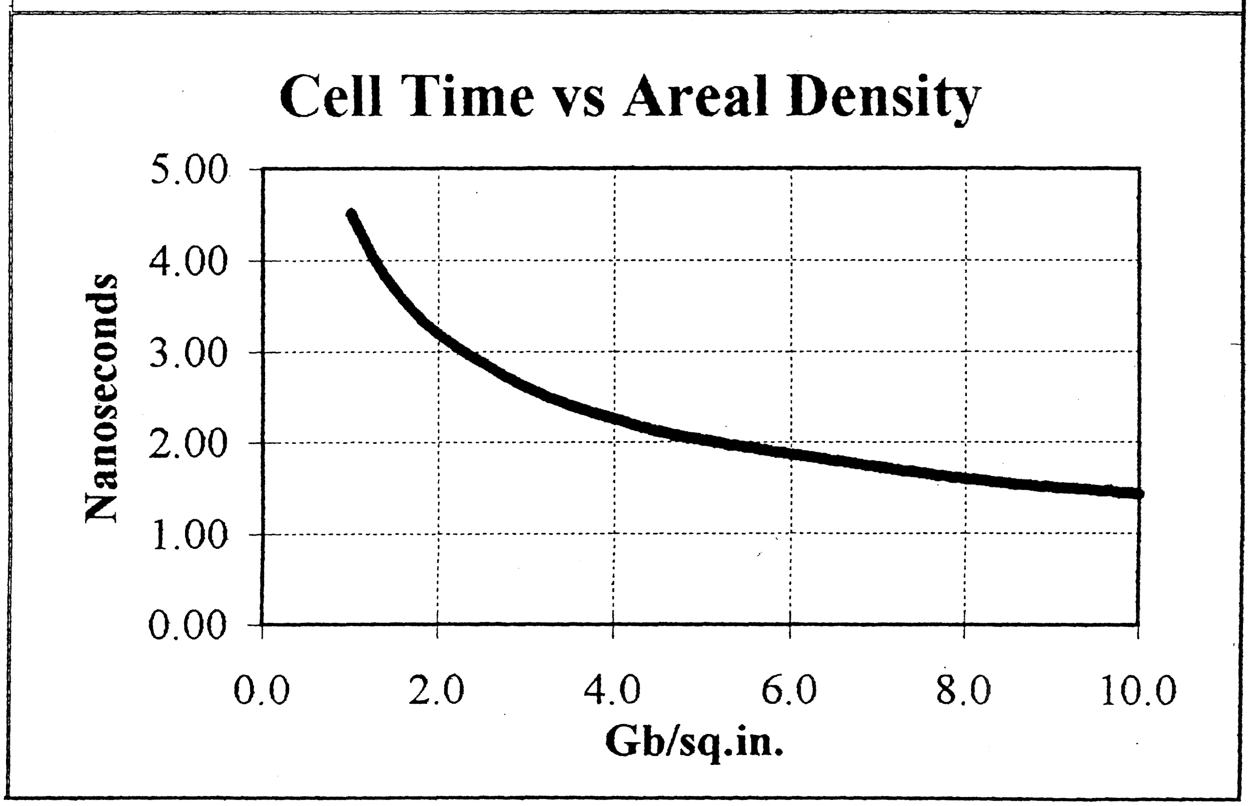
Cell Time vs Areal Density
5.00
4.00
3.00
2.00
1.00
0.00
Nanoseconds
0.0
2.0
4.0
6.0
8.0
10.0
Gb/sq.in.

(32)

Write Field Risetime Improvements

- **Reduce write head inductance**
    - **short yoke length**
    - **narrow yoke width**
    - **reduce number of turns**
    - **reduce head capacitance**

- **Reduce eddy current damping in head yoke**
    - **laminate yoke with insulating spacers**
    - **increase resistivity of yoke material**
    - **reduce magnetic permeability**
    - **reduce thickness of magnetic layers**

For step-input of applied field (H_a), flux density (B) response is

$$\frac{B}{\mu H_a} = 1 - \frac{8}{\pi^2}\sum_1^{\infty} \frac{\sin^2(n\pi/2)}{n^2} \exp\left(-n^2 \frac{t}{\tau}\right)$$

$$where\ \tau = \frac{4 \cdot 10^{-9} \mu P^2}{\pi \rho};\ P(cm);\ \rho\ (ohm-cm)$$

Ref: Bozorth "Ferromagnetism," 784f, Van Nostrand (1951).

Measured and Calculated B(t)

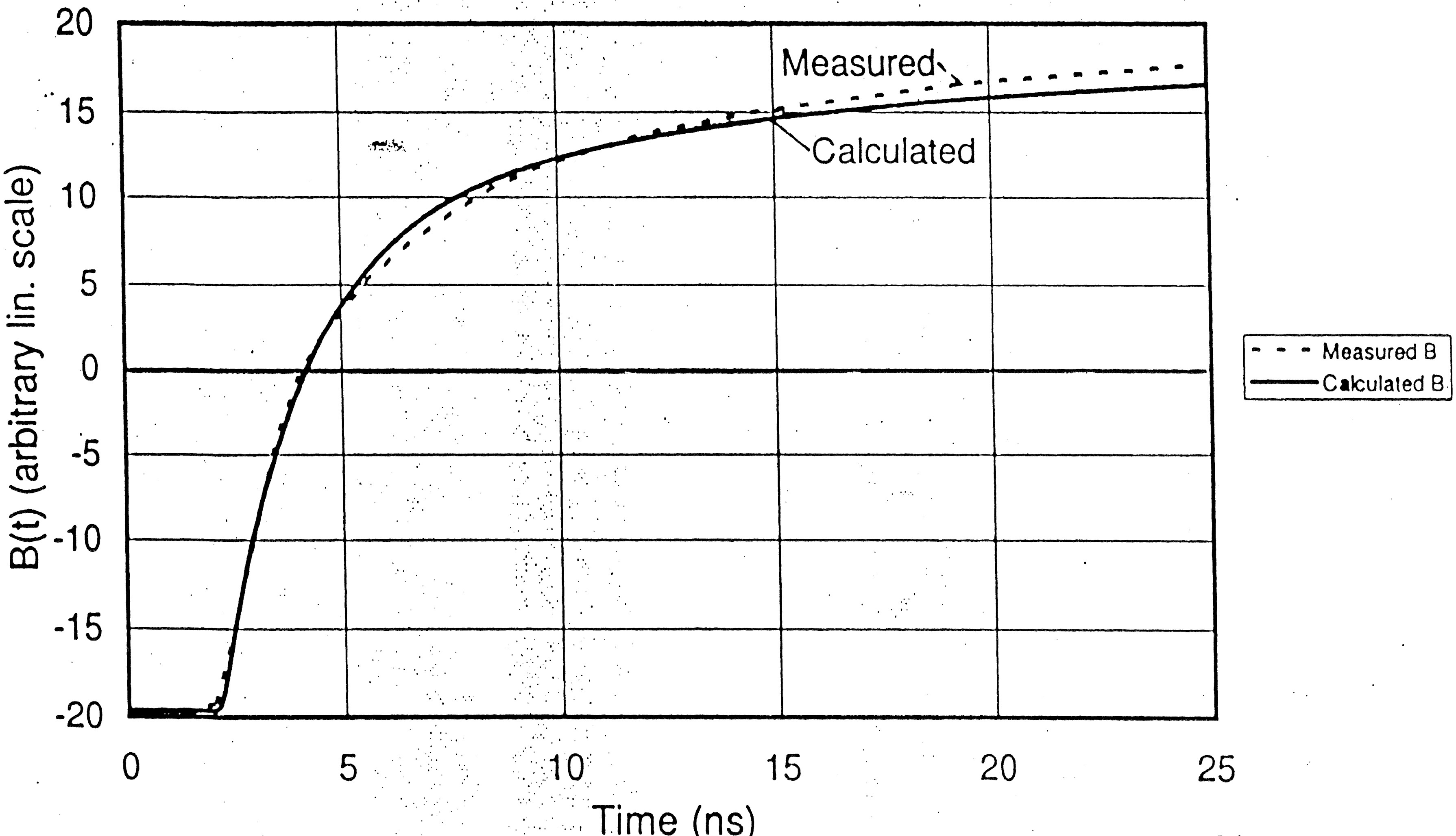

Klaassen K.B., Van Peppen J.C.L.,
"Flux reversal time in thin-film write heads",
Digest INTERMAG'95, paper HB-02, April 18-21 1995,
San Antonio, TX.

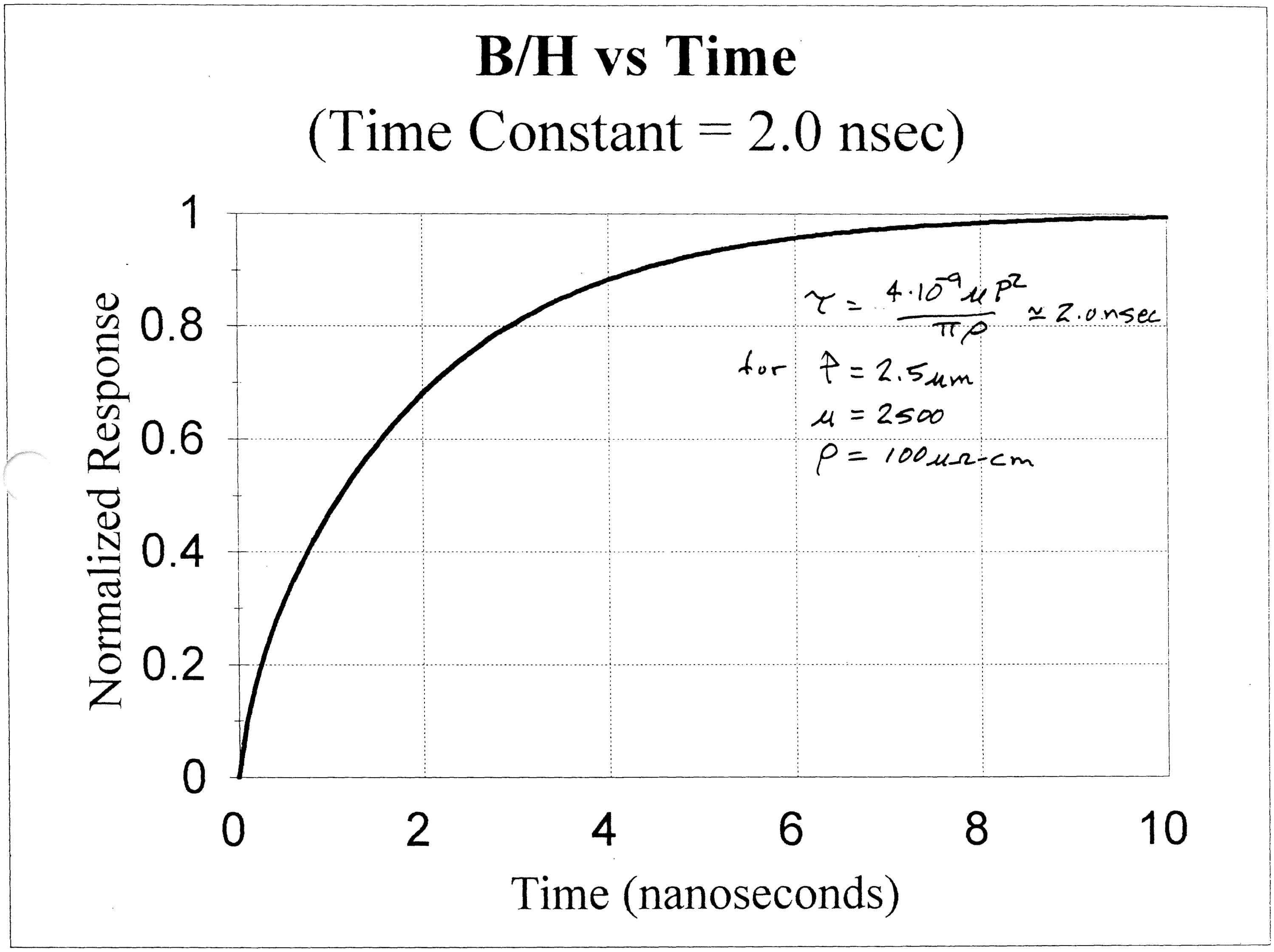
B/H vs Time
(Time Constant = 2.0 nsec)
Normalized Response
1
0.8
0.6
0.4
0.2
0
0
2
4
6
8
10
Time (nanoseconds)
$\tau = \frac{4 \cdot 10^{-9} \mu P^2}{\pi \rho} \simeq 2.0$ nsec
for $P = 2.5 \mu m$
$\mu = 2500$
$\rho = 100 \mu\Omega$-cm

Ref: P. Thayamballi

MODEL:

WRITING FIELD IN MEDIA IS SEPARATED INTO

$$H(x,y,t) = H_0(t)\, h(x-vt,\, y) \tag{1}$$

SPATIAL COORDINATE SYSTEM IS ATTACHED TO THE HEAD

KARLQUSIT HEAD FIELD APPROXIMATION FOR h(x-vt, y) *IS USED TO SOLVE FOR LOCATION x(H) AS A FUNCTION OF TIME*

$$x = -vt + \sqrt{\left\{\left(\frac{g}{2}\right)^2 - y^2 + \frac{gy}{\tan\left(\pi H / H_0(t)\right)}\right\}} \tag{2}$$

g REPRESENTS THE WRITING HEAD GAP,

y HEAD-MEDIA SEPARATION

Ho(t) FIELD AT GAP CENTERLINE

ASSUME HYPERBOLIC TANGENT FORM FOR Ho(t)

$$H_0(t) = H(0) + (H_{\max} - H(0))\tanh(t/\tau) \tag{3}$$

CONVERT FROM 10-90% RISETIME T_r *TO OBTAIN* τ

$$\tau = T_r / (\tanh^{-1} 0.9 - \tanh^{-1} 0.1) \tag{4}$$

Ref: P. Thayambulli

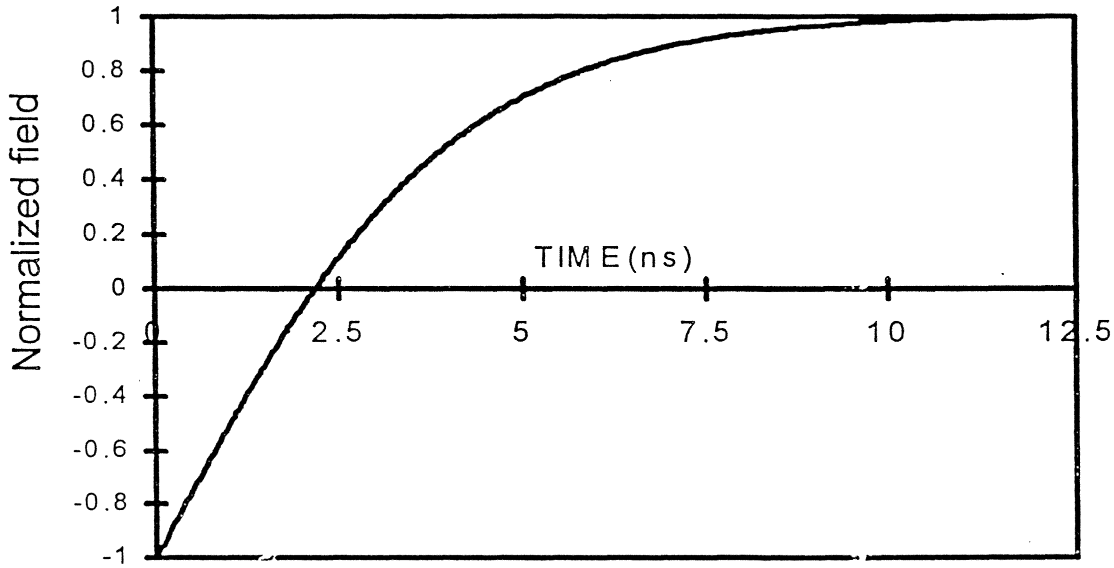

Fig. 1. Deep Gap Field Ho(t) switching from negative to positive with 7 ns risetime

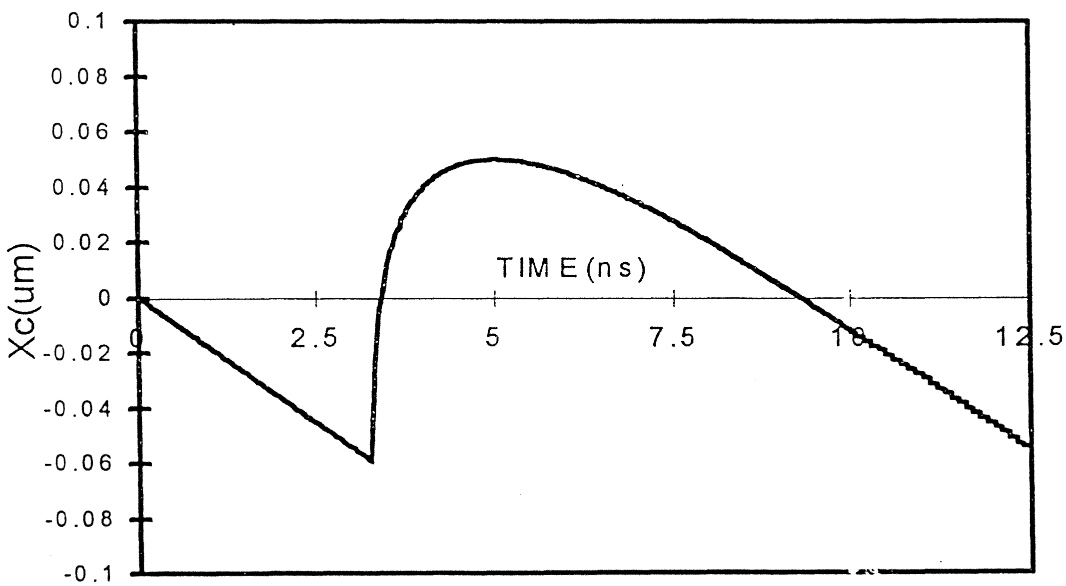

Fig. 2. Location of *H=Hcr* in the medium as a function of time according to Eq.(2).

Ref: P. Thayamballi

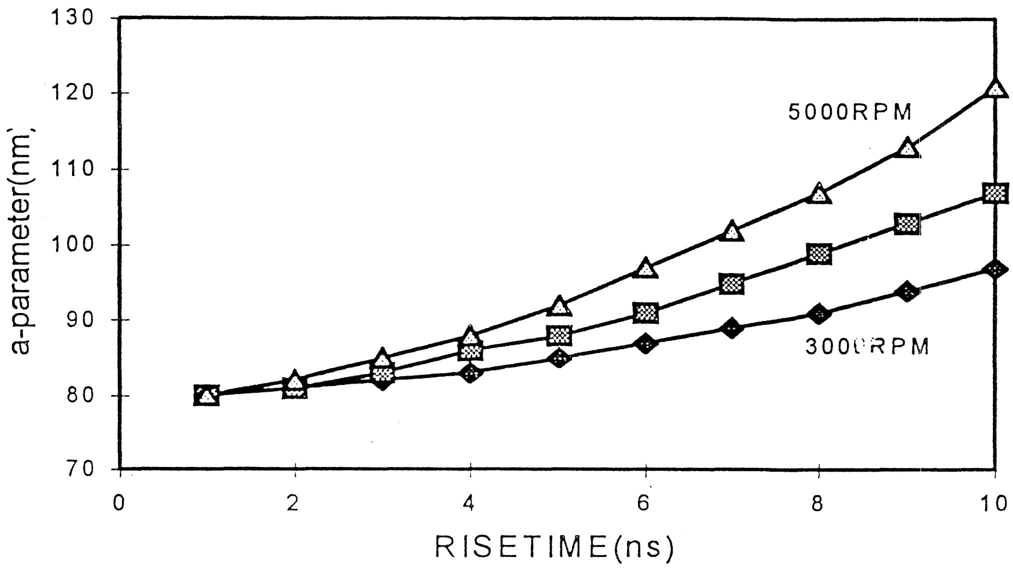

Fig.3. Calculated Transition parameters for 3000, 4000 and 5000 RPM.

Mr 680 emu/cc, δ 35 nm. Hc 1900 Oe , SS 0.85.
d 63 nm. velocity 1819 cm/sec at 4000 RPM.

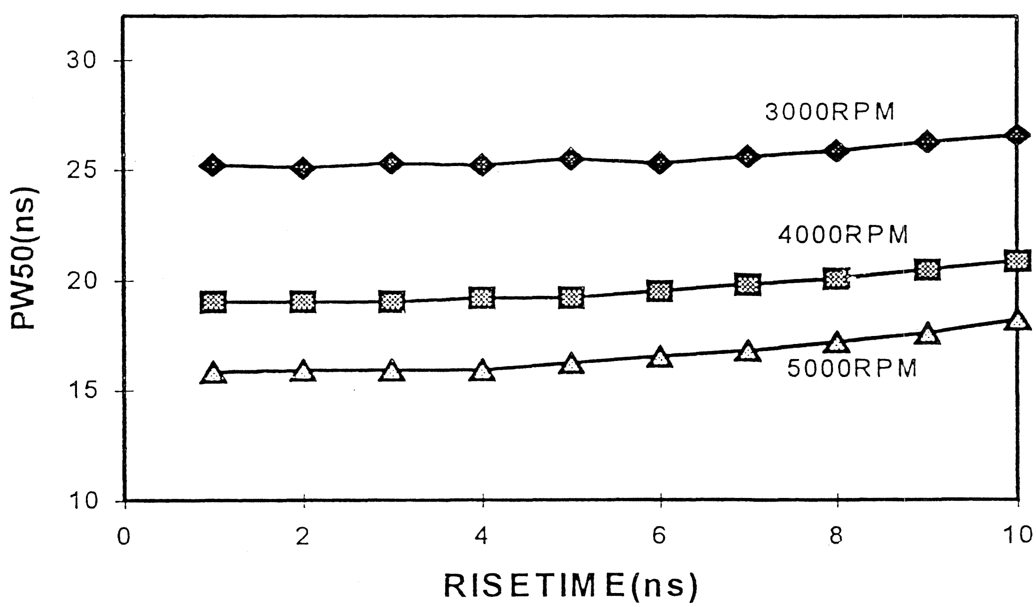

Fig.4. Calculated variation of PW50 for the cases shown in Fig. 3.

WRITE HEAD POLE TRIMMING

Ref: C. Tsang (IBM), IDEMA (1996)

- Gap Field = 1.0 (normalized)
- Contours show constant fields relative to gap $H_0 = 1.0$

SYMMETRICAL WRITE HEAD FIELD CONTOUR

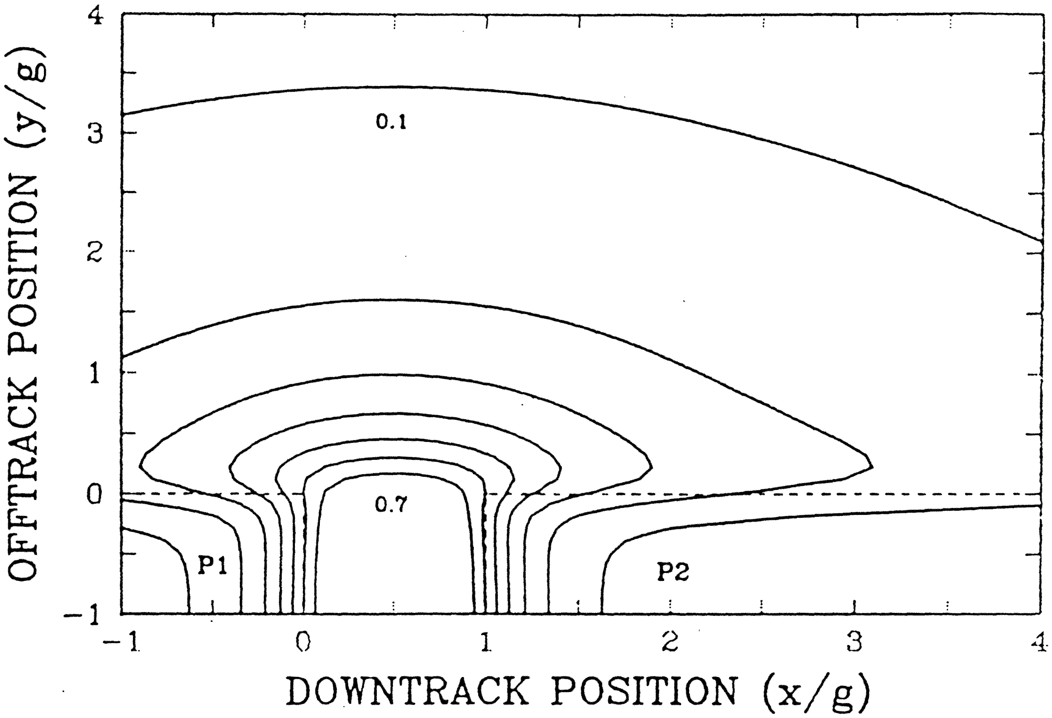

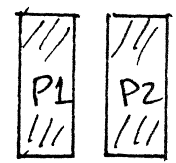

ASYMMETRICAL WRITE HEAD FIELD CONTOUR

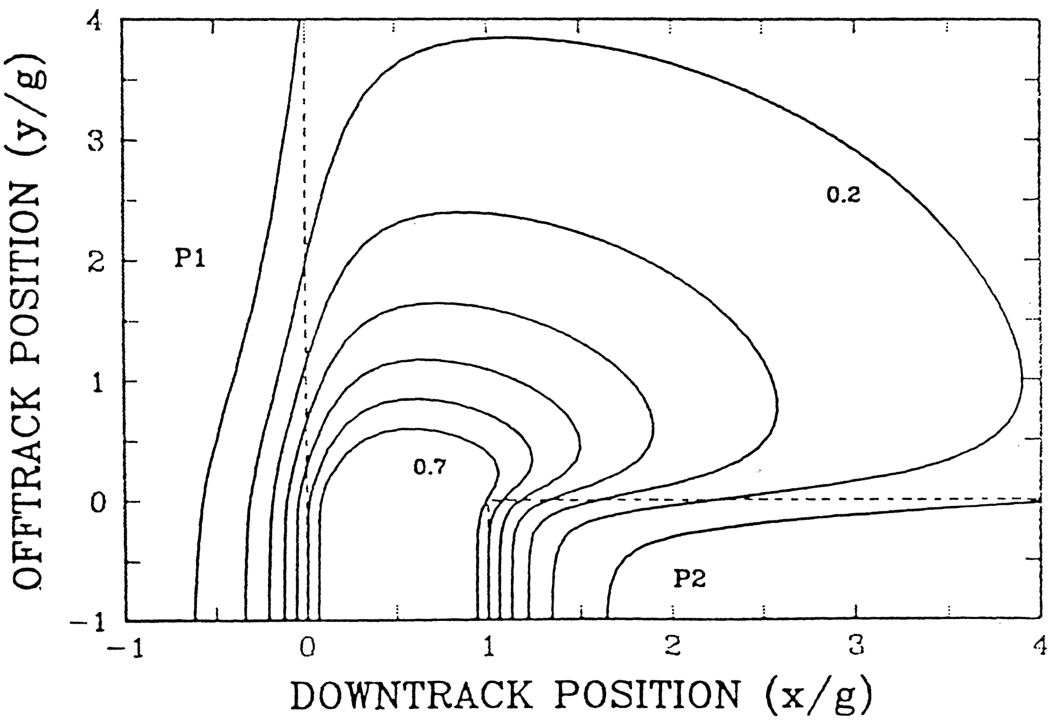

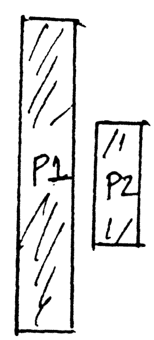

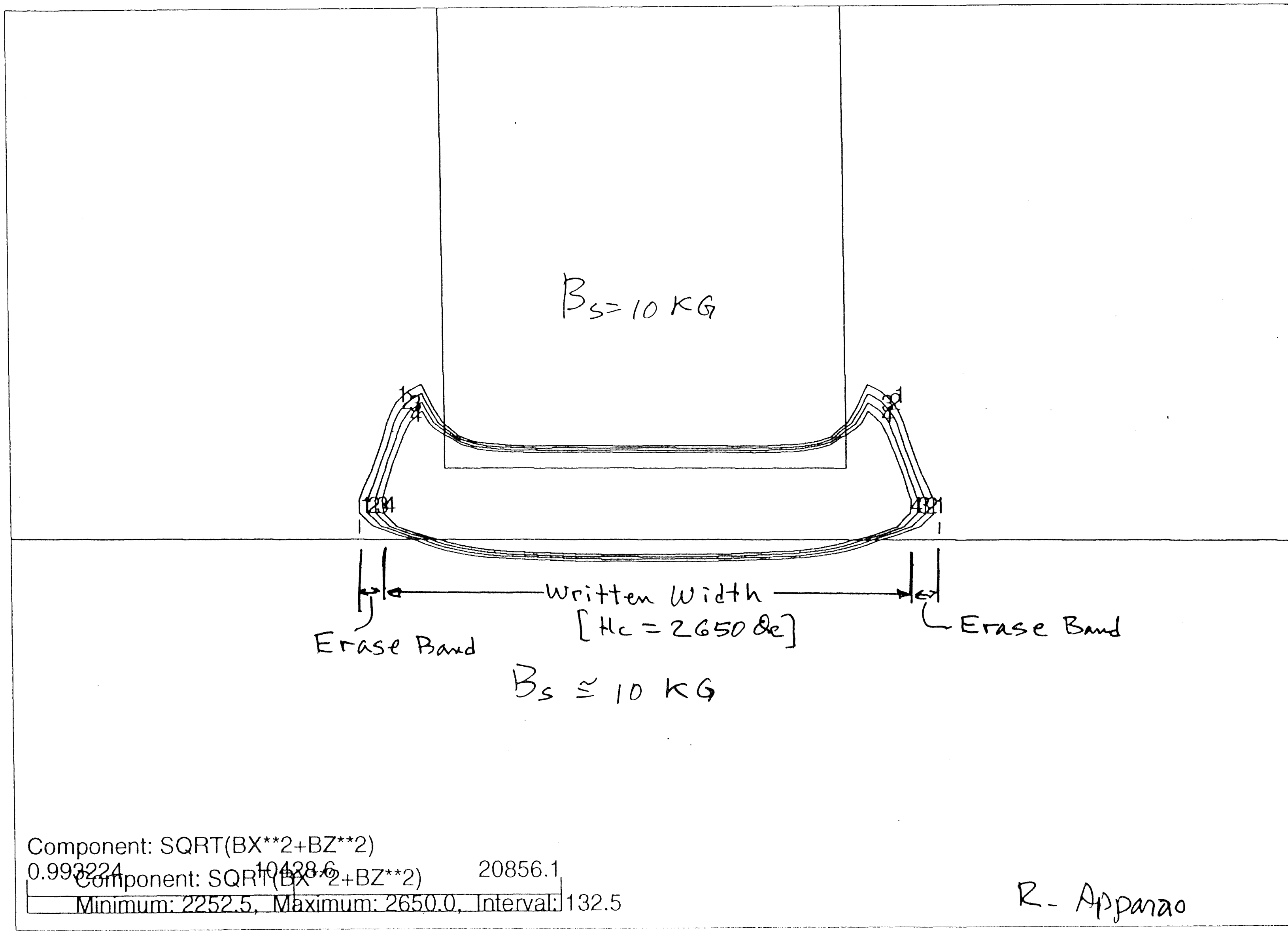

Bs= 10 KG
Written Width
[Hc = 2650 Oe]
Erase Band
Erase Band
Bs ≅ 10 KG
Component: SQRT(BX**2+BZ**2)
0.993224
10428.6
20856.1
Component: SQRT(BX**2+BZ**2)
Minimum: 2252.5, Maximum: 2650.0, Interval: 132.5
R. Apparao

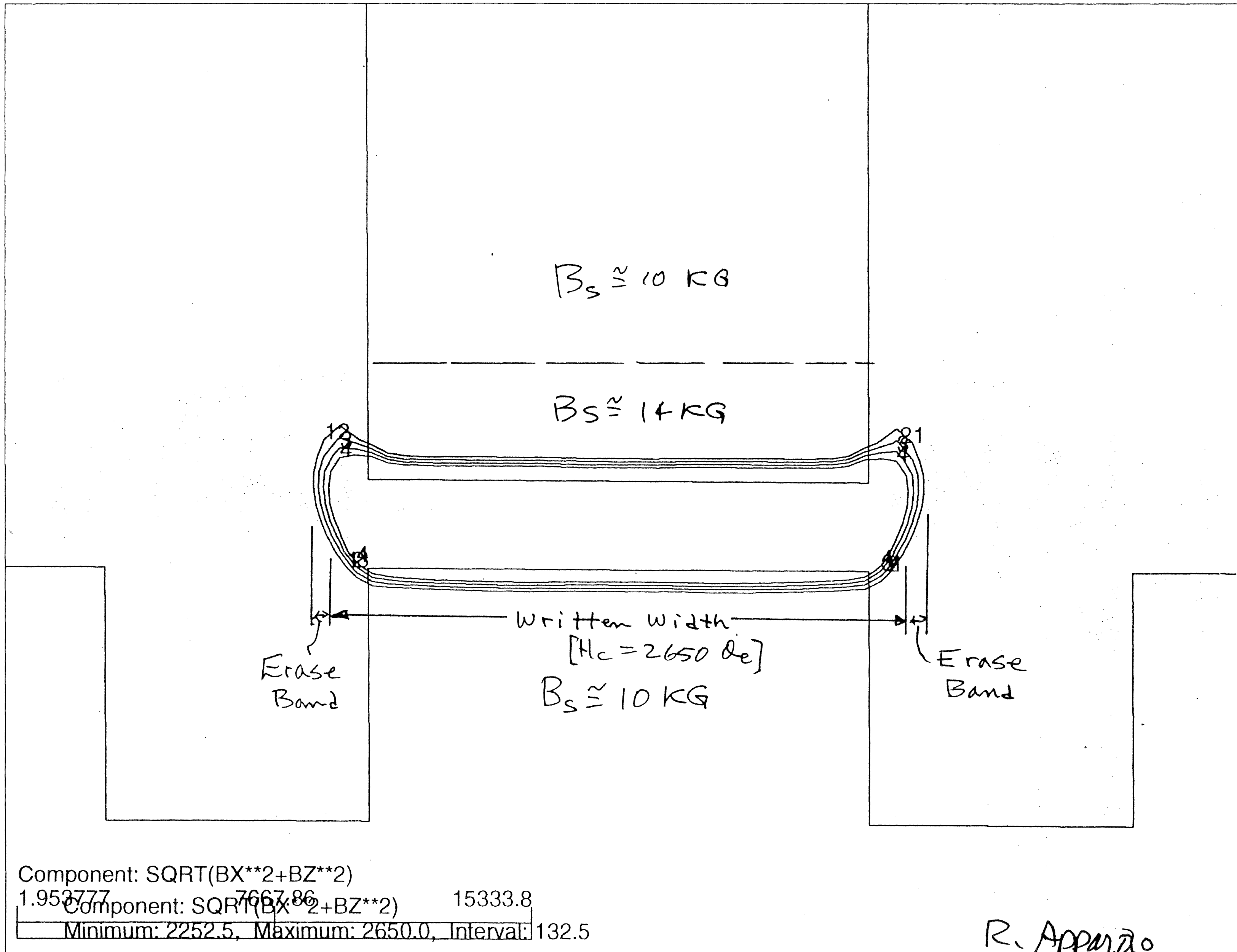

$B_s \cong 10$ KG
$B_s \cong 14$ KG
Written width
[$H_c = 2650$ Oe]
Erase Band
Erase Band
$B_s \cong 10$ KG
Component: SQRT(BX**2+BZ**2)
1.953777
7667.86
15333.8
Component: SQRT(BX**2+BZ**2)
Minimum: 2252.5, Maximum: 2650.0, Interval: 132.5

R. Apparao

Transition Parameter and Dependence on Head/Medium Properties

Ref: N. Bertram, "Theory of Magnetic Recording," Chap. 8

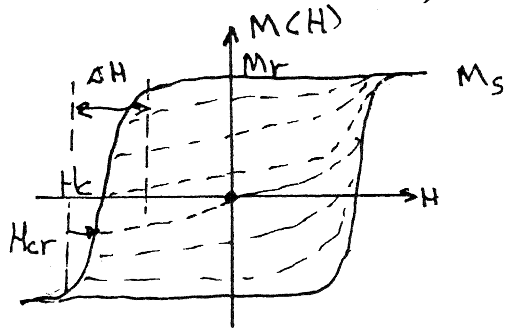

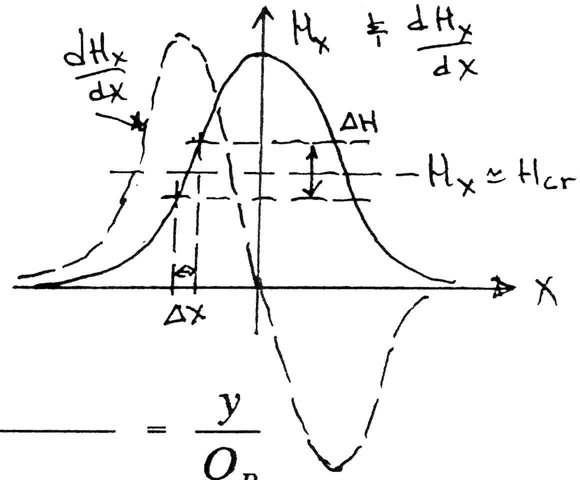

$$a_{dHx} = \frac{H_{cr}}{\frac{dH_h}{dx}(at\ H_x = H_{cr})} = \frac{y}{Q_B}$$

$$where\ H_{cr} = \frac{H_c}{R};\quad R = \frac{S^* + 3}{4}$$

$$Q_B = \frac{2x_o}{\pi g} \cdot \frac{H_o}{H_{cr}} \cdot \sin^2\left(\frac{\pi H_{cr}}{H_o}\right)$$

$$where\ \frac{x_o}{g} = \frac{1}{2}\sqrt{1 - (2y/g)^2 + \frac{4y}{g\tan(\pi H_{cr}/H_o)}}\ ;\quad (for\ H_o \geq$$

Williams-Comstock Theory for Transition Parameter

$$\frac{a_1}{R} = \frac{(1-S^*)}{\pi} \cdot a_{dHx} + \sqrt{\left[\frac{(1-S^*)}{\pi} \cdot a_{dHx}\right]^2 + \frac{2 a_o a_{dHx}}{R}}$$

$$\textit{where } a_o = \frac{2 M_r \delta}{H_c}$$

$$a_{WC} = \frac{a_1}{2R} + \sqrt{\left(\frac{a_1}{2R}\right)^2 + \frac{\pi a_o a_1}{4}}$$

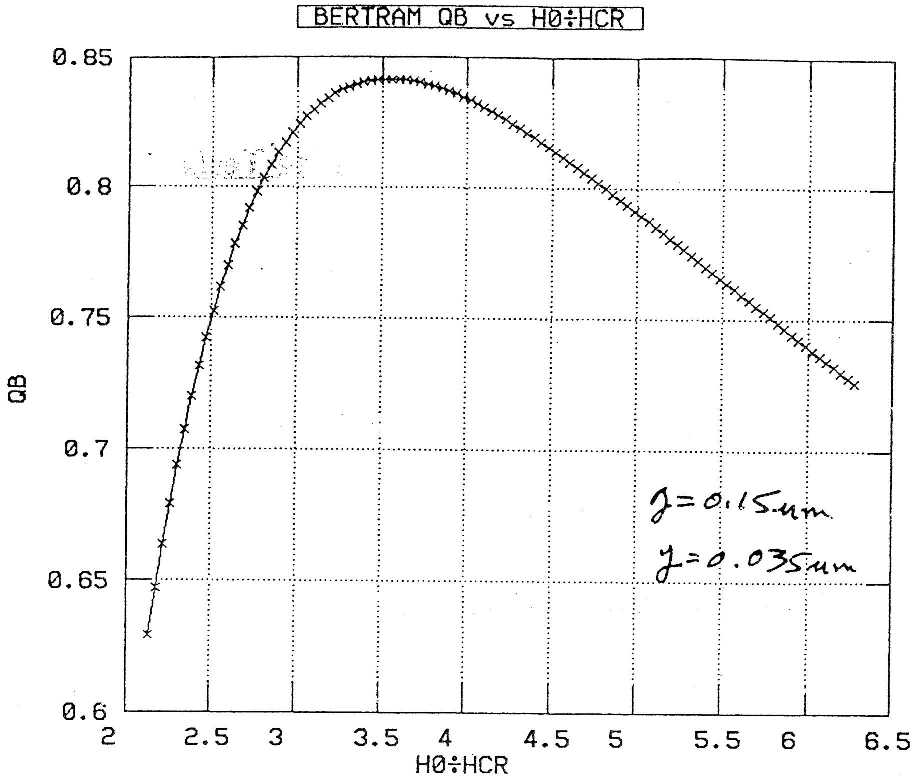
BERTRAM QB vs H0÷HCR
QB
H0÷HCR
g=0.15um
y=0.035um

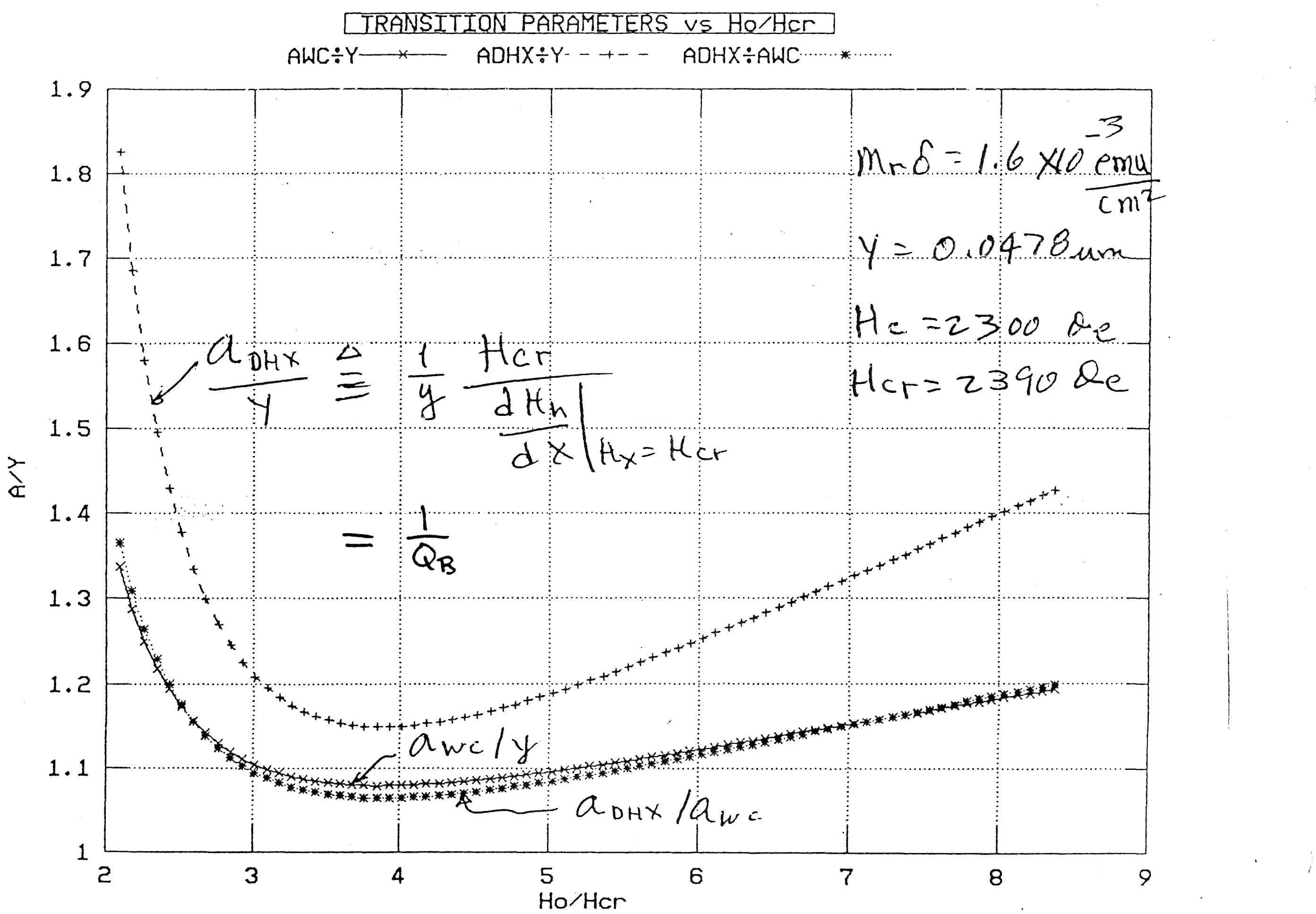
TRANSITION PARAMETERS vs Ho/Hcr
AWC÷Y
ADHX÷Y
ADHX÷AWC
A/Y
Ho/Hcr
Mrδ = 1.6 x10^-3 emu/cm^2
Y = 0.0478um
Hc = 2300 Oe
Hcr = 2390 Oe
a_DHX / y ≜ 1/y · Hcr / (dHn/dx)|Hx=Hcr
= 1/QB
awc/y
aDHX/awc

Magnetic and Electrical Writing and Reading Tests

- Read Head Signal (LF, MF, HF)

- Pulsewidth @50% (PW50)

- Amplitude Resolution (HF/LF, HF/MF, MF/LF)

- Amplitude Asymmetry of Read Output

- Amplitude Coefficient of Variation (ACOV)

- Offtrack-induced Amplitude Variation (Side-COV or SCOV)

- Overwrite (OW)

- Non-linear Transition Shift (NLTS)

- Error Rate vs Threshold (Sequenced Amplitude Margin)

- Pos. and Neg. Amplitude vs Bias Current (Bias Curves)

- Error Rate vs Offtrack Position (Bathtub Curve)

- Offtrack Capability vs Adjacent Track Pitch ("747" Curve)

- Read Signal Properties vs Write Current (Saturation Curves)

- Read Amplitude vs Offtrack Position (Track Amplitude Profile)

-